Interactie tussen waterstroming en macrofyten:
een experimentele en numerieke studie van stroming en sedimentatie in vegetatiepatches

Interaction between Water Flow and Macrophytes:
an Experimental and Numerical Study of Flow and Sedimentation in Vegetation Patches

Dieter Meire

Promotor: prof. dr. ir. P. Troch
Proefschrift ingediend tot het behalen van de graad van
Doctor in de Ingenieurswetenschappen

Vakgroep Civiele Techniek
Voorzitter: prof. dr. ir. P. Troch
Faculteit Ingenieurswetenschappen en Architectuur
Academiejaar 2013 - 2014

UNIVERSITEIT
GENT

ISBN 978-90-8578-718-1
NUR 956
Wettelijk depot: D/2014/10.500/64

Universiteit Gent
Faculteit Ingenieurswetenschappen en Architectuur
Vakgroep Civiele Techniek
Labo voor Hydraulica

Supervisor

Prof. dr. ir. P. Troch

Exam Committee

Prof. dr. ir. L. Taerwe (Ghent University)
Prof. dr. ir. H. Nepf (MIT, USA)
Prof. dr. ir. A. Folkard (Lancaster University, UK)
Prof. dr. ir. N. Verhoest (Ghent University)
Prof. dr. ir. T. De Mulder (Ghent University)
Prof. dr. S. Temmerman (University of Antwerp)
dr. ir. P. Rauwoens (Ghent University)

Research institute

Ghent University
Faculty of Engineering and Architecture

Department of Civil Engineering
Hydraulics Laboratory
Sint-Pietersnieuwstraat 41
B-9000 Ghent, Belgium

Tel.: +32-9-264.32.81
Fax.: +32-9-264.35.95

Research funded by a PhD-grant of the Special Research Fund of Ghent University (BOF).

Acknowledgements

Voor ik aan dit doctoraatsproject begon, vernam ik uit goede bron dat een doctoraat voor 10 % uit inspiratie bestaat en het overige uit transpiratie. Dat leek mij serieus overdreven in het begin, zeker wanneer het onderwerp van het onderzoek koele beekjes met waterplanten is. Gaandeweg werd de rol van dat zweten, als belangrijk deel van het doctoraatsonderzoek echter duidelijker, zeker tijdens de stevige eindsprint, in die laatste iets (te) intense maanden. Zo'n rit van start tot finish doe je nooit alleen, even uit de wind gezet worden kan deugd doen en een duwtje in de rug is meermaals noodzakelijk. Bij deze wil ik dan ook een aantal mensen bedanken voor hun bijdrage aan dit manuscript.

Prof. Peter Troch, mijn promoter, wil ik bedanken om mij de mogelijkheid te bieden om met een doctoraatsonderzoek te starten en mij gedurende dit doctoraat de vrijheid te geven om dat zelf zijn eigen, definitieve vorm te geven. Hiernaast wil ik zeker ook em. prof. Ronny Verhoeven danken voor de hartelijke ontvangst en toffe sfeer op het Labo Hydraulica en Prof. Tom De Mulder, om mij de kans te geven om nog één jaartje langer hier te vertoeven als assistent !

I also want to thank prof. Heidi Nepf to give a stranger/student from a small country far away the opportunity to join your lab in Parsons building. I enjoyed every moment of my time at the Vassar street and want to thank all the colleagues at MIT, for discussion moments or the TGIF's organised by the social committee. Especially thanks to John Kondziolka, for the many hours together cleaning the lab flumes and weighing tiny slides, and of course the lunches and frisbee hours !

Naast onderzoek was er ook ander werk, zoals lesgeven. In het bijzonder wil ik al mijn thesisstudenten bedanken, het leukste werk was voor mij dikwijls het helpen van anderen met hun werk: Ederic Keirsebelik, Richard Asamudu, Jan Putteman, Bert Schepens, Bruno Van Damme, Stephan Creëelle, Jef Benoit, Pieter Corthier, Pieter Claes, Steven Langenaken en Robin Lobelle.

Het Labo voor Hydraulica is gedurende de (iets langer dan gemiddelde) duur van mijn doctoraat totaal van samenstelling veranderd. Ik kwam aan als jong(ste) broekie en vertrok op twee enkelingen na, als persoon met de langste staat (van dienst) op het labo. Allen wil ik bedanken voor de toffe werksfeer: jong en oud, gepensioneerd & (nog) actief: Stefaan Bliki, Davy Haerens, Marcel Anteunis, Lien De Backer, Manuella de Kerpel, Yvan Blom, Binod Adhikari, Boudewijn DeCrop, Tomas Boelens, Laurent Schindfessel, Rebecca Roldan, Liesbet De Doncker, Geert Verhoeven, Stephan Creëelle, Anke Herremans, Serge Tichko and Edawi Wheida. Tomas (van Oyen) en Pieter Rauwoens, bedankt voor de vele discussies en praktische hulp bij de implementatie van de code ! Kevin, voor je enthousiasme ! Rest nog: Sieglien. Vanaf dag 1 samen op den bureau, al snel vergezeld door een schaap. Merci voor de vele toffe (bureau-)momenten.

Dit doctoraat was ook niet mogelijk geweest zonder de inbreng van de Ecobe collega's. Kerst, bedankt voor de vele discussie-uren, het samen schrijven en werken aan meerdere projecten ! Ook Jonas en Veerle wil ik bedanken, voor gezamenlijke meetcampagnes of enige uren computerwerk. Dimitri, die Pixy ... het spectaculaire eindresultaat was dan allesbehalve het beoogde resultaat, de „trainingen" waren altijd een leuk gebeuren.

Naast veel werk is er nog altijd vanalles daarbuiten! Merci aan alle vrienden voor de verfrissende en ontspannende momenten tussendoor. Speciale dank aan de Zomerstraat voor de aangename (en lekkere) keukenmomenten het laatste jaar en Sander, voor een koffiemomentje tijdens het dipje van de dag. Ik zal ze missen.

Een speciale woordje van dank is voor mijn ouders. Bedankt voor alle kansen die jullie mij gaven, alle tijd die jullie spendeerden en voor jullie onvoorwaardelijke steun en geloof. En broertjes, bedankt voor jullie onvoorwaardelijke capaciteit tot afleiding ...

En tot slot : Olivia ! Merci voor alles, je sceptische blik in je ogen wanneer ik over mijn tijdsplanning bezig was, en de resulterende koppigheid in mij waardoor het dan toch soms lukte, ... de vele toffe ontspanningsmomenten tussendoor en de steun en begrip op de lastige momentjes.

Allemaal bedankt !!

Dieter
Augustus 2014

Table of Contents

Acknowledgements **i**

List of Figures **vii**

List of Tables **xiii**

Nomenclature **xv**
1 List of symbols xv
2 List of acronyms xvii

Nederlandse Samenvatting **xix**

English summary **xxiii**

1 Introduction and Objectives **1**
1.1 Vegetated Flows: a fluvial context 1
1.2 Objectives 7
1.3 Outline of the PhD-manuscript 8

2 Macrophytes avoiding Hydrodynamic Stress **11**
2.1 Abstract 11
2.2 Introduction 12
2.3 Materials and methods 15
2.4 Results 20
2.5 Discussion 28
2.6 Conclusion 31

3 Interaction Between Neighbouring Vegetation Patches **33**
3.1 Abstract 33
3.2 Introduction 34
3.2.1 Previous work on flow adjustment to a single patch 35
3.2.2 Previous work on flow adjustment to a pair of obstructions 37
3.3 Material and methods 39
3.3.1 Velocity measurements 39
3.3.2 Deposition Experiments 41
3.3.3 Flow Visualization 43

3.4 Results 43
3.4.1 Velocity profiles on Patch Centerlines 43
3.4.2 Velocity Profiles on Centerline Between Patches 45
3.4.3 Deposition 56
3.5 Discussion 61

4 Depth-averaged Shallow Water Equations 63
4.1 Introduction 63
4.2 The Navier-Stokes Equations 63
4.3 From Navier-Stokes to Shallow Water Equations 65
4.4 Finding the depth-averaged Shallow Water Equations 67
4.5 Focus on turbulence assumptions 72
4.5.1 Algebraic Model 73
4.5.2 One-equation and two-equations model 74
4.6 Adapting the 2D-SWE for flow with vegetation 74

5 Implementation of the 2D-SWE in STRIVE 77
5.1 Introduction 77
5.2 The acronym STRIVE 77
5.2.1 What is STRIVE? 77
5.2.2 Flowchart of STRIVE 78
5.2.3 Extension of the STRIVE package 80
5.3 Numerical discretisation of flow equations 80
5.3.1 Introduction 80
5.3.2 Properties of numerical discretisation methods 81
5.3.3 Numerical grids 81
5.3.4 Discretisation methods 83
5.4 The TRIM methods 85
5.4.1 Introduction 85
5.4.2 Equations 86
5.4.3 Grid 86
5.4.4 Numerical approximation 87
5.5 The Lagrangian operator 89
5.6 Boundary conditions 92
5.6.1 Options for boundary conditions 92
5.6.2 Boundary corrections 93
5.7 Stability criteria 94
5.8 Implementation of vegetation 94
5.9 Implementation of the numerical method 94
5.10 Basic validation of the model 94
5.10.1 Conservation of mass 94
5.10.2 Backwater curves 97
5.11 Conclusion 97

6 Resistance of Vegetation 99
6.1 Introduction . . . 99
6.2 Flow resistance . . . 99
6.3 Flow resistance equations . . . 100
6.4 Energy losses caused by vegetative elements . . . 102
6.5 Resistance and vegetation: an overview . . . 103
6.5.1 Splitting the resistance into components . . . 103
6.5.2 Experience, tables and photographs . . . 104
6.5.3 The n-VR relationship . . . 106
6.5.4 Relation between vegetation biomass and Manning coefficient . . . 107
6.5.5 Blockage factors . . . 108
6.5.6 Velocity profiles . . . 109
6.5.7 The drag coefficient C_D . . . 120
6.6 An overview of studies using the 2D-SWE for vegetated flows . . . 123
6.7 Conclusion . . . 125

7 Simulation Results 127
7.1 Introduction . . . 127
7.2 Uniform vegetation . . . 127
7.2.1 Selection of the experiments . . . 128
7.2.2 Methodology . . . 129
7.2.3 Results . . . 131
7.3 Configurations with vegetation on 1 side . . . 136
7.3.1 Overview of the experimental studies . . . 136
7.3.2 Model settings . . . 137
7.3.3 Results . . . 138
7.4 Patches of vegetation . . . 149
7.4.1 Overview of the experimental studies . . . 149
7.4.2 Model Settings . . . 149
7.4.3 Results . . . 151
7.5 Patches of vegetation in a side-by-side configuration . . . 158
7.5.1 Overview of the experimental study . . . 158
7.5.2 Model Settings . . . 160
7.5.3 Results . . . 162
7.6 Discussion and Conclusion . . . 168

8 Conclusions and Recommendations for future Research 175
8.1 Answers on specific Research Questions. . . . 175
8.2 Recommendations for future Research . . . 178

References 181

A Appendix: Vegetation characteristics 197
A.1 Definition of geometric variables 197
A.2 Relation between geometric variables 197
A.3 Coefficients to calculate velocity profiles. 198
A.3.1 Parameters of Baptist et al. (2007) 198
A.3.2 Parameters of Klopstra et al. (1997) 199

B Appendix: Parameters of uniform vegetation 201

C Appendix: Model Description 207
C.1 Numerical approximation: full-matrix 207
C.2 Implementation in the STRIVE2D package 208
C.2.1 System module 208
C.2.2 Transwater module 212

D Appendix: List of publications 217
D.1 International journal publications - a1 217
D.2 International conference publications - p1 218
D.3 International conference proceedings - c1 218
D.4 National conference proceedings - c1 219

List of Figures

1.1 Examples of macrophytes for each described morphology. From top to bottom: (a) Common Reed (*Phragmites australis*, as an example of emergent vegetation; (b) *Callitriche platycarpa*, as an example of submerged vegetation (c) *Nuphar Lutea* as an example of floating plants with roots and (d) *Lemna* as an example of free-floating plants. 2

1.2 Schematic description of the relationships between the main components of the aquatic ecosystems under consideration. 3

1.3 Photographs of patchy configuration of vegetation in the rivers Desselse Nete and Zwarte Nete. 5

1.4 Schematic description of the potential feedback- and cascade processes with a heterogeneous distribution of vegetation patches. . . 6

2.1 Schematic overview of the in-situ flume. 15

2.2 An explanatory key for the 3-dimensional results from the test section with three viewpoints: plan view, cross section view and longitudinal view. The test section is longitudinally divided into three zones and divided into two cross sections. 16

2.3 Plan view of the stream wise (a), lateral (b) and vertical (c) depth-averaged velocities, expressed relatively compared to the incoming velocities. 20

2.4 Vertical profiles of the mean stream wise velocity in a cross section before the vegetation (a), through the vegetation (b) and behind the vegetation (c). 22

2.6 Plot indicating the relative zones of erosion and sedimentation (in cm) between the measurements of day 1 and day 4 within the test section of the field flume. Positive values indicate sedimentation, negative values indicate erosion. 23

2.5 Distribution of the turbulent stresses - $< u'w' >$, - $< u'v' >$ and - $< v'w' >$ in a cross section view through the vegetation (a), in a longitudinal view adjacent to the patch, on the edge between patch side and free flowing side (b) and in a longitudinal view through the vegetation (c). 24

2.7 (a) stream velocity deceleration behind the patch (%) in function of patch length and (b, c) stream velocity acceleration adjacent to the patch (%) in function of patch width, relative to flume width (%), and canopy depth, relative to total water height (%). 27
2.8 Measured drag force acting on a patch in function of patch length and repeated for three different stream velocities (■ = 0.1 m/s; ◆ = 0.2 m/s; ▲ = 0.3 m/s). These values are compared with calculated drag forces acting on the same patches in a rigid scenario. 29

3.1 Flow pattern around a porous patch, based on the characteristics explained in Zong and Nepf (2012) and Chen et al. (2012). The bottom plot depicts the stream wise velocity along the centerline of the patch. 36
3.2 Schematic top-view of the flume close to the model vegetation patches (circles), not to scale. The positions of the velocity measurements are indicated by heavy crosses, the positions of the deposition slides are indicated by gray rectangles. 40
3.3 Overview photographs of the deposition measurements. 42
3.4 Time-mean, streamwise velocity U normalized by the upstream velocity U_∞, along streamwise coordinate (x) on patch centerlines. (A) Dense patches with gap width Δ/D = 0.5 (B) Dense patch pair with gap width Δ/D = 0 (C) Sparse patch pair with gap spacings Δ/D = 0 and 0.5. 45
3.5 Time-mean, streamwise velocity U normalized by the upstream velocity U_∞, along streamwise coordinate (x) on the centerline between the patches. (top) High-flow blockage case (bottom) Low-flow blockage case. 48
3.6 Maximum velocities at the center of the gap and 5 cm behind the dense (De) and sparse (Sp) patches for the different patches diameters (D = 11 and D = 22 cm) as a function of the gap width Δ/D. 50
3.7 Length of the potential core of the gap jet L_j is a linear function of gap width Δ for the sparse and dense patches. 51
3.8 Example of fitting measured centerline velocity, U_c, to the jet spreading model to obtain the kinematic spreading coefficient γ_u for the sparse patch case with Δ = 5 cm. 52
3.9 Minimum velocity on the centerline between patches (U_{min}) as a function of gap width (Δ/D, $D = 22$ cm). 53
3.10 Lateral velocity profiles of streamwise velocity behind two dense patches (D = 22 cm) with a gap width of 11 cm. 55
3.11 Streamwise velocity (U, top) and turbulent kinetic energy (TKE, bottom) versus streamwise position (x/D) along the centerline between two patches (center, y = 0) and along a patch centerline (patch, y = ($D + \Delta$)/2). 56

3.12 Images of Rhodamine WT injected at the center of the gap between the two patches (y = 0) and the edge of one patch (y = Δ/2+D) at a gap width of Δ/D = 0.5. A dense patch pair (image left) and sparse patch pair (image right) is shown. 56
3.13 Deposition results for a gap distance of 11 cm ($\Delta/D = 0.5$) for two dense patches. 59
3.14 Deposition results for a gap distance of 2 cm ($\Delta/D = 0.1$) for two dense patches. 59
3.15 Deposition results for a gap distance of 0 cm ($\Delta/D = 0$) for two dense patches. 59
3.16 Deposition results for a gap distance of 11 cm ($\Delta/D = 0.5$) for two sparse patches. 60
3.17 Deposition results for a gap distance of 2 cm ($\Delta/D = 0.1$) for two sparse patches. 60
3.18 Deposition results for a gap distance of 0 cm ($\Delta/D = 0$) for two sparse patches. 60
3.19 Two patches in relatively close proximity can create a secondary deposition zone due to the interactions of their wakes (top) that, over time, may cause enhanced growth and lead to patches merging together and growing beyond a lateral scale of D (bottom) . . 62

4.1 Left: Definition of the Cartesian coordinate system, with indication of x, y and z orientation. Right: Definition of reference plane and indication of the variables z_s, z_b, H and η. 66

5.1 Flow chart of STRIVE, originally set up for a 1D-framework. . . . 78
5.2 A spatial distribution of vegetation in a river reach, with its implication on the velocity vector field. 79
5.3 Example of structured ((a) and (b)) and unstructured grid types (c). Grid (a) is a rectangular, orthogonal, structured grid. Grid (b) is a curvilinear, orthogonal structured grid and grid (c) is an unstructured grid. 82
5.4 Example of collocated (left) and staggered grid (right). 83
5.5 Different approximations of a derivative of a function f with an arbitrary argument x (adapted from Ferziger and Peric (2002)). . . 84
5.6 Schematisation of the grid and indication of the position where the variables are calculated. Figure from Martin (2004). 86
5.7 Schematisation of the path tracing on the grid. 90
5.8 Flow chart of the basic structure of STRIVE2D. 95
5.9 Flow chart of the Dynamics module of STRIVE2D with two modules implemented: the System and Transwater module. 96

6.1 Point, cross-section and reach resistance space scales. 101
6.2 Patches placed in a flow, experiencing (a) form drag and (b) viscous drag. 102

6.3 Photograph of river to estimate Manning's roughness. 106
6.4 The relation of the Manning coefficient n with the product of V and R. 107
6.5 A schematised, representative cross-section occupied with vegetation patches. The thick line indicates the wetted perimeter as defined: (a) Conventionally (b) Effective wetted perimeter. 109
6.6 Schematised vertical profile for a submerged vegetation canopy, representing a 2-layer approach. 111
6.7 Vertical velocity profile, as schematised in a three-layer approach. The figure is taken from Hu et al. (2013). 117
6.8 Depth-average velocity predicted by different equations for a dense canopy in function of the submergence rate k/H. 120
6.9 Depth-average velocity predicted by different equations for a sparse canopy in function of the submergence rate k/H. 120
6.10 Overview of the different cutting management strategies investigated by Leu et al. (2008). 123
6.11 Model results presented by Ball et al. (1996) for a patch, modelled using a drag coefficient C_D of respectively 1.9 (above) and 19 (below) and a Manning coefficient of respectively 0.3 and 0.94. . . 124

7.1 Indication of geometrical parameters on planview, the vegetation section is indicated by a gray zone. 128
7.2 Overview of the experimental data used to validate the resistance models, presented by the range of submergence (k/H) and the Reynolds number (Re_H) based on the flow depth (H). 129
7.3 Overview of the relationship between observed and predicted Manning coefficients for the different cases. 133
7.4 Overview of the relationship between observed and predicted Manning coefficients for all cases. 136
7.5 Overview of the definition of the parameters L_v and B_v for experiments with emergent vegetation on one side of the flume. 137
7.6 Planview of the averaged, streamwise velocities U normalised by the upstream velocity U_∞. 139
7.7 Model simulations of a longitudinal profile through the vegetation at y = 0.2 m for sparse (top) and dense (bottom) vegetation at low flow conditions. 140
7.8 Normalised streamwise velocity at the leading edge (x = 0 m) and in the developed region (x = 7 m) of the vegetation patch in function of the drag coefficient C_D. 141
7.9 Model simulations of a longitudinal profile for the sparse (top) and dense (bottom) vegetation at different flow conditions, namely low flow (Ul), medium flow (Um) and high flow (Uh) for C_D = 2. . . 144
7.10 Model simulations of a lateral profile for the sparse (top) and dense (bottom) vegetation at low flow conditions. 146

7.11 Model simulations of a lateral profile for the dense vegetation at high flow conditions. 148
7.12 Overview of the configuration with an emergent vegetation patch of diameter D in the center of the flume. The vegetation zone is indicated by the gray area. 149
7.13 Planview of a simulation result of the normalised streamwise velocity for a patch with a density of 3333 dowels per unit area and a drag coefficient C_D of 2. 151
7.14 Measurement (Zong and Nepf, 2012) and simulation results, using a value of 1, 2 and equation7.7 for C_D for the velocity in the steady wake zone behind the patch. 153
7.15 Mean Manning coefficient in the patch for simulations with C_D = 1, C_D = 2 and C_D calculated using the method of Tanino and Nepf (2008). 153
7.16 Overview of centerline velocity profiles of the normalised stream wise velocity. Simulations are shown for patches consisting of 12833 dowels per m^2 in the left plot and 3333 dowels per m^2 in the plot on the right. 154
7.17 Planview of the simulation output after 5000 s (top) and time-averaged simulations (bottom). 155
7.18 The normalised stream wise velocity in the centerline of the patch. Simulations are shown for different values of α_0. 155
7.19 Planview of the viscosity coefficient ν_t using a depth-averaged parabolic eddy viscosity model (top) and a depth-averaged mixing length model (bottom). 156
7.20 Planview of a simulation result after 20 000 s of simulation. The normalised stream wise velocity for a patch with a density of 12833 dowels per unit area and a drag coefficient C_D of 2 is depicted. . . 157
7.21 Planview of a simulation result after 10 200 s of simulation. The normalised stream wise velocity for a patch with a density of 12833 dowels per unit area and a drag coefficient C_D of 2 is depicted. . . 158
7.22 Time-evolution of the normalised streamwise U and lateral V velocity at three points on the centerline of the patch, indicated in Figure 7.21. 159
7.23 Time-evolution of the normalised streamwise U and lateral V velocity at three points on the centerline of the patch, indicated in Figure 7.21. 159
7.24 Overview of all the configurations (combination of patch sizes and gap distances) used in the experiments of Vandenbruwaene et al. (2011) and simulated with the 2D-model. 161
7.25 Planview of the streamwise velocity U for patch sizes D of 2 m and a gap distance of Δ = 0.3 m. 162
7.26 Lateral, normalised velocity profiles of the stream wise velocity U over one half of the flume. Both measurements and simulations for 3 different gap spacings and 3 different patch sizes are shown. 163

7.27 Lateral, normalised velocity profiles of the stream wise velocity U over one half of the flume. Both measurements and simulations for 3 different patch sizes are shown, with a size of respectively D = 3 m, D = 2 m and D = 1 m. The gap distance Δ is constant and amounts 0.3 m. 164
7.28 Lateral, normalised velocity profiles of the streamwise velocity U, one half of the flume is shown. Simulations for 3 different patch sizes, with a size of respectively D = 3 m, D = 2 m and D = 1 m. The gap distance Δ is constant and 0.3 m. 165
7.29 Lateral velocity profiles of the streamwise velocity U over one half of the flume. Both measurements and simulations for 4 different gap spacings, Δ = 3 m, Δ = 1.3 m, Δ = 0.3 m and Δ = 0 m are shown. The patch size is constant and equal to 2 m. 166
7.30 Three lateral, normalised velocity profiles of the streamwise velocity U over one half of the flume are depicted at x = 1.75 m, x = 5 m and x = 7 m. 167
7.31 Lateral velocity profiles of the streamwise velocity U over one half of the flume for different incoming velocities U_∞ of 0.1 m/s, 0.2 m/s and 0.3 m/s respectively. 168
7.32 Distribution of the calculated residence times using a 1D-approach (uniform vegetation) and 2D-approach (vegetation on 1 side). The number of dowels was equal for both calculations. 173

C.1 Grid layout for the 2D-SWE using a cartesian, staggered grid. . . 208
C.2 Position of the computational nodes for water surface elevation. . 209
C.3 Definition of the neighbouring cells of cell (i,j). 210
C.4 Definition of the neighbouring faces of cell (i,j). 210
C.5 Non regular grid with several options. Every white box represents a section with another option and has its own length. 211
C.6 Non regular grid with several options. Every white box represents a section with another option and has its own length. 211

List of Tables

2.1 Sedimentation quantity and median grain size derived after 4 days with circular plate sediment traps. 25
2.2 Average values with standard error of patch characteristics at an incoming stream velocity of 0.1 m/s (U_I) and the changes of these values with increasing stream velocities compared to U_I. 26
2.3 Values of C_D and β (see equation 2.5) for the different canopy lengths and different incoming velocities. 28

3.1 Summary of measurements performed. 39
3.2 Steady wake velocities U_1 normalized by the upstream velocity U_∞ for D = 22 cm. The steady wake length L_1 is estimated from longitudinal transects in U, as in Zong and Nepf (2012). 46
3.3 Parameters describing the velocity evolution on the centerline for sparse and dense patches at different gap distances. 47
3.4 Overview of the kinematic spreading coefficients γ_u for the different gap spacings for the dense and sparse patches. 52
3.5 Overview of the deposition measurements. 57

5.1 Overview of the options implemented for the calculation of the Lagrangian trajectory (LT), the advection and diffusion terms. . . 92
5.2 Overview of a backwater curve calculation. 97

6.1 Reference tables for Manning's n values from Chow (1959). A selection for channels with vegetative flow involved is made. . . . 105
6.2 Overview of empirical relations between the blockage factor B and Manning coefficient n or n_4 for different studies. 110
6.3 Table with an overview of the expressions to calculate the Manning roughness parameter n based on the depth-averaged velocity description, by different authors. 121
6.4 Overview of studies using the depth-averaged Shallow Water Equations to study vegetated flows. 126

7.1 Overview of the experiments with uniform vegetation used to validate the performance of the implemented vegetation resistance models and the range of parameter values used herein. 129

7.2 Goodness of fit (GOF) values for the comparison between the measured Manning coefficients and the model results with the methods of Baptist et al. (2007) and Huthoff et al. (2007) as resistance formulas. 132
7.3 Parameters of the linear fit $y = ax + b$ between measured and predicted Manning coefficients. 134
7.4 Parameters of the linear fit $y = ax$ between measured and predicted Manning coefficients. 135
7.5 Parameters of the linear fit $y = ax$ between measured and predicted Manning coefficients for all cases together. 136
7.6 Overview of the flow and vegetation parameters of the experiments by Zong and Nepf (2011). 138
7.7 Overview of the Manning coefficient values used in the simulations for different values of the drag coefficient C_D and low flow (Ul), medium flow (Um) and high flow (Uh) conditions. 142
7.8 Overview of the flow characteristics. U_1 is the velocity in the vegetation patch, U_2 is the velocity next to the vegetation patch. . . . 143
7.9 Overview of the flow characteristics. L_0 indicates the upstream adjustment length, x_D the length of the diversion zone. 145
7.10 Overview of the average eddy diffusivity $\bar{\nu}_t$ in the simulations with different values for the proportional constant α_0. 147
7.11 Overview of the flow parameters of the experiments by Zong and Nepf (2012). 150
7.12 Overview of the velocity U_1 behind the patches, for patches with different densities. 152
7.13 Overview of the flow and vegetation parameters of the experiments by Vandenbruwaene et al. (2011). 160
7.14 Maximum velocities in the transect 0.25 m from the trailing edge of the vegetation patch. Both simulations (Sim) and experimental (Exp) values are given. 163
7.15 Flow characteristics on the vegetation centerline. 169
7.16 Flow characteristics on the centerline of the flume, in the center of the gap between the patches. 170

B.1 Overview of the experimental data of uniform vegetation used to validate the model with vegetation resistance formulae. 202
B.2 Table Cont'd 203
B.3 Table Cont'd 204
B.4 Table Cont'd 205
B.5 Table Cont'd 206

Nomenclature

1 List of symbols

a	$[1/\mathrm{m}]$	frontal area per unit volume
A	$[\mathrm{m}^2]$	wetted area
A_v	$[\mathrm{m}^2]$	blocked cross-section by vegetation
α_0	[-]	constant of proportionality
α_1	[-]	constant of proportionality
B	[m]	flume width
B	[-]	blockage factor
β	[-]	exponent drag formula
c	[-]	depth-averaged volumetric concentration of vegetation
C	$[\mathrm{m}^{1/2}/\mathrm{s}]$	Chézy coefficient
C_1	[-]	constant of proportionality
C_D	[-]	drag coefficient
C_f	[-]	friction factor
D	[m]	diameter of the patch
d	[m]	stem diameter
d_p	[m]	zero-plane displacement (in logarithmic profile)
D_{50}	[m]	median grain size
Δ	[m]	gap width, patch separation
δ	[m]	shear layer width
η	[m]	undisturbed water level
ϵ	[m]	fitting parameter
f	[-]	Darcy-Weisbach friction coefficient
F_d	[N]	drag force
f_k	[1/s]	frequency of the von Kàrmàn vortex street
g	$[\mathrm{m}/\mathrm{s}^2]$	gravitational constant (9.81)
γ_u	[-]	kinematic spreading coefficient
H	[m]	water depth
i	[m/m]	energy slope

k	[m]	vegetation height
k_s	[m]	Nikuradse equivalent sand roughness
κ	[-]	von Kàrmàn constant (0.41)
L_0	[m]	upstream adjustment length
L_j	[m]	length of the jet
L_m	[m]	length from trailing edge of vegetation to minimum velocity zone
m	$[1/\mathrm{m}^2]$	number of stems per unit area
μ	$[\mathrm{Ns/m}^2]$	dynamic viscosity
n	$[\mathrm{s/m}^{1/3}]$	Manning coefficient
n_4	$[\mathrm{s/m}^{1/3}]$	Manning coefficient for vegetation
ν	$[\mathrm{m}^2/\mathrm{s}]$	kinematic viscosity
ν_t	$[\mathrm{m}^2/\mathrm{s}]$	turbulent kinematic viscosity
ν_t^H	$[\mathrm{m}^2/\mathrm{s}]$	horizontal kinematic viscosity
ν_t^V	$[\mathrm{m}^2/\mathrm{s}]$	vertical kinematic viscosity
ϕ	[-]	solid volume fraction
Q	$[\mathrm{m}^3/\mathrm{s}]$	discharge
R	[m]	hydraulic radius
Re	[-]	Reynolds number
ρ	$[\mathrm{kg/m}^3]$	mass density of water
S	[-]	stability parameter
St	[-]	Strouhal number
S_0	[m/m]	bottom slope
t	[s]	time
T	[-]	cross-sectional spatial variability parameter
τ_0	$[\mathrm{N/m}^2]$	bed shear stress
τ_{bx}	$[\mathrm{N/m}^2]$	bed shear stress in x-momentum equation
τ_{by}	$[\mathrm{N/m}^2]$	bed shear stress in x-momentum equation
τ_v	$[\mathrm{N/m}^2]$	vegetation shear stress
U	[m/s]	depth-averaged streamwise velocity
u	[m/s]	streamwise velocity
u'	[m/s]	turbulent fluctuation on streamwise velocity
u^*	[m/s]	shear velocity
U_∞	[m/s]	upstream velocity
U_{max}	[m/s]	maximum velocity in the gap
U_{min}	[m/s]	minimum velocity in the centerline between the patches
U_1	[m/s]	velocity in the steady wake zone
U_2	[m/s]	velocity next to the patch
U_s	[m/s]	depth-averaged velocity in surface layer
U_v	[m/s]	depth-averaged velocity in vegetation layer

V	[m/s]	depth-averaged lateral velocity
v	[m/s]	lateral velocity
v'	[m/s]	turbulent fluctuation on lateral velocity
V_x	[m/s]	depth-averaged streamwise velocity
V_y	[m/s]	depth-averaged lateral velocity
V_z	[m/s]	depth-averaged vertical velocity
w	[m/s]	vertical velocity
w'	[m/s]	turbulent fluctuation on vertical velocity
x	[m]	streamwise position
y	[m]	lateral position
z	[m]	vertical position
z_b	[m]	position of the bottom
z_s	[m]	position of the free surface

2 List of acronyms

ADV	Acoustic Doppler Velocimeter
CTD	Diver measuring Conductivity, Temperature and Depth
DM	Dry Matter
ECM	Electromagnetic Current Meter
PTV	Particle Tracking Velocimetry
USDA	United States Department of Agriculture
SD	Standard Deviation
SE	Standard Error
SNR	Signal to Noise Ratio
STRIVE	STReam RIVer Ecosystem model
SWE	Shallow Water Equations
TKE	Turbulent kinetic energy
TRIM	Tidal, Residual, Inter-tidal Mud-flat
2D-SWE	two-dimensional Shallow Water Equations

Nederlandse Samenvatting

Macrofyten, een andere benaming voor aquatische macroscopische planten, komen voor in aquatische omgevingen die relatief ondiep zijn, waar de hydrodynamische energie beperkt is en die chemisch gezond genoeg zijn om vegetatiegroei mogelijk te maken. Als zodanig vormen kleine (laagland-)rivieren, oeverzones, moerassen en overstromingsgebieden de habitat van deze macrofyten. Macrofyten dragen niet alleen bij tot de biodiversiteit van dergelijke habitats, immers, zij spelen een belangrijke rol in het functioneren van aquatische ecosystemen doordat zij de habitat vormen voor andere soorten zoals vissen, macro-invertebraten,... en bovendien een belangrijke rol spelen in de biogeochemie van dergelijke gebieden.

Aquatische habitats worden beschouwd als uiterst waardevolle ecosystemen die een breed scala aan ecosysteemdiensten leveren. Deze variëren van habitatdiensten (voor andere organismen), regulerende diensten (zuiveringsprocessen, het afvlakken van stormpieken,...), voorzienende (voedsel, water) en culturele diensten (toerisme, recreatie, culturele tradities). De ecosysteemdiensten die door aquatische habitats, gekenmerkt door de aanwezigheid van waterplanten, worden geleverd, bedragen wereldwijd naar schatting een waarde van $ 10 triljoen Costanza et al. (1997). Vanwege hun grote waarde, worden deze habitats beschermd door, onder andere, internationale verdragen zoals de Ramsar Conventie, de EU Habitatrichtlijn, e.a. Binnen de EU verplicht de Kaderrichtlijn Water alle lidstaten om een goede ecologische toestand te bereiken voor hun oppervlakte wateren tegen 2015. Vanwege hun grote belang, wordt aquatische vegetatie beschouwd als een belangrijke parameter voor het beoordelen van deze status.

Aquatische ecosystemen worden beïnvloed door talloze menselijke activiteiten: de lozing van grote hoeveelheden voedingsstoffen die leiden tot eutrofiëring, de lozing van verontreinigende stoffen; het aanpassen van de morfologie en het sturen van de stroming door belangrijke infrastructuurwerken; onderhoudswerken zoals het baggeren van rivieren en het maaien van vegetatie. Om een dergelijke, vooropgestelde goede ecologische toestand te bereiken, moeten, naast een verandering van de attitude ook talrijke en kostbare maatregelen genomen worden, om een waterkwaliteit en morfologische toestand te verkrijgen voor dewelke het optreden van een natuurlijke rivier vegetatie mogelijk wordt. In voorgaande onderzoeken werd een STRIVE (STReam RIVer Ecosystem) rivierecosysteem-model opgericht, een ecosysteem model waarin verschillende aspecten van het aquatische ecosysteem werden gekoppeld (transport van stoffen en water, vegetatie groei, waterkwaliteit parameters,...). Als zodanig kan de werking van het ecosysteem als een volledig, gekoppeld systeem worden bestudeerd, bv. de invloeden van boven genoemde menselijke interventies op weerstand, waterkwaliteit,...kunnen worden beoordeeld en de meest accurate en effectieve maatregelen geselecteerd.

Echter, gedurende lange tijd, werden macrofyten door waterbouwkundige ingenieurs beschouwd als weinig meer dan weerstandsobjecten in rivieren, leidend tot een daling van de gemiddelde stroming en bijgevolg toenemende waterdieptes. Consequent waren hydraulische studies gericht op lange, uniforme vegetatiezones, voor het karakteriseren van de stromingsweerstand en het beschrijven van de verticale structuur en turbulentie. In het veld daarentegen, is de verspreiding van planten in rivieren verre van homogeen, maar wordt vooral een heterogene plantengroei waargenomen. Onderzoek naar het effect van vegetatie op stroming en sedimentatie, wanneer heterogene patches en / of ruimtelijk verdeeld configuraties worden beschouwd, zijn schaars en bijgevolg blijven hieromtrent nog veel vragen onbeantwoord. De algemene doelstelling van dit doctoraatsonderzoek is om bij te dragen tot een dieper inzicht in het effect van vegetatiepatches op stroming en sedimentatie. Dit fundamenteel onderzoek wordt uitgevoerd door veldstudies, laboratoriumstudies en numerieke simulaties.

In een eerste deel werd het gedrag van een *Callitriche platycarpa* patch onderzocht, onder verschillende niveaus van hydrodynamische stress. Veldwerk werd uitgevoerd in de Zwarte Nete, een laagland rivier met een gemiddelde diepte van 0.5 m en een snelheid van 0.10 m/s . Een *in-situ* stroomgoot werd gebouwd rond een geïsoleerde *C. platycarpa* patch, met als opzet om de snelheden aan de inlaat te variëren, en als zodanig ook de snelheden in de test sectie. In het vrij-stromende gedeelte naast de patch werd een toename van de snelheden van ca. 10 - 30 % waargenomen relatief tov. de inlaat. De diepte-gemiddelde snelheden achter de patch verminderden met 50 - 70 %. Voor de Reynolds schuifspanningen werden maximumwaarden opgemeten aan de bovenkant van de patch en aan de zijkant, met maximale waarden gaande tot 8 $\mathrm{cm}^2\ \mathrm{s}^{-2}$. Tijdens de experimenten werd ook de evolutie van de bathymetrie opgemeten. De zones met de hoogste sedimentatie werden waargenomen juist afwaarts van de patch. Een zone met slechts marginale verandering werd waargenomen langs de vrij-stromende kant naast de patch, in overeenstemming met waarnemingen van de bodemschuifspanning. Aangezien de snelheden in de *in-situ* flume niet voldoende verhoogd konden worden, werd geen erosie waargenomen.

Additioneel werden, in functie van verschillende opwaarts opgelegde snelheden, andere kenmerken van een *Callitriche* patch opgemeten. Vanwege de flexibiliteit van de patch, werd bij toenemend debiet, waargenomen dat de patch zijn frontale oppervlak vermindert door een diepere positie in de waterkolom aan te nemen en eveneens meer gestroomlijnd wordt door een aanpassing van zijn lengte-breedte verhouding. Zowel de dieptepositie van de patch en de lengte / breedte verhouding hebben een temperend effect op de stroomversnelling naast de patch.

In een tweede deel werd het effect van twee geïsoleerde patches, geplaatst in een zij-aan-zij configuratie loodrecht op de stroming, op stromings- en sedimentatiepatronen rond deze patches onderzocht. Daartoe werden, met behulp van houten stokjes, ronde patches gebouwd met een diameter D, en geplaatst in een labo goot met een vaste diepte (0.13 m) en stroomopwaartse snelheid (U = 0.1 m/s). Zowel de dichtheid werd gevarieerd, van 3 % tot 10 %, als de afstand tussen de patches (Δ), gaande van Δ / D = 0 tot 0.6.

Er werd waargenomen dat zowel de lengte van de zogzones na de patches (L_1) als de snelheid in deze zogzones (U_1) onafhankelijk waren van de afstand tussen de patches. Voorts bleken formules die de snelheid U_1 en lengte L_1 voorspellen, en opgesteld zijn op basis van experimentele metingen voor afzonderlijke, geïsoleerde patches, eveneens geldig voor een configuratie met 2 patches naast elkaar. In het centrum tussen de twee patches kon een consistent snelheidsprofiel worden waargenomen voor alle onderzochte gevallen. In alle gevallen waarin Δ / $D > 0$, kan een identieke maximale snelheid worden vastgesteld, onafhankelijk van de tussenafstand tussen de patches. De grootte van deze maximale snelheid kon worden voorspeld ahv. een eenvoudige uitdrukking voor behoud van massa tussen de vegetatiezone en de vrij stromende zones naast de patch. Deze maximale snelheid U_{max} werd aangehouden over een afstand L_j. De afstand L_j bleek lineair afhankelijk van de tussenafstand Δ. Na deze afstand L_j, kwamen de zogzones van beide patches samen en nam de snelheid in de centrumlijn tussen de patches af tot een minimum op een afstand L_m van de patches. De intensiteit van deze minimale snelheid kon worden voorspeld door een behoud van massa tussen de twee centra van de patches (D + Δ), net achter de patches. Achter deze minimale snelheid zone, recupereert de stroming en herstelt zich naar uniforme stroming .

Een eerste, belangrijke depositiezone werd waargenomen in de onmiddellijke zogzone van de patches. Het samenkomen van zogzones van beide patches, en de bijbehorende, lokale minimumsnelheid leidde tot een lokaal maximum in de depositie op de middellijn tussen de patches, maar stroomafwaarts van de patches. Indien in deze secondaire zone van depositie nieuwe vegetatie groei mogelijk wordt, zal de verhoogde weerstand op de middellijn de snelheid tussen het stroomopwaarts gelegen paar van patches vertragen, wat leidt tot gunstige voorwaarden voor de fusie van patches.

In een derde deel werden de diepte-gemiddelde ondiep water vergelijkingen in een 2D hydraulische routine voor het STRIVE-ecosysteemmodel geïmplementeerd. Eerst werden de verschillende veronderstellingen om deze diepte-gemiddelde ondiep water vergelijkingen (2D-SWE) af te leiden, samengevat. Ten tweede werd de semi-Lagrangiaanse, semi-impliciete numerieke discretisatie methode, die werd geselecteerd voor de implementatie van de 2D-SWE, beschreven. Om de invloed van de vegetatie te beschrijven werden verschillende weerstandsformuleringen in de literatuur gevonden. Een overzicht van deze verschillende benaderingen is gegeven, en een benadering werd geselecteerd die de weerstand veroorzaakt door vegetatie berekent via een weerstandscoëfficiënt, op basis van vegetatie eigenschappen zoals de dichtheid van de vegetatie (stengels), de stengel diameters, vegetatiehoogte, en een hypothetisch logaritmisch profiel boven de vegetatie.

Deze implementatie werd gevalideerd aan de hand van experimentele resultaten voor verschillende vegetatie configuraties. Voor de simulaties met configuraties van vegetatie die zich bevond over de gehele breedte van het kanaal en configuraties van lange patches, die slechts een deel van de kanaalbreedte innamen, werden goede overeenkomsten gevonden met de experimentele resultaten, voor respectievelijk de weerstandswaarden en snelheidsprofielen. De sleepcoëfficiënt C_D bleek een belangrijke kalibratieparameter voor de simulaties van lange vegetatiepatches die gedeeltelijk de breedte van het kanaal vullen. Ook voor geïsoleerde patches, bleek de kalibratie van deze parameter belangrijk en bovendien afhankelijk van de geïmplementeerde weerstandsterm. Bij densere patches traden oscillaties op, die het mengingsproces na de patch bepalen en waardoor de snelheidsprofielen relatief goed overeenkwamen met de metingen. Deze oscillaties vereisten wel adequate maatregelen aan de grenzen van het simulatiedomein, opdat stabiele simulaties zouden verkregen worden. Voor minder dense patches, waren deze oscillaties niet aanwezig. Het geïmplementeerde, algebraïsche model voor de viscositeitsterm leidde niet tot een goede representatie van het mengproces en bijgevolg een onderschatting van de snelheiden vergeleken met de metingen. Voor patches in een zij-aan-zij configuratie werd de verdeling van snelheden naast en tussen de patches goed voorspeld. Aangezien algemeen redelijk goede resultaten werden verkregen, kan deze hydrodynamische routine worden gekoppeld met modules van vegetatiegroei, sediment transport, etc. om samen een ruimtelijk verdeeld ecosysteemmodel voor aquatische ecosystemen te vormen.

De combinatie aan variabiliteit in biologische (flexibiliteit van planten, biomassa (dichtheid), vegetatiehoogte,...) en geometrische aspecten (oppervlakte en verspreiding van planten) resulteert in complexe stromingspatronen en bijbehorende erosie - sedimentatie patronen. Deze werden beschreven ahv. veld- en laboratoriumonderzoek. Om het functioneren en de langere termijn evolutie van aquatische ecosystemen te bestuderen, is een koppeling van verschillende modules, welke elk een deelaspect van het ecosysteem beschrijven, noodzakelijk om cascade- en feedback mechanismen te implementeren die het ecosysteem vorm geven. Het hydraulische model gebaseerd op de 2D-SWE werd getest en beschouwd als een nuttige implementatie als hydraulische routine van dergelijk ecosysteemmodel.

English summary

Macrophytes are defined as aquatic macroscopic plants and occur in aquatic environments which are relatively shallow, have limited hydrodynamic energy and are chemically healthy enough to allow vegetation growth. As such, small (lowland) rivers, river banks, wetlands and floodplains form the habitat of these macrophytes. Macrophytes not only contribute to the biodiversity of these habitats, they play a key role in the functioning of aquatic ecosystems by providing habitat for other species like many fishes, macro-invertebrates,... and by playing an important role in the biogeochemistry.

Aquatic habitats are considered extremely valuable ecosystems delivering a wide range of ecosystem services. These range from habitat services (for other organisms), regulating services (purification processes, damping of flood peaks,...), provisioning (food, water) and cultural services (tourism, recreation, cultural habits). These ecosystem services provided by aquatic habitats characterized by the presence of macrophytes are estimated to represent globally an annual value of $10 trillion Costanza et al. (1997). Because of their importance, these habitats have been protected by, amongst others, international treaties as the Ramsar convention, EU Habitat directive, etc. Within the EU, the Water Framework Directive obliges all the member states to attain a good ecological status for their surface waters by 2015. Aquatic vegetation is considered as an important parameter to assess this status.

Aquatic ecosystems have been impacted by many human activities: discharge of excessive amounts of nutrients leading to eutrophication, discharge of pollutants; changing morphology and altering flows by engineering works: maintenance works as dredging and vegetation mowing. To reach a good ecological status as required, a change of attitude together with numerous and expensive measures, have to be taken to attain a water quality and river morphology allowing for the occurrence of a natural river vegetation. In previous research projects, a STRIVE (STReam RIVer Ecosystem) model was established, an ecosystem model in which aspects of the aquatic ecosystem (surface water transport, vegetation growth, water quality parameters,...) were coupled. As such, the functioning of the ecosystem as a complete system can be studied, eg. to assess the influences of these human interventions on resistance, water quality,... and to be able to select the most accurate and effective measures.

However, for a very long time, hydraulic engineers considered macrophytes as no little more than resistance objects in flows, reducing the average flow and therefore increasing water depths. Consistently, hydraulic studies have focused on long, uniform meadows, characterizing the bulk flow resistance and describing the vertical flow structure and turbulence. In the field, the distribution of plants in rivers is far from homogeneous, instead mostly a patchy pattern is observed. Studies on the effects of vegetation on flow and sedimentation, when heterogeneous patches and/or spatially distributed configurations are considered, are scarce and still many questions remain unanswered. The general objective of this PhD-research is to contribute to a deeper insight into the effect of vegetation patches on flow and sedimentation. This fundamental research is performed by field studies, lab studies and numerical simulations.

In a first part, the behaviour of a patch of *Callitriche Platycarpa* was examined, under different levels of hydrodynamic stress. Field work was performed in the Zwarte Nete, a lowland river with an average depth of 0.5 m and velocity of 0.10 m/s. An *in-situ* field flume was built around an isolated patch of *C. platycarpa*, with the idea to change the velocities at its inlet, and therefore change the velocities in the test section. In the free flowing section next to the patch, an increase of the velocities of approx. 10 - 30 % was observed compared to the upstream velocity. The depth-averaged velocities behind the patch were reduced by 50 - 70 %. For the Reynolds stresses, maximal values were found on the top of the canopy and adjacent to the canopy, with maximum values going up to 8 $\mathrm{cm}^2\ \mathrm{s}^{-2}$. During the course of the experiments, the evolution of the bathymetry was measured. The zones of highest sedimentation were observed behind the patch. A zone of marginal change was observed on the free flowing side, consistent with observations of the bed shear stress. However no erosion was observed, as the velocities in the *in-situ* flume could not be increased enough.

Additionally, different patch characteristics of a *Callitriche* patch were measured in function of a range of incoming velocities. Because of its flexibility, it was observed that with increasing discharge, the patch reduces its frontal area by taking a deeper position in the water column and becomes more streamlined by adapting its length to width ratio. This means that both canopy depth and patch length/width ratio have a tempering effect on flow acceleration adjacent to the patch.

In a second part, the effect of two isolated patches, which are placed in a side-by-side configuration, on the flow and sedimentation patterns around these patches are assessed. To evaluate this effect, patches with diameter D, made of wooden dowels, were placed in a lab flume, with a fixed water depth (0.13 m) and upstream velocity (U = 0.1 m/s). Both the density of the patches, ranging from 3% till 10%, and the gap spacing Δ between the patches, ranging from Δ/D = 0 till 0.6, were varied.

It was observed that both the length of the wake zone behind the patches (L_1) and the velocity in this wake zone (U_1) were independent from the gap spacing. Furthermore, formulas to predict the magnitude of U_1 and L_1, which are established for single, isolated patches, remain valid for a configuration with 2 side-by-side patches. Looking at the centerline of the flume, in the middle of the gap between the two patches, a consistent velocity profile could be observed for all examined cases. In all cases where $\Delta/D > 0$, a similar maximum velocity could be observed, independent of the gap width. The magnitude of this maximum velocity could be predicted adequately by simple conservation of mass between the vegetation zone and the free flowing side zones. This peak velocity U_{max} persisted over a distance L_j. The distance of L_j was shown to be linearly dependent on the gap width. Beyond L_j, the wakes merged and the centerline velocity decayed to a minimum at a distance Lm. The intensity of this minimum velocity can be predicted by a conservation of mass between the two centers of the patches (D + Δ) just behind the patches. Behind this minimum velocity zone, flow starts to accelerate and recover towards uniform flow.

A first, major deposition zone was observed in the direct wake of the patches. The merging of wakes and associated velocity minimum produced a local maximum in the deposition on the centerline between the patches, but downstream from the patches. If this secondary region of enhanced deposition promotes new vegetation growth, the increased drag on the centerline could slow velocity between the upstream patch pair, leading to conditions favorable to their merging.

In a third part, the depth-averaged Shallow Water Equations were implemented in a 2D hydraulic routine for the STRIVE ecosystem model. First, the different assumptions to derive the depth-averaged shallow water equations (2D-SWE) were summarized. Secondly, the semi-Lagrangian, semi-implicit numerical discretisation method, which was selected to implement the 2D-SWE, is described. To account for the effect of vegetation, different resistance formulas are described in literature. An overview of these methods is given, and a method was selected which links the vegetative drag, calculated based on vegetation characteristics such as vegetation density, stem diameters, vegetation height and an assumed logarithmic profile above the vegetation, to a resistance coefficient.

In cases where vegetation occurred over the whole width of the channel and in long patches capturing only a part of the channel width, good agreements were found between model simulations and experimental results, respectively for the resistance values and velocity profiles. For simulations of long patches which partly fill the flume, the drag coefficient was found to be an important calibration factor. Also for isolated patches, the calibration of the drag parameter was found to be important and depending on the implemented resistance term. In the case of denser patches, oscillations appear, which account for mixing which results in velocity profiles agreeing relatively well with the measurements. However, adequate measures at the boundaries have to be taken to obtain stable simulations. For sparser patches, these oscillations were not present and the implemented algebraic model for viscosity does not result in a good representation of the mixing process. For patches in a side-by-side configuration, the distribution of the velocities next and in between the patches were well represented. As reasonable results were obtained, this hydrodynamic routine can be coupled with modules of vegetation growth, sediment transport, etc. to form together a spatially-distributed ecosystem model for aquatic ecosystems.

The combination of a variability of biological (flexibility of plants, biomass (density), vegetation height,...) and geometrical parameters (area and distribution of plants) results in complex flow patterns and associated erosion sedimentation patterns. These are described both by field and laboratory investigations. To account for the functioning and longer term evolution of these ecosystems, a coupling of different modules, each describing an aspect of the ecosystem, should be used to study cascade and feedback mechanisms shaping the ecosystem. The hydraulic model based on the 2D-SWE has been shown to be a useful implementation to make part of such ecosystem model as hydraulic routine.

1 Introduction and Objectives

1.1 Vegetated Flows: a fluvial context

Macrophytes are defined as aquatic macroscopic plants (Bal, 2009) and occur in aquatic environments which are relatively shallow, have limited hydrodynamic energy (Folkard, 2011) and are chemically healthy enough to allow vegetation growth. As such, small (lowland) rivers, river banks, wetlands and floodplains form the habitat of these macrophytes. A wide diversity of macrophytes species can be found (Schaminée et al., 1995). They can be classified into several groups, based on their morphology, namely emergent, submerged, floating and free-floating plants, as shown in Figure 1.1. However, frequently exceptions can be noted, especially for flowers or even for parts of the entire growth cycle (Bloemendaal and Roelofs, 1988).

These macrophytes play a key role in the aquatic habitats, e.g. by providing habitat for many fishes, macro-invertebrates,... (Grenouillet et al., 2002; Harrison et al., 2004). The aquatic habitats, in turn, are considered as extremely valuable ecosystems (Mitsch and Gosselink, 1993). Boerema et al. (2014) lists a wide range of ecosystem services (habitat, regulating, provisioning and cultural services) provided by aquatic vegetation. Nepf (2012a) refers to an estimated global, annual value of \$ 10 trillion of ecosystem services provided by aquatic vegetation, as calculated by Costanza et al. (1997). Not withstanding the importance, we have

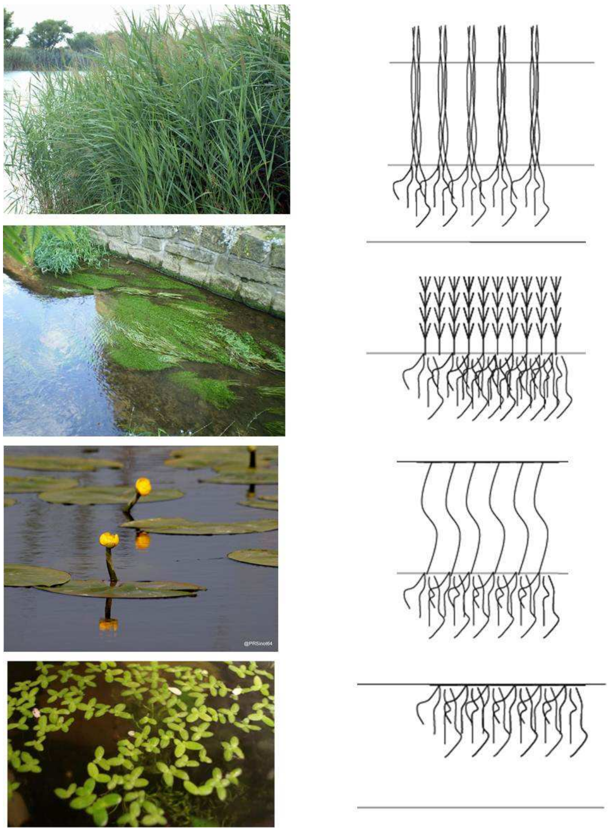

Figure 1.1: Examples of macrophytes for each described morphology. From top to bottom: (a) Common Reed (*Phragmites australis*, as an example of emergent vegetation; (b) *Callitriche platycarpa*, as an example of submerged vegetation (c) *Nuphar Lutea* as an example of floating plants with roots and (d) *Lemna* as an example of free-floating plants. The sketches are taken from Folkard (2011), the pictures are respectively from $http://www.lorenzsokseedsllc.com$, $Botany.cz$, $http://alkmaardoorpatricksinot.blogspot.be$ and $www.gamalenforum.be$

impacted and deteriorated these systems by excess discharge of nutrients and pollutants leading to eutrophication, anoxia and bad chemical water quality. Water courses have also been changed by different forms of river engineering and management strategies such as dredging and vegetation mowing (Boerema et al., 2014).

According to the Water Framework Directive (EU, 2000), surface waters should attain a good ecological status by 2015. Aquatic vegetation is considered as an important parameter to assess this status (Annex. 5, EU (2000)). To attain this good quality, numerous and expensive measures will have to be taken to attain a water quality and river morphology allowing for a natural occurence of river vegetation. It is important to study these influences by hydraulic and ecological modelling, to see its effects on resistance, water quality, . . . and be able to select the most accurate and effective measures.

As stated by Folkard (2011), vegetated flows are particularly well-suited to interdisciplinary study, as they are, by definition, characterised and formed by a combination of physical, morphological and biological phenomena. As such, the study of macrophytes in its ecosystem context, needs an integration of knowledge from several scientific disciplines. The role of macrophytes and its linkage with other components of the ecosystem is schematised in Figure 1.2.

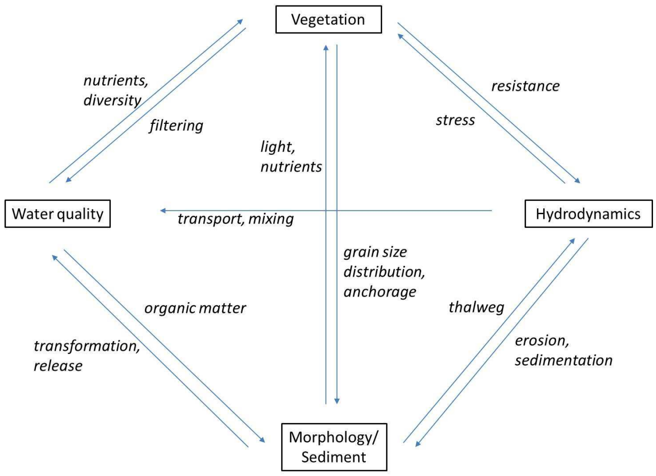

Figure 1.2: Schematic description of the relationships between the main components of the aquatic ecosystems under consideration.

In the scheme presented in Figure 1.2, four main components of aquatic ecosystems with vegetated flows can be distinguished, namely a biological component, the *vegetation* (macrophytes), a physical component, the *hydrodynamics*, a geological component, *morphology and sediment* and a chemical component, the *water quality*. These components are linked in various ways and some examples are discussed hereafter.

For many decades, vegetation has been considered by hydraulic engineers as an additional *resistance* element in river reaches. Various studies have been aiming to describe this effect on a purely empirical basis, e.g. Chow (1959) or by taking into account some vegetation characteristics, e.g. Baptist et al. (2007); Petryk and Bosmajian (1975). On the other hand, the effect of flow velocities on macrophytes have been considered as well. Both the abundance and diversity of macrophytes are stimulated at low to medium velocities, and growth is restricted at higher velocities (Franklin et al., 2008; Madsen et al., 2001). This can be considered as a result of conflicting processes of mass transport on the one hand and drag disturbances, felt by the plants as *stress*, on the other hand (Franklin et al., 2008). Flow velocities and turbulence characteristics, shortly the hydrodynamics of the system, will influence *erosion* and *sedimentation* processes (Van Rijn, 1993). On the other hand, local variations of the flow speed can be caused by channel morphology, which is a long-term result of *sedimentation* and *erosion* processes. Clear links between morphology and macrophytes can be found as well. Simply, deeper places in the river reach are places where no macrophytes can grow, shallower places experience more *light* penetration. On the other hand substrate stability is a significant controlling factor because a stable substrate allows rooting and establishment of macrophyte communities (Franklin et al., 2008; Riis and Biggs, 2003). Mobile substrates prevent this, resulting in a limited potential for community development. An increased deposition of particulate organic matter can be observed due to reduced velocities, resulting for example in a retention of phosphorus by up to 25% of the total amount (Schulz et al., 2003).

The described linkages between the different components of the aquatic ecosystem are easy to understand and grasp assuming uniform vegetation stands. However, the distribution of plants in the river is far from homogeneous, in stead not seldom a patch formation is observed, as shown in Figure 1.3

None of the relations described above are fixed in a temporal or spatial context. Because of the presence of vegetation, areas next to the patches will experience higher stream velocities and areas with low velocities are found in and behind the patches itself (e.g. Bouma et al. (2009); Zong and Nepf (2010) and Figure 1.4). This heterogeneity will probably sustain itself, as higher velocities next to the patch can lead to erosion, especially of the fine sediments, and can result in deeper zones, both effects are negative to the establishment or growth of (new) vegetation. The lower velocities and sedimentation in the patches and just behind, on the contrary, are supposed to be benificial for plant growth. The consideration of these cascade and feedback mechanisms to understand the functioning and evolution of aquatic ecosystems is crucial (Schoelynck, 2011; Schoelynck et al., 2012b).

Because of the described feedback mechanisms, an ecosystem will evolve during the course of time. Amongst others, Tal and Paola (2007) have shown experimentally how the interaction of flow and vegetation results in an evolution from a braided morphology to a single-thread meandering channel. Temmerman et al. (2007) show that on tidal flats with dynamic patches, flow is diverted to channels. Here erosion is observed, and denser vegetation resulted in higher channel densities. It can be concluded that growing in patches, vegetation can act as ecological

Figure 1.3: Photographs of patchy configuration of vegetation in the rivers Desselse Nete and Zwarte Nete (photos taken by Kerst Buis).

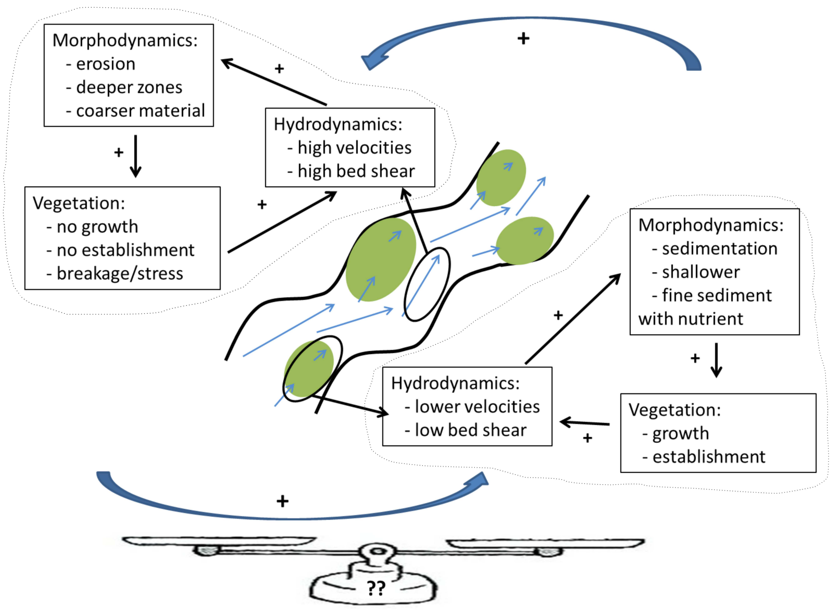

Figure 1.4: Schematic description of the potential feedback- and cascade processes in case of a heterogeneous distribution of vegetation patches. The green areas represent vegetation patches. The blue arrows indicate the velocity vectors, the black arrows indicate the feedback effects between different components of the system and the large arrows indicate the feedback effects between the vegetated and non-vegetated areas of the river stretch. The '+' symbol indicates an enhancing effect.

engineers (Jones et al., 1994) meaning that they are capable of adapting the environment with positive and/or negative feedbacks on other organisms (Schoelynck, 2011). Several hypothesis are used to couple small-scale feedbacks with large(r)-scale landscape evolutions. One of them, spatial self-organisation, is the process where large-scale ordered spatial patterns emerge from disordered initial conditions through local interactions between organisms and their environment; and has been demonstrated for many ecosystems (Rietkerk and Van de Koppel, 2008). Recently, scale-dependent feedbacks have been shown to be an explanatory mechanism for the patchy pattern of *Callitriche platycarpa* Kütz. vegetation in lowland rivers (Schoelynck et al., 2012b); analogue to *Spartina anglica* C.E.Hubb patches on flood plains (Bouma et al., 2009; Temmerman et al., 2007; van Wesenbeeck et al., 2008).

Previous research has led to the construction of a STReam RIVer Ecosystem model (STRIVE), a numerical model in which several parts of the ecosystem are implemented, in different modules, and coupled as an ecosystem model package (De Doncker, 2008). Because of its complexity, numerical simulations can be very useful for a better understanding of aquatic ecosystems. However, as the STRIVE model was limited to a 1D-approach, along the length of the river, several (spatially) dominated feedback mechanisms could not be assessed.

1.2 Objectives

The effects of vegetation on flow, mixing, transport and sedimentation in uniform vegetation stands have been studied thoroughly in the past (Jarvela, 2005; Lopez and Garcia, 2001; Nepf, 1999; Petryk and Bosmajian, 1975; Stephan and Gutknecht, 2002). However, the effects of vegetation on flow and sedimentation, when heterogeneous patches or spatial distributed configurations are considered, are less abundant (examples are e.g. Bennett et al. (2002); Sukhodolov and Sukhodolova (2010); Tsujimoto (1999); Vandenbruwaene et al. (2011); Zong and Nepf (2010, 2012)) and still many questions remain unanswered. The general objective of this PhD-research is to contribute to a deeper insight into the effect of vegetation patches on flow and sedimentation. This fundamental research is performed by field studies, lab studies and numerical simulations.

Within the general objective of research, the following 3 specific research questions are addressed.

1. How is a patch of *Callitriche Platycarpa sp.* avoiding hydrodynamic stress?

   The flow pattern under base flow around a patch of *Callitriche Platycarpa sp.* was examined in a field site in the north-east of Belgium, to localise the zones of high and low velocities and its intensities. By using an *in situ* flume, the hydrodynamic conditions were changed and the effect on velocities and local erosion/sedimentation patterns were examined. Additionally, the behaviour of a *C. platycarpa* patch under different conditions of hydrodynamic stress has been examined in a laboratory flume, to estimate the effect of the patch flexibility.

2. How are patches in a side-by-side configuration influencing the flow field and sedimentation patterns compared to single, isolated patches?

   As our interest lies in the effect of the spatial configuration of patches on the flow patterns, a simple side-by-side configuration was selected to study in a laboratory flume. Some studies have been performed looking at the effect of one single patch on the wake velocities and sedimentation patterns in this wake zone (Ortiz and Nepf, 2014; Tanaka and Yagisawa, 2010; Zong and Nepf, 2012) . Recently, Vandenbruwaene et al. (2011) considered the flow next and in between two patches of vegetation in such a side-by-side configuration. Sumner (2010) describes the wake behaviour behind a pair of cylinders, but the characteristics of the wake zone behind a pair of patches (2 porous objects) was not yet studied in detail. The focus in this study is to determine the influence of interpatch distance, patch density and patch diameter on the flow and the deposition patterns in the wake of a pair of side-by-side patches. A better knowledge of these processes can create a better understanding of how vegetation patches can merge together into a single but larger patch.

3. Can we use the depth-averaged shallow water equations and an appropriate resistance model to simulate flow fields influenced by vegetation?

   The variety of parameters which can be tested in the case of studies with spatial configurations is huge. Therefore, numerical modelling can be a helpful tool. Indeed not only the plant characteristics can be varied (e.g. vegetation height, vegetation density, flexibility,...) but also its geometrical characteristics on smaller (e.g. patch diameter, patch length to width ratio, patch shape,...) and larger scale (e.g. patch distances, patch surface, patch configuration,...). In this study, the potential of the 2D-depth-averaged shallow water equations to simulate velocity fields in the case of several configurations, namely uniformly distributed vegetation, patches on 1 side of a flume and isolated patches is assessed. A suitable resistance model based on vegetation characteristics is sought for to couple with the shallow water equations. When reliable results are obtained, this hydrodynamic routine can be coupled with modules of vegetation growth, sediment transport, etc. to form together an ecosystem model for aquatic ecosystems.

1.3 Outline of the PhD-manuscript

This PhD-manuscript consists of 8 chapters, which are summarised and presented below. In Chapter 1 the general layout and research questions are posed, together with an overview of the PhD-manuscript.

Chapter 2 presents a field-study in the small lowland river Zwarte Nete, to assess the influence of one patch on the complexity of the flow pattern and its effect on the morphology and sediment transport. In Chapter 3, a lab-experiment is presented which answers the question on how two side-by-side patches are influencing the flow and sedimentation processes compared to the situation of an isolated patch. The following chapters, Chapter 4 & 5 and 6, are dealing with the setting-up of the model. In Chapter 4, the depth-averaged shallow water equations (2D-SWE) which are implemented are presented, together with the assumptions to derive these equations from the Navier-Stokes equations. Chapter 5 addresses the numerical solution of these 2D-SWE. In Chapter 6 an overview on the effect of vegetation on flow resistance and its implementation in numerical models is presented. Chapter 7 treats the description of the model results, which are grouped in an increasing order of complexity or heterogeneity. First, the results of experiments with vegetation presence over the whole width of the flume are compared with the model results, focusing on the predicted flow resistance. Furthermore, vegetation on 1 side of the flume and vegetation patches are considered. A final validation test of the model is done with experimental work on patches of real vegetation in a side-by-side configuration.

In Chapter 8, the general conclusions of the PhD-research are summarised. As research is a never ending story, a lot of questions remain unanswered and new questions have appeared. These are put together in Chapter 8 as well, as recommendations for further research.

2

Submerged Macrophytes avoiding a Negative Feedback in Reaction to Hydrodynamic Stress

2.1 Abstract

In most aquatic ecosystems, hydrodynamic conditions are a key abiotic factor determining species distribution and aquatic plants abundance. Recently, local differences in hydrodynamic conditions have been shown to be an explanatory mechanism for the patchy pattern of *Callitriche platycarpa Kütz.* vegetation in lowland rivers. These local conditions consists of specific areas of increased shear zones, resulting in additional plant stress and erosion of the sediment on the one hand and local decreased shear zones resulting in zones favourable to plant growth and sedimentation of bed material on the other hand. In this study, the process of this spatial plant-flow-sedimentation interaction has been illustrated quantitatively by *in-situ* flume measurements. By disturbing the incoming discharge on a single patch in such flume, we have quantified the behaviour and influence of a *C. platycarpa* patch under normal field conditions (base flow). Additionally, the behaviour of a *C. platycarpa* patch under different conditions of hydrodynamic stress has been examined in a laboratory flume. Indeed, flexible, submerged macrophytes are capable to adapt patch dimensions with changing stream velocities. At times of modest hydrodynamic stress, the species takes a position near the water surface and optimises its leaf stand, thereby maximising its photosynthetic capacity.

At times of peak discharge, the patch will bend down towards the river bed and become more confined and streamlined, as such averting the stream velocity and diminishing the risk of breaking or being uprooted.

In this chapter[1], the processes of local hydrodynamic conditions on the patch and the patch intriguing life strategy of avoiding negative feedback is shown.

2.2 Introduction

The interaction between macrophytes and the hydrodynamic regime in a stream has been a subject of research for over decades now. Part of this interest originates from hydraulic engineers interested in the way plants steer flow velocity patterns and water heights to give more accuracy to present-day models that are often exclusively based on (abiotic) river characteristics and physical laws (De Doncker et al., 2009). Others are interested how this diversity in flow patterns can influence the streams ecology (Schoelynck et al., 2012b), geomorphology (Gurnell et al., 2010) or management (Bal and Meire, 2009). Many studies have looked at this on a single-plant scale (Bal et al., 2011) or on uniformly distributed vegetation (Champion and Tanner, 2000). However, the difficulty in studying the plant-flow interactions under natural conditions is compounded by the fact that plants often form patches, together with non-colonised spaces or spaces colonised by different types of vegetation (Sukhodolov and Sukhodolova, 2010). That is why only few have studied patch behaviour in situ with changing discharges and stream velocities from an ecological point of view (Sand-Jensen and Pedersen, 2008, 1999) or from a hydraulic engineering point of view (Sukhodolov and Sukhodolova, 2010). Statzner et al. (2006) concluded that conventions, grounded on physical principles are strictly necessary for the characterisation of flow-plant interactions. However, sufficiently detailed data sets that would allow rigorous examination of flow-plant interactions relevant for natural conditions are still unavailable (Sukhodolov and Sukhodolova, 2010). This work is one of the first to address this scientific lacuna.

Recently, scale-dependent feedbacks have been shown to be an explanatory mechanism for the patchy pattern of *Callitriche platycarpa* Kütz. vegetation in lowland rivers (Schoelynck et al., 2012b); analogue to Spartina anglica C.E.Hubb patches on flood plains (Bouma et al., 2009; Temmerman et al., 2007; van Wesenbeeck et al., 2008). Spatial self-organisation of ecosystems is the process where large-scale ordered spatial patterns emerge from disordered initial conditions through

[1]This chapter is based on the following article: *Schoelynck, J., Meire, D., Bal, K., Buis, K., Troch, P., Meire, P. and Temmerman, S. (2013) Submerged macrophytes avoiding a negative feedback in reaction to hydrodynamic stress. Limnologica, 43, 371-380.*, where J. Schoelynck and D. Meire contributed equally.

local interactions between organisms and their environment; and has been demonstrated for many ecosystems Rietkerk and Van de Koppel (2008). So-called scale-dependent feedbacks between organisms and their environment are often considered as a necessary condition for self-organised patchiness to form (Lejeune et al., 2004; Rietkerk and Van de Koppel, 2008). The scale-dependent feedback principle implies that the presence of an organism has a positive feedback effect that is short-ranged (i.e. local facilitation through resource concentration or stress reduction) and a negative feedback effect that is long-ranged (i.e. inhibition in its surroundings by resource depletion or stress concentration). It was clearly shown that these habitat modifications have a short-range positive feedback on plant productivity on flood plains (van Wesenbeeck et al., 2008) and in freshwater rivers (Schoelynck et al., 2012b). Biomass slows down the current inside and in the immediate vicinity of vegetation patches, promoting the deposition of sediment and organic matter. This generally results in greater and deeper light penetration (Horppila and Nurminen, 2003) and a higher nutrient availability (Brock et al., 1985; Webster and Benfield, 1986). Alongside the patch, enhanced stream velocity can lead to erosion (Sand-Jensen and Mebus, 1996). This can lead to a depletion of nutrient availability and an increase of physical disturbance (Sand-Jensen and Madsen, 1992); hence a long-range negative feedback on plant productivity. This was shown on flood plains (van Wesenbeeck et al., 2008), but erosion could not be withheld as an explanatory factor in freshwater rivers, despite the clear presence of a negative feedback, proven with transplantation experiments (Schoelynck et al., 2012b).

This difference between intertidal *S. anglica* and freshwater river *C. platycarpa* may be explained by the difference in plant stiffness. The very stiff *S. anglica* is mostly emerged at times of peak discharges forcing all the water on flood plains to divert around the patch, leading to high flow velocities. Aquatic river vegetation is in general much more flexible and mostly submerged, so that water will tend to flow over it. This may result in more modest accelerations alongside the patches. It was therefore suggested that for aquatic river vegetation at base flow regimes, the proposed dynamics are most likely to be important but erosion is not the main negative feedback acting upon patch growth, but rather enhanced flow velocity and reduced sedimentation (Schoelynck et al., 2012b). Nevertheless, during high-discharge events, stream velocities can impose erosion around aquatic river vegetation patches (Sand-Jensen and Mebus, 1996) and may govern drag and the probability of uprooting (Sand-Jensen and Pedersen, 2008). Flow acceleration can be the most important stressor for *C. platycarpa* to grow (Riis and Biggs, 2003; Riis et al., 2000). Subjected to a given current velocity, macrophytes experience a drag force 25 times higher than terrestrial plants exposed to a similar wind speed (Denny and Gaylord, 2002). Biotic resistance is related with substrate stability or with low shear stress during stressful events (Lancaster and Hildrew, 1993). Additionally, mechanical stress originating from hydrodynamic drag forces is a main structuring factor in aquatic vegetation communities (Biggs, 1996; Spink and Rogers, 1996).

In this current study, the interaction between a flexible submerged macrophyte patch of *C. platycarpa* and the hydrodynamic regime in a stream has been studied in situ as well as under laboratory conditions in order to understand the patch behaviour with changing stream velocities. In situ flume experiments are often used to study reach scale phenomenons (Gibbins et al., 2007; Schanz et al., 2002) and provide an excellent tool to work under the natural environmental conditions that are present in the studied ecosystem. It was preferred in the present study to measure the effect of plant-velocity interaction on turbulence, bed shear stress and hence possible erosion. By manipulating the incoming discharge, the existing equilibrium between velocity, bathymetry and vegetation becomes unbalanced, increasing the possibility to measure adequately critical zones of hydrodynamic stress. Laboratory flume tests are used to adequately measure changes in patch dimensions with changing incoming velocity. The change of patch characteristics may temper the magnitude of the effects in the critical stress zones. Hence, results of the laboratory flume experiments will help to understand field flume results. Against this background, the following research questions are addressed:

1. Where are the zones around a patch with a lower or higher stream velocity compared to incoming stream velocity?

2. Can we recognise specific critical zones near the patch edges with high turbulence values causing a risk of erosion, patch uprooting or stem breakage?

3. Do zones with enhanced or reduced stream velocity or turbulent stress correspond with zones of erosion or sedimentation respectively?

4. What is the importance of the free flowing zone above the patch in terms of averting incoming water and what is the consequence for the stream velocity alongside the patch?

In this study, ecology and river hydraulics are integrated by performing in situ high resolution 3D-velocity measurements. Understanding and accurate prediction of transport processes in vegetative mosaics of fluvial ecosystems is a precondition for further developments in ecological modelling and can only be advanced through a series of case studies under natural conditions (Sukhodolov and Sukhodolova, 2010).

2.3 Materials and methods

The *in situ* flume measurements were performed in September 2009 in the Zwarte Nete, a typical lowland river in the NE of Belgium. Water runs through a sandy river bed (median grain size D_{50} = 167 μm) with an average stream velocity around 0.1 m/s and an average discharge of 0.2 m^3/s in September. The river study site is 4.5 m wide, water depth rarely exceeds 1 m and the water-surface slope is on average 0.12 %. The aquatic vegetation comprises seven common true aquatic species but is dominated by *Callitriche platycarpa* Kütz. growing in a mosaic pattern of distinct and confined patches, covering 20 % of the river. It has a dense submerged biomass of flexible stems with small leaves. Stems can end in rosette shaped floating leaves surrounding flowers in spring.

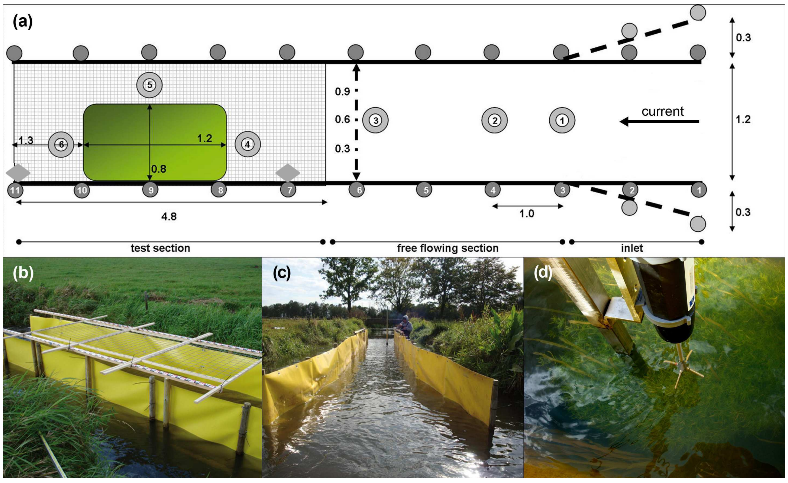

Figure 2.1: Schematic overview of the in situ flume. Dark grey bullets represent the poles numbered consecutively 1 to 11 from upstream to downstream. Light grey bullets represent the poles 1 and 2 after widening the inlet from 1.2 m to 1.8 m. Grey circles represent plate sediment traps numbered consecutively 1 to 6 from upstream to downstream. Perpendicular to the field flume around pole n°6, discharge was measured at 0.3, 0.6 and 0.9 m from the left bank side of the field flume. CTD-divers are attached to poles n°7 and 11 (grey diamonds). Starting in between poles 6 and 7, a mesh represents the test section covering the entire patch (green rectangle) and is prolonged 1.3 m downstream and 2.3 m upstream. It covered the entire width of the field flume. Note that no measurements were carried out in a 0.1 m vicinity of the field flume borders. The presence of the mesh covering the test section as well as the presence of the wide inlet are illustrated with pictures.

A field flume was constructed around an average sized *C. platycarpa* patch (± 1.2 m long, ± 0.8 m wide, 115 g dry mass m^{-2}) at the beginning of the experiment. The patch canopy had an average inclination between 20 °and 30 °with the

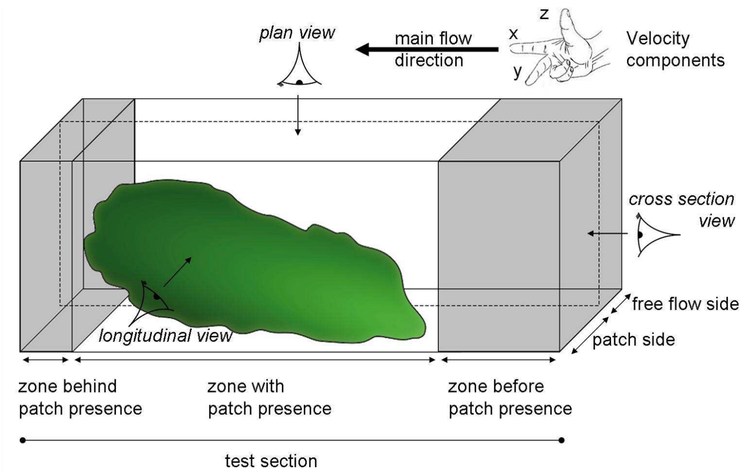

Figure 2.2: An explanatory key for the 3-dimensional results from the test section. There are three viewpoints: plan view, cross section view and longitudinal view. The test section is longitudinally divided into three zones: before patch presence, with patch presence and behind patch presence and divided into two cross sections: a free flow side without patch presence and a side with patch presence. The main stream flows from right to left as a result of stream wise (x), lateral (y) and vertical (z) velocities. Positive velocities are orientated corresponding to the right-hand law with fingertips of index finger, middle finger and thumb representing the positive direction of the x, y and z velocity respectively.

river bed and a free flowing space of minimum 0.10 m water was present above each patch. This results in a blockage area of 58 % (definition by Green (2006): vegetated area in cross section divided by total cross section area). The field flume itself was 1.2 m wide and 10 m long and built from PVC coated sails attached to two rows of 11 wooden poles (See Fig 2.1). The poles were anchored in the river bed at 1 m distance to each other. The first two meters at the upstream part of the field flume (poles 1-3) were adjustable to be able to widen the inlet, and enhancing incoming discharge on day 2 of the experiment. The test section was 4.8 m long at the downstream end of the field flume (halfway pole 6 and 7 to pole 11) with the *C. platycarpa* patch situated around poles 8-10 at the left bank side of the field flume and filling 75 % of the flume's width. A free flowing section of 5 m between the end of the inlet and the beginning of the patch was created (poles 3-8). In this section, all vegetation and other obstacles were removed to ensure a uniform incoming stream velocity.

To minimise possible side effects, no measurements were carried out in the 0.1 m vicinity of the field flume borders, leaving a test section of 1 m wide and 4.8 m long. Measurements were performed on day 1 of the experiment, to obtain initial conditions, on day 2 before and after changing the inlet position and on days 3 and

4. On top of the field flume, a permanent grid with a mesh size of 8 by 8 cm was attached. Bathymetry was measured in each mesh with a regular measuring stick (error = 0.5 cm), yielding a measurement density of 156 measurements per m^2. To verify the sediment quantity that settled during the experiment, six circular plate sediment traps were placed after construction of the field flume. Three traps were located in the middle in the free flowing section downstream of the inlet (near poles 3, 4 and 6), one trap just in front of the patch, one trap adjacent to the patch and one trap just behind the patch (Fig. 2.1). Sediment from the traps was collected on day 5, dried for 48 h at 70°C and weighed. Grain size distribution was determined using a laser diffraction unit (Mastersizer S, Malvern Instruments, Worcestershire, UK). Detailed, 3-dimensional velocity measurements in the flume's test sections were performed using an Acoustic Doppler Velocimeter (ADV Vectrino, Nortek AS, Rud, Norway). ADV measurements were collected over a sampling period of 90 seconds at a sampling rate of 25 Hz. As post-processing, spikes and data with a poor quality (standard quality threshold values are: SNR $<$ 15 dB and correlation $<$ 0.70) were removed and replaced by an interpolation of neighbouring samples. For an explanatory key clarifying the 3-dimensional results, see Fig. 2.1(e). Velocity components u, v, w [m/s] represent the stream wise, lateral and vertical direction respectively and u', v' and w' [m/s] the fluctuations around the mean values $< u >$,$< v >$,$< w >$, which are formulated by:

$$
\begin{aligned}
u' &= u - < u > \\
v' &= v - < v > \\
w' &= w - < w >
\end{aligned}
\tag{2.1}
$$

V_x, V_y and V_z [m/s] represent the depth-averaged velocities over a measurement profile, averaged over the measuring time period:

$$
\begin{aligned}
V_x &= \frac{1}{H}\sum_i h_i < u_i > \\
V_y &= \frac{1}{H}\sum_i h_i < v_i > \\
V_z &= \frac{1}{H}\sum_i h_i < w_i >
\end{aligned}
\tag{2.2}
$$

i represents measurement i of the velocity profile, h_i the height (m) over which measurement i is representative and H represents the total water depth [m]. The Reynolds stresses $< u'w' >$, $< u'v' >$, $< v'w' >$ $[\mathrm{m}^2/\mathrm{s}^2]$ are obtained by averaging the multiplication of the velocity fluctuations of the different velocity components over the total measuring period N:

$$
\begin{aligned}
< u'w' > &= \frac{1}{N}\sum_{t=1}^{N} u'_t w'_t \\
< u'v' > &= \frac{1}{N}\sum_{t=1}^{N} u'_t v'_t \\
< v'w' > &= \frac{1}{N}\sum_{t=1}^{N} v'_t w'_t
\end{aligned}
\tag{2.3}
$$

The bed shear stress τ_0, can be calculated by:

$$
\tau_0 = 0.5\rho C_1 \left(< u'^2 > + < v'^2 > + < w'^2 >\right) = 0.5\rho C_1 TKE \tag{2.4}
$$

where C_1 is a proportional constant with a value of 0.19 (Biron et al., 2004) and TKE the turbulent kinetic energy [$\mathrm{m}^2/\mathrm{s}^2$]. Calculations are based on measurements close to 10 % of the water depth. Measurements were performed in three longitudinal sections: through the vegetation, on the edge of vegetation and free flowing zone and next to the vegetation, and at least four cross sections: inlet of measurement area, just before patch presence, within the patch and behind patch. Vertical profiles were measured with measurements at 5 to 9 depths per profile and with 0.30 m maximum distance between each profile. Discharge measurements in the river (upstream of the field flumes' location) and in the field flume itself were obtained according to the velocity-area method, using an ElectroMagnetic Flow meter with flat probe (EMF; Valeport model 801, Totnes, UK) to measure velocities. EMF measurements were collected over a sampling period of 60 seconds at a sampling rate of 1 Hz. River discharge was measured on a daily basis with a width interval of 0.5 m and a depth interval of 0.1 m. Flume discharges were also measured on a daily basis at 0.3, 0.6 and 0.9 m from the left bank side of the field flume near pole n°6 with a depth interval of 0.1 m (see Fig. 2.1). Water levels were continuously monitored using CTD-divers attached to poles n°7 and 11 (See Fig. 2.1; Eijkelkamp, Giesbeek, NL).

Laboratory measurements were carried out in a racetrack shaped flume at the Netherlands Institute of Ecology Centre for Estuarine and Marine ecology (NIOO-CEME) in Yerseke (NL). The laboratory flume is 17.6 m long and 0.6 m wide. Measurements were carried out at a water height of 0.4 m and at adjustable stream velocities of 0.1, 0.2 and 0.3 m/s generated by a conveyor belt. Water passes through a collimator before reaching the study section to create a uniform stream velocity. A more detailed description of this laboratory flume can be found in Bouma et al. (2005). A *C. platycarpa* patch was attached with its root side to the bottom of the laboratory flume at the study section leaving a submerged canopy, resembling natural conditions. The patch was smaller than the one used in the field flume (1.10 ± 0.10 m long, 0.50 ± 0.05 m wide) to fit the laboratory flume, resulting in a blockage area of 67 %. For each incoming stream velocity, the following patch parameters were measured: length [m], width [m], depth [m] of the canopy's upper and lower surface in the water column on each 0.1 m of canopy length, canopy angle with the laboratory flume bottom [°] and biomass volume $[\mathrm{m}^3]$. Length, width and canopy depths were measured with a ruler (error = 0.5 cm), the patch angle was derived from longitudinal photos of the patch and biomass volume was derived afterwards from a water level rise in a container after immersing the patch. Projected frontal area $[\mathrm{m}^2]$, length/width ratio and total patch volume $[\mathrm{m}^3]$ were mathematically derived from length, width and canopy depth measurements. By subtracting biomass volume from patch volume, the volume of free space inside the patch is calculated, which accounts for patch porosity. After all measurements were done at three velocities, the canopy was shortened twice by 0.2 m by cutting. After every cut, another cycle of 3 velocities and successive measurements followed. Finally, all was repeated for three replicate patches. The EMF velocity meter was used to measure incoming stream velocity and velocity alongside the patch both at the depth of the patch canopy. Note that this depth differed depending on the stream velocity that was set and on the canopy length and results can therefore only be compared relatively.

Additionally to these measurements, one patch (1.09 m long, 0.47 m wide) was attached to a force transducer that was recessed into the bottom of the flume causing the least disturbance possible. This transducer consists of a stiff solid platform, carried by two steel cantilever beams with four temperature-corrected strain gauges mounted in pairs on opposite sides of each of the two steel cantilevers (for details see Bouma et al. (2005)). Calibration was done according to Stewart (2004). Voltage output of this transducer was linear with forces up to 10 N. On top of this transducer, a metal strip is present to attach any object (in casu a *C. platycarpa* patch). The patch was subjected to a series of different stream velocities (0.1, 0.2 and 0.3 m/s). The drag force (mV, converted to N), as well as canopy length [m] and projected frontal area $[\mathrm{m}^2]$ were measured as described for the previous series of measurements. Next, the canopy was shortened by 0.2 m by cutting; followed by another cycle of 3 velocities and successive measurements. This was repeated several times until 0.2 m patch remained. The measured drag forces (as a function of patch length) are compared with theoretical drag forces calculated for a scenario with rigid patches. Hydrodynamic forces acting upon an object can be calculated with the formula of Denny (1994):

$$F = 0.5 C_D \rho A U^{\beta} \tag{2.5}$$

with C_D = drag coefficient (2.1 for rigid objects and less than 2.1 for flexible objects that reconfigure by bending), ρ = density (1000 $\mathrm{kg/m^3}$ for fresh water), A = frontal area [$\mathrm{m^2}$], U = incoming velocity [m/s] and β = 2 for rigid objects and less than 2 for flexible objects that reconfigure by bending (Vogel, 1994). Comparing measured and theoretic values is indicative of the effect of bending on avoiding hydrodynamic stress.

SAS 9.2 (SAS Institute inc., Cary, USA) was used to perform all statistical analyses. A Wilcoxon Signed Rank test (non-parametric alternative of paired t-test) was performed comparing two sample groups that were not independent. A Pearson correlation test was applied to test for relations between variables. Figures are made using the linear interpolation algorithm from Akima (1978) for irregularly spaced data, no extrapolation of data to the boundaries was performed.

2.4 Results

Only small water level fluctuations were recorded (about 5 %) and overall river discharge remained stable around 0.20 $\pm$ 0.02 $\mathrm{m^3/s}$ during the whole field measurement period. In the field flume, discharge before changing the inlet position was 0.07 $\pm$ 0.06 $\mathrm{m^3/s}$. After widening the inlet position, the discharge increased 24 % to 0.09 $\pm$ 0.06 $\mathrm{m^3/s}$.

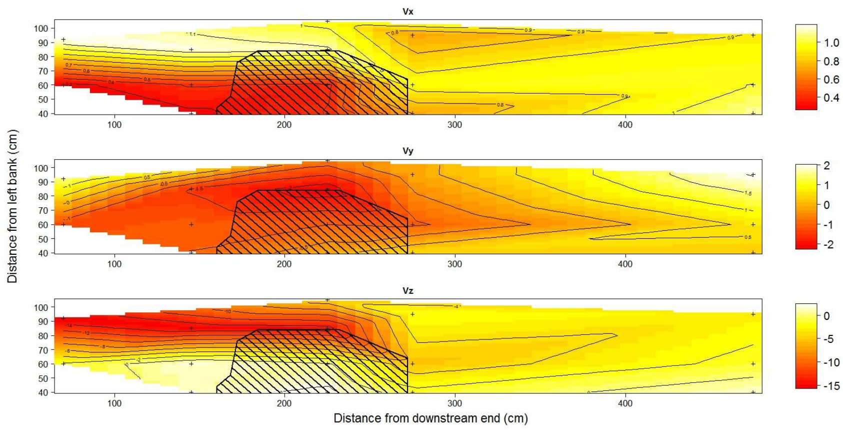

Figure 2.3: Plan view of the stream wise (a), lateral (b) and vertical (c) depth-averaged velocities, expressed relatively compared to the incoming velocities (V_x = 14.09 cm/s, V_y = 0.56 cm/s, V_z = 0.13 cm/s). Positive velocities are oriented corresponding to the right-hand law (see Fig. 2.2). The patch is represented by a hatched polygon. Measurements are obtained on day 4 of the experiment in the field flume.

Where are the zones around a patch with a lower or higher stream velocity compared to incoming stream velocity?

Results are shown in plan view, as relative values compared to the incoming stream velocity (Fig. 2.3). Uniform flow conditions were well developed at the entrance which evolves to inhomogeneous flow conditions in the vicinity of the vegetation patch. Maximum (depth-averaged) stream wise velocities, V_x were consistently found on the free flow side in the zone behind patch presence and are typically 10 % to 30 % higher than the incoming (depth-averaged) velocities. Minimum stream wise velocities are found behind the patch itself where the incoming velocity is reduced by 50 % to 70 %. As such, the difference between the stream wise velocity behind and next to the patch ranges a factor of 2.5 to 4. Also in the transverse velocities, V_y, a quite clear pattern can be recognised. Above the patch, the water is moving towards the free flowing side. However, sometimes the measurement point on the left bank reveals a small value in the opposite direction and as such a diverging stream flow over the patch can be observed. This will likely be more pronounced in solitary patch stands. In the zone behind patch presence, a flow from the free flowing side towards the zone behind the patch is observed. In the vertical direction, V_z shows a clear upwards trend parallel to the plant obstruction and a downwards trend behind the patch, which can be clearly seen on the free flowing side.

Focusing on the flow velocity profiles, measured by EMF, clear distinctions between the different regions can be observed, as is depicted in Figure 2.4. In the cross sections measured before the vegetation, the normal logarithmic boundary profile is observed (Figure 2.4a). This profile is also seen in the profile of the free flowing side of the cross sections through the vegetation (Figure 2.4b). However, the profiles in the (dense) vegetation show very low and constant values in the vegetation, due to the drag exerted by the plant stems, and a steep increase above the vegetation. The profile at the edge of the vegetation shows a double-maximum, with a smaller maximum velocity below the patch and a higher maximum above the canopy. It should be noted that maximum velocities at the free-surface, in Figure 2.4b, are equal in all profiles.

Can we recognise specific critical zones near the patch edges with high turbulence values causing a risk of erosion, patch uprooting or stem breakage?

More insight in the flow structure can be obtained by analysing the components of the turbulent stresses, which represent the momentum transport due to turbulent motions (Wu, 2007). The spatial distribution of components - $< u'w' >$, - $< u'v' >$ and - $< v'w' >$ (u', v' and w' represent the stream wise, lateral and

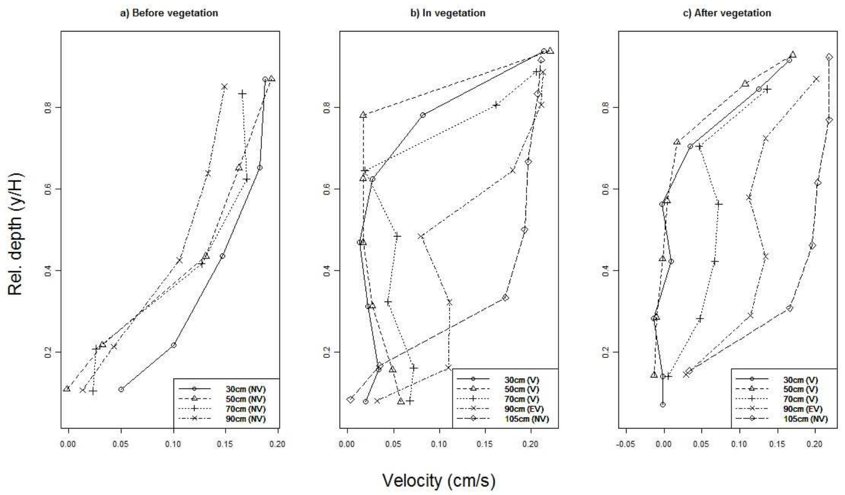

Figure 2.4: Vertical profiles of the mean stream wise velocity in a cross section before the vegetation (a), through the vegetation (b) and behind the vegetation (c). ❍, Δ, $+$, X, ✧ are stream wise velocity measurements respectively located at 30 cm, 50 cm, 70 cm, 90 cm and 105 cm from the left edge of the in situ flume. In the legend: (NV), (V) and (EV) respectively stands for No Vegetation, Vegetation and Edge of Vegetation

vertical velocity fluctuations respectively, calculated according to eq. 2.1, and the $<>$ symbol denotes a time average) are shown in three different views: a cross section view through the patch (Fig. 2.5a), a longitudinal view on the edge between patch side and free flowing side (Fig. 2.5b) and a longitudinal view along the patch (Fig. 2.5c). Critical zones with increased values of the first component $< u'w' >$, can be noted adjacent to the patch (Fig. 2.5a), near the downstream end of the vegetation on the border between the patch and the free flowing side (Fig. 2.5b) and in the measuring zone just before patch presence and on the downstream end of the patch (Fig 2.5c). Zones of increased turbulence close to the bottom indicate an increased risk for erosion in these specific zones (Knight et al., 2010). Maximal values go up to 8 $\mathrm{cm}^2\mathrm{s}^{-2}$ and are consistently found in the top layer of the vegetation and just behind it (Fig. 2.5c). The second, transversal, component - $< u'v' >$ shows a heterogeneous spatial pattern which is more or less equal to the first component and values are in the same order of magnitude. The most pronounced, negative values are found on the border between the vegetation and the free flow zone, more specifically below the patch (Fig. 2.5a,b). The values of the third component - $< v'w' >$ are consistently smaller than these of the other shear stress components. Nevertheless, these momentum fluxes are still important for transport processes because of their contribution to mechanical dispersion of substances, as they are indicative of rotational motions, their spatial pattern reveals the presence of secondary circulation (Sukhodolov and Sukhodolova, 2010). Adjacent to the patch, values are highest near the bottom towards the patch (Fig. 2.5a). In the longitudinal section on the edge of the vegetation, maximum values are found near the downstream end of the vegetation on the border between the patch and the free flowing side (Fig. 2.5b). In the longitudinal sections through the vegetation maximum values are found behind the plant patch, on the height of the canopy itself (Fig. 2.5c).

A fundamental variable in river studies to link flow conditions to sediment transport is the bed shear stress τ_0. Calculations are based on measurements close to 10 % of the water depth and shown as vectors in Fig. 2.6. In the field flume, a larger bottom shear stress can be observed in the region next to the patch, where depth-averaged velocities are high (see Fig. 2.3). High values can also be observed in the measurements at the entrance.

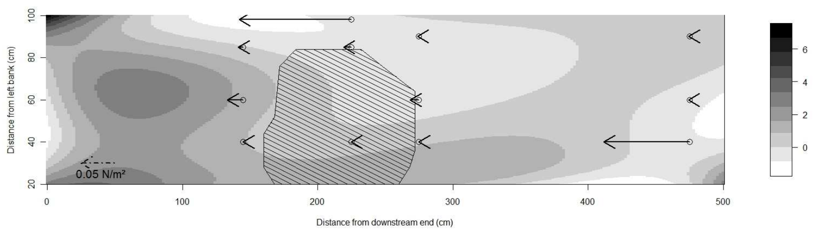

Figure 2.6: Plot indicating the relative zones of erosion and sedimentation (in cm) between the measurements of day 1 and day 4 within the test section of the field flume. Positive values indicate sedimentation, negative values indicate erosion. Arrows show the near bed shear stresses (Nm^{-2}), calculated from the TKE values at the bottom. The start point of the arrow (indicated with o) denotes the location of the measuring point.

Do zones with enhanced or reduced stream velocity or turbulent stress correspond with zones of erosion or sedimentation respectively?

The change in bathymetry between day 1 and day 4 in the field flume is depicted in Figure 5. It can be noted that mainly sedimentation, indicated in Figure 2.6 as positive values, is observed. The zones of highest sedimentation are observed behind the patch. The zone of most intense erosion or marginal change is observed in the free flowing side and more precisely in the zone shortly behind patch presence, on the free flowing side. These patterns are not exactly confirmed by the results from sediment traps (Table 2.1), the lowest values are indeed found next to the patch, but a higher DM content is observed just before the patch in stead of just behind. In the free flowing section before the test section, sedimentation gradually decreases to about one-third of its initial quantity. Once entering

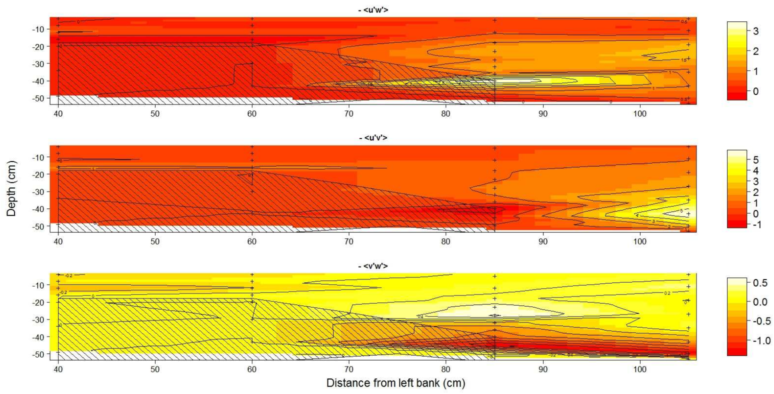

(a)

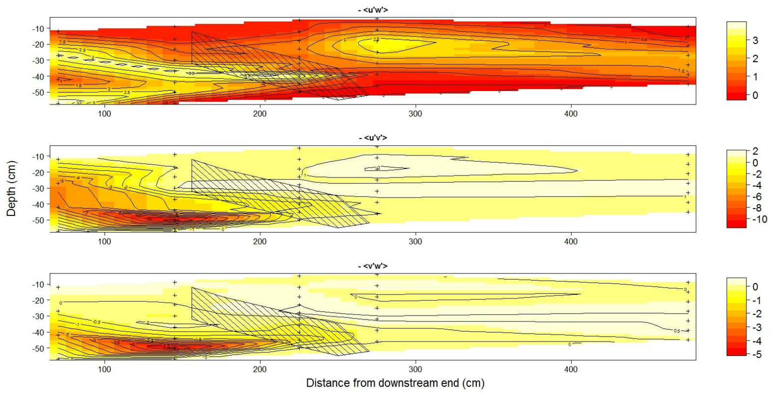

(b)

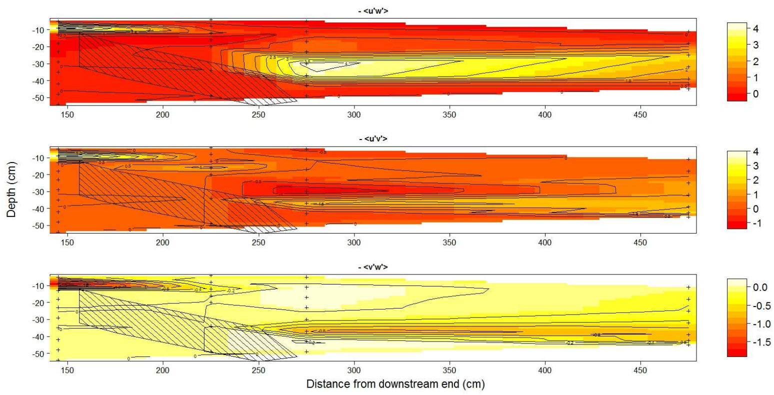

(c)

Figure 2.5: Distribution of the turbulent stresses - $< u'w' >$, - $< u'v' >$ and - $< v'w' >$ in a cross section view through the vegetation (a), in a longitudinal view adjacent to the patch, on the edge between patch side and free flowing side (b) and in a longitudinal view through the vegetation (c). Absolute values are expressed in $\mathrm{cm}^2\mathrm{s}^{-2}$. The patch is represented by a hatched polygon. Measurements are obtained on day 4 of the experiment in the field flume.

the test section, differences are observed around the patch. Highest sedimentation is observed before the patch, compared to very low sedimentation adjacent to the patch and an intermediate sedimentation behind the patch. Grain size can be categorized as fine to medium sized sand based on the Udden (1914) and Wentworth (1922) scales. Overall, D_{50}'s are in the same order of magnitude and no clear trends are observed. A good qualitative agreement between the bed shear stress (indicated as vectors) and the bathymetry is shown in Fig. 2.6. As the scales of both measurements per flume are quite different (616 times 0.08 m x 0.08 m measurements for topography compared to 15 point measurements for velocity), no quantitative analysis is performed.

Table 2.1: Sedimentation quantity (dry mass: DM; $\mathrm{g/m^2}$) and median grain size (D_{50}; $\mu\mathrm{m}$) derived after 4 days with circular plate sediment traps. For the exact location of the traps, see Fig. 2.1a.

			field flume	
trap		location	DM $[\mathrm{g/m^2}]$	D_{50} $[\mu\mathrm{m}]$
1	Free Flowing Section	End of inlet	2206	119
2		1 m behind inlet	2068	111
3		Begin test section	822	148
4	Test Section	Before patch	6312	180
5		Adjacent to patch	930	161
6		Behind patch	3458	164

What is the importance of the free flowing zone above the patch in terms of averting incoming water and what is the consequence for the stream velocity alongside the patch?

Table 2.2 shows the results of different patch characteristics from the laboratory flume study at a stream velocity of 0.1 m/s (= 0.024 $\mathrm{m^3/s}$) and the differences when incoming stream velocities were doubled and tripled. It is clear from Table 2 that with increasing discharge, the patch reduces its frontal area by taking a deeper position in the water column. It becomes more streamlined by adapting its length/width ratio (Wilcoxon Signed Rank, $p<0.001$). A threefold increase of the incoming velocity results in a reduction of more than 30% of the patch frontal area ($p<0.001$) due to a halving of the original canopy angle with the horizontal ($p<0.001$) and a 13% decrease of the patch width ($p=0.004$). As a result, both patch volume and porosity decline at the highest speed ($p=0.011$). All these changes have undoubtedly an impact on the relative amount of free space over and alongside the patches affecting the proportion and speed of water that will flow there. The flow velocity behind the patch is zero, independent from patch

Table 2.2: Average values with standard error of patch characteristics at an incoming stream velocity of 0.1 m/s (U_I) and the changes of these values with increasing stream velocities to 0.2 m/s (U_{II}) and 0.3 m/s (U_{III}) compared to U_I. Significant differences with U_I were tested with a Wilcoxon Signed Rank Test, n = 11, significant p-values are accentuated bold.

Parameter		value at U_I	Change in parameter value			p-value
Frontal area	[cm^2]	1360.0 ± 30	U_{II} vs U_I	(%)	-20 ± 4	0.002
			U_{III} vs U_I	(%)	-35 ± 3	0.001
Patch length	[cm]	85 ± 6	U_{II} vs U_I	(%)	5 ± 1	< 0.001
			U_{III} vs U_I	(%)	8 ± 1	< 0.001
Patch width	[cm]	43.5 ± 0.9	U_{II} vs U_I	(%)	-7 ± 2	0.029
			U_{III} vs U_I	(%)	-13 ± 1	0.004
l/b ratio		2.0 ± 0.2	U_{II} vs U_I	(%)	13.0 ± 2.3	< 0.001
			U_{III} vs U_I	(%)	23.7 ± 1.6	< 0.001
Volume	[cm^3]	50000 ± 3000	U_{II} vs U_I	(%)	6 ± 4	ns
			U_{III} vs U_I	(%)	-9 ± 3	0.011
Porosity	[cm^3]	50000 ± 3000	U_{II} vs U_I	(%)	6 ± 4	ns
			U_{III} vs U_I	(%)	-9 ± 3	0.011
Canopy depth	[cm]	0.2 ± 0.2	U_{II} vs U_I	(cm)	5.6 ± 1.0	0.006
			U_{III} vs U_I	(cm)	10.2 ± 1.2	0.006
Canopy angle	[°]	19 ± 1	U_{II} vs U_I	(°)	-6 ± 3	0.001
			U_{III} vs U_I	(°)	-10 ± 3	0.001

length (Figure 2.7a), but this does not exclude flow through the patch. It is expected that the flow enters the patch at the front, but is then diverged out of the patch towards the free surface layer and/or towards the free flowing area next to the patch (Sand-Jensen and Mebus, 1996). Hence, all water eventually flows over or alongside the patch. The flow acceleration next to the patch reacts positively to patch width (Pearson correlation, p<0.001; Figure 2.7b) but negatively to canopy depth (p<0.001; Figure 2.7c). However, patch width and canopy depth are not completely independent as they both change simultaneously with higher incoming velocities (Table 2.2). This means that both canopy depth and patch length/width ratio have a tempering effect on flow acceleration adjacent to the patch. This was confirmed by field data from both in situ flumes after adjusting the inlet (data points represented by black squares in Figure 2.7c). The bending of the patch also had a significant effect on the drag force (Fig. 2.8) measured with the force transducer. The fits for C_D and β (see equation 2.5), using a non-linear least square fit in the R software, are presented in Table 2.3. All measured drag forces increased with increasing canopy length which corresponds to the theoretically calculated alternatives for a rigid canopy. The calculated alternatives were 2, 4 and 7 times higher for 0.1, 0.2 and 0.3 m/s respectively. These values are indicative for the effect of bending on avoiding hydrodynamic stress.

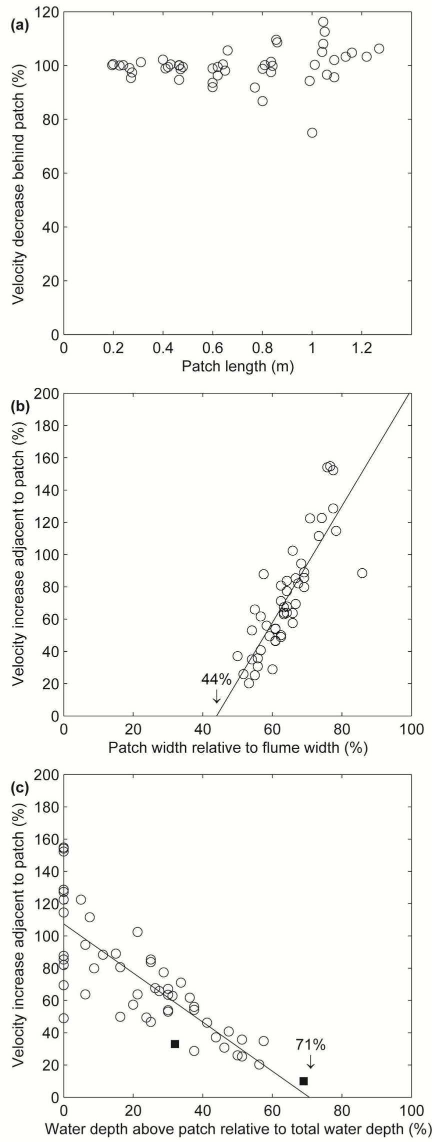

Figure 2.7: (a) stream velocity deceleration behind the patch [%] in function of patch length [m] and (b, c) stream velocity acceleration adjacent to the patch [%] in function of patch width, relative to flume width [%], and canopy depth, relative to total water height [%]. Panels (b) and (c) show significant relations (Pearson correlation test, $p < 0.001$, n = 49). In panel (b), the relation is extrapolated according to the trend y = 36 x - 159 until the starting point of velocity increment. In panel (c), the relation is extrapolated according to the trend y = -1.5 x + 107 until the velocity adjacent to the patch no longer increases. The ■ data point in panel (c) represents a similar result from the field flume.

Table 2.3: Values of C_D and β (see equation 2.5) for the different canopy lengths, measured with 3 incoming velocities, and for all canopy lengths together.

Patch Length [m]	C_D [-]	β [-]
0.2	1.54 ± 0.38	1.63 ± 0.18
0.4	1.29 ± 0.05	1.43 ± 0.03
0.6	1.06 ± 0.02	1.31 ± 0.02
0.8	1.2 ± 0.58	1.47 ± 0.36
1.0	1.02 ± 0.04	1.28 ± 0.04
1.2	1.2 ± 0.12	1.28 ± 0.08
All	1.2 ± 0.16	1.39 ± 0.1

2.5 Discussion

In and around a *C. platycarpa* patch, stream velocity is altered as a result of the, partially, blocking effect of the patch itself. This was clearly demonstrated in both flume experiments. A stream-wise current acceleration up to 30 % of the incoming velocity was recorded next to the patch in the field flume as well as a current deceleration up to 70 % behind the patch. Both values correspond to values previously published by Schoelynck et al. (2012b) for artificial structures that mimic submerged vegetation. Deceleration behind and acceleration next to the patch showed to be patch size dependent in the lab flume experiment. Current alteration is proposed to induce scale-dependent feedbacks between the organism and environment which is generally considered as a necessary condition for self-organised patchiness to form (Lejeune et al., 2004; Rietkerk and Van de Koppel, 2008).

A deeper insight in the flow structure can help to recognise critical zones of potential positive (i.e. increased sedimentation) or potential negative feedbacks (risk of erosion, uprooting or stem/leaf breakage). On the one hand, inside the patches and especially in the wake behind, sedimentation as positive feedback did occur to a significant extent. The bathymetric map (Fig. 2.6) shows sedimentation zones that correspond to the zones of low near bed shear stress (indicated by the arrows in Fig. 2.6), calculated from the turbulent kinetic energy and depth-averaged velocities (which can be related to bed shear stress too (Biron et al., 2004). On the other hand, four different critical zones have been identified where a negative feedback can occur. One is located at the downstream end of the patch at the height of the top layer of the canopy itself. As the region around the top of the vegetation has the highest velocity gradients in the velocity profile, this region has the highest shear and turbulence production is maximal (Folkard, 2011). It is not unlikely that extra tissue reinforcement is necessary to overcome this mechanical stress originating from drag forces (Bal et al., 2011; Schoelynck et al., 2012a), though this was not looked at in the present study. The other three are found near the bottom. The bathymetric map shows eroded zones that correspond to the zones of high near bed shear stress (Fig. 2.6). However, erosion was minimal and bed topography remained stable. The bed shear stress was probably not large enough to induce erosion. To get a mean grain size of 167 $\mu\mathrm{m}$ to move, a minimal bed shear stress of 0.15 to 0.16 Nm^{-2} is needed according to the Shields diagram (Van Rijn, 1993). The bed shear stresses calculated in the field flumes rarely exceed this threshold during the measurement period, which is characterized by base flow, and as such no erosional areas were observed.

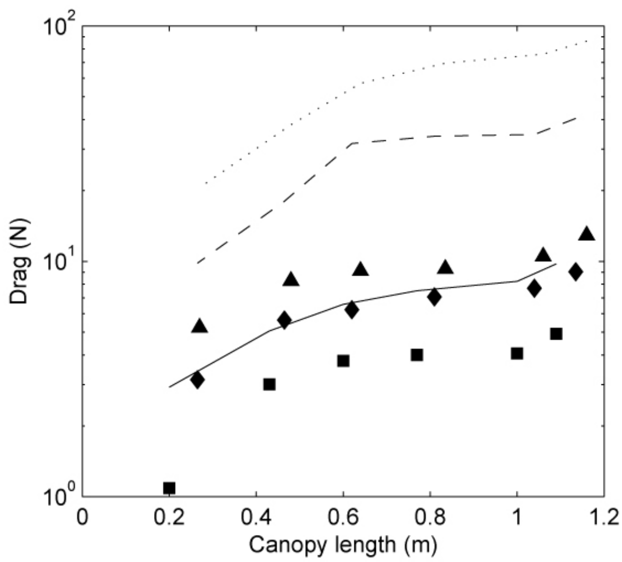

Figure 2.8: Measured drag force acting on a patch in function of patch length and repeated for three different stream velocities (■ = 0.1 m/s; ◆ = 0.2 m/s; ▲ = 0.3 m/s). These values are compared with calculated drag forces (■ = 0.1 m/s; ◆ = 0.2 m/s; ▲ = 0.3 m/s) acting on the same patches in a rigid scenario (See Eq. 2.5 with C_D = 2.1, β = 2). Note the logarithmic scale on the y-axis.

Two main reasons for *C. platycarpa* to avoid/reduce a negative feedback can be pointed out. First, hydrodynamic stress can increase the drag, not only on individual shoots or leaves, but also on the entire patch. To avoid stem- or leaf breakage, strength tissue can be produced, but involves expensive energetic costs for the plant (Schoelynck et al., 2010, 2012a). Secondly, the total above ground drag force must be balanced with below ground root anchorage strength. Anchorage increases with root size and substrate type (Schutten et al., 2005) but also with increasing sediment stability (Angers and Caron, 1998; Castellanos et al., 1994; Thorne, 1990). Slow velocities near the river bed have less eroding capacity, hence stabilising plant roots. Plants or patches thus benefit twice from less acceleration and a tempered negative feedback effect. This allows them to basically avoid shear stress, or at least partially, and to grow under dynamic circumstances such as rivers or to overcome peak discharge events as will be discussed later.

Laboratory flume results clearly demonstrate this proposed shear stress avoiding strategy. As the incoming stream velocity increases, the patch takes more and more a position near the bottom. Both canopy depth and patch length/width ratio have a tempering effect on flow acceleration adjacent to the patch. This was confirmed by field data from the in situ flume. It allows more water to flow over the patch, resulting in two positive effects: (i) reduction of the drag force on the patch and (ii) reduction of the uprooting risk. First, together with its more streamlined character, the patch experiences much less drag force in comparison to a rigid form (up to 7 times for the highest velocity tested). This will almost certainly reduce the root anchorage strength needed to balance the aboveground drag and diminishing the risk for uprooting. Secondly, this uprooting risk is once more reduced as less flow acceleration results in reduced near bed shear stress (as discussed above). Scouring around stems and roots is a major problem for emergent species, especially juveniles (Bouma et al., 2009). It is, however, less likely for *C. platycarpa* as the patch behaves as a streamlined bulb during rough hydraulic conditions.

There is, however, a downside to this strategy. Bending depends on the length and thickness of the shoots (Manz and Westhoff, 1988) with longer shoots generally being more flexible and thicker shoots being less flexible. The size of the patch is also important as its volume determines the buoyancy of the patch. The extent of bending is thus species specific (Sand-Jensen, 2003) and therefore, along with the flow speed, determines the height within the water column at which the leaves are located (Green, 2005). This can harm photosynthetic success threefold: (i) light attenuates with depth (ii) by self-shading due to the stacking of leaves on top of each other and (iii) by an increased biomass density (Sand-Jensen and Pedersen, 1999). The latter was confirmed in the laboratory flume experiments. The first two negative feedbacks may be overcome by a shade tolerance, with saturation points ranging from 10 % to 50 % compared with full sun light (Spencer and Bowes, 1990). Changing surface area to volume ratio, however, proved to influence photosynthesis and dark respiration negatively (Madsen et al., 1993), especially by hampering nutrient- and gas exchange (Cornelisen and Thomas, 2004; Morris et al., 2008).

Nevertheless, this intriguing mechanism of avoiding a negative feedback seems a fairly good strategy for plants to survive in running water. We therefore suggest that for aquatic river vegetation at base flow regimes, the presence of scale-dependent feedbacks, proposed in Schoelynck et al. (2012b) are most likely to be important. However, erosion does not seem to be the main negative feedback acting upon patch growth, but rather enhanced flow velocity and reduced sedimentation. Nevertheless, during high-discharge events, stream velocities could impose erosion around aquatic river vegetation patches (Sand-Jensen and Mebus, 1996) and may govern drag and the probability of uprooting (Sand-Jensen and Pedersen, 2008). We state that with temporarily high discharges, the surplus of water is diverted to the open spaces in between the patches and, most importantly, to the open space that arose above the patch while bending. This protects the canopy to high stream velocities. The potentially temporary reduced photosynthetic and growth conditions probably do not outweigh the risk of uprooting. If the increased discharges would hold longer, physiological stress (from reduced photosynthetic and growth conditions) is likely to become more important (Bal et al., 2011).

Self-organised ecosystem patchiness, based on scale-depend feedbacks has important implications for ecosystem functioning, as it increases ecosystem productivity, resilience and resistance to environmental fluctuations, as compared with spatially homogeneous ecosystems (see Rietkerk and Van de Koppel (2008) and references therein). To get further insight in the interrelationship between flow, sedimentation and plant survival in a river stretch dominated by a patchy and submerged vegetation, an integrated model can be useful where flow hydrodynamics, plant growth and sedimentation processes are coupled. If the focus lies on the flow-vegetation interaction, a 3D approach seems most appropriate to represent the complex, highly three dimensional flows. If sedimentation and resulting topography effects are of interest, which are processes acting on longer temporal scales, a 2D approach can be sufficient, as it needs less computational effort (important for long model simulation runs) and is still capable of representing local patterns of bed shear stress, which are observed. In any case, for hydraulic engineers, a proper implementation of vegetation presence, dynamics and flexibility will be crucial for accurate results. For aquatic ecologists, accurate in situ hydrodynamic measurements can be very useful in explaining different ecological phenomena.

2.6 Conclusion

In this chapter, complementary results of field- and laboratory flume studies clearly show that the presence of vegetation alters the normal open-channel flow into a complex, three-dimensional flow field and according patterns of the turbulent stresses. This results in a local differentiation of sedimentation and the river system adapts to this situation. Local sedimentation provides the patch with a positive feedback; the potential harmful effects of a negative feedback are partly avoided by the patches. From our study, it can be concluded that the limit on growth is not due to erosion, but rather to increased flow speeds and therefore a lack of deposition. Macrophytes reconfigure at higher velocities by bending and taking a deeper position in the water column. This process also results in a zero increase of the velocity adjacent to the patch, for a relative patch width of 44 % and relative plant height of 29 %. The flexibility of the plant clearly results in lower drag forces, compared to rigid objects. Patch reconfiguration probably reduces temporarily the own optimal growth conditions, but will likely not outweigh the risk on uprooting.

3

Interaction between Neighbouring Vegetation Patches: Impact on Flow and Deposition

3.1 Abstract

Flow and sedimentation around patches of vegetation are important to landscape evolution, and a better understanding of these processes would facilitate more effective river restoration and wetlands engineering. In wetlands and channels, patches of vegetation are rarely isolated and neighboring patches influence one another during their development. In this experimental study[1], an adjacent pair of emergent vegetation patches were modeled by circular arrays of cylinders with their centers aligned in a direction that was perpendicular to the flow direction. The flow and deposition patterns behind the pair of patches are described for two stem densities and for different patch separations (gap widths). The wake pattern immediately behind each individual patch was similar to that observed behind an isolated patch, with a velocity minimum directly behind each patch that produced a well-defined region of enhanced deposition in line with the patch. For all gap widths (Δ), the velocity on the centerline between the patches was elevated to a peak velocity U_{max} that persisted over a distance L_j. Although U_{max} was not a

[1]This chapter is based on the following article: *Meire, D., Kondziolka, J. and Nepf, H.M. (2014) Interaction between neighboring vegetation patches: Impact on flow and deposition. Water Resour. Res., 50, doi:10.1002/2013WR015070.*

function of gap width, L_j decreased with decreasing gap width. Beyond L_j, the wakes merged and the centerline velocity decayed to a minimum at a distance L_m. The merging of wakes and associated velocity minimum produced a local maximum in deposition on the centerline between the patches, but downstream from the patches. If this secondary region of enhanced deposition promotes new vegetation growth, the increased drag on the centerline could slow velocity between the upstream patch pair, leading to conditions favorable to their merging.

3.2 Introduction

Macrophytes are important ecosystem engineers (Jones et al., 1994) that have a significant effect on both freshwater and marine environments (Corenblit et al., 2007; Dollar, 2004). The ecosystem services they provide include decreasing erosion (Schulz et al., 2003), reducing turbidity (Jones et al., 2012), improving water quality (Chambers and Prepas, 1994; Madsen et al., 2001), and providing habitat for many species (Kemp et al., 2000). The hydraulic behavior near macrophytes is important, because it influences all of these processes, as well as the evolution of the macrophyte stand.

Traditionally, hydraulic studies have focused on long, uniform meadows, characterizing the bulk flow resistance (e.g. Jarvela, 2005; Kouwen and Unny, 1975; Nikora et al., 2008; Stephan and Gutknecht, 2002) and describing the vertical flow structure and turbulence characteristics (e.g. Lopez and Garcia (2001), and review in Nepf (2012a)). However, vegetation is often found in patches of finite length and width, rather than continuous segments (Naden et al., 2006; Sand-Jensen and Madsen, 1992; Schoelynck et al., 2012b; Temmerman et al., 2007), so that recent attention has been focused on the study of finite patches of vegetation, both in the laboratory and in the field (Bouma et al., 2009; Chen et al., 2012; Cotton et al., 2006; Zong and Nepf, 2012). The interaction between neighboring patches has also been considered (Vandenbruwaene et al., 2011). It has been proposed that the feedback between finite patches and flow can lead to large-scale, ordered spatial patterns, a process called spatial self-organization (Rietkerk and Van de Koppel, 2008). This mechanism of landscape evolution has been demonstrated for a wide variety of ecosystems, such as mussel beds (van de Koppel et al., 2005), diatoms (Weerman et al., 2010), vegetation on tidal flats (van Wesenbeeck et al., 2008), and vegetation in lowland rivers (Schoelynck et al., 2012b). In each case, the introduction of an organism produces positive feedbacks (stress reduction, accumulation of nutrients) and negative feedbacks (stress enhancement, depletion of nutrients), which influence the pattern of growth. For example, Bouma et al. (2009) show for intertidal macrophytes (*Spartina anglica*) that, above a certain threshold of vegetation density, sediment is trapped within the vegetation (positive feedback) and erosion is observed next to the vegetation (negative feedback).

In shallow aquatic habitats, where macrophytes can establish, changes in the near-bed velocity will influence sediment transport and thus the bathymetry, and these biogeomorphic feedbacks are important to macrophyte development. Sites of erosion are places of lower nutrient availability that lead to less favorable conditions for plant growth (van Wesenbeeck et al., 2008). Sites of deposition, in contrast, are where seeds and organic matter will tend to accumulate, leading to favorable conditions for plant growth (Gurnell et al., 2005). In this study, the bed of the laboratory flume is not movable, and as such no bed transport is taken into account. The focus is instead on the deposition of suspended sediments. Deposition of fine sediments in flow influenced by vegetation has been related to the characteristics of the mean and turbulent velocity field through laboratory studies (Chen et al., 2012) and field studies (Cotton et al., 2006; Sand-Jensen, 1998; Schoelynck et al., 2012b). Chen et al. (2012) modelled patches of emergent vegetation in a laboratory flume. They found that net deposition was generally inhibited in areas of high turbulent kinetic energy (TKE) or high velocity, likely due to resuspension, and generally enhanced in areas of low TKE and low velocity. In particular, a region of low velocity and low TKE occurred directly behind the patch over a length-scale of several patch diameters, and enhanced deposition was observed within this region. This is consistent with several field studies. Schoelynck et al. (2012b) placed model patches of vegetation in a real stream and measured the velocity around the patches. Reduced velocities inside and behind the mimic vegetation allowed for sediment to settle in these areas. Tanaka and Yagisawa (2010) and Tsujimoto (1999) also observed the deposition of fine material in the wake of individual circular patches. The current work builds on the previous studies of individual patches to consider the interaction between two adjacent patches. We explore how the spacing between patches influences the pattern of flow distribution and deposition in the wakes of the two patches.

3.2.1 Previous work on flow adjustment to a single patch

To understand how a patch wake is influenced by its neighbor, we must first understand the characteristics of flow past an isolated patch. Flow past an isolated patch is depicted in Figure 3.1. The patch diameter is D [cm], and the patch density is described by a, which is the frontal area per unit volume [1/cm]. For a given stem density, m $[1/\mathrm{cm}^2]$, and mean stem diameter, d $[\mathrm{cm}]$, $a = m \cdot d$. U_∞ is the uniform streamwise velocity far upstream of the patch. The streamwise coordinate is x, with $x = 0$ at the leading edge of the patch. The lateral coordinate is y, with

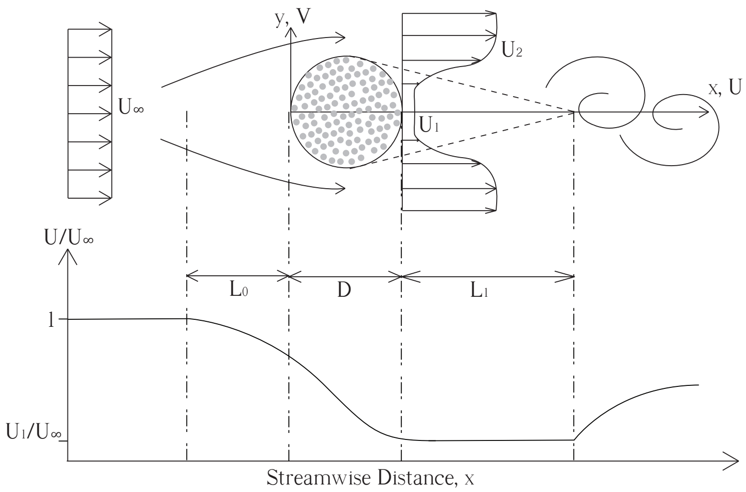

Figure 3.1: Flow pattern around a porous patch, based on the characteristics explained in Zong and Nepf (2012) and Chen et al. (2012). D represents the patch diameter, L_0 represents the length of the upstream adjustment region, L_1 represents the length of the steady wake zone, and U is the streamwise component of the velocity. The streamwise coordinate is x, and x = 0 at the leading edge of the patch. The lateral coordinate is y, and y = 0 on the patch centerline. U_1 is the streamwise velocity of the slower-moving fluid directly behind the patch ($y = 0$, $x = D$) and U_2 is the streamwise velocity of the faster-moving fluid outside the patch wake ($y > D/2$, $x = D$). The bottom plot depicts the streamwise velocity along the centerline of the patch.

$y = 0$ at the centerline of the patch. The time-averaged velocity in the streamwise and lateral directions is denoted U and V, respectively. At a distance L_0 upstream of the patch, the flow starts to decelerate and deflect laterally (Rominger and Nepf, 2011). As the fluid passes around and through the patch, a shear layer forms at each side of the patch between the slower-moving fluid behind the patch (U_1) and the faster-moving fluid outside the patch wake (U_2). The inner edge of each shear layer is depicted with a dashed line in Figure 3.1. Zong and Nepf (2012) showed that the distance from the edge of the patch to the inner edge of the shear layer (δ) grows linearly with streamwise distance (x) from the patch, consistent with linear shear layer growth (e.g. Champagne et al., 1976). The growth rate depends on the velocity difference, $\Delta U = U_2 - U_1$ and the mean velocity within the shear layer, $\bar{U} = 0.5\ (U_1+U_2)$.

$$\frac{d\delta}{dx} = S_\delta \frac{\Delta U}{\bar{U}} \tag{3.1}$$

S_δ is an empirical parameter equal to 0.10 ± 0.02 for emergent vegetation patches (Zong and Nepf, 2012). The shear-layers formed on either side of the patch meet at the patch centerline at a distance L_1 from the patch (Figure 3.1), where

$$L_1 = \frac{\frac{D}{2}\bar{U}}{S_\delta \Delta U} \tag{3.2}$$

Over this distance the velocity on the patch centerline U_1 remains unchanged. This velocity may be predicted from the non-dimensional flow blockage, $C_D aD$, where C_D [-] is the drag coefficient for the stems within the patch (Chen et al., 2012). Beyond this region, ($x > D + L_1$), a von Kármán vortex street may develop, depending on the value of the flow blockage parameter and solid volume fraction (ϕ) (Zong and Nepf, 2012). Specifically, for ϕ less than approximately 4%, vortex streets do not form. When present, the oscillation frequency associated with the patch-scale von Kármán vortex street, f_k, is comparable to that for a solid object of the same diameter, D. Specifically, the Strouhal number $St = f_k D/U_\infty = 0.2$ (Zong and Nepf, 2012).

3.2.2 Previous work on flow adjustment to a pair of obstructions

In this study, we consider the flow and deposition patterns near a pair of side-by-side model vegetation patches, each with diameter D. We can draw on some existing literature for side-by-side circular cylinders. The wake characteristics for this geometry depend on the distance between the two cylinders and the Reynolds number ($Re_D = U_\infty\ D/\nu$), where ν $[\mathrm{cm}^2/\mathrm{s}]$ is the kinematic viscosity (Sumner, 2010). Three types of flow behavior are summarized by Sumner (2010). When the distance between the two cylinders Δ is larger than about 1.2 times the cylinder diameter (D), parallel vortex streets are observed, predominantly in anti-phase (Sumner, 2010; Sumner et al., 1999). As the cylinders are brought closer together, and Δ becomes less than 1.2 times the cylinder diameter, a biased flow pattern develops in which flow through the gap is deflected toward one of the cylinders. The deflection angle of the gap flow increases as Δ/D decreases. The cylinder towards which the flow is deflected has a narrower and shorter near-wake zone and higher frequency shedding than the neighbouring cylinder. Finally, at separation distances less than 10-20% of the diameter, the two cylinders behave as a single bluff-body, as indicated by the formation of a single von Kármán vortex street that scales with the total width across both cylinders and has a lower frequency of vortex shedding compared with an individual cylinder. The flow between the two cylinders behaves as bleed flow (streamwise flow through the obstruction), which lengthens the streamwise extent of the vortex formation region (Sumner et al., 1999).

The interaction between porous cylinders (a model for vegetation patches) has not been characterized as thoroughly as the interaction of solid cylinders. Vandenbruwaene et al. (2011) considered the change in flow distribution close to a pair of vegetation patches. The goal of their study was to understand under what conditions adjacent patches would merge together, rather than remain separated by a channel. Their velocity measurements were taken adjacent to and in between patches of different diameter (D) and different separation distances (Δ). Acceleration of flow, i.e. elevated velocity, between the patches was observed for all conditions; however, the acceleration decreased, compared with the acceleration at the outer edges of the patches, below a gap width $\Delta/D \approx 0.1$. From these observations alone, one might conclude that adjacent patches cannot merge, since flow acceleration, which would tend to promote erosion and inhibit plant growth, will always be maintained in the space between the patches. However, we hypothesize that a different conclusion might be reached if we consider the flow development in the wake of the patches. As described above, the wake behind a single patch is a region of sediment deposition and potential vegetation growth. Based on the solid-cylinder literature (above) we anticipate that for some interpatch distances, a merged wake may form behind the pair of patches that resembles the wake of a larger, single patch and, as such, will have a region of enhanced deposition at some point behind and on the centerline between the two patches. Deposition and vegetation growth within the merged wake could eventually influence the flow distribution between the upstream patches and allow the patch to merge. Motivated by this hypothesis, the focus in this study is to determine the influence of interpatch distance, patch density and patch diameter on the flow and the deposition pattern in the wake of a pair of side-by-side patches.

3.3 Material and methods

Measurements were performed in a recirculating flume 16 m long and 1.2 m wide. The flow depth (H = 14 cm) was set by a downstream, adjustable weir and the discharge set by a variable-speed pump drawing water from the downstream tailbox to the upstream headbox. The discharge was 1000 l/min, resulting in a depth-averaged velocity U_∞ of approximately 10 cm/s.

Table 3.1: Summary of measurements. D is the diameter of the patch, d is the cylinder diameter, a is the frontal area per unit volume, ϕ is the solid volume fraction of the patch and Δ is the gap distance between the patches.

Type		Sparse	Dense	Sparse	Dense
D	[cm]	11 ± 0.8	11 ± 0.8	22 ± 0.8	22 ± 0.8
d	[mm]	3.2 ± 0.1	3.2 ± 0.1	3.2 ± 0.1	3.2 ± 0.1
a	[cm^{-1}]	0.15 ± 0.02	0.43 ± 0.03	0.13 ± 0.01	0.40 ± 0.01
aD	[-]	1.6	4.8	2.9	8.6
ϕ	[%]	3.7	11.	3.3	10.
Δ	[cm]	0, 1, 2, 3, 4.5, 6, 8, 10, 12	0, 1, 2, 3, 4.5, 6, 8, 10, 12	0, 2, 5, 8, 11, 14	0, 2, 5, 8, 11, 14
Deposition		No	No	Yes; Δ = 0, 2, 11	Yes; Δ = 0, 2, 11

Circular patches of model vegetation were placed 7 m from the flume entrance. The patches were constructed from wooden dowels and extended through the water surface to mimic emergent vegetation. The dowels had a diameter of d = 3.2 mm, a height of 16 cm and were held in a perforated PVC board. The boards consisted of 5.1 holes per square centimeter with centers staggered by 4.8 mm. Tests were performed with patches of two diameters D (11 and 22 cm) at both high and low flow blockage. The patch density for the high flow blockage case was $a \approx 0.4$ cm^{-1}, which corresponded to a solid volume fraction of $\phi = (\pi/4)ad \approx 10\%$. For the low flow blockage case, $\phi \approx 3.3\%$ and $a \approx 0.13$ cm^{-1}. A summary of the different tests is given in Table 3.1. The distance between the patches Δ (cm) was varied by placing PVC strips of variable width in between the patch boards. The distance Δ was varied from Δ/D = 0 to a maximum of Δ/D = 1.

3.3.1 Velocity measurements

The discharge rate was measured by an electromagnetic current meter (Siemens, Sitrans F M Magflo, Mag 5000). Velocity measurements were made using a 3D

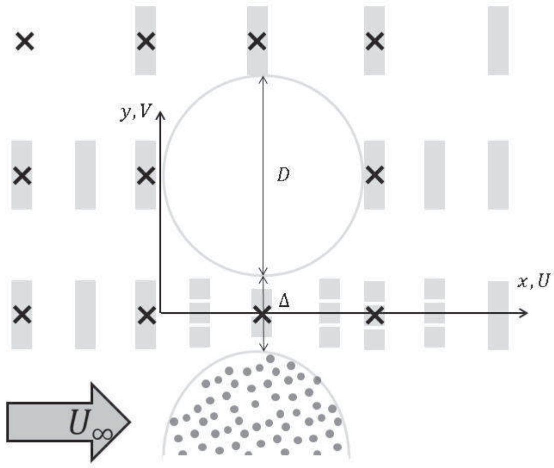

Figure 3.2: Schematic top-view of flume close to the model vegetation patches (circles), not to scale. The coordinate axis in the horizontal plane is shown, with velocities U and V in the directions of x and y, respectively, with x = 0 at the patch leading edge and y = 0 on the centerline between the patches. The vertical axis is upwards (not depicted). Two patches, divided by a gap Δ, consist of staggered arrays of dowels. The positions of the velocity measurements are indicated by heavy crosses, the positions of the deposition slides are indicated by gray rectangles.

Vectrino (Vectrino Velocimeter, Nortek AS), which measures velocity using the acoustic Doppler technique. The sampling volume of the ADV was located at mid-depth (z = 7 cm). Based on vertical profiles of streamwise velocity (data not shown) the velocity did not vary above z = 6 cm. The coordinate system is defined with the streamwise coordinate x = 0 at the upstream edge of the patches and the lateral coordinate y = 0 at the center of the gap between the patches, as shown in Figure 3.2. Measurements were recorded at a rate of 25 Hz for a period of at least 240 s. The integral time scale (T) was calculated for representative data points and was generally 1-2 s, with a maximum of 11 s within the region of the wake influenced by the von Kármán vortex street, such that the sampling time captured at least $22T$ and generally $180T$, values which the authors found sufficient to determine average characteristics. The data were processed in MATLAB to filter data points that had especially low values in signal to noise ratio (SNR $<$ 15), correlation (corr $<$ 70) or amplitude (amp $<$ 90) (McLelland and Nicholas, 2000). A Doppler noise correction was performed on the data based on the spectral method described in Voulgaris and Trowbridge (1998). The mean time-averaged velocities, respectively (U, V, W) for the (x, y, z) directions, were taken as the average of the remaining measurements over the recording period. Fluctuations around the mean, denoted u', v', w', were found by subtracting the mean velocity from each instantaneous record. The turbulent kinetic energy per unit mass (TKE) was then determined as

$$TKE = \frac{1}{2}(\overline{u'^2} + \overline{v'^2} + \overline{w'^2}) \tag{3.3}$$

in which the overbar denotes a time average. Measurements were made from 2.2 m upstream to 5 m downstream of the patches. The measurement positions were spaced more tightly close to the patches.

3.3.2 Deposition Experiments

Deposition experiments were carried out with a model sediment that was scaled to provide a desired ratio of settling velocity V_s to open-channel bed friction velocity. As this work was motivated by the previously noted feedback between deposition and plant growth (Gurnell et al., 2005), the chosen conditions mimic the transport of organic matter and fine sediment, which produce substrate high in nutrient content and favorable to plant growth. In the experiments, the shear velocity at the bed u^* = 0.7 cm/s, estimated for the bed drag coefficient specific to the flume in this study (C_f = 0.006, White and Nepf (2007)). 10 μm glass sphere particles (Potters Industry, Valley Forge, PA) were selected with a settling velocity V_s = 0.01 cm/s, so that V_s/u^* = 0.014, which is within the range expected in the field (V_s/u^* = 0.002 to 0.3, see discussion in Ortiz and Nepf (2014)). In addition, the conditions are similar to a previous study (Zong and Nepf (2010)), in which clear differences in deposition were observed between the open channel and vegetated regions of a channel.

Before the start of a deposition experiment, the flume was drained and cleaned to remove sediment that accumulated during previous experiments. Glass microscope slides (VWR VistaVision Microscope Slides) with a small thickness (1 mm) and an area of 7.5x2.5 cm or 2.5x2.5 cm were thoroughly washed, dried in an oven at 70 degrees Celsius for 4 hours, labeled, and then weighed. Slides were placed in 5 longitudinal profiles, partially shown in Figure 3.2 and Figure 3.3: on the centerline of the gap between the two patches (y = 0), on the centerline of each patch (y = $\pm$ ($D + \Delta$)/2), and on the outside edge of each patch (y = $\pm$ D+Δ/2). The longitudinal spacing between the slides was smaller close to the patch and increased with distance from the patch. To begin the experiment, 600 g of glass particles (resulting in an initial concentration of ca. 0.13 g/l) was mixed in a small container and the mixture was poured into the tailbox of the flume. The particles were mixed over the flow depth directly when entering the flume and a uniform condition over the flume length was observed within 2 minutes, based on visual observation. The particles were recirculated in the flume for 4 hours. The flow was slowly decelerated to avoid waves, the flume was drained, and then the flume was left to dry for at least 2 days. The slides were baked at 70 degrees Celsius to remove additional moisture and then weighed. The weight difference before and after the experiment is defined as the net deposition $(\mathrm{g/cm^2})$. Three configurations, Δ/D = 0.5, Δ/D = 0.1, and Δ/D = 0, were tested for each patch density. Three repetitions were performed for each set of conditions. A control experiment with no patches in the flume was also performed.

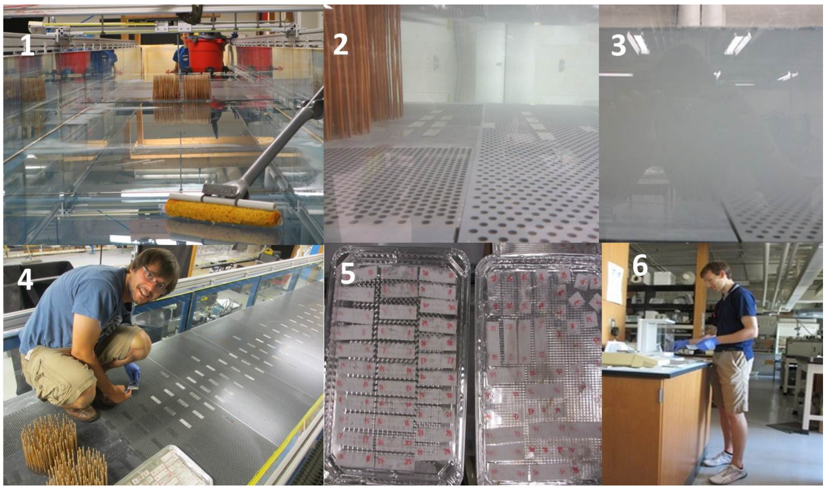

Figure 3.3: Overview photographs of the deposition measurements. (1) Cleaning of the flume, (2) placing the slides, (3) adding suspended sediments in the water, (4) picking up the slides, (5) slides with sediment, (6) weighing the slides.

The net deposition mean (μ_{ri}) and standard error (SE_{ri}) of each point were computed using the three replicates for each experimental configuration. To isolate deviations from the mean channel deposition, the mean of each experiment (μ_r) was subtracted from each individual data point. The standard error for the samples in the control experiment (SE_c) was also computed. We considered a point to have enhanced net deposition, relative to the control, if the net deposition differed from the experiment mean by more than the sum of the standard errors:

$$\mu_{ri} - \mu_r > SE_{ri} + SE_c \tag{3.4}$$

A spatial, linear interpolation was performed, using the algorithm of Akima (1978), to obtain contour plots of net deposition.

3.3.3 Flow Visualization

Characteristics of the wake downstream of the patches were revealed through dye streamlines. Rhodamine WT was injected through a needle oriented parallel to the flow and with an exit velocity that matched the free stream. The positions of the needles were varied to produce streaklines originating from different points upstream and around the patches. Directional lights were clipped to the sides of the flume and directed through the glass sidewalls to avoid water surface reflections and to evenly illuminate the flow depth. The lights extended for a distance of about 1.2 m downstream from the patch. The camera was mounted on a frame upstream of the patches oriented to capture the entire lighted downstream area. Remote capture software was used to avoid disturbing the camera during operation. ImageJ software was used to enhance the contrast and intensity of the dye.

3.4 Results

3.4.1 Velocity profiles on Patch Centerlines

We first consider whether a neighboring patch influences the near field evolution behind each patch by comparing the wakes behind side-by-side patches (Figure 3.4) with the wake behind an isolated patch. In particular, we consider the parameters U_1 and L_1 (described in the Introduction and shown in Figure 3.1) and evaluate their dependencies on the interpatch distance Δ. The steady wake zone L_1, as defined in Zong and Nepf (2012), extends from the trailing edge of the patch to the first measurement point at which the velocity starts to increase. Consistent with this definition and when present, part of the recirculation zone is included, as indicated in Figure 3.4a. This recirculation zone is a zone with negative velocities, flow returns behind the (dense) vegetation patch due to under pressure. U_1 is the average, streamwise velocity in this zone excluding the recirculation zone, e.g. U_1/U_∞ = 0.02 $\pm$ 0.01 for the left patch (P_L) and 0.03 $\pm$ 0.01 for the right patch (P_R, Figure 3.4a).

The steady wake length (L_1) and velocity (U_1) were found to be unaffected by the interpatch distance. For the dense patch (D = 22 cm, a = 0.4), U_1/U_∞ was between 0.02 and 0.05 (Table 3.2), agreeing within uncertainty with the value of 0.03, found for isolated patches of a similar flow blockage (Chen et al., 2012). Based on observations with isolated patches, Chen et al. (2012) proposed a steady wake length for high flow blockage ($C_DaD > 4$) of L_1 = 2.5 ($\pm$ 0.4) D. In the side-by-side configuration, it is found that L_1 = 2.4 ($\pm$ 0.1) D (Table 3.2). However, for the case Δ = 0 cm, a strong asymmetry was observed between two high-flow-blockage patch wakes (Figure 3.4b). Specifically, the gap flow veers towards the right-hand patch (P_R, Figure 3.4b), shortening L_1 behind the right-hand patch

(P_R) and lengthening it behind the left-hand patch (P_L). This deflection of centerline flow is similar to that observed for side-by-side solid cylinders in the Δ/D range of 0 to 0.2 described in the Introduction. This asymmetry is not observed for any other gap spacing. Based on numerical modelling of our experimental setup (Janzen J., personal communication), this asymmetry persists even in wider channels, suggesting that it is not related to the presence of the walls.

L_1 and U_1 are also independent of the gap width for the sparse patches (aD = 2.9, ϕ = 3.3) as well, as seen in Table 3.2. Consistent with observations for isolated patches, both L_1 and U_1 are larger for the sparse case than the dense case. In the case of isolated patches, Chen et al. (2012) proposed the following equations to predict the velocity and length of the near wake region behind low flow blockage patches, ($C_D aD < 4$):

$$U_1/U_\infty = 1 - 0.26(\pm 0.02) C_D aD \tag{3.5}$$

$$L_1/D = 2.5 \left[\frac{8 - C_D aD}{C_D aD} \right] \tag{3.6}$$

Assuming C_D = 1, equation 3.5 predicts U_1/U_∞ = 0.25 ± 0.05. This is slightly smaller than the average for all paired cases (0.32 ± 0.02; Table 3.2), but still in reasonable agreement given the potential error in the assumption C_D = 1. Similarly, the length-scale L_1 observed behind the paired patches is not affected by gap width and is also in good agreement with the value predicted by equation 3.6 (96 cm, Table 3.2). The asymmetry observed in the dense cases at Δ = 0 cm was not observed for any of the sparse cases. This can clearly be seen in Table 3.2, as L_1 for every patch is equal within uncertainty.

Based on these comparisons (Figure 3.4, Table 3.2), we conclude that the characteristics of the wake directly behind each patch (U_1, L_1) are not affected by a neighboring patch, except in the limit of dense patches approaching zero gap width, and (U_1, L_1) can be predicted from models developed for isolated patches (equations 3.5 and 3.6, Chen et al. (2012)).

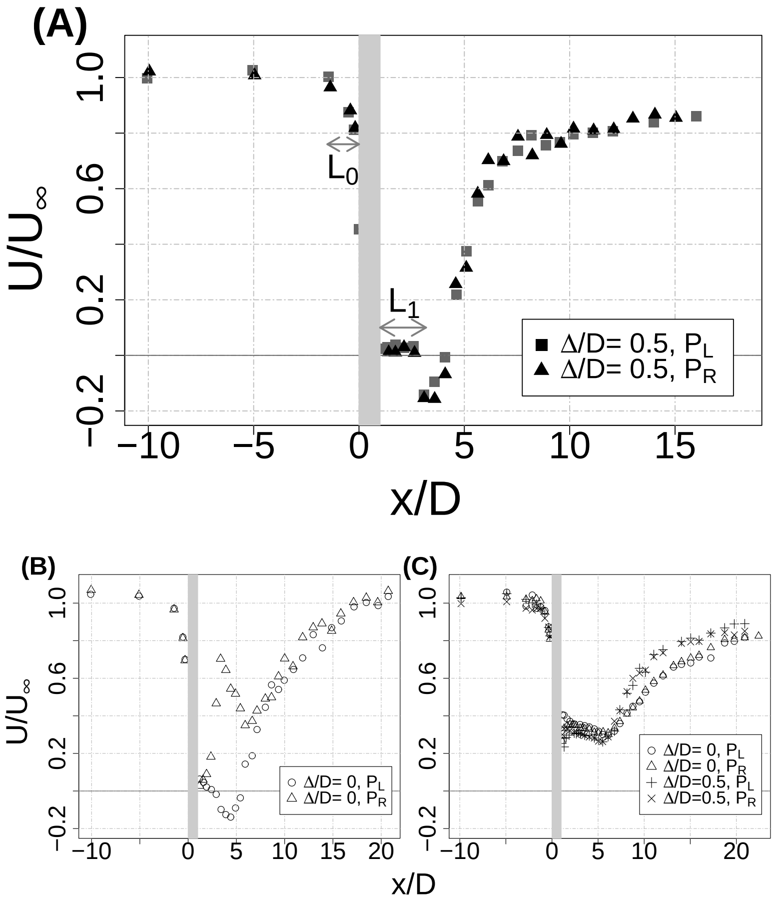

Figure 3.4: Time-mean, streamwise velocity U normalized by the upstream velocity U_∞, along streamwise coordinate (x) on patch centerlines. Left-hand and right-hand patches are denoted by P_L and P_R, respectively. The position of the patches is indicated by the gray bar. (A) Dense patches (D=22 cm, aD = 8.6, ϕ = 10%) with gap width Δ/D = 0.5. L_0 is the upstream adjustment length, and L_1 the steady wake length. The steady wake velocity (U_1) is approximately constant over L_1 followed by a zone of recirculation. (B) Dense patch pair (D=22 cm, aD = 8.6, ϕ = 10%) with gap width Δ/D = 0. Note asymmetry in wakes. (C) Sparse patch pair (D=22 cm, aD = 2.9, ϕ = 3%) with gap spacings Δ/D = 0 and 0.5.

3.4.2 Velocity Profiles on Centerline Between Patches

The mean streamwise velocity along the centerline between the patches (U_c) is depicted in Figure 3.5 for gap widths Δ = 0, 2, 5, 8, 11, and 14 cm (Δ/D = 0 to 0.6). The profiles are essentially identical upstream of the patches, with decelera-

Table 3.2: Steady wake velocities U_1 normalized by the upstream velocity U_∞ for D = 22 cm. The error bars indicate the standard deviation of the velocity measurements within the steady wake zone. The steady wake length L_1 is estimated from longitudinal transects in U, as in Zong and Nepf (2012). The error bars indicate half of the sampling distance between the measurement points. The single patch values are calculated based on equations found in Chen et al. (2012) (equations 3.5 and 3.6 for the sparse cases). (*) indicates that the value is given in Chen et al. (2012).

		Dense		Sparse	
		U_1/U_∞	L_1 (cm)	U_1/U_∞	L_1 (cm)
Δ = 0 cm	*Left*	0.03 ± 0.02	75 ± 5	0.34 ± 0.03	101 ± 6
	Right	0.04 ± 0.02	12 ± 5	0.33 ± 0.03	100 ± 6
Δ = 2 cm	*Left*	0.04 ± 0.02	53 ± 5	0.32 ± 0.03	99 ± 6
	Right	0.05 ± 0.03	53 ± 5	0.33 ± 0.02	99 ± 6
Δ = 11 cm	*Left*	0.03 ± 0.01	52 ± 5	0.29 ± 0.02	100 ± 6
	Right	0.02 ± 0.01	57 ± 5	0.30 ± 0.02	100 ± 6
	Single	0.03 ± 0.01*	55 ± 7	0.25 ± 0.05	96 ± 7

tion beginning about L_0 = $2D$ upstream, consistent with L_0 for a single patch of diameter D (Rominger and Nepf, 2011; Zong and Nepf, 2012). This suggests that the approaching flow feels the patches as two distinct objects of size D. Note that the upstream adjustment scales on the patch width, with little influence from patch shape, and in particular patch length, as shown specifically in Rominger and Nepf (2011). Similarly, Vandenbruwaene et al. (2011) showed that flow adjustment to circular and square patches was not significantly different. In the centerline velocity profiles the deviation between gap width conditions begins only $1D$ upstream of the patches. The flow accelerates between the patches, reaching a maximum (U_{max}) directly behind the patches ($x/D = 1$). The maximum centerline velocity is sustained over a distance L_j. The flow on the centerline exiting the gap is similar to a turbulent jet, for which this region of constant, maximal velocity (L_j) is called the potential core (e.g. Lee and Chu, 2003). The potential core is eroded by shear layers growing from either side of the gap toward the gap center. The centerline velocity begins to decelerate when these shear layers meet, which occurs closer to the patch (shorter L_j) as the gap width decreases. In the dense patch cases, the deceleration is followed by a sustained region of minimum velocity (U_{min}) beginning at a distance L_m behind the patch (Figure 3.5a). Finally, when the shear layers formed at the outermost edges of the patch-pair grow to the centerline, the centerline velocity begins to increase. Predictive models for specific regions of the wake evolution are discussed in more detail in the following sections.

Table 3.3: Parameters describing the velocity evolution on the centerline for sparse and dense patches at different gap distances. L_0 is the upstream adjustment length, U_{max} is the maximum centerline velocity, U_∞ is the far upstream incoming velocity, U_{min} is the minimum centerline velocity, L_m is the distance from the trailing edge of the patches to the point where the centerline velocity reaches U_{min} and $L_{m,2}$ is the distance from the trailing edge of the patch to the end of the constant velocity zone where the centerline velocity is equal to U_{min}. L_{TKE} is the length behind the trailing edge of the patches where the TKE reaches a maximum. U_∞ is 9.4 ± 0.3 cm/s for the dense patches and 9.3 ± 0.3 cm/s for the sparse patches.

Case	L_0 [cm]	U_{max}/U_∞ [-]	U_{min}/U_∞ [-]	L_j [cm]	L_m [cm]	$L_{m,2}$ (cm)	L_{TKE} [cm]
Dense, Δ = 0	44 ± 5	1.14 ± 0.2	0.07 ± 0.01	-	87 ± 6	160 ± 7	199 ± 7
Dense, Δ = 2	41 ± 5	1.64 ± 0.09	0.25 ± 0.02	5 ± 4	75 ± 4	161 ± 7	65 ± 7
Dense, Δ = 5	42 ± 5	1.67 ± 0.06	0.42 ± 0.03	17 ± 3	111 ± 5	223 ± 8	79 ± 4
Dense, Δ = 8	37 ± 5	1.66 ± 0.07	0.56 ± 0.03	28 ± 4	134 ± 6	223 ± 8	89 ± 4
Dense, Δ = 11	36 ± 5	1.66 ± 0.06	0.60 ± 0.04	30 ± 4	135 ± 6	210 ± 7	80 ± 5
Dense, Δ = 14	37 ± 5	1.65 ± 0.06	0.67 ± 0.03	36 ± 5	149 ± 7	223 ± 10	99± 5
Sparse, Δ = 0	32 ± 5	1.01 ± 0.08	0.49 ± 0.01	-	209 ± 10	265 ± 10	282 ± 7
Sparse, Δ = 2	37 ± 5	1.40 ± 0.06	0.61 ± 0.01	6 ± 4	209 ± 10	309 ± 10	67 ± 4
Sparse, Δ = 5	37 ± 6	1.39 ± 0.06	0.66 ± 0.01	21 ± 3	254 ± 10	-	89 ± 4
Sparse, Δ = 8	32 ± 5	1.40 ± 0.06	0.76 ± 0.01	45 ± 5	290 ± 10	-	140 ± 5
Sparse, Δ = 11	37 ± 5	1.40 ± 0.06	0.80 ± 0.01	67 ± 5	290 ± 15	-	140 ± 6
Sparse, Δ = 14	37 ± 5	1.38 ± 0.06	0.83 ± 0.01	89 ± 5	290 ± 15	-	171 ± 7

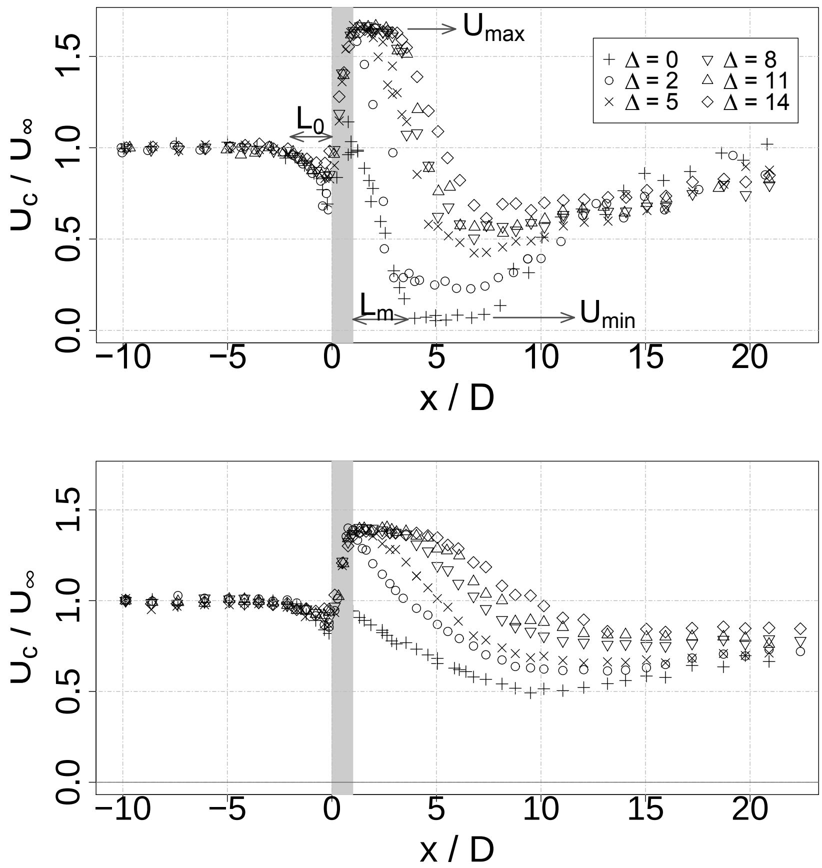

Figure 3.5: Time-mean, streamwise velocity U normalized by the upstream velocity U_∞, along streamwise coordinate (x) on the centerline between the patches ($y = 0$). The position of the patches is indicated by the gray bar. Gap widths given in the legend are expressed in cm. (top) High-flow blockage case (D = 22 cm, aD = 8.6, ϕ = 10%). U_{max} is indicated for all the cases, U_{min} and L_m are indicated for Δ = 0 cm. (bottom) Low-flow blockage case (D = 22 cm, aD = 2.9, ϕ = 3.3%)

3.4.2.1 Upstream adjustment region

The upstream adjustment length, L_0, denotes the distance upstream of the obstruction at which the velocity begins to deviate from its far upstream value. For both porous and solid obstructions L_0 scales with D (Belcher et al., 2003; Rominger and Nepf, 2011). We find that, within uncertainty, L_0 is not a function of patch density or gap width (Figure 3.5). L_0 = 40 $\pm$ 4 cm for dense and 36 $\pm$ 3 cm for sparse patches. This corresponds to L_0 = 1.8 ($\pm$0.2) D for the dense patches and L_0 = 1.7 ($\pm$0.2) D for the sparse patches. This agrees within uncertainty with the results of Rominger and Nepf (2011) of L_0 = 2.0 ($\pm$ 0.4) D, for a single patch, and suggests that the approaching flow sees each patch as a distinct obstruction, i.e. there is no upstream interaction. It is somewhat surprising that this result holds even for Δ = 0. However, since the patches are circular, even at Δ = 0 preferential flow occurs on the centerline, indicating that hydrodynamically the patches have yet not effectively merged. The magnitude of the upstream velocity reduction on the centerline has a dependency on the gap width. The velocity reduction is more pronounced for smaller Δ, with a maximum reduction for Δ = 0, and greater for the dense patches (40% upstream reduction) than for the sparse patches (20%).

3.4.2.2 Maximum gap velocities

The maximum centerline velocity (U_{max}) is shown in Figure 3.6. At small gap widths the Vectrino probe head could not fit between the two patches. For consistency across all cases, we compare the velocity measured at a specific point: on the gap centerline and 5 cm downstream of the trailing edge of the patch pair (x = D + 5 cm). For the larger patches (D = 22 cm), U_{max} is the same for all $\Delta/D >$ 0, and U_{max} is larger for the denser patches. Again, because of the circular patch shape, flow goes between the patches even for Δ/D = 0, although the magnitude (U_{max}) is diminished relative to $\Delta > 0$ (Figure 3.6). U_{max} is smaller for the small diameter patches (D = 11 cm in Figure 3.6), because a narrower region of flow is deflected. In addition, $U_{max} < U_\infty$ for Δ = 0. Excluding the Δ = 0 cases, U_{max} is observed to be equal to U_2, the magnitude of velocity on the outermost edge of each patch (see Figures 3.1 and 3.10). Similar to the scaling of L_0, discussed above, this further suggests that the flow approaching the patches sees them as individual obstructions, i.e. there is no upstream interaction.

Because this experiment was conducted in a channel, U_{max} can be predicted from mass conservation. Defining the flume width (B),

$$U_\infty HB = U_1 H(2D) + U_{max} H\Delta + U_2 H(B - 2D - \Delta) \tag{3.7}$$

Using the fact that U_{max} = U_2, and solving for U_{max},

$$U_{max} = (U_\infty B - U_1 2D)/(B - 2D) \tag{3.8}$$

Using measured values of U_∞ and U_1, the values of U_{max} can be predicted from (3.8), and these predictions are shown as horizontal lines in Figure 3.6. Excluding the cases of zero gap width, for which $U_{max} \neq U_2$, equation 3.8 predicts the maximum velocity within 10%, but consistently underestimates, because (3.8) assumes U_{max} is uniform over Δ, whereas the measured value is taken at the centerline, which is likely a local maximum. Note that (3.8) may not be valid in a wider channel, since U_2 will eventually decay away from the patches.

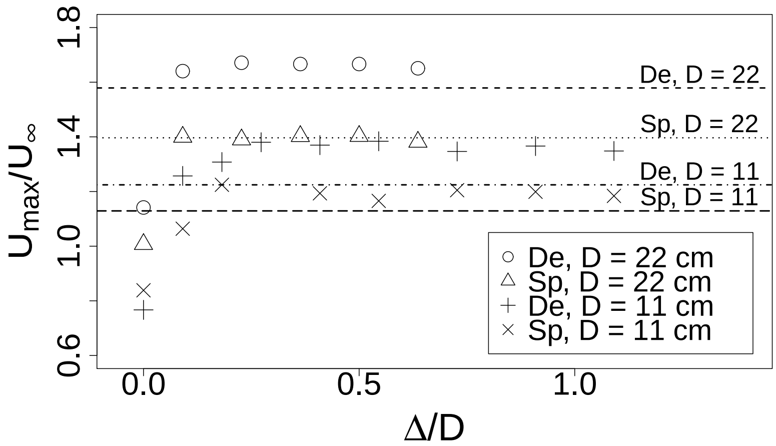

Figure 3.6: Maximum velocities at the center of the gap and 5 cm behind the dense (De) and sparse (Sp) patches for the different patches diameters (D = 11 and D = 22 cm) as a function of the gap width Δ/D. The uncertainty on the measurements is comparable with the size of the symbols. The lines represent the value of U_{max} calculated with equation 3.8, using the average U_1/U_∞ given in Table 3.3 and the geometric features given in Table 3.1.

3.4.2.3 Potential core region

The flow exiting the gap evolves like a jet. In this study, the jet Reynolds number Re_j = $U_j\Delta/\ \nu$, with ν = 10^{-6} m^2/s, is always greater than 2000. As such, the jet is turbulent (Lee and Chu, 2003). Close to the nozzle of a jet, there is a wedge-like region of undiminished mean velocity, called the potential core (Rajaratnam, 1976). The length of the potential core, L_j, is linearly dependent on the width of the jet, with typical ratios of 3 to 6 (Lee and Chu, 2003; Rajaratnam, 1976). Larger values are noted for jets with a coflow (Lee and Chu, 2003). In this study, the jet width corresponds to the gap width, Δ.

L_j is defined as the distance from the trailing edge of the patches (x = D) to the last measurement point where U_c=U_{max} within uncertainty (Table 3.3). As expected from the analogy with jets, a linear relationship is observed between L_j and Δ (Figure 3.7). We assume that L_j = 0 for Δ = 0. For the dense patches,

$$L_j = \; 2.8\,(\pm 0.2)\,\Delta \qquad (R^2 = 0.91) \tag{3.9}$$

For the sparse patches,

$$L_j = \; 6.0\,(\pm 0.3)\,\Delta \qquad (R^2 = 0.96) \tag{3.10}$$

L_j/Δ is greater for the sparse case because U_1, which acts as a co-flow, is higher for the sparse patches.

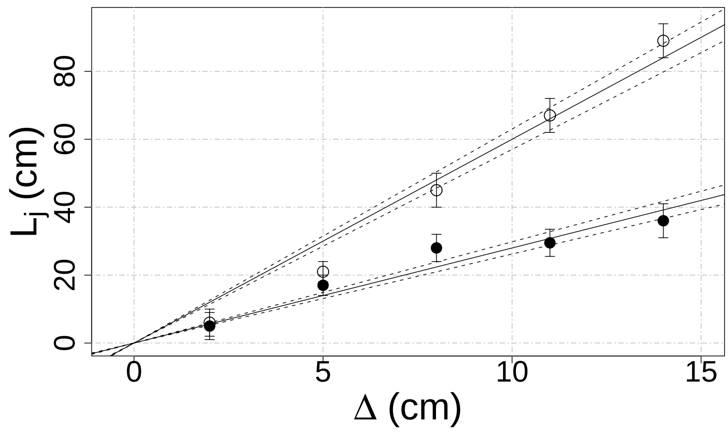

Figure 3.7: Length of the potential core of the gap jet L_j is a linear function of gap width Δ for the sparse (open circles) and dense patches (solid circles). The best-fit (equations 3.9 and 3.10) is shown with solid lines and the uncertainty with dashed lines.

3.4.2.4 Deceleration region

Beyond the distance L_j, the centerline velocity (U_c) decreases (Figure 3.5), as lower momentum fluid is entrained at the jet edge. For a jet of initial velocity U_{max} and initial width Δ, U_c should evolve as follows (Giger et al., 1991)

$$\left(\frac{U_{max}}{U_c}\right)^2 = \gamma_u \left(\frac{x}{\Delta} - \frac{x_0}{\Delta}\right) \tag{3.11}$$

γ_u is the kinematic spreading coefficient and x_0 the virtual origin which, for our coordinate system, encompasses the patch diameter (D) and the potential core length (L_j). An example of fitting (3.11) to the measured values of U_c (Figure 3.8) clearly shows a region of linear growth for $(U_{max}/U_c)^2$ between x/Δ = 5 and 40, verifying our assumption of jet evolution. The kinematic spreading coefficient γ_u is 0.92 ($\pm$ 0.04) for the dense patches (Table 3.4). This value is much higher than values in the literature for free planar turbulent jets, which range from 0.13 to 0.21 (Giger et al., 1991; Lee and Chu, 2003; Rajaratnam, 1976), meaning that the observed deceleration is faster. This difference is likely due to the difference in turbulence level. Giger et al. (1991) report a peak level of turbulence of $u'/U_c \approx 0.25$, whereas for the dense patches the peak value is $u'/U_c \approx 0.5$. The higher level of turbulence contributes to faster mixing which leads to a more rapid deceleration of U_c. Similarly, Gaskin et al. (2004) observed that a doubling of the

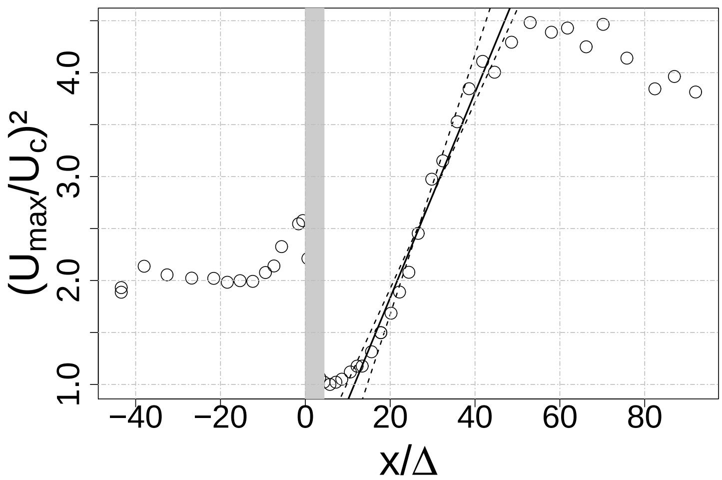

Figure 3.8: Example of fitting measured centerline velocity, U_c, to the jet spreading model (equation 3.11) to obtain the kinematic spreading coefficient γ_u for the sparse patch case with Δ = 5 cm. The result of the best-fit for γ_u is 0.099 $\pm$ 0.005. The variation on the results, because of point selection, is presented by dashed lines.

turbulence level increased the spreading coefficient from 0.2 to 2.6. For the sparse patches, γ_u = 0.11 ($\pm$ 0.04), which is an order of magnitude less than the dense cases (Table 3.4), meaning that the observed deceleration is slower. The sparse patch value is in line with values reported by Giger et al. (1991) (γ_u = 0.11) for similar levels of turbulence, u'/U_c = 0.23 and 0.25 for present study and Giger et al. (1991) respectively.

Table 3.4: Overview of the kinematic spreading coefficients γ_u for the different gap spacings for the dense (D = 22 cm, ϕ = 10, aD = 8.6) and sparse (D = 22 cm, ϕ = 3.3, aD = 2.9) patches.

Δ [cm]	Dense patches γ_u	Sparse patches γ_u
2	0.94 $\pm$ 0.10	0.042 $\pm$ 0.005
5	0.87 $\pm$ 0.05	0.099 $\pm$ 0.01
8	0.91 $\pm$ 0.08	0.121 $\pm$ 0.006
11	0.96 $\pm$ 0.09	0.140 $\pm$ 0.010
14	0.95 $\pm$ 0.09	0.138 $\pm$ 0.005
Avg.	0.92 $\pm$ 0.04	0.11 $\pm$ 0.04

3.4.2.5 Centerline minimum velocity

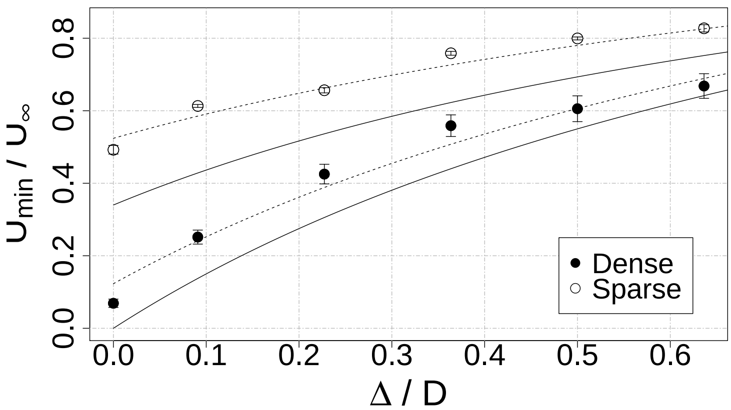

Figure 3.9: Minimum velocity on the centerline between patches (U_{min}) as a function of gap width (Δ/D, $D = 22$ cm). A simple blending model (equation 3.13) provides reasonable agreement (solid line). The agreement is improved by including an offset tot the gap width (ϵ in equation 3.14). The best fits, shown by dashed lines, yield ϵ = 1.8 cm (dense patches) and ϵ = 4.8 cm (sparse patches).

At a distance L_m from the patches, the velocity levels off to a constant, minimum value, U_{min} (Figure 3.5a). The magnitude of U_{min} can be predicted from a simple model that accounts for the mixing of the jet with the lower velocity fluid in the wakes to either side of the jet. The lowest centerline velocity should occur just as the fluid at each wake centerline (the lowest wake velocity) is blended with the jet. This occurs when the blending distance, W_m, extends between the two wake centerlines, $W_m = D/2 + \Delta + D/2 = D + \Delta$. As mixing extends beyond this length-scale, higher momentum fluid is added and the centerline velocity will start to increase. From conservation of mass over distance W_m we can approximate that

$$U_{min}(D + \Delta) = U_1 D + U_{max}\Delta \tag{3.12}$$

Dividing by U_∞, and noting that for dense patches ($C_D aD > 4$) one can assume $U_1 \ll U_{max}$:

$$\frac{U_{min}}{U_\infty} = \frac{U_{max}(\Delta/D) + U_1}{U_\infty(1 + (\Delta/D))} \overset{(C_D aD>4)}{\approx} \frac{U_{max}}{U_\infty}\frac{(\Delta/D)}{(1 + (\Delta/D))} \tag{3.13}$$

As noted above (Figure 3.6), due to the circular patch geometry, an elevated velocity, U_{max}, occurs at the centerline even when Δ = 0. To account for this, we add an offset (ϵ) to allow for the apparent gap even as Δ goes to zero.

$$\frac{U_{min}}{U_\infty} = \frac{U_{max}((\epsilon+\Delta)/D)+U_1}{U_\infty(1+((\epsilon+\Delta)/D))} \overset{(C_D aD>4)}{\approx} \frac{U_{max}}{U_\infty}\frac{((\epsilon+\Delta)/D)}{(1+((\epsilon+\Delta)/D))} \quad (3.14)$$

The parameter ϵ is found by fitting (3.14) to observed values of U_{min} using a nonlinear, least-square estimate employing a Gauss-Newton algorithm; ϵ = 1.8 ($\pm$ 0.4) cm for the dense patches ($C_D aD$ = 8.6) and ϵ = 4.8 ($\pm$ 0.4) cm for the sparse patches ($C_D aD$ = 2.9), shown in Figure 3.9. Because we expect this offset to be larger for larger mean stem spacing, it makes sense that ϵ is larger for the sparse patches. However, we caution that the parameter ϵ is likely to be case specific, dependent on the shape, density, and homogeneity of the patches. Future work should consider how to predict ϵ from these various factors.

L_m is the distance from the trailing edge of the patches (x = D) to the point where the decelerating jet reaches its minimal velocity (U_{min}). For both the sparse and dense patches, L_m increases in a roughly linearly fashion with gap width (data in Table 3.3) and is consistently larger for the sparse cases than the dense cases. Importantly, L_m represents the point at which the two individual patch wakes merge to form a single, larger wake. The two distinct wakes, in the near field, are separated by the gap flow. In the far field the two wakes merge together to form a single wake. The evolution from a pair of wakes to wake merger is shown through a sequence of lateral transects (Figure 3.10). For the case shown (dense patches, Δ/D = 0.5), L_m = 135 cm. For $x \leq$ 96 cm, the elevated centerline velocity separates two distinct and symmetric wakes of lower velocity. After L_m, at x = 160 cm, the centerline velocity is a minimum, and the velocity profile is consistent with a single wake spanning both patches.

3.4.2.6 TKE

In section 3.2.4 we noted that the deceleration of the centerline velocity was more rapid between dense patches than between sparse patches. This is shown again in Figure 3.11. For both the dense (open symbols) and sparse (filled symbols) patches, the centerline velocity (circles) decelerates and the patch velocity (triangles) accelerates over the same streamwise distances, x/D = 3 to 5 for dense patches and x/D = 5 to 10 for sparse patches. These regions correspond to peaks in turbulent kinetic energy (TKE, Figure 3.11) associated with the formation of a von Kármán vortex street behind each patch (e.g. Figure 3.1). The peak TKE is significantly higher for the dense patches, consistent with previous studies of isolated patches (Chen et al., 2012), and this explains why the deceleration of centerline velocity is more rapid. The dense patches produce a stronger velocity

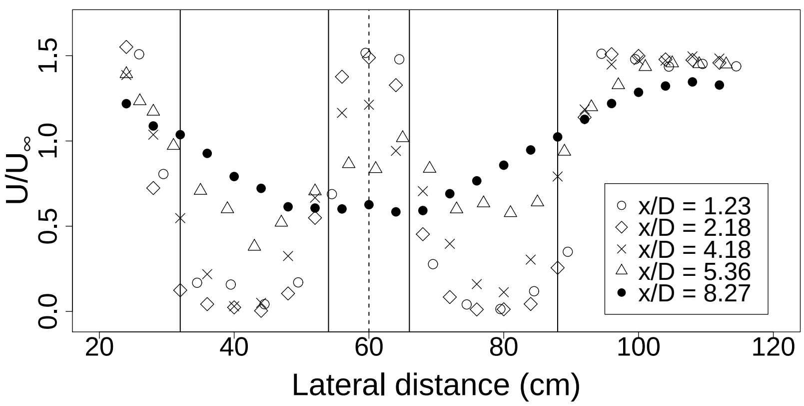

Figure 3.10: Lateral velocity profiles of streamwise velocity behind two dense patches (D = 22 cm) with a gap width of 11 cm. Profiles at distances of 5, 26, 70, 96 and 160 cm behind the trailing edge of the patch or resepctively x/D = 1.23, 2.18, 4.18, 5.36, 8.27 (identified in legend). The dashed, vertical line indicates the centerline between the patches, and the solid vertical lines represent the edges of the patches.

differential ($U_2 - U_1$ in Figure 3.1), which drives stronger and more coherent von Kármán vortices (Chen et al., 2012; Zong and Nepf, 2012). Further, the peak in TKE occurs at the same streamwise position both between (center) and in line with (patch) the patches, suggesting that the von Kármán vortices contribute to mixing across the gap. This is also evident in the evolution of dye released from the center of the gap ($y = 0$) and at the outer edge of one patch ($y = \Delta/2 + D$) as shown in Figure 3.12. Behind the dense patches, both dye traces exhibit lateral oscillations associated with von Kármán vortex streets starting at 80 cm. This corresponds to the peak in TKE (Figure 3.11). Importantly, the lateral traces are synchronized and the lateral excursion is comparable to the total merged wake $(2D + \Delta)$. This supports the conclusion that the von Kármán vortex streets contribute to mixing across the gap, enhancing the deceleration of the centerline velocity. The dye traces also indicate that there are two distinct streets (one behind each patch), i.e. although in phase, the dye traces do not merge into a single vortex. This is consistent with the fact that the observed oscillation frequency (0.1 Hz) scales with the diameter of the single patch, i.e. $f_k \approx 0.2U_\infty/D$ (Zong and Nepf, 2012). Similar trends are observed for the sparse patches, but the von Kármán vortices form further downstream and are less distinct (Figure 3.12), consistent with their weaker contribution to TKE (Figure 3.11). Finally, in both cases the von Kármán vortex formation occurs at the same position relative to the individual patches as observed behind isolated patches, i.e. at L_1 (Chen et al., 2012).

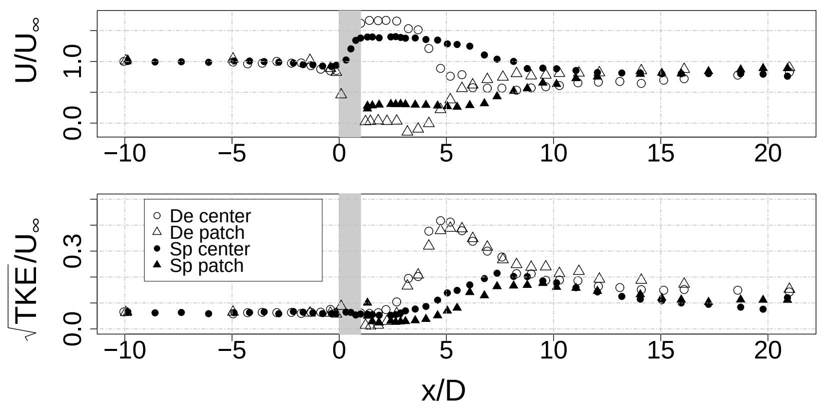

Figure 3.11: Streamwise velocity (U, top) and turbulent kinetic energy (TKE, bottom) versus streamwise position (x/D) along the centerline between two patches (center, y = 0) and along a patch centerline (patch, $y = (D + \Delta)/2$). Both dense patch (De, aD = 8.6) and sparse patch (Sp, aD = 2.9) conditions are shown. The gap width is Δ/D = 0.5 and D = 22 cm.

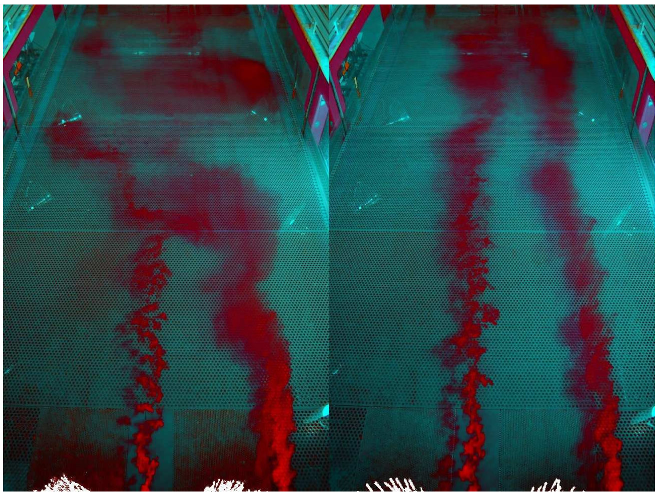

Figure 3.12: Images of Rhodamine WT injected at the center of the gap between the two patches (y = 0) and the edge of one patch (y = Δ/2+D) at a gap width of Δ/D = 0.5. A dense patch pair (image left) and sparse patch pair (image right) is shown. Flow is from bottom to top. The downstream edge of the patches is just visible in the figure

3.4.3 Deposition

We now connect the main characteristics of the velocity field to the patterns of deposition. In particular, the wake interaction that produces a local minimum velocity on the centerline between the patches is examined for its potential to enhance deposition. Under control conditions, with no patches in the flume, deposition was uniformly distributed (within a variation of 10%) and specifically showed no tendency in the streamwise direction, indicating that the deposition was not supply limited (data not shown). With the patches in the flume, distinct patterns of deposition were observed, as shown in Figures 3.13, 3.14, 3.15 for the dense cases and Figures 3.16, 3.17, 3.18 for the sparse cases.

Table 3.5: Overview of the deposition measurements. L_{dep} indicates the length of enhanced deposition behind and in line with the individual patches, defined from the trailing edge of the patch. $L_{dep,C}$ indicates the point on the centerline, measured from the trailing edge of the patch, where enhanced deposition is first observed, marking the start of the secondary deposition zone. The uncertainties on L_{dep} and $L_{dep,C}$ are defined by 50% of the distance between the measurement points. (*) indicates that the deposition zone in line with the patch connects to the secondary deposition zone.

	L_{dep} [cm]	$L_{dep,C}$ [cm]
Dense, Δ = 0 cm	44 ± 6 *	44 ± 6
Dense, Δ = 2 cm	47 ± 6 / 105 ± 6*	105 ± 6
Dense, Δ = 11 cm	47 ± 6	155 ± 7
Sparse, Δ = 0 cm	90 ± 8 *	90 ± 8
Sparse, Δ = 2 cm	140 ± 8 *	147 ± 8
Sparse, Δ = 11 cm	230 ± 7	-

Directly upstream of the patch pair, deposition was enhanced over a distance comparable to the upstream flow adjustment ($L_0 \approx 2D$). Gurnell et al. (2001) and Zong and Nepf (2010) also observed enhanced deposition upstream of a patch, which was attributed to diminished local bed stress due to flow decelaration approaching the patch. Downstream of the patch pairs, three key features can be identified: a zone of enhanced deposition immediately behind each patch, a zone of reduced deposition in between the patches, and a secondary zone of enhanced deposition on the centerline between the patch pair. The zones of enhanced deposition, as defined in the methods, are noted by heavy black lines over the color contours. Behind each patch there is always a zone of higher deposition, which can be related to the individual wake of each patch. For all gap widths and both patch densities, the longitudinal extent of this zone is comparable to the steady wake zone L_1 determined from velocity records. Only for the sparse case with Δ = 11 cm is the deposition clearly longer than L_1 (Tables 3.3 and 3.5; and shown as an arrow in each of Figures 3.13 to 3.18). These observations agree well with the observations for single patches, which are described in Chen et al. (2012).

Zones of reduced deposition occurred between the patches. The length of this zone, $L_{reduced}$, is longer than the potential core in the jet region L_j (indicated by arrows in Figure 3.13 to 3.18). This can be explained by the fact that TKE peaks in the decelaration zone and the velocity remains elevated above the control U_∞ for distances longer than L_j. Consistent with this, $L_{reduced}$ is longer for the sparse patches compared to the dense patches because the deceleration of the jet core is slower and extends over a longer streamwise distance. An exception is the sparse case at Δ = 0 cm, for which deposition was reduced over a shorter distance (Figures 3.15 and 3.18).

The zone of secondary deposition on the centerline is a unique feature of the interaction between the two patch wakes. This second zone of deposition extends laterally over the width of the two patches and gap (Δ + $2D$). The leading edge of this zone moves closer to the patches as the gap decreases (e.g. Figures 3.13 through 3.15). $L_{dep,C}$ indicates the length between the trailing edge of the patches and the start of the secondary deposition zone on the centerline (Table 3.5). $L_{dep,C}$ is compared with L_m, the distance between the trailing edge of the patch and the position where the minimum velocity on the centerline is reached (Table 3.3 and indicated by arrows on Figures 3.13 to 3.18). With the dense patches, for Δ = 2 and 11 cm, the secondary deposition zone can easily be recognized and $L_{dep,C}$ is slightly larger than L_m (on average ca. 20 cm). At Δ/D = 0, the secondary zone merges with the deposition zone of the individual patches. For the sparse patches it is more difficult to separate the deposition in the individual patch wakes from the deposition in the merged wake, consistent with the less distinct velocity patterns observed for the sparse cases. In contrast to the dense cases, no clear correlation between L_m and a point of increased deposition on the centerline was identified. For the largest gap spacing ($\Delta/D = 0.5$), for which the centerline minimum velocity is the highest, a secondary deposition zone was not observed.

We caution that the results presented here are for a single sediment size, concentration, and flow field. While suggestive of possible deposition patterns, the observed patterns may not be representative of all systems. For example, if the mean velocity is below the threshold for particle motion, a further depression of the velocity in the patch wakes may not lead to enhanced deposition. Similarly, different thresholds of settling velocities of the sediment (associated with the d_{50} of the sediment) may result in different extents and intensities of the deposition zones.

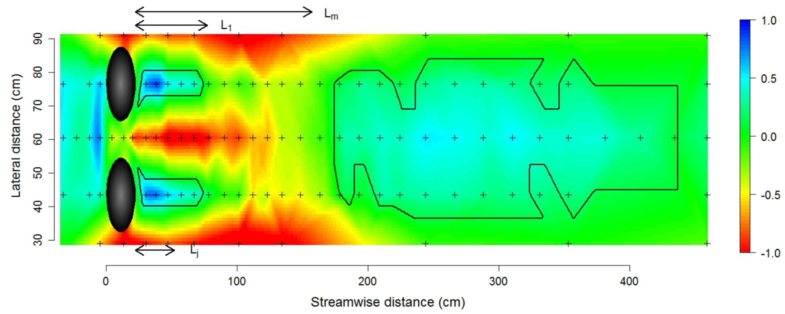

Figure 3.13: Deposition results for a gap distance of 11 cm ($\Delta/D = 0.5$) for two dense patches. The patches are indicated by the black ellipses. Results are in $\mathrm{mg/cm^2}$. Flow direction is from left to right. For each experiment the mean deposition per unit area was subtracted from the measurements such that 0 indicates the average mean value. The indicated values of L_m, L_j and L_1 are based on the velocity measurements (summarized in Table 3.3) and measured from the back of the patch.

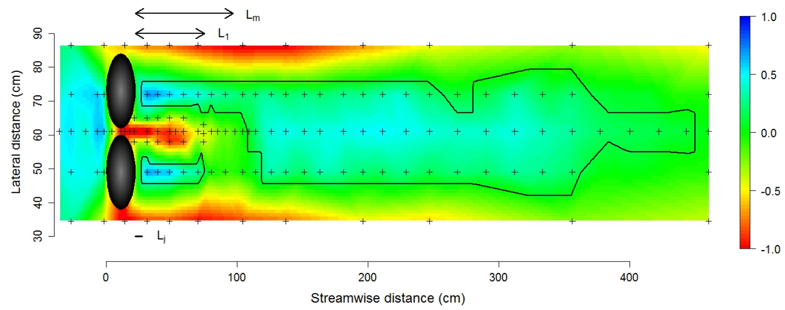

Figure 3.14: Deposition results for a gap distance of 2 cm ($\Delta/D = 0.1$) for two dense patches. See Figure 3.13 caption.

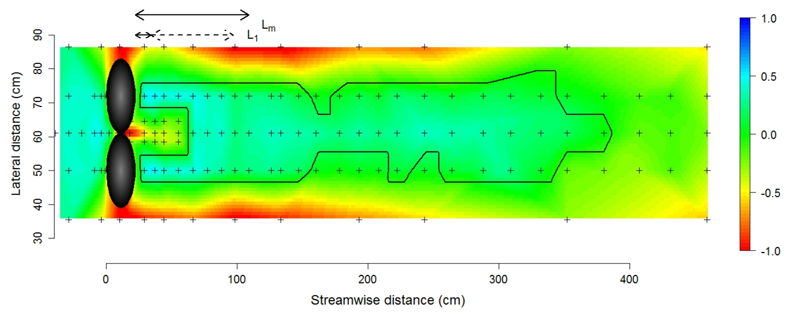

Figure 3.15: Deposition results for a gap distance of 0 cm ($\Delta/D = 0$) for two dense patches. See Figure 3.13 caption.

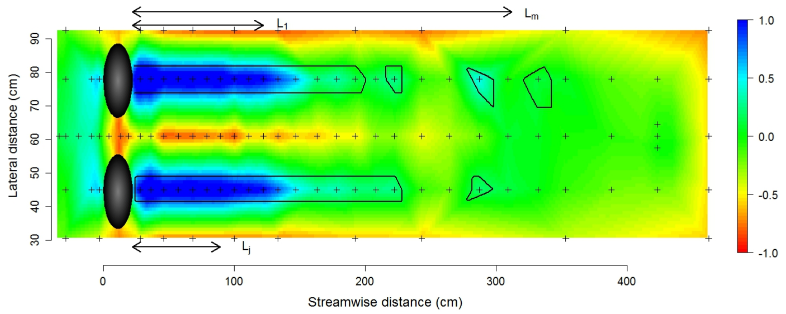

Figure 3.16: Deposition results for a gap distance of 11 cm ($\Delta/D = 0.5$) for two sparse patches. See Figure 3.13 caption.

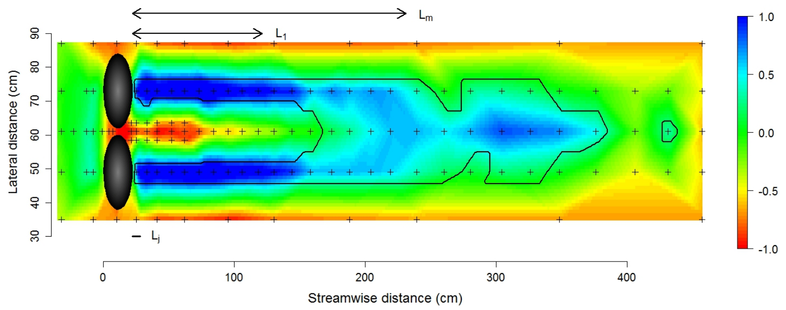

Figure 3.17: Deposition results for a gap distance of 2 cm ($\Delta/D = 0.1$) for two sparse patches. See Figure 3.13 caption.

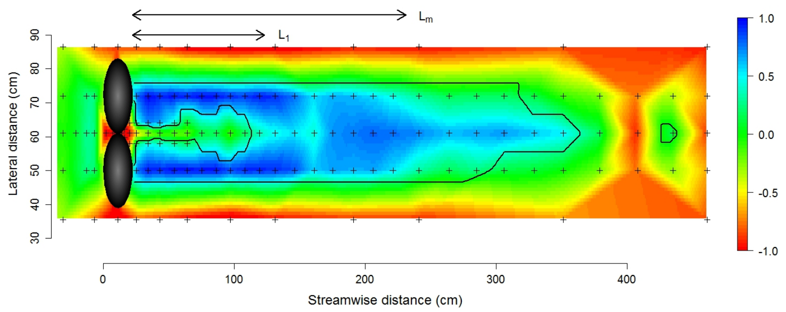

Figure 3.18: Deposition results for a gap distance of 0 cm ($\Delta/D = 0$) for two sparse patches. See Figure 3.13 caption.

3.5 Discussion

Our measurements have shown that the velocity and deposition patterns that occur directly behind individual patches are not significantly altered by laterally aligned neighboring patches. Specifically, directly behind each patch there is enhanced deposition that corresponds to a region of diminished mean velocity and turbulence. The length of this region (L_1) increases as the patch density decreases, and it can be predicted from linear shear layer growth (Zong and Nepf, 2012). However, a neighboring patch can influence the velocity and deposition beyond L_1. In particular, wake merging can produce a velocity minimum on the centerline between the patches at a distance L_m downstream from the patches. The distance L_m is a linear function of gap width. We observe that the velocity minimum produces a region of enhanced deposition that spans the distance across both patch wakes (Figures 3.13 to 3.18). The deposition enhancement is observed to increase as the minimum velocity decreases, which occurs with increasing patch density and decreasing gap width (Figure 3.5). This secondary region of deposition may provide a positive feedback that eventually allows the two patches to merge. Consider neighboring patches, with diameters D, as shown in Figure 3.19 (top). A first deposition zone is observed immediately behind each patch, corresponding with L_1. Additionally, the interaction of patch wakes leads to a secondary deposition zone on the centerline between the patches. If this secondary zone of enhanced deposition facilitates the establishment and growth of vegetation, it will provide additional drag and flow blockage on the centerline between the original patches, which could reduce or completely halt the flow between the patches, setting up flow conditions that would allow for patch merging (Figure 3.19, bottom). Thus, the patches' influence on flow at several diameters downstream produces a positive feedback that may eventually allow the original patches to grow laterally, i.e. from a patch of width D to a merged patch of width $2D + \Delta$ (Figure 3.19, bottom). Previous descriptions of vegetation-flow feedbacks identified positive feedbacks only for streamwise patch growth (e.g. Bouma et al., 2009) and negative feedbacks for lateral growth. By considering the interaction between neighboring patches we have identified a new, positive feedback for lateral growth.

The strength and location of the secondary deposition zone depends on the flow blockage of the upstream patches and the distance Δ between them. For dense patches, the distance to the start of the secondary zone from the back of the patches, $L_{dep,C}$, can be physically linked to the distance for the centerline velocity U_c to reach U_{min}. Once the centerline velocity reaches U_{min} the sediment begins to deposit, and the slightly greater values of $L_{dep,C}$, can be taken as the time for the sediment to settle the height of the water column. Using the predictive model

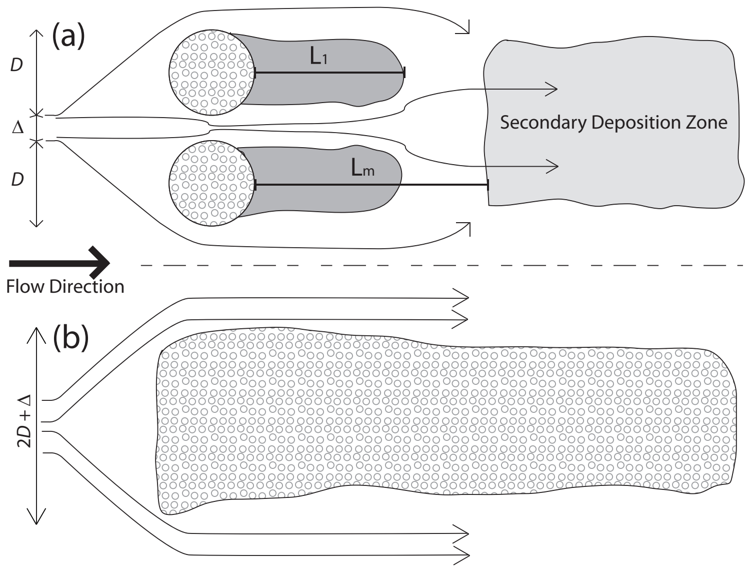

Figure 3.19: Two patches in relatively close proximity can create a secondary deposition zone due to the interactions of their wakes (top) that, over time, may cause enhanced growth and lead to patches merging together and growing beyond a lateral scale of D (bottom).

for U_c outlined in this study and previous models for isolated patches (Chen et al., 2012; Zong and Nepf, 2012), the deposition caused by a pair of patches may be predicted, providing a way to incorporate this newly identified feedback into the modeling of landscape evolution.

4

Deriving the depth-averaged Shallow Water Equations

4.1 Introduction

In this chapter the derivation of the depth-averaged Shallow Water Equations from the Navier-Stokes equations is discussed. An overview is given of the assumptions which should be made to obtain these depth-averaged Shallow Water Equations, indicated with the acronym 2D-SWE. Furthermore, some models to account for the effect of turbulence are considered and possible adaptations made to the 2D-SWE for flows with vegetation are presented.

4.2 The Navier-Stokes Equations

The Navier-Stokes equations, which describe the instantaneous motion of fluid flow, are based on the basic physical concepts of conservation of mass and conservation of momentum (Newton's second law) applied on an infinitesimal small control volume of fluid (Kundu et al., 2012; Monin and Yaglom, 1971; Wu, 2007). A continuity equation (eq. 4.1) is present independent of the used dimension (1D, 2D, 3D), the number of momentum equations (eq. 4.2) is equal to the number of dimensions considered.

$$\frac{\partial \rho}{\partial t} + \frac{\partial \rho u_i}{\partial x_i} = 0 \tag{4.1}$$

$$\frac{\partial \rho u_i}{\partial t} + \frac{\partial \rho u_i u_j}{\partial x_j} = F_i - \frac{\partial p}{\partial x_i} + \frac{\partial \tau_{ij}}{\partial x_j} \tag{4.2}$$

In this system of partial differential equations (4.1 and 4.2), expressed using the Cartesian tensor notation, ρ represents the density of the fluidum [$\mathrm{kg/m^3}$], water in the course of this manuscript. u_i and u_j [m/s] represent the instantaneous components of the velocity, along the i and j coordinate axis respectively, t the time [s], F_i represents the external forces on the fluid body [$\mathrm{N/m^3}$] along the i coordinate axis (e.g. gravity), p represents the pressure [Pa] and τ_{ij} the stresses on the flow [$\mathrm{N/m^2}$], both the normal and shear stresses. In these equations, the Einstein's summation convention is adopted, meaning that when an index is used twice in a single term, the summation is carried out over all values of that index, e.g. $\frac{\partial \rho u_i}{\partial x_i}$ is equal to $\sum_{i=1}^{3} \frac{\partial \rho u_i}{\partial x_i}$.

Water is considered as a Newtonian fluid, meaning that the viscous stress can be related to the strain rate, as expressed in equation 4.3. μ represents the dynamic viscosity [Ns/$\mathrm{m^2}$] and its variation in space (because of temperature dependency) is almost always considered negligible.

$$\tau_{ij} = \mu \left(\frac{\partial u_i}{\partial x_j} + \frac{\partial u_j}{\partial x_i} \right) \tag{4.3}$$

Applying the definition in equation 4.3 to equation 4.1 and 4.2 results in the Navier-Stokes equations for a single-phase fluid (eqs. 4.4 and 4.5). Herein is ∇^2 a Laplacian operator.

$$\frac{\partial \rho}{\partial t} + \frac{\partial \rho u_i}{\partial x_i} = 0 \tag{4.4}$$

$$\frac{\partial \rho u_i}{\partial t} + \frac{\partial \rho u_i u_j}{\partial x_j} = F_i - \frac{\partial p}{\partial x_i} + \mu \nabla^2 u_i \tag{4.5}$$

This system of equations contains 4 equations and 4 unknowns (u_i in three components, p). In general, this set of non-linear equations cannot be solved analytically. Moreover, this set of equations cannot be solved directly because of limited computer power and often, even no practical interest exists in the very small scale motions. In the 19th century, Osborne Reynolds proposed to average the Navier-Stokes equations over a time period with length T, which should be much longer than the scale of turbulence fluctuation, much longer than an infinitesimal period ∂t. According to the Reynolds decomposition, the instantaneous quantity of the state variables (ϕ) can be divided into a mean quantity ($\bar{\phi}$) and a fluctuating quantity (ϕ').

$$\phi = \bar{\phi} + \phi' \tag{4.6}$$

Using definition 4.6 for the variables under interest, the Navier-Stokes equations (4.4 and 4.5) can be written as:

$$\frac{\partial \rho}{\partial t} + \frac{\partial \rho \overline{u_i}}{\partial x_i} = 0 \tag{4.7}$$

$$\frac{\partial \rho \overline{u_i}}{\partial t} + \frac{\partial \rho \overline{u_i}\,\overline{u_j}}{\partial x_j} = \overline{F_i} - \frac{\partial \bar{p}}{\partial x_i} + \mu \nabla^2 \overline{u_i} - \frac{\partial \rho \overline{u_i' u_j'}}{\partial x_j} \tag{4.8}$$

This set of equations (4.7 and 4.8) is called the Reynolds-Averaged Navier-Stokes equations (RANS) for water flow. By applying the Reynolds-averaging procedure, an extra term appears in the set of equations, which is a correlation of the fluctuating velocities $\overline{u_i' u_j'}$. This term, called the Reynolds stress or turbulent stress, physically denotes the transport of momentum due to turbulent eddies of various sizes. Due to this correlation terms, the RANS set of equations is not closed, as no extra equations appear, but extra variables arise (a total of four equations and ten unknown variables ($\bar{p}$, $\bar{u}$, $\bar{v}$, $\overline{w}$, $\overline{u'v'}$, $\overline{u'w'}$, $\overline{v'w'}$, $\overline{u'^2}$, $\overline{v'^2}$, $\overline{w'^2}$) is found. Extra equations should be added to close the set of equations, described in section 4.5. For simplicity of notation, we will omit the $\overline{\text{bar}}$ notation to indicate Reynolds-averaged variables from now on. Unless specifically mentioned, all variables further on are Reynolds averaged.

4.3 From Navier-Stokes to Shallow Water Equations

The Navier-Stokes equations describe conservation of mass and momentum. To attain the "Shallow Water Equations", some additional assumptions have to be made (Casulli, 2012; Vreugdenhill, 1994; Wu, 2007). Incompressible fluid is assumed, meaning that the density ρ is independent from the pressure. This results in the expression that $\partial \rho / \partial t$ = 0 and the fact that the water density ρ is independent of the position, $\partial \rho / \partial x_i$ = $\rho \partial / \partial x_i$. As such, the continuity equation (4.7) reduces to:

$$\frac{\partial u}{\partial x} + \frac{\partial v}{\partial y} + \frac{\partial w}{\partial z} = 0 \tag{4.9a}$$

or

$$\bigtriangledown \cdot \vec{u} = 0 \tag{4.9b}$$

stating that the velocity vector field $\vec{u}$ is divergence free, or the magnitude of the vector field source or sink at a given point is 0. The momentum equations, in respectively the x (eq. 4.10), y (eq. 4.11) and z (eq. 4.12) direction, written for a Cartesian, rectangular coordinate system (depicted in Figure 4.1), read as:

$$\frac{\partial u}{\partial t} + \frac{\partial uu}{\partial x} + \frac{\partial uv}{\partial y} + \frac{\partial uw}{\partial z} = \frac{1}{\rho}F_x - \frac{1}{\rho}\frac{\partial p}{\partial x} + \frac{1}{\rho}\frac{\partial \tau_{xx}}{\partial x} + \frac{1}{\rho}\frac{\partial \tau_{xy}}{\partial y} + \frac{1}{\rho}\frac{\partial \tau_{xz}}{\partial z} \tag{4.10}$$

$$\frac{\partial v}{\partial t} + \frac{\partial uv}{\partial x} + \frac{\partial vv}{\partial y} + \frac{\partial vw}{\partial z} = \frac{1}{\rho}F_y - \frac{1}{\rho}\frac{\partial p}{\partial y} + \frac{1}{\rho}\frac{\partial \tau_{yx}}{\partial x} + \frac{1}{\rho}\frac{\partial \tau_{yy}}{\partial y} + \frac{1}{\rho}\frac{\partial \tau_{yz}}{\partial z} \tag{4.11}$$

$$\frac{\partial w}{\partial t} + \frac{\partial uw}{\partial x} + \frac{\partial vw}{\partial y} + \frac{\partial ww}{\partial z} = \frac{1}{\rho}F_z - \frac{1}{\rho}\frac{\partial p}{\partial z} + \frac{1}{\rho}\frac{\partial \tau_{zx}}{\partial x} + \frac{1}{\rho}\frac{\partial \tau_{zy}}{\partial y} + \frac{1}{\rho}\frac{\partial \tau_{zz}}{\partial z} \tag{4.12}$$

here, u, v and w are the velocity component in the stream wise x, lateral y and vertical z direction (Figure 4.1). In a natural water body with a free surface, some further simplifications can be made.

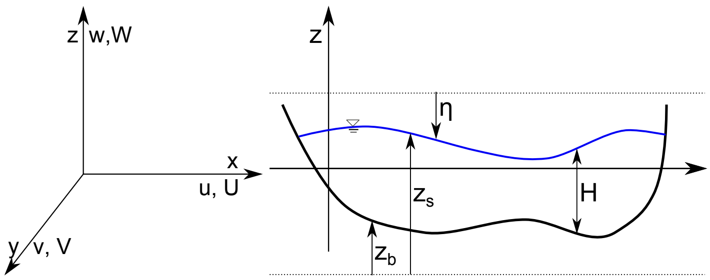

Figure 4.1: Left: Definition of the Cartesian coordinate system, with indication of x, y and z orientation. Right: Definition of reference plane and indication of the variables z_s, z_b, H and η.

For the derivation of the Shallow Water Equations, also indicated by SWE, boundary conditions at the free water surface and bottom are set. The kinematic condition of the free surface, assuming that the free water surface can be expressed as a single valued function $z = z_s(x, y, t)$, is given as:

$$\frac{dz_s}{dt} = \frac{\partial z_s}{\partial t}\frac{\partial t}{\partial t} + \frac{\partial z_s}{\partial x}\frac{\partial x}{\partial t} + \frac{\partial z_s}{\partial y}\frac{\partial y}{\partial t} = \frac{\partial z_s}{\partial t} + u_s\frac{\partial z_s}{\partial x} + v_s\frac{\partial z_s}{\partial y} = w_s \tag{4.13}$$

In equation 4.13, u_s, v_s and w_s are the stream wise, lateral and vertical velocity component at the free surface z_s. By definition, $dz_s/dt = w_s$. At the bottom boundary, another condition is set (equation 4.14), expressing that the velocity components perpendicular to the solid boundaries must vanish, as no flow can cross that boundary. The bed can be expressed by a single valued function $z = z_b(x, y)$ (t is omitted, as the bed is considered solid, or at least slowly varying compared to the water flow).

$$\frac{dz_b}{dt} = u_b \frac{\partial z_b}{\partial x} + v_b \frac{\partial z_b}{\partial y} + w_b = 0 \tag{4.14}$$

In shallow flows, which are studied in this manuscript, the vertical accelerations can be assumed very small compared to the vertical external forces (gravity) and the pressure gradient. Also the vertical viscosity can be assumed very small (Casulli, 2012). If both these inertia and viscous terms can be omitted from eq. 4.12, this shallow water assumptions simplify eq. 4.12 to eq. 4.15. This equation is essentially an expression of the hydrostatic pressure equation.

$$\frac{\partial p}{\partial z} = -g \tag{4.15}$$

Integrating eq. 4.15 from bottom (z_b) to surface (z_s), and assuming constant density over depth, equation 4.16 results, with Pa_{Atm} the atmospheric pressure [Pa].

$$p = g \int_{z_b}^{z_s} \rho \mathrm{d}z + Pa = \rho g (z_s - z_b) + Pa_{Atm} \tag{4.16}$$

The set of equations for the Shallow Water Equations, using eq. 4.15, results in the following set of equations, called the 3D Shallow Water Equations

$$\frac{\partial u}{\partial x} + \frac{\partial v}{\partial y} + \frac{\partial w}{\partial z} = 0 \tag{4.17}$$

$$\frac{\partial u}{\partial t} + \frac{\partial uu}{\partial x} + \frac{\partial uv}{\partial y} + \frac{\partial uw}{\partial z} = -g \frac{\partial z_s}{\partial x} - \frac{1}{\rho}\frac{\partial p}{\partial x} + \frac{1}{\rho}\frac{\partial \tau_{xx}}{\partial x} + \frac{1}{\rho}\frac{\partial \tau_{xy}}{\partial y} + \frac{1}{\rho}\frac{\partial \tau_{xz}}{\partial z} \tag{4.18}$$

$$\frac{\partial v}{\partial t} + \frac{\partial uv}{\partial x} + \frac{\partial vv}{\partial y} + \frac{\partial vw}{\partial z} = -g \frac{\partial z_s}{\partial y} - \frac{1}{\rho}\frac{\partial p}{\partial y} + \frac{1}{\rho}\frac{\partial \tau_{yx}}{\partial x} + \frac{1}{\rho}\frac{\partial \tau_{yy}}{\partial y} + \frac{1}{\rho}\frac{\partial \tau_{yz}}{\partial z} \tag{4.19}$$

4.4 Finding the depth-averaged Shallow Water Equations

As a final step towards the two dimensional, depth-averaged SWE, an integration of the SWE between bottom and free surface should be performed (Bousmar, 2002; Chaudry, 1993; Vreugdenhill, 1994; Wu, 2007). For an arbitrary variable ϕ, its depth-averaged value Φ can be defined as:

$$\Phi = \frac{1}{(z_s - z_b)} \int_{z_b}^{z_s} \phi \mathrm{d}z = \frac{1}{H} \int_{z_b}^{z_s} \phi \mathrm{d}z \tag{4.20}$$

The depth integral is applied between the free surface z_s of the fluid body and the bottom z_b (as indicated in Figure 4.1), and the water depth H is defined as the difference between z_s and z_b. For the integration of equation 4.17, the integration and differential operators are inverted using the rule of Leibniz (eq. 4.21):

$$\int_{a(y,t)}^{b(y,t)} \frac{\partial f}{\partial x} \mathrm{dx} = \frac{\partial \int_{a(y,t)}^{b(y,t)} f(x,y,t)dx}{\partial t} + f(a,y,t)\frac{\partial a}{\partial t} - f(b,y,t)\frac{\partial b}{\partial t} \tag{4.21}$$

Applying definition (eq. 4.20) and the rule of Leibniz (eq. 4.21) on equation 4.17, results in the following equation:

$$\begin{gathered} \frac{\partial}{\partial x} \int_{z_b}^{z_s} u \,\mathrm{d}z - u_s \frac{\partial z_s}{\partial x} + u_b \frac{\partial z_b}{\partial x} + \\ \frac{\partial}{\partial y} \int_{z_b}^{z_s} v \,\mathrm{d}z - v_s \frac{\partial z_s}{\partial y} + v_b \frac{\partial z_b}{\partial y} + \\ + w_s - w_b = 0 \end{gathered} \tag{4.22}$$

Using equation 4.20 to substitute the integrals

$$\begin{gathered} \frac{\partial HU}{\partial x} + \frac{\partial HV}{\partial y} - \left(u_s \frac{\partial z_s}{\partial x} + v_s \frac{\partial z_s}{\partial y} - w_s \right) \\ + \left(u_b \frac{\partial z_b}{\partial x} + v_b \frac{\partial z_b}{\partial y} - w_b \right) = 0 \end{gathered} \tag{4.23}$$

and equations 4.13 and 4.14, equation 4.23 can be simplified:

$$\frac{\partial \eta}{\partial t} + \frac{\partial HU}{\partial x} + \frac{\partial HV}{\partial y} = 0 \tag{4.24}$$

where H is the total water depth [m], U the depth-averaged velocity according to the x-coordinate [m/s], V the depth-averaged velocity along the y-axis [m/s] and η the position of z_s from a reference plane [m]. The temporal derivative of the free-surface level ∂z_s / ∂t is replaced by the derivate of η, which indicates z_s from a reference level (see Figure 4.1).

For the momentum equations (equations 4.18 and 4.19), a similar approach can be used. Applying the depth-averaging integration on the momentum equation in the stream wise direction (4.18), and using the Leibnitz rule (eq. 4.21) to invert the integration and derivation operators, results in:

$$\begin{aligned}\frac{\partial}{\partial t}\int_{z_b}^{z_s} u\,\mathrm{d}z - u_s\frac{\partial z_s}{\partial t} + u_b\frac{\partial z_b}{\partial t} + \frac{\partial}{\partial x}\int_{z_b}^{z_s} uu\,\mathrm{d}z - u_s^2\frac{\partial z_s}{\partial x} + u_b^2\frac{\partial z_b}{\partial x} + \\ \frac{\partial}{\partial y}\int_{z_b}^{z_s} uv\,\mathrm{d}z - u_s v_s\frac{\partial z_s}{\partial y} + u_b v_b\frac{\partial z_b}{\partial y} + u_s w_s - u_b w_b = \\ -gH\frac{\partial z_s}{\partial x} - \frac{1}{\rho}\frac{\partial}{\partial x}\int_{z_b}^{z_s}\tau_{xx}\,\mathrm{d}z - \frac{1}{\rho}\tau_{xx,s}\frac{\partial z_s}{\partial y} + \frac{1}{\rho}\tau_{xx,b}\frac{\partial z_b}{\partial y} + \\ \frac{1}{\rho}\frac{\partial}{\partial y}\int_{z_b}^{z_s}\tau_{xy}\,\mathrm{d}z - \frac{1}{\rho}\tau_{xy,s}\frac{\partial z_s}{\partial y}\,\mathrm{d}z + \frac{1}{\rho}\tau_{xy,b}\frac{\partial z_b}{\partial y} + \frac{1}{\rho}(\tau_{xz,s} - \tau_{xz,b})\end{aligned} \tag{4.25}$$

To simplify equation 4.25, we look at the different terms with integrals. The first term, only a function of u, can be easily integrated, using the definition in equation 4.20, resulting in equation 4.26:

$$\frac{\partial}{\partial t}\int_{z_b}^{z_s} u\,\mathrm{d}z = \frac{\partial(HU)}{\partial t} \tag{4.26}$$

The integration of the other terms lead to dispersion terms, as a velocity product is present in the integration. The velocity u, which is Reynolds-averaged, will vary locally along the depth and as such, the square of the depth-averaged velocity will not be equal to the depth-integration of the squared value. At all depths, u can be written as a function of U:

$$u = U + (u - U) \tag{4.27}$$

In the limit case, of perfect uniform velocity over the depth, the second term will vanish. Using equation 4.27 in the integral of u^2 results in equation 4.28, with term 2 equalling zero, and finally resulting in equation 4.29.

$$\begin{gathered}\frac{\partial}{\partial x}\int_{z_b}^{z_s} uu\,\mathrm{d}z = \\ \frac{\partial}{\partial x}\int_{z_b}^{z_s} U^2\,\mathrm{d}z + 2\frac{\partial}{\partial x}\int_{z_b}^{z_s}(u-U)U\,\mathrm{d}z + \frac{\partial}{\partial x}\int_{z_b}^{z_s}(u-U)^2\,\mathrm{d}z =\end{gathered} \tag{4.28}$$

$$\frac{\partial(HU^2)}{\partial x} + \frac{\partial}{\partial x}\int_{z_b}^{z_s}(u-U)^2\mathrm{d}z \tag{4.29}$$

A similar approach can be followed for the third integral, where in stead of uu the integrandum is uv, resulting in equation 4.30

$$\frac{\partial}{\partial x}\int_{z_b}^{z_s} uv\,\mathrm{d}z = \frac{\partial(HUV)}{\partial y} + \frac{\partial}{\partial y}\int_{z_b}^{z_s}(u-U)(v-V)\,\mathrm{d}z \tag{4.30}$$

Using equations 4.26, 4.29 and 4.30 in equation 4.25, and defining T_{xx}, T_{xy} [Pa] as depth-integral values of the Reynolds stresses τ_{xx} and τ_{xy}, gives:

$$\begin{aligned}
\frac{\partial(HU)}{\partial t} + \frac{\partial(HU^2)}{\partial x} + \frac{\partial(HUV)}{\partial y} + \\
\frac{\partial}{\partial x}\int_{z_b}^{z_s}(u-U)^2\,\mathrm{d}z + \frac{\partial}{\partial y}\int_{z_b}^{z_s}(u-U)(v-V)\,\mathrm{d}z \\
-u_s\left(\frac{\partial z_s}{\partial t} + u_s\frac{\partial z_s}{\partial x} + v_s\frac{\partial z_s}{\partial y}\right) + u_s w_s \\
+u_b\left(\frac{\partial z_b}{\partial t} + u_b\frac{\partial z_b}{\partial x} + v_b\frac{\partial z_b}{\partial y}\right) - u_b w_b = \\
-gH\frac{\partial z_s}{\partial x} - \frac{1}{\rho}\frac{\partial(HT_{xx})}{\partial x} + \frac{1}{\rho}\frac{\partial(HT_{xy})}{\partial y} + \\
\frac{1}{\rho}\left(\tau_{xz,s} - \tau_{xx,s}\frac{\partial z_s}{\partial y} - \tau_{xy,s}\frac{\partial z_s}{\partial y}\right) \\
+\frac{1}{\rho}\left(-\tau_{xz,b} + \tau_{xx,b}\frac{\partial z_b}{\partial y} + \tau_{xy,b}\frac{\partial z_b}{\partial y}\right)
\end{aligned} \tag{4.31}$$

To further simplify equation 4.31, some new definitions are used. As such, τ_{sx} is the x-component of the shear stress at the water surface [Pa], defined as in equation 4.32. The x-component of the shear stress at the bottom [Pa] is defined as in equation 4.33.

$$\tau_{sx} = \tau_{xz,s} - \tau_{xx,s}\frac{\partial z_s}{\partial x} - \tau_{xy,s}\frac{\partial z_s}{\partial y} \tag{4.32}$$

$$\tau_{bx} = \tau_{xz,b} - \tau_{xx,b}\frac{\partial z_b}{\partial x} - \tau_{xy,b}\frac{\partial z_b}{\partial y} \tag{4.33}$$

Applying these definitions (eqs. 4.32 and 4.33), together with the boundary conditions at the free surfaces (eq. 4.13) and at the bottom (eq. 4.14) on equation 4.31 results in:

$$\begin{aligned}
\frac{\partial(HU)}{\partial t} + \frac{\partial(HU^2)}{\partial x} + \frac{\partial(HUV)}{\partial y} + \\
\frac{\partial}{\partial x}\int_{z_b}^{z_s}(u-U)^2\,\mathrm{d}z + \frac{\partial}{\partial y}\int_{z_b}^{z_s}(u-U)(v-V)\,\mathrm{d}z \\
= -gH\frac{\partial z_s}{\partial x} - \frac{1}{\rho}\frac{\partial(HT_{xx})}{\partial x} + \frac{1}{\rho}\frac{\partial(HT_{xy})}{\partial y} + \frac{1}{\rho}(\tau_{sx} - \tau_{bx})
\end{aligned} \tag{4.34}$$

Throughout this manuscript, the wind stress will be omitted, as we work in smaller rivers where the wind has only minor effects. Also the dispersion terms, $D_{xx} = \frac{\partial}{\partial x}\int_{z_b}^{z_s}(u-U)^2\,\mathrm{d}z$ and $D_{xy} = \frac{\partial}{\partial x}\int_{z_b}^{z_s}(u-U)(v-V)\,\mathrm{d}z$ will be omitted.

In most studies, the dispersion terms are combined with the turbulent stresses (Wu, 2007) or omitted (Cea et al., 2007), only e.g. when secondary vertical currents are important e.g. in sharp bends, dispersion should be added explicitly.

$$\begin{aligned}\frac{\partial(HU)}{\partial t}+\frac{\partial\left(HU^2\right)}{\partial x}+\frac{\partial(HUV)}{\partial y}=\\ -gH\frac{\partial z_s}{\partial x}+\frac{1}{\rho}\frac{\partial(HT_{xx})}{\partial x}+\frac{1}{\rho}\frac{\partial(HT_{xy})}{\partial y}-\frac{1}{\rho}\tau_{bx}\end{aligned} \tag{4.35}$$

A very similar approach can be followed for the y-momentum equation, resulting in:

$$\begin{aligned}\frac{\partial(HV)}{\partial t}+\frac{\partial(HUV)}{\partial x}+\frac{\partial\left(HV^2\right)}{\partial y}=\\ -gH\frac{\partial z_s}{\partial y}+\frac{1}{\rho}\frac{\partial(HT_{yx})}{\partial x}+\frac{1}{\rho}\frac{\partial(HT_{yy})}{\partial y}-\frac{1}{\rho}\tau_{by}\end{aligned} \tag{4.36}$$

In the end, combining equations 4.24 for the continuity equation and equations 4.35 and 4.36 for respectively the stream wise and lateral momentum equation, results in the following set of equations, called the depth-averaged Shallow Water Equations or Saint-Venant equations.

$$\begin{array}{ccccccccc}\frac{\partial\eta}{\partial t} & +\frac{\partial(HU)}{\partial x} & +\frac{\partial(HV)}{\partial y} & = & 0 & & & & \\ \frac{\partial(HU)}{\partial t} & +\frac{\partial\left(HU^2\right)}{\partial x} & +\frac{\partial(HUV)}{\partial y} & = & -gH\frac{\partial\eta}{\partial x} & +\frac{1}{\rho}\frac{\partial(HT_{xx})}{\partial x} & +\frac{1}{\rho}\frac{\partial(HT_{xy})}{\partial y} & -\frac{1}{\rho}\tau_{bx} \\ \frac{\partial(HV)}{\partial t} & +\frac{\partial(HUV)}{\partial x} & +\frac{\partial\left(HV^2\right)}{\partial y} & = & -gH\frac{\partial\eta}{\partial y} & +\frac{1}{\rho}\frac{\partial(HT_{yx})}{\partial x} & +\frac{1}{\rho}\frac{\partial(HT_{yy})}{\partial y} & -\frac{1}{\rho}\tau_{by} \\ (1) & (2) & (2) & & (3) & (4) & (4) & (5)\end{array} \tag{4.37}$$

In this set of equations, H, U and V are respectively the water depth [m], stream wise velocity [m/s] and lateral velocity [m/s]. These three variables are the principal variables (state variables) of interest when solving the 2D-SWE. T_{xx}, T_{xy}, T_{yy} are the depth-averaged Reynolds stresses [Pa], and τ_b represents the bed shear stress [Pa]. The main assumptions made for the derivation of the depth-averaged Shallow Water Equations are (1) in-compressibility of the fluid and (2) a hydrostatic pressure assumption, which comes from the assumption that vertical and horizontal scales can be separated. Furthermore, for this manuscript, dispersion terms, Coriolis forces and wind stress are omitted. The different terms (1 to 5) in the equations above, all have a physical explanation and can be listed as follows:

1. *Local acceleration*. These terms represent the rate of change in time of the state variables (η, U and V) at a given point (x, y). These are the only terms representing the non-stationarity of flow. Obviously, in case of steady flow, these terms can be omitted.

2. *Convective acceleration*. The convective acceleration is the rate of change of the velocity (acceleration) due to a change of position of fluid particles in the fluid.

3. *Surface slope*. This term represents the action of the gravity force, which is, in the case of free surface flow under study, the main driving force.

4. *Reynolds stresses*. These terms, consisting of T_{ij}, represent the depth-averaged shear and normal stresses. By a Boussinesq approach, they can be linked to gradients of the depth-averaged velocities. These terms are more explicitly handled in section 4.5.

5. *Bottom stresses*. For an in depth overview of this term, the reader is referred to Chapter 6.

4.5 Focus on turbulence assumptions

Of all terms in the depth-averaged shallow water equations (eq 4.37) the depth-averaged values of the shear stresses T_{xx}, T_{xy} and T_{yy} [Pa] have been discussed the least till now. Using the Boussinesq approach, the stresses T_{ij} can be written as a function of the strain rate, as is done for the molecular viscosity (eq 4.3). In stead of the molecular viscosity, a turbulent eddy viscosity coefficient ν_t $[\mathrm{m}^2/\mathrm{s}]$ is used as a proportional constant. Combining the molecular ν and eddy viscosity ν_t, results in:

$$\frac{\tau_{ij}}{\rho} = (\nu + \nu_t)\left(\frac{\partial u_i}{\partial x_j} + \frac{\partial u_j}{\partial x_i}\right) \tag{4.38}$$

As in fully, turbulent flows, the mixing due to turbulent effects is much larger compared to the molecular diffusion, the molecular coefficient in equation 4.38 can be omitted (Cea et al., 2007; Wu, 2007). In a depth-averaged approach, the depth averaged shear-stresses can be written as in equations 4.39 till 4.41 (Bousmar, 2002; Wu, 2007), with k the turbulent kinetic energy:

$$T_{xx} = 2\rho\nu_t\left(\frac{\partial U}{\partial x}\right) - \frac{2}{3}\rho k \tag{4.39}$$

$$T_{xy} = T_{yx} = \rho\nu_t\left(\frac{\partial U}{\partial y} + \frac{\partial V}{\partial x}\right) \tag{4.40}$$

$$T_{yy} = 2\rho\nu_t \left(\frac{\partial V}{\partial x}\right) - \frac{2}{3}\rho k \tag{4.41}$$

or as (Cea et al., 2007; Vionnet et al., 2004):

$$T_{ij} = \rho\nu_t \left(\frac{\partial U_i}{\partial x_j}\right) \tag{4.42}$$

The latter approach is used in this manuscript. The turbulent eddy viscosity ν_t [m^2/s] should be determined by an additional turbulence model. The eddy-viscosity ν_t can be assumed constant, or being estimated locally by an expression. Depending on the complexity incorporated, the models to calculate ν_t can be algebraic equations, or one- or two equation models, and are presented hereafter. A short overview is given below, focusing most on the algebraic expressions, as these are used throughout this manuscript, because of its simplicity.

4.5.1 Algebraic Model

A first approach, the parabolic eddy viscosity model, uses the concept of equilibrium state of the flow, where the hydrostatic pressure and shear stress are balanced. When a logarithmic profile in the depth is assumed, the model assumes a parabolic profile for the eddy viscosity $\nu_t(z)$, based on conceptual arguments regarding mixing length:

$$\nu_t(z) = u^*\kappa z \left(1 - \frac{z}{H}\right) \tag{4.43}$$

with u^* the friction velocity [m/s], κ the von Kàrmàn constant [-] and H the water depth [m]. Integrating over the depth results in a depth-averaged value for ν_t, with U^* the depth-averaged friction velocity [m/s] and H the water depth [m], given by

$$\nu_t = \alpha_0 U^* H \tag{4.44}$$

The value of α_0, a proportional constant, is theoretically equal to 1/6 κ or 0.068. In literature, a range of 0.06 till 0.3 are generally found for α_0 (Ball et al., 1996; Vionnet et al., 2004), but even values as high as 1 can be found (Wu et al., 2004). The friction velocity U^* is defined as $\sqrt{\tau_b/\rho}$, which, applied to a 2D context, respectively results in:

$$U_{x*} = \sqrt{\frac{C_f \rho U \sqrt{U^2 + V^2}}{\rho}} \tag{4.45}$$

$$U_{y*} = \sqrt{\frac{C_f \rho V \sqrt{U^2 + V^2}}{\rho}} \tag{4.46}$$

with C_f a friction coefficient, defined as $C_f = U^{*2}/\left|U^2\right|$. The value of the friction coefficient C_f can be determined by the Manning coefficient (of the channel bed) as $C_f = gn^2/H^{1/3}$ (Vionnet et al., 2004; Wu, 2007). Another algebraic model is the depth-averaged mixing length model. The total eddy viscosity coefficient is split into a horizontal (ν_t^h) and a vertical component (ν_t^v). The total eddy viscosity (ν_t) is computed as:

$$\begin{aligned}\nu_t &= \sqrt{(\nu_t^h)^2 + (\nu_t^v)^2} \\ &= l_s^2 \sqrt{2\left(\frac{\partial U}{\partial x}\right)^2 + \left(\frac{\partial U}{\partial y} + \frac{\partial V}{\partial x}\right)^2 + 2\left(\frac{\partial V}{\partial y}\right)^2 + \left(2.34\frac{u^*}{\kappa H}\right)}\end{aligned} \tag{4.47}$$

with l_s the characteristic horizontal turbulent length scale [m]. l_s can be assumed to be dependent on the water depth H, as this sets the size of the turbulent eddies, which however leads to an underestimation of ν_t in case the turbulent structures are larger than the water depth (Cea et al., 2007). A value of α_1 between 0.2 and 1.2 are found (Cea et al., 2007; Wu, 2007; Wu et al., 2004). Furthermore, near the walls, an adaptation on the expression for the inner domain part is used, taking into account the distance to the wall d_{wall} (equation 4.48)

$$l_s = min\left(\alpha_1 \kappa H, \kappa d_{wall}\right) \tag{4.48}$$

It should be mentioned however that a lot of codes of practices exist for the use of an appropriate ν_t value. In many situations, high values are chosen to damp any possible oscillations.

4.5.2 One-equation and two-equations model

Unlike previous models, for the one- and two-equation models, additional transport equations need to be solved. In the one-equation model, an equation to calculate the turbulent energy k is stated. A well known example for the two-equation models is the k-ϵ model, where an equation for the turbulent energy k and the dissipation rate ϵ is stated. The final turbulent eddy viscosity is found as a function of the calculated k and ϵ. For the use in depth-averaged modeling adapted depth-averaged k-ϵ models exist. As these methods are not used in this manuscript, they are not explicitly stated here. For further information, the reader is referred to e.g. Wu (2007), Cea et al. (2007), Wu et al. (2004), Rodi (1993).

4.6 Adapting the 2D-SWE for flow with vegetation

The 2D depth-averaged Shallow Water Equations (eqs. 4.37) can be adapted for flow in vegetated channels as in equations 4.49, 4.50 and 4.51 (Wu, 2007), where

c is the depth-averaged volumetric concentration of vegetation [-], m is the vegetation density [$1/\mathrm{m}^2$], F_d the drag force [N] and D_{ij} represent the momentum dispersion transports.

$$\frac{\partial\left[\rho(1-c)\eta\right]}{\partial t}+\frac{\partial\left[\rho(1-c)HU\right]}{\partial x}+\frac{\partial\left[\rho(1-c)HV\right]}{\partial y}=0 \tag{4.49}$$

$$\begin{aligned}\frac{\partial\left[(1-c)HU\right]}{\partial t}+\frac{\partial\left[(1-c)HU^2\right]}{\partial x}+\frac{\partial\left[(1-c)HUV\right]}{\partial y}&=\\ -\rho g(1-c)H\frac{\partial z_s}{\partial x}+\frac{1}{\rho}\frac{\partial\left[(1-c)H(T_{xx}+D_{xx})\right]}{\partial x}&\\ +\frac{1}{\rho}\frac{\partial\left[(1-c)H(T_{xy}+D_{xy})\right]}{\partial y}-(1-c)\tau_{bx}-mF_{dx}&\end{aligned} \tag{4.50}$$

$$\begin{aligned}\frac{\partial\left[(1-c)HV\right]}{\partial t}+\frac{\partial\left[(1-c)HUV\right]}{\partial x}+\frac{\partial\left[(1-c)HV^2\right]}{\partial y}&=\\ -\rho g(1-c)H\frac{\partial z_s}{\partial y}+\frac{1}{\rho}\frac{\partial\left[(1-c)H(T_{yx}+D_{yx})\right]}{\partial x}&\\ +\frac{1}{\rho}\frac{\partial\left[(1-c)H(T_{yy}+D_{yy})\right]}{\partial y}-(1-c)\tau_{by}-mF_{dy}&\end{aligned} \tag{4.51}$$

In these equations (4.49, 4.50 and 4.51) two main differences with the original (eq. 4.37) are added. First, to each term, a $(1-c)$ factor was added, which represents the volume taken by the water (c is the volumetric concentration of vegetation). However, e.g. Wu (2007) states that for lower vegetation densities, the factor $(1-c)$ can be omitted, however no threshold indication is given.

Second, in the momentum equations in x- and y-direction, a drag force term with its respective components F_{dx} and F_{dy} is added, which indicates the drag force of the flow on the vegetation elements. This drag term is stated here explicitly as a separated term. The addition of such an extra term is one of both approaches which can be followed. The other approach which can be found is the addition or incorporation of the effect of the vegetation in the bed roughness term (the second last term of the momentum equations 4.50 and 4.51). Following this approach, the roughness coefficient (e.g. Manning or Chézy coefficient) is adapted to take into account the effect of vegetation. Several approaches to translate vegetation characteristics into roughness coefficients have been proposed in the past and an overview is given in Chapter 6. Both the former (Leu et al., 2008; Wu et al., 2004) and the latter approach (Ball et al., 1996; Zhang et al., 2013) have been used.

In this manuscript, the latter approach is used, and as such no additional drag term is taken into account. The only exception made is for the simulation of isolated patches (section 7.4), where the implementation of the additional drag term is compared with the implementation of vegetation roughness using the bed friction term (and therefore the Manning coefficient). Furthermore no porosity factor was incorporated as well. This approach is consistent with the previous studies on vegetated waterways (De Doncker, 2008), where in a 1D concept, biomass of vegetation is coupled with the Manning coefficient in the river reach.

5
Implementation of the 2D-SWE in STRIVE

5.1 Introduction

In this chapter, the STRIVE model, an integrated ecosystem model used for the study of vegetated river reaches, is introduced and described. An overview of the basic properties of numerical models is given, together with a description of the semi-implicit, semi-Lagrangian method, which is used to implement the depth-averaged Shallow Water Equations as hydraulic routine in the STRIVE model.

5.2 The acronym STRIVE

5.2.1 What is STRIVE?

In previous studies, in a common effort of the Vrije Universiteit Brussel (VUB), the University of Antwerp (UA) and Ghent University (UGent), a STReam-RIVer-Ecosystem package, with the acronym STRIVE, was developed (Buis et al., 2007; De Doncker, 2008; De Doncker et al., 2011). The aim of this numerical package is to construct an integrated river ecosystem model, containing different components of these aquatic ecosystems. With such integrated model, cascade and feedback effects can be taken into account, along with their effect on retention, transport and transformation of matter (e.g. water, nitrate, solutes, etc.) in a river reach ecosystem.

The STRIVE package was created within the FEMME environment, acronym for ”Flexible Environment for Mathematical Modelling of the Environment” and developed by NIOO, the Dutch Institute of Ecology (Soetaert et al., 2002). This FORTRAN90-based environment was designed for implementing, solving and analysing mathematical models in ecology (Soetaert et al., 2002). FEMME contains a diversity of integration routines, steady-state solvers, fitting routines, allows running Monte Carlo or sensitivity analyses, etc.

5.2.2 Flowchart of STRIVE

An example of the flow chart of STRIVE[1] is given in Figure 5.1. In this flow chart, the most important relations between the model components and so the different processes which take place in the ecosystem are depicted (De Doncker, 2008). The different system components are described in different modules, and as such a flexible toolbox of modules can be used, depending on the problem set. The main components under study are the macrophytes, surface water and the water bottom.

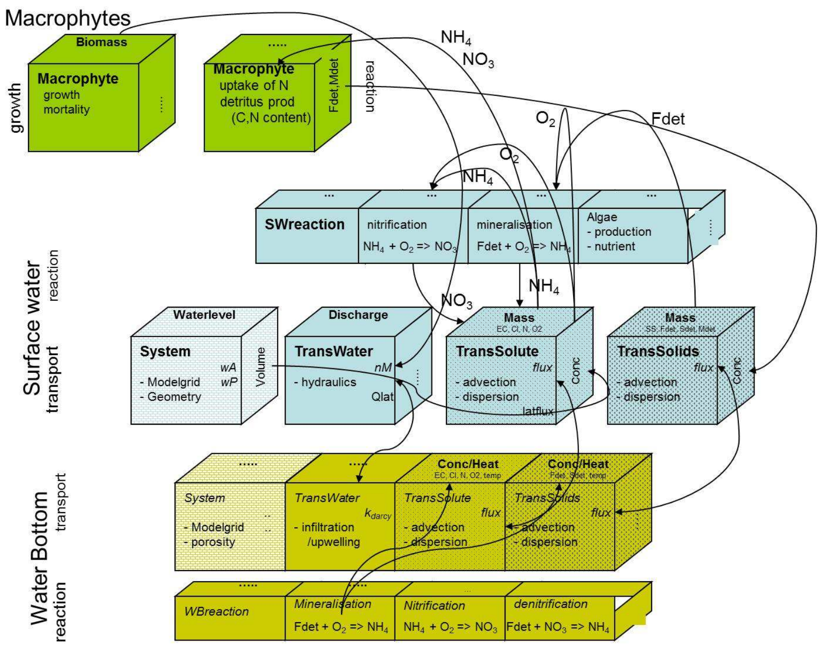

Figure 5.1: Flow chart of STRIVE, originally set up for a 1D-framework (after K. Buis).

[1] The System and Transwater module for the 2D-SWE were developed by Dieter Meire. Some adaptations to the 1D Transwater module were developed as well by Dieter Meire, see e.g. Meire et al. (2010), but these are not discussed in this manuscript.

For a situation where only macrophytes and surface water are of interest, an example is given in Figure 5.2. The following links could be used: the presence of macrophytes (in a spatial pattern) results in a spatially distributed resistance coefficient based on the macrophytes characteristics (e.g. biomass, number of stems, average stem diameter, vegetation height,...). This distributed field is used as an input for the surface water calculations, a hydraulic routine. This module, using the 2D-depth-averaged SWE (see chapter 4), will generate in return predictions of the non-uniform velocity field and water heights. This heterogeneous velocity field can again be used as an input for the vegetation growth model (e.g. stress on the plants because of velocity magnitude, bending of the plants due to upstream velocity, water depth above plant determines light availability,. . .), resulting in an increase or decrease of vegetation biomass, which can be used as input for the next simulation of water velocities and depths. The characteristic time of every component of the system can be very different (e.g. water flow can change in the order of seconds, vegetation grows more slowly), and as such a wise use of the time updates for the different components is important.

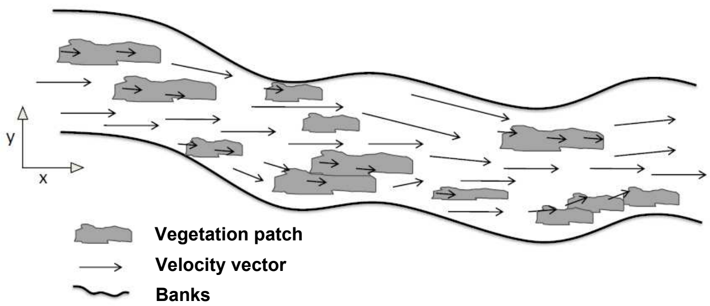

Figure 5.2: A spatial distribution of vegetation in a river reach, with its implication on the velocity vector field (after K. Buis and Keirsebelik (2009)).

As described in the Introduction and indicated in Figure 1.3, the morphodynamics also play an important role in vegetated rivers. The bathymetry, which is the result of erosion and sedimentation processes, is defined in the System module. The transport of sediments, either erosion or sedimentation, is implemented in the TransSolids module. This module is addressed for the implementation of particle transport equations. In the example above and throughout this manuscript, no attention is paid to the ”‘Water Bottom”’ component, and as such this module is not considered further on. In the System module, an extension was made from a 1D to a 2D grid. In the Transwater module, a 2D flow set was added and linked with the macrophytes module through resistance implementations based on vegetation characteristics.

5.2.3 Extension of the STRIVE package

In this manuscript, the extension of the STRIVE package, more precisely the Geometry and Transwater module, from a 1D to a 2D framework is described. Some characteristics for the numerical integration of the 2D-depth-averaged Shallow Water Equations were put forward at the start of the project, and are listed below:

1. *Time - step*: as the aim of the STRIVE-users will be to run, apart from steady-state solutions, developments of the river reach over e.g. a vegetation season, larger time steps in the calculations should be possible.

2. *Dry - wet transitions*: the numerical method should be able to handle dry-wet transitions, which e.g. occur when floodplains or surrounding land starts to flood. Furthermore, the ability to capture dry-wet transitions makes it possible to use the numerical code also for floodplains (marshes, ...) where the effect of macrophytes is considered as essential as well.

3. *Transcritical flow*: a transition from subcritical to supercritical flow, occuring e.g. when a river starts to flood from the river banks into a floodplain area, should be able to be simulated as well.

5.3 Numerical discretisation of flow equations

5.3.1 Introduction

The partial differential equations listed and derived in Chapter 4 can only be solved analytically in specific cases, for very specific boundary conditions. In general, these equations need to be solved numerically. This means that the domain of interest (Ω) needs to be represented or divided into a finite number of points (Ω_i), which form the computational grid. The continuous partial differential equation, represented by F can be transformed to an approximate, discrete function F_i in each of these computational points.

$$F(\Omega) \longrightarrow F_i(\Omega_i) \tag{5.1}$$

In the next sections, section 5.3.2, 5.3.3 and 5.3.4 the basic properties, types and characteristics of the numerical methods for open-channel hydraulics will be shortly discussed. This summary is based on information found in Wu (2007), Ferziger and Peric (2002), Versteeg and Malalasekera (1995) and Vreugdenhill (1994). For further information, the reader is referred to these references.

5.3.2 Properties of numerical discretisation methods

Four general properties of numerical discretisation methods can be defined: stability, convergence, consistency and accuracy. These criteria are explained and discussed below.

Stability

In the first place, a numerical solution method needs to be stable. This means that the round-off errors which appear during the numerical solution process, are not magnified throughout this process. For iterative methods, this results in methods which are not diverging. For temporal, unsteady problems, this means that the solution is bounded if the exact solution is bounded.

Convergence

A numerical method is considered to be convergent, if the approximate solution resulting from the set of algebraic equations approaches the original differential equation as the grid spacing tends to go to 0. Shortly, this means:

$$\text{if } \ \Delta x \to 0 \ \text{ then } F_i \to F \tag{5.2}$$

Consistency

The system of discretised equations is considered to be consistent with the original differential equation if it is equivalent to the differential equation at each grid point when the grid spacing reduces to zero.

Accuracy

The numerical accuracy indicates how good the numerical method approximates the solution of the differential equation, as numerical solutions are only approximate solutions. If a method is said to be second order accurate, this means that the residual order O is proportional to Δx^2. In general, using an n-th order numerical method, the residual R can be written as:

$$R = F(x) - F_i(x_i) = O(\Delta x^n) \tag{5.3}$$

The residual term on the right-hand side can be obtained with a Taylor series expansion. For complex systems, however, as numerical schemes with different accuracies may be used for the equations and boundary conditions, the overall accuracy is difficult to judge.

5.3.3 Numerical grids

The physical domain which is modeled needs to be divided into a finite number of computational nodes or control volumes, depending on the numerical discretisation scheme used (see section 5.3.4). A variety of grid types can be found. The main differences are explained below, especially applied on a 2D domain space.

A first distinction can be made between structured and unstructured grids (see Figure 5.3). In structured grids, the simplest grids, the number of subdivisions in one direction is constant. This means for a 2D grid, that a certain amount of cells $Nrows$ and $Ncols$ divide the domain in the x- and y-direction. Therefore, each cell in the computational grid can be identified unambiguously using two indices (i, j). A further division can be made between regular and curvilinear grids. The former case is depicted in Figure 5.3a, for the latter case, the grid lines can be arbitrary curves in space (Figure 5.3b). Unstructured grids are more complex to generate, but have a higher flexibility. On an unstructured grid the number of neighbouring cells is variable as is the shape of one cell. An unstructured grid must contain at least two types of information, namely all nodes and their coordinates, and all cells and the related information, namely which nodes constitute each individual cell.

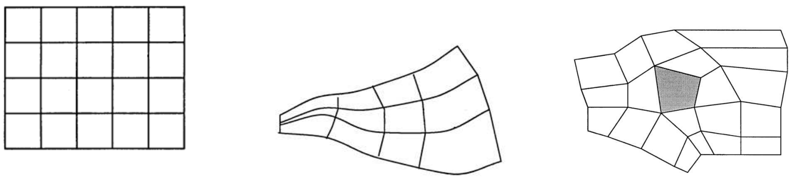

(a) (b) (c)

Figure 5.3: Example of structured ((a) and (b)) and unstructured grid types (c). Grid (a) is a rectangular, orthogonal, structured grid. Grid (b) is a curvilinear, orthogonal structured grid and grid (c) is an unstructured grid. (Figures after: $\mathrm{www.ifu.ethz.ch/GWH/education/graduate/Hydraulik_{II}/Vorlesungen/k5_{E}N.pdf}$)

For the Shallow Water Equations, three variables have to be calculated, namely the velocity components U and V [m/s] and the water depth H [m]. If the velocity variables are computed on the same place as the pressure variable (here the water depth), the grid is called collocated (see Figure 5.5). In a staggered grid, the velocities and pressure variables are not calculated on the same spot. The velocity nodes can be positioned on the midpoint of the faces, whereas the water depth nodes are calculated in the center of the computational node (Fig 5.5). Both grid types are used to solve the depth-averaged Shallow Water Equations.

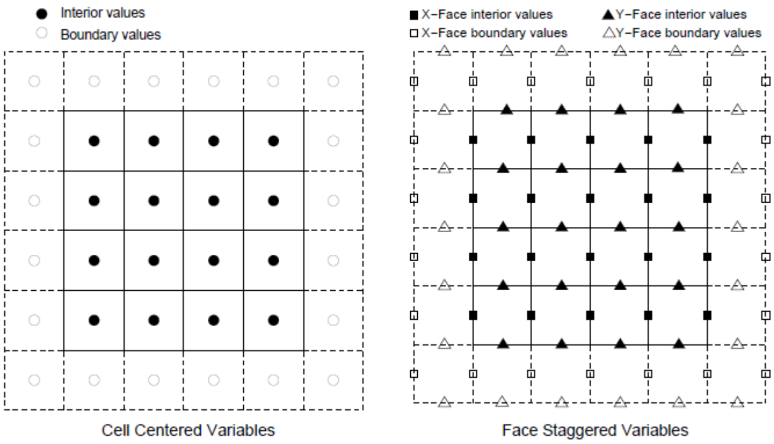

Figure 5.4: Example of collocated (left) and staggered grid (right). Only the position of the velocity nodes U and V is indicated, the water depth (or pressure) is calculated on the center of the grid node in both cases. Figures after Mignone (2012).

5.3.4 Discretisation methods

For the description of open-channel hydraulics, three main discretisation methods are used: respectively finite difference, finite volume and finite element methods. Using a finite difference method, a differential equation is discretized by approximating differential operators with difference operators at each point. Using the finite volume method, the differential equation is integrated over each control volume. In the finite element method, the differential equation is multiplied by a weight function and integrated over the entire domain. An approximate solution is constructed using shape functions and optimized by requiring the weighted integral to have a minimum residual (Wu, 2007). The finite elements method will not be discussed here, the reader is e.g. referred to Zienkiewicz and Taylor (2000) for more information.

The oldest discretisation method is the finite difference approach. As stated before, the differential terms are approximated by difference operators at each point. This idea is directly borrowed from the definition of a derivative itself:

$$\frac{\partial f}{\partial x} = \lim_{\Delta x \to 0} \frac{f(x + \Delta x) - f(x)}{\Delta x} \tag{5.4}$$

In a simple, one-dimensional case, the first, spatial derivative of a function f can be approximated by a forward-difference approach (eq. 5.5) or a backward-difference approach (5.6), both resulting in a first-order scheme. Another option is the central-difference approach 5.7, resulting in a second-order scheme. These approaches are visually shown in Figure 5.5 for a derivative of an arbitrary variable.

$$\left(\frac{\partial f}{\partial x}\right)_i \approx \frac{f_{i+1} - f_i}{\Delta x} \tag{5.5}$$

$$\approx \frac{f_i - f_{i-1}}{\Delta x} \tag{5.6}$$

$$\approx \frac{f_{i+1} - f_{i-1}}{2\Delta x} \tag{5.7}$$

Other, more complex differences schemes as exponential, higher order schemes (e.g. QUICKEST,...) are developed as well. Each approach has advantages and disadvantages, and their use will be dependent on the case-specific problem. These schemes are described in e.g. Ferziger and Peric (2002); Wu (2007) and many others.

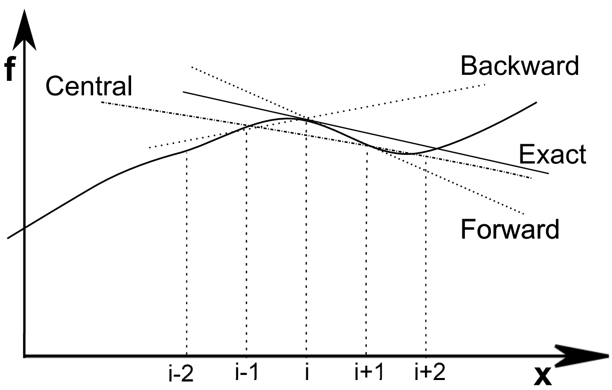

Figure 5.5: Different approximations of a derivative of a function f with an arbitrary argument x (adapted from Ferziger and Peric (2002)).

In the finite volume approach, the differential equations are integrated over each computational control volume. The finite volume uses the integral form of the conservation equation of a quantity ϕ as a starting point (Ferziger and Peric, 2002; Versteeg and Malalasekera, 1995):

$$\int_{CV} \frac{\partial (\rho\phi)}{\partial t} \mathrm{dV} + \int_{CV} div\,(\rho\phi\vec{u})\,\mathrm{dV} = \int_{CV} div\,(\Gamma grad\phi)\,\mathrm{dV} + \int_{CV} S_\phi \mathrm{dV} \tag{5.8}$$

The net flux through the boundary of the control volume (CV), for convective and diffusive fluxes, can be written as a surface integral over the control volume faces (A), written for a vector $\vec{a}$:

$$\int_{CV} div\vec{a}\mathrm{dV} = \int_A \vec{n}\cdot\vec{a}\mathrm{dA} = \sum_{i=1}^{4}\int_{A_i} a\mathrm{dA} \tag{5.9}$$

with a a normal component of the convective or diffusive flux, normal to the face of the control volume.

5.4 The TRIM methods

5.4.1 Introduction

The method used to discretise the depth-averaged Shallow Water Equations in this manuscript, is a finite volume numerical approximation, which is semi-implicit and semi-Langrangian and presented in e.g. Casulli and Cheng (1992). This type of numerical discretisation has the advantage compared to explicit methods that larger timesteps can be taken (the Courant number is less restrictive), whereas still wetting-drying properties and transcritical jumps can be resolved. As such, the main criteria mentioned in section 5.2 are fulfilled. The description of the numerical model is mainly based on Casulli (2012); Casulli and Cheng (1992) and Martin (2004).

TRIM is an acronym for ”Tidal, Residual, Inter-tidal Mud-flat” model, developed by Cheng et al. (1993) and one of the first publications using this kind of methods. Further on, this semi-implicit, semi-Lagrangian methods are often indicated as ”TRIM” methods. In these types of methods, the velocity divergence of the momentum equation is solved implicitly, as is done with the free surface elevation term in the momentum equation. However, the advective and diffusive terms appearing in the momentum equations, are treated using a Lagrangian method. By using the Lagrangian method, fully explicit terms can be avoided, which makes larger time steps possible.

The TRIM group of numerical methods, approximating the governing equations for a particular problem, in a 1D, 2D and 3D framework, have been used for different situations and over different scales of interest. A number of studies, using the TRIM method, are listed, to grasp the diversity of scales for which this method is used. Casulli (1990); Casulli and Cheng (1992) presented the method to study flow in estuaries and tidal embayments, such environments were also studied by Casulli and Stelling (2011); Casulli and Walters (2000); Casulli and Zanolli (2002); Chen et al. (2009); Cheng et al. (1993). Also for larger ocean scale the numerical technique has been applied, e.g. Zhang and Baptista (2008) and for large lakes by e.g. (Laval et al., 2003). On smaller scale, Lloyd and Stansby (1997a,b); Stansby and Lloyd (1995) used the methodology to study a flow around a conical island. Ball et al. (1996) looked at the velocities in the wake of a group of piles (see section 6.6). Furthermore, the numerical technique has been used to study dam-break flows (Martin, 2004), flow in arterial systems (Casulli et al., 2012), etc.

5.4.2 Equations

An overview of the depth-averaged Shallow-Water Equations was given in Chapter 4. The resulting depth-averaged Shallow Water Equations, presented in Eq. 4.37, are repeated here (Equation 5.10), using an algebraic turbulence model and the Manning coefficient to represent the bed shear stress.

$$\begin{aligned}
\frac{\partial \eta}{\partial t} + \frac{\partial (HU)}{\partial x} + \frac{\partial (HV)}{\partial y} &= 0 \\
\frac{\partial U}{\partial t} + U\frac{\partial U}{\partial x} + V\frac{\partial U}{\partial y} &= -g\frac{\partial \eta}{\partial x} + \nu_t \left(\frac{\partial^2 U}{\partial x^2} + \frac{\partial^2 U}{\partial y^2}\right) - \frac{gn^2 U\sqrt{U^2+V^2}}{H^{4/3}} \\
\frac{\partial V}{\partial t} + U\frac{\partial V}{\partial x} + V\frac{\partial V}{\partial y} &= -g\frac{\partial \eta}{\partial y} + \nu_t \left(\frac{\partial^2 V}{\partial x^2} + \frac{\partial^2 V}{\partial y^2}\right) - \frac{gn^2 V\sqrt{U^2+V^2}}{H^{4/3}}
\end{aligned} \tag{5.10}$$

In these equations (5.10), H is the water depth [m], η the position of the water surface from a reference [m] (see Figure 4.1), U and V respectively the stream wise and lateral velocity component [m/s].

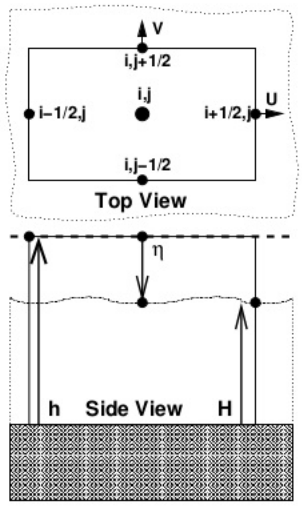

Figure 5.6: Schematisation of the grid and indication of the position where the variables are calculated. Figure from Martin (2004).

5.4.3 Grid

A rectangular, finite volume grid is used to solve the 2D-SWE (eq. 5.10). A staggered configuration of the variables, called the Arakawa-C grid, is used to discretise the equations. As indicated in Figure 5.6, the velocity components U and V are defined in the midpoints of the faces. The free surface elevation, η, is defined in the center point of each cell.

5.4.4 Numerical approximation

The continuity equation is discretised as written in Equation 5.11. The superscript N and $N+1$ represents the value of a variable at respectively the present time and a future time, Δt later than present. The subscript $i(+1/2), j(+1/2)$ represent the value of a variable at a certain position $i(+1/2), j(+1/2)$ on the grid.

$$
\begin{aligned}
\eta_{i,j}^{N+1} = \eta_{i,j}^{N} - \theta \frac{\Delta t}{\Delta x} & \left(H_{i+1/2,j}^{N+1} U_{i+1/2,j}^{N+1} - H_{i-1/2,j}^{N+1} U_{i-1/2,j}^{N+1} \right) \\
-\theta \frac{\Delta t}{\Delta y} & \left(H_{i,j+1/2}^{N+1} U_{i,j+1/2}^{N+1} - H_{i,j-1/2}^{N+1} U_{i,j-1/2}^{N+1} \right) \\
-(1-\theta) \frac{\Delta t}{\Delta x} & \left(H_{i+1/2,j}^{N} U_{i+1/2,j}^{N} - H_{i-1/2,j}^{N} U_{i-1/2,j}^{N} \right) \\
-(1-\theta) \frac{\Delta t}{\Delta y} & \left(H_{i,j+1/2}^{N} U_{i,j+1/2}^{N} - H_{i,j-1/2}^{N} U_{i,j-1/2}^{N} \right)
\end{aligned}
\tag{5.11}
$$

The value of H [m] on the faces can be calculated by an average from the calculated values in the cell centers or by the maximum value from the adjacent cell centers. Expression 5.11 is an implicit function, as on both sides of the equation unknowns of the next time step are present. The degree of implicitness can be changed by changing the value of θ. In case θ = 1, the method is called fully implicit, when θ is lower than 0.5 the method becomes unstable, for values between 0.5 and 1 the method is called semi-implicit.

The momentum equations in x and y direction are discretised, respectively in equations 5.12 and 5.13, where FU and FV are the Langrangian operators of the advection and diffusion terms (discussed in section 5.5).

$$
\begin{aligned}
U_{i+1/2,j}^{N+1} = FU_{i+1/2}^{N} - \theta \frac{g\Delta t}{\Delta x} \left(\eta_{i+1,j}^{N+1} - \eta_{i,j}^{N+1} \right) - (1-\theta) \frac{g\Delta t}{\Delta x} \left(\eta_{i+1,j}^{N} - \eta_{i,j}^{N} \right) \\
-gn^2 \Delta t \frac{\left[\left(U_{i+1/2,j}^{N} \right)^2 + \left(V_{i+1/2,j}^{N} \right)^2 \right]^{0.5}}{{H_{i,j}^{N}}^{4/3}} U_{i+1/2,j}^{N+1}
\end{aligned}
\tag{5.12}
$$

$$
\begin{aligned}
V_{i,j+1/2}^{N+1} = FV_{j+1/2}^{N} - \theta \frac{g\Delta t}{\Delta y} \left(\eta_{i,j+1}^{N+1} - \eta_{i,j}^{N+1} \right) - (1-\theta) \frac{g\Delta t}{\Delta y} \left(\eta_{i,j+1}^{N} - \eta_{i,j}^{N} \right) \\
-gn^2 \Delta t \frac{\left[\left(U_{i,j+1/2}^{N} \right)^2 + \left(V_{i,j+1/2}^{N} \right)^2 \right]^{0.5}}{{H_{i,j}^{N}}^{4/3}} V_{i,j+1/2}^{N+1}
\end{aligned}
\tag{5.13}
$$

Equations 5.12, 5.13 can be written in a more compact form, using variables G and A, as:

$$U_{i+1/2,j}^{N+1} = \frac{G_{i+1/2,j}^{N}}{A_{i+1/2,j}^{N}} - \theta\frac{g\Delta t}{\Delta x}\left(\eta_{i+1,j}^{N+1} - \eta_{i,j}^{N+1}\right)\frac{H_{i+1/2,j}^{N}}{A_{i+1/2,j}^{N}} \tag{5.14}$$

$$V_{i,j+1/2}^{N+1} = \frac{G_{i,j+1/2}^{N}}{A_{i,j+1/2}^{N}} - \theta\frac{g\Delta t}{\Delta y}\left(\eta_{i,j+1}^{N+1} - \eta_{i,j}^{N+1}\right)\frac{H_{i,j+1/2}^{N}}{A_{i,j+1/2}^{N}} \tag{5.15}$$

with A and G defined as:

$$A_{i+1/2,j}^{N} = H_{i+1/2,j}^{N} + gn^2\Delta t\frac{\sqrt{\left(U_{i+1/2,j}^{N}\right)^2 + \left(V_{i+1/2,j}^{N}\right)^2}}{H^{1/3}} \tag{5.16}$$

$$G_{i+1/2,j}^{N} = H_{i+1/2,j}^{N}FU_{i+1/2,j}^{N} - H_{i+1/2,j}^{N}(1-\theta)\frac{g\Delta t}{\Delta x}(\eta_{i+1,j}^{N} - \eta_{i,j}^{N}) \tag{5.17}$$

Substituting equations 5.14 and 5.15, with only the variable η as unknown at time step $N+1$, into equation 5.11 results in an equation with only one unknown variable η^{N+1} (eq. 5.18):

$$\begin{aligned}
\eta_{i,j}^{N+1} = \eta_{i,j}^{N} - \theta\frac{\Delta t}{\Delta x}\Bigg(& H_{i+1/2,j}^{N+1}\left[\frac{G_{i+1/2,j}^{N}}{A_{i+1/2,j}^{N}} - \theta\frac{g\Delta t}{\Delta x}\left(\eta_{i+1,j}^{N+1} - \eta_{i,j}^{N+1}\right)\frac{H_{i+1/2,j}^{N}}{A_{i+1/2,j}^{N}}\right] + \\
& H_{i-1/2,j}^{N+1}\left[\frac{G_{i-1/2,j}^{N}}{A_{i-1/2,j}^{N}} - \theta\frac{g\Delta t}{\Delta x}\left(\eta_{i,j}^{N+1} - \eta_{i-1,j}^{N+1}\right)\frac{H_{i-1/2,j}^{N}}{A_{i-1/2,j}^{N}}\right]\Bigg) - \\
& \theta\frac{\Delta t}{\Delta y}\Bigg(H_{i,j+1/2}^{N+1}\left[\frac{G_{i,j+1/2}^{N}}{A_{i,j+1/2}^{N}} - \theta\frac{g\Delta t}{\Delta x}\left(\eta_{i,j+1}^{N+1} - \eta_{i,j}^{N+1}\right)\frac{H_{i,j+1/2}^{N}}{A_{i,j+1/2}^{N}}\right] + \\
& H_{i,j-1/2}^{N+1}\left[\frac{G_{i,j-1/2}^{N}}{A_{i+1/2,j-1/2}^{N}} - \theta\frac{g\Delta t}{\Delta x}\left(\eta_{i,j}^{N+1} - \eta_{i,j-1}^{N+1}\right)\frac{H_{i,j-1/2}^{N}}{A_{i,j-1/2}^{N}}\right]\Bigg) \\
& -(1-\theta)\frac{\Delta t}{\Delta x}\left(H_{i+1/2,j}^{N}U_{i+1/2,j}^{N} + H_{i-1/2,j}^{N}U_{i-1/2,j}^{N}\right) \\
& -(1-\theta)\frac{\Delta t}{\Delta y}\left(H_{i,j+1/2}^{N}U_{i,j+1/2}^{N} + H_{i,j-1/2}^{N}U_{i,j-1/2}^{N}\right)
\end{aligned} \tag{5.18}$$

The algebraic set of equations results in a matrix of $i \cdot j$ unknown η_{ij}^{N+1} free surface values. This forms a penta-diagonal, positive matrix. The full matrix equation is given in Appendix C.1. Such a matrix can be efficiently solved using a preconditioned conjugate gradient method. The sparse matrix is written in a compressed sparse row format (CSR) consisting of three vectors: a vector with the values of the non-zero elements, a vector of column indices of these non-zero elements and a vector containing the positions of previous vectors where a new row starts (Saad, 1994). This matrix format is solved using the LINPACK-preconditioned conjugate gradient solver.

5.5 The Lagrangian operator

A characteristic of the TRIM methods is the use of a Lagrangian operator to represent the advective and eventually viscous terms. For this path tracing, an interpolation of the velocities from the surrounding, Eulerian grid points is used, why the method is called semi-Lagrangian. Consider first a general advection-diffusion equation in two space dimensions for a random variable c, given in equation 5.19:

$$\frac{\partial c}{\partial t} + u\frac{\partial c}{\partial x} + v\frac{\partial c}{\partial y} = \mu\left(\frac{\partial^2 c}{\partial x^2} + \frac{\partial^2 c}{\partial y^2}\right) \tag{5.19}$$

Equation 5.19, with $c(x, y, t)$, can be written as a total or substantial derivative:

$$\frac{dc}{dt} = \mu\left(\frac{\partial^2 c}{\partial x^2} + \frac{\partial^2 c}{\partial y^2}\right) \tag{5.20}$$

A simple, discretisation of equation 5.20 is given as:

$$\begin{aligned} \frac{c_{i,j}^{N+1} - c_{i-a,j-b}^{N}}{\Delta t} &= \mu\left(\frac{c_{i-a+1,j-b}^{N} - 2c_{i-a,j-b}^{N} + c_{i-a-1,j-b}^{N}}{\Delta x^2}\right) \\ &+\mu\left(\frac{c_{i-a,j-b+1}^{N} - 2c_{i-a,j-b}^{N} + c_{i-a,j-b-1}^{N}}{\Delta y^2}\right) \end{aligned} \tag{5.21}$$

Here, a and b are respectively defined as $(u\Delta t)/\Delta x$ and $(v\Delta t)/\Delta y$, which are local Courant numbers. Values of c at point (i, j) at a time $N + 1$ are related to values of c at a point $(i - a, j - b)$ at time N. The point $(i - a, j - b)$, which is presumably not located on a grid point, is located on a streamline passing through the point (i, j) at time $N + 1$. As the point $(i - a, j - b)$ is not located on a calculation point, the value of c should be obtained by interpolation. This process is clearly explained in Figure 5.7. The interpolation technique used to find $c_{i-a,j-b}$ will determine the accuracy, numerical diffusion and spurious oscillations (Casulli and Cheng, 1992).

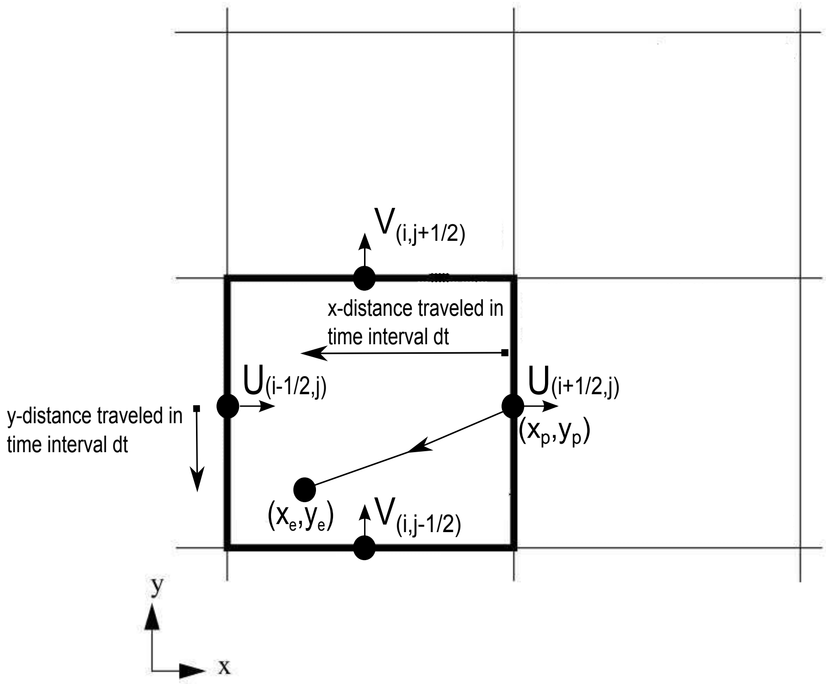

Figure 5.7: Schematisation of the path tracing on the grid . A backtracing curve is shown from a calculation node of the U- velocities (x_p, y_p) to an end point (x_e, y_e), reached after Δt. After Pollock (1994).

Several approaches can be followed for the path tracing, e.g. an Eulerian integration, a Runge-Kutta integration or semi-analytical integration methods (e.g. Pollock (1994)). Both Eulerian and Runge-Kutta methods are used in the developed model.

The Lagrangian operator, defined in eqs. 5.12 and 5.13, can be found as described in equation 5.22, with a and b determined by the Lagrangian path tracing.

$$\begin{aligned} FU^N_{i+1/2,j} &= U^N_{i+1/2-a,j-b} \\ +\nu_t\Delta t &\left(\frac{U^N_{i+1/2-a+1,j-b} - 2U^N_{i+1/2-a,j-b} + U^N_{i+1/2-a-1,j-b}}{\Delta x^2}\right) \\ +\nu_t\Delta t &\left(\frac{U^N_{i+1/2-a,j-b+1} - 2U^N_{i+1/2-a,j-b} + U^N_{i+1/2-a-1,j-b-1}}{\Delta y^2}\right) \end{aligned} \tag{5.22}$$

In this equation (eq. 5.22), a and b indicate the start position point of the path line of the particle, as indicated in Figure 5.7. The first term represents the role of the advection, the second and third term represent the role for the viscous effects in the x and y direction. A similar expression can be set up for the Lagrangian operator FV for the y momentum equation (5.13). As mentioned before, the local Courant numbers (a and b) are seldom integer values, and as such the values of $U^N_{i+1/2-a,j-b}$ and $V^N_{i-a,j+1/2-b}$ need to be interpolated. For the advection terms, both a bi-linear and bi-cubic Lagrangian interpolation is implemented. For the bi-linear interpolation of a variable Φ, the following relation is used (eq. 5.23).

$$\Phi_f = \alpha_1\Phi_{downw} + \alpha_2\Phi_{upw} \tag{5.23}$$

where Φ_{upw} and Φ_{downw} are respectively the value of the variable under consideration upwind and downwind from the point f. The weighing coefficients α_1 and α_2 are defined as:

$$\alpha_1 = \frac{X_{downw} - X_f}{X_2 - X_1} \tag{5.24}$$

$$\alpha_2 = \frac{X_f - X_{upw}}{X_1 - X_2} \tag{5.25}$$

(5.26)

with X_1, X_2 the position of Φ_{upw} and Φ_{downw} (on the grid) and X_f the position of the variable Φ_f which should be estimated. For the bi-cubic Lagrangian interpolation, a symmetric interpolation scheme is used. The implemented coefficients are, following Manson et al. (2001):

$$\Phi_f = \alpha_0 \Phi_{downw,2} + \alpha_1 \Phi_{downw} + \alpha_2 \Phi_{upw} + \alpha_3 \Phi_{upw,2} \tag{5.27}$$

with α_0, α_1, α_2, α_3 defined as:

$$\alpha_0 = \frac{(X_f - X_1)(X_f - X_2)(X_f - X_3)}{(X_0 - X_1)(X_0 - X_2)(X_0 - X_3)} \tag{5.28}$$

$$\alpha_1 = \frac{(X_f - X_0)(X_f - X_2)(X_f - X_3)}{(X_1 - X_0)(X_1 - X_2)(X_1 - X_3)} \tag{5.29}$$

$$\alpha_2 = \frac{(X_f - X_0)(X_f - X_1)(X_f - X_3)}{(X_2 - X_0)(X_2 - X_1)(X_2 - X_3)} \tag{5.30}$$

$$\alpha_3 = \frac{(X_f - X_0)(X_f - X_1)(X_f - X_2)}{(X_3 - X_0)(X_3 - X_1)(X_3 - X_2)} \tag{5.31}$$

(5.32)

For the diffusion terms a bi-linear interpolation for the velocities is used. An explicit implementation is implemented as well in the model. An overview of the implementation of the advective and viscous terms in the model is given in Table 5.1.

Table 5.1: Overview of the options implemented for the calculation of the Lagrangian trajectory (LT), the advection and diffusion terms.

Lagrangian trajectory	Euler integration
	Runge-Kutta (4th order)
Advection	LT - Bi-linear
	LT - Bi-cubic
Diffusion	LT - Bi-linear
	Explicit

5.6 Boundary conditions

5.6.1 Options for boundary conditions

At the edges of the grid domain, boundary conditions should be imposed. At the upstream side, a closed boundary condition, which does not allow flow through the domain edge and an open boundary condition, which allows flow through the domain edge can be selected. Only a Dirichlet boundary condition, which sets a specific boundary condition value, is available at the upstream end for the following variables:

- Flux $[\mathrm{m^3/s/m}]$
- Velocity $[\mathrm{m/s}]$

- Depth $[\mathrm{m}]$

At the downstream side, a closed boundary condition and an open, Dirichlet boundary condition for the following variables can be selected:

- Velocity $[\mathrm{m/s}]$
- Depth $[\mathrm{m}]$

5.6.2 Boundary corrections

As the implementation of patches in the model, generated small perturbations of the water surface (small waves) which were reflected at the downstream boundary, some measures needed to be implemented to avoid the reflection of these oscillations into the computational domain. Two methods were implemented, namely the use of an analytical solution at the downstream boundary, which is weighing increasingly towards the downstream boundary and a sponge layer, meaning a zone at the downstream reach where the viscosity value is (artificially) increased to damp the oscillations.

5.6.2.1 Analytical solution

A first method discussed, is the merging of an analytical soluation with the computed solution at the downstream end of the grid domain. For this type of downstream boundary treatment, the methodology of Afshar (2010) was followed. In a part of the domain, the relaxation zone, the computed solution is modified according to a desired analytical solution. These analytical solutions are calculated backwater-curves, calculated with the model with the same parameter and boundary conditions as the situation under study, but without a heterogeneous friction matrix. The velocity (stream wise and lateral) and water height in the relaxation zone are calculated as:

$$\begin{aligned} U &= C(x)U_{computed} + (1 - C(x))U_{analytical} \\ V &= C(x)V_{computed} + (1 - C(x))V_{analytical} \\ \eta &= C(x)\eta_{computed} + (1 - C(x))\eta_{analytical} \end{aligned} \tag{5.33}$$

with $C(x)$ a weighting coefficient depending on the longitudinal position of the domain, and x a normalised coordinate ranging between 0, at the beginning of the relaxation zone, and 1 at the end of this zone. Afshar (2010) proposes equation 5.34 for the weighing coefficient C.

$$C(x) = 1 - x^6 \tag{5.34}$$

This function was derived for wave generation, but showed to be effective to damp the oscillations due to a patch presence too (see Chapter 7).

5.6.2.2 Sponge layer

At the end of the domain, the diffusivity is increased artificially, by increasing the value of ν_t. Using such increased diffusivity, oscillations and gradients can be damped efficiently. It should be mentioned that, in the part of the domain where the value of ν_t is adapted, this value has no reference anymore to a physical background. Obviously, the (maximum) selected value for ν_t has to be below the maximum value to obtain stable calculations.

5.7 Stability criteria

The stability of the method is depending on the choice of the explicit advection operator F, which is used to solve the advective and viscous terms. In other words if F is stable, the model is stable. For F, a semi-Lagrangrian approach is selected which results in the following stability criterion:

$$\Delta t \leq \left[2\nu_t\left(\frac{1}{\Delta x^2}+\frac{1}{\Delta y^2}\right)\right]^{-1} \tag{5.35}$$

In other words, the stability is independent of the advection terms, only the viscous terms (coefficient) have an influence (Casulli, 2012). For advection dominated problems, this restriction is less restrictive than the CFL criterion for explicit schemes (Casulli, 2012).

5.8 Implementation of vegetation

The implementation of vegetation in the model is discussed in Chapter 6

5.9 Implementation of the numerical method

In Figure 5.8 the flow chart of the basic structure of the model is shown, using two basic packages of STRIVE, namely the SYSTEM module and the TRANSWATER module. This structure is following the main structure of FEMME. For the main module, namely the Dynamics module, the flow chart is given in Figure 5.9, a more detailed pseudo-code is presented in Appendix C.2.2.1.

5.10 Basic validation of the model

5.10.1 Conservation of mass

The conservation of mass is described in the continuity equation, and as such also the numerical method should be mass conservative. This was checked for all runs.

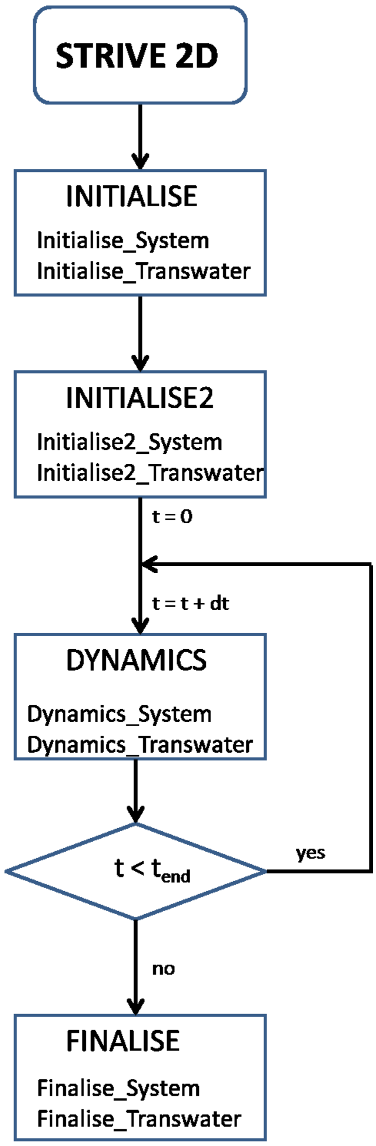

Figure 5.8: Flow chart of the basic structure of STRIVE2D.

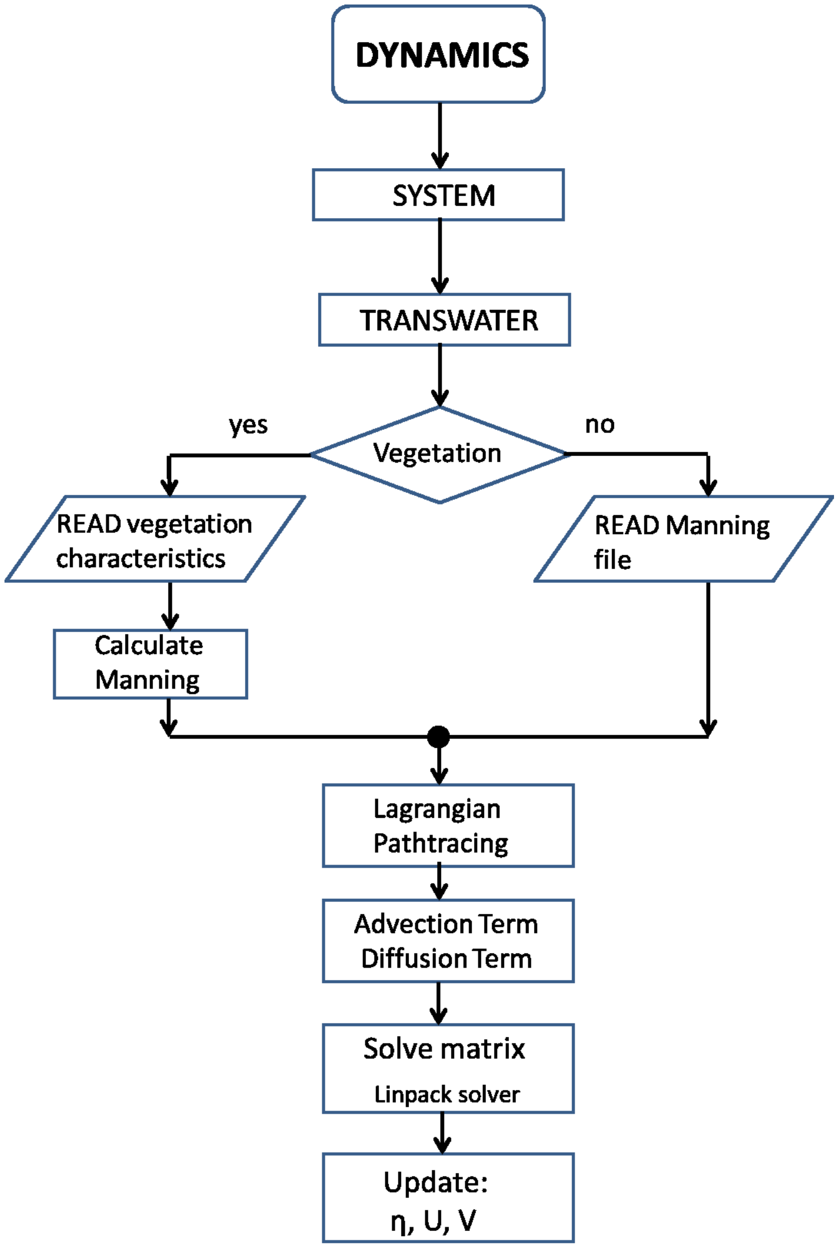

Figure 5.9: Flow chart of the Dynamics module of STRIVE2D with two modules implemented: the System and Transwater module.

5.10.2 Backwater curves

Table 5.2: Overview of a backwater curve calculation. The reach has a length of 1350 m and a width of 15 m, the Manning coefficient of 0.1 $\mathrm{s/m^{1/3}}$ is constant over the reach. S_0 is the bottom slope [m/m], Z_{up} the upstream water level [m], Z_{down} the downstream water level [m], Q_{2D} the discharge calculated with the 2D-model, Q_{1D} the discharge calculated with the 1D-model.

Case	S_0 [m/m]	Z_{up} [m]	Z_{down} [m]	Q_{2D} [m^3/s]	Q_{1D} [m^3/s]
1	0.0000	**1.094**	0.56	*2.353*	2.14
	0.0000	*1.046*	0.56	**2.14**	2.14
2	0.0002	**1.094**	0.56	*3.075*	2.81
	0.0002	*1.045*	0.56	**2.81**	2.81

The model was validated for several backwater curves, which were also used to test the 1D-hydraulic module for STRIVE (De Doncker, 2008). The considered reach has a length of 1350 m and a width of 15 m, the Manning coefficient of 0.1 $\mathrm{s/m^{1/3}}$ is constant over the reach. In Table 5.2 an overview of the performed simulations is given, in bold the chosen boundary condition is indicated, in italic the resulting value calculated by the model. It can be seen in Table 5.2 that the discharge calculated in the 2D model is always larger compared to the 1D model. Consistent with this, the observed upstream water height is smaller. It can be concluded that the flow is experiencing less resistance, despite the same Manning coefficient, 0.1 $\mathrm{s/m^{1/3}}$ in both simulations. As indicated in Chapter 6, the Manning coefficient in 1D- and 2D hydraulic models are not identical.

5.11 Conclusion

An overview of discretisation methods to solve the 2D-SWE is given in this Chapter. The selected discretisation method, a Semi-Implicit, Semi-Lagrangian method indicated by 'TRIM' model, is explained in detail. Its implementation in the STRIVE model, together with the implemented options for the different processes, is indicated.

6
Resistance of Vegetation

6.1 Introduction

An important term in the Shallow Water Equations is the bed friction term, which accounts for flow resistance. However, vegetation has a big influence on flow resistance in rivers, and therefore a good description of the vegetation roughness is very important. Several methods have been proposed and an overview of approaches to account for vegetative roughness is presented in this chapter. Furthermore, a selection of studies is discussed, in which the 2D-SWE are used for vegetated flows, focusing on small patches of vegetation rather than large vegetated zones as e.g. floodplains. The overview in this chapter is used to select an appropriate resistance model for vegetation within the STRIVE ecosystem model.

6.2 Flow resistance

For a given boundary surface, which may be a rigid surface (e.g. concrete), a mobile surface (e.g. a sand bed) or a flexible surface (e.g. vegetation), the energy losses in a given reach leading to a flow resistance arise from near-boundary turbulence and macro-flow structures in that reach (Morvan et al., 2008). Following Rouse (1965), flow resistance can be classified into four different components (Yen, 2002), which are enumerated distinctly here, but are related elements:

1. surface or skin friction (e.g. surface texture, grain roughness)

2. form resistance or drag (e.g. surface geometry, bed forms, flow separation)

3. wave resistance from free surface distortion

4. resistance associated with local acceleration or flow unsteadiness

The resistance can be expressed as a dimensionless, symbolic function:

$$F(Re, K, \eta, N, Fr, Un) \tag{6.1}$$

where Re the Reynolds number [-], K the relative roughness (k_s/R) [-] with k_s the Nikuradse equivalent sand roughness [m] and R the hydraulic radius [m]. η is the cross-sectional geometric shape [-], N non-uniformity of the channel [-], Fr the Froude number [-] and Un the degree of flow unsteadiness [-]. Rouse (1965) states that the Moody diagram is a special case of function 6.1, for straight, constant pipes in steady uniform flow, with only two of the six parameters (Re, k_s/R) retained.

6.3 Flow resistance equations

From a practical engineering point of view, in the 18th and 19th century, several relationships to account for the resistance have been established empirically. One of the earliest equations linking the discharge in an open channel to a resistance coefficient, is that of Chézy, A. (1768):

$$Q = CA\sqrt{RS} \tag{6.2}$$

$$V_a = C\sqrt{RS} \tag{6.3}$$

where Q is the discharge [m^3/s], A the wetted area [m^2], R the hydraulic radius [m], V_a the mean channel velocity [$\mathrm{m/s}$], S the energy slope [m/m] and C the Chézy coefficient [$\mathrm{m}^{1/2}/\mathrm{s}$]. Another resistance coefficient is the Darcy-Weisbach resistance coefficient f [-], defined as in equations 6.4 and 6.5.

$$Q = \sqrt{\frac{8g}{f}}A\sqrt{RS} \tag{6.4}$$

$$V_a = \sqrt{\frac{8g}{f}}\sqrt{RS} \tag{6.5}$$

Yet, another relationship linking a resistance coefficient to flow and geometry parameters, and probably the most widespread in open-channel hydraulics was given by Manning (1891), where the Manning coefficient is used as resistance factor n [s/m$^{1/3}$].

$$Q = \frac{AR^{2/3}\sqrt{S}}{n} \tag{6.6}$$

$$V_a = \frac{R^{2/3}\sqrt{S}}{n} \tag{6.7}$$

The different resistance coefficients, defined in equations 6.3, 6.5, 6.7, can be linked as follows:

$$C = \sqrt{\frac{8g}{f}} = \frac{R^{1/6}}{n} \tag{6.8}$$

Yen (2002) states that there is no clear theoretical advantage of one coefficient over the others, as they can be easily related (equation 6.8). As the Manning coefficient n is implemented in the model because previous studies concerning vegetative resistance in the Hydraulics Lab used this as resistance parameter, we are mainly focusing on this expression as resistance coefficient. Computation or measurements in open-channels can be made reach by reach, cross-section to cross section or even point-by-point, and the resistance coefficient should be determined accordingly. This range of spatial scales is shown in Figure 6.1 (Yen, 2002).

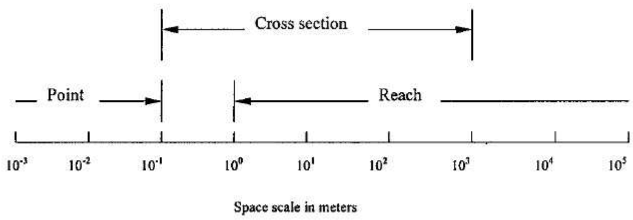

Figure 6.1: Point, cross-section and reach resistance space scales. From Yen (2002).

The resistance coefficients account for the dissipation of energy and momentum which is not explicitly implemented in the simplified formulae, as such it does not appear explicitly in the 3D Navier-Stokes equations (Morvan et al., 2008). However it appears in the 2D and 1D Shallow Water Equations, however not the same physical processes are modeled explicitly in 1D and 2D shallow water models. Therefore, using the same friction factor in both models may result in different results. In a 1D framework, the resistance parameter is used to represent the shear stress exerted by the bed and the banks (see eq. 6.9, rewritten from equation 6.7), as is clear in the definition because of the use of the hydraulic radius R, defined as the wetted area (A) divided by the wetted perimeter (P). However, in a depth-averaged, 2D model framework, the friction factor is used to represent the shear stress exerted at the base of a vertical water column (Morvan et al., 2008), with the water depth H used in definition 6.10 in stead of the hydraulic radius R.

$$S_x = \frac{n^2 V_a^2}{R^{4/3}} \tag{6.9}$$

$$S_x = \frac{n^2 U \sqrt{U^2 + V^2}}{H^{4/3}} \tag{6.10}$$

6.4 Energy losses caused by vegetative elements

Before an overview of methods used to describe vegetation roughness is given, it should be asked how vegetation is causing (extra) resistance in a river reach. Vegetation is not only an extra resistance in river reaches, not seldom it is the main source of flow resistance (Baptist et al., 2007; Green, 2005; Luhar and Nepf, 2013). Obstacles placed in a flow experience drag, which can be split into form- and friction-drag (Folkard, 2011; Kundu et al., 2012). Form drag is originating from normal forces, a reduced pressure is observed at the downstream side of the object (here vegetation) because of flow separation. Tangential forces at the surfaces are causing the friction drag. Following the physical law of action-reaction (Newton's third law), the vegetation applies an equal force on the flow, and as such a "resistance" is experienced by the flow due to these obstacles. Luhar and Nepf (2013) and Folkard (2011) define three different, important scales: the blade & shoot scale, the patch scale and the reach scale. The relative importance of the scales is dependent on flow characteristics, bio-mechanical characteristics of the vegetation stand (sparse, dense) and the geometrical distribution of patches in the river reach.

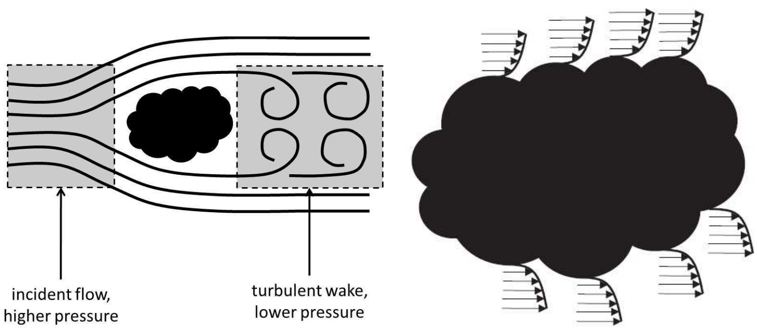

(a) (b)

Figure 6.2: Patches placed in a flow, experiencing (a) form drag and (b) viscous drag. Taken from Folkard (2011).

As mentioned, flow around vegetation canopies, patches or stems can be complex, and the physical processes contributing to the dissipation of energy intertwining. As such, the description of thé roughness coefficient for vegetation is a difficult task. In the following section, an overview is given of the different frameworks to characterise vegetation resistance, together with its main assumptions and limitations. As numerous studies on vegetation resistance can be found in literature, it was the aim to give an overview of different approaches used, rather than a summation of all available publications.

6.5 Resistance and vegetation: an overview

In the following section, different approaches to account for vegetative resistance in models are considered. In general, these approaches start from a theoretical basic concept and use additional parameters which are calibrated in an empirical way.

6.5.1 Splitting the resistance into components

Many authors (eg. Cowan (1956)) splitted the channel resistance into several terms, where every term represents a physical phenomenon responsible for resistance (De Doncker, 2008; Knight et al., 2010). Accordingly, the Manning coefficient n, as defined in equation 6.7, can be splitted:

$$n = (n_b + n_1 + n_2 + n_3 + n_4) \cdot m \tag{6.11}$$

where

n_b = Manning coefficient for basic roughness value, for a straight, uniform channel (0.020 - 0.028 s/$\mathrm{m}^{1/3}$)

n_1 = Manning coefficient for bottom irregularities (0 - 0.020 s/$\mathrm{m}^{1/3}$)

n_2 = Manning coefficient for channel geometry variations (0 - 0.015 s/$\mathrm{m}^{1/3}$)

n_3 = Manning coefficient for obstacles (0 - 0.060 s/$\mathrm{m}^{1/3}$)

n_4 = Manning coefficient for vegetation

m = correction factor for meandering (1 - 1.3)

where the indicated values for n are found in De Doncker (2008). It should however be mentioned that this partitioning is somewhat artificial, as the different components will influence each other and they are difficult to be measured separately. Studies looking to characterise the vegetative resistance are often performed in straight, channels or flumes without other obstacles, to isolate as much as possible the effect of the vegetation on the resistance. In this way, equation 6.11 can be reduced and rewritten as follows:

$$n_4 = n - n_b \tag{6.12}$$

Some authors used other, alternative versions of this equation, e.g. Morin (2000) notes

$$n^2 = n_b^2 + n_4^2 \tag{6.13}$$

There are several ways to estimate the resistance coefficient n, or particularly the resistance due to vegetation n_4. Below, an overview is given how these different terms, albeit together or seperated, are estimated based on measurements, experience or theoretical derivations.

6.5.2 Experience, tables and photographs

Based on simple descriptions of rivers, resistance used to be estimated using tables (Chow, 1959; Green, 2005; Henderson, 1966; Knight et al., 2010). In Table 6.1 an overview is given of Manning values for flow with vegetation elements, given in Chow (1959), but many other look-up tables can be found (Yen, 1991). A maximum value is found of 0.120 $\mathrm{s/m^{1/3}}$, which is much lower than the values found by De Doncker et al. (2009) (where values up to 0.5 $\mathrm{s/m^{1/3}}$ are found for the Bierbza river (Poland) and up to 0.4 for the river Aa (Belgium)) and many others. Another, very empirical way to estimate roughness is the use of photographs of rivers with a well known roughness value. A photograph of a river reach, for which the roughness coefficient is known, is taken and used as a reference (Figure 6.3). It should be noted that the use of such tables or figures is subjective, and the accuracy will be very dependent on the knowledge (of the local field) and experience of the hydraulic engineer.

Table 6.1: Reference tables for Manning's n values $[\mathrm{s/m^{1/3}}]$ from Chow (1959). A selection for channels with vegetative flow involved is made. For each case, a minimum, mean and maximum Manning value is indicated.

Type of Channel and Description	**Min**	**Mean**	**Max**
1. Main Channels (< 30 m width)			
a. clean, straight, full stage, no rifts or deep pools	0.025	0.03	0.033
b. same as above, but more stones and weeds	0.03	0.035	0.04
c. sluggish reaches, weedy, deep pools	0.05	0.07	0.08
d. very weedy reaches, deep pools, or floodways with heavy stand of timber and underbrush"	0.075	0.1	0.15
2. Excavated or Dredged Channels			
a. Earth, straight, and uniform			
1. clean, recently completed	0.016	0.018	0.02
2. clean, after weathering	0.018	0.022	0.025
3. gravel, uniform section, clean	0.022	0.025	0.03
4. with short grass, few weeds	0.022	0.027	0.033
b. Earth winding and sluggish			
1. no vegetation	0.023	0.025	0.03
2. grass, some weeds	0.025	0.03	0.033
3. dense weeds or aquatic plants in deep channels	0.03	0.035	0.04
4. earth bottom and rubble sides	0.028	0.03	0.035
5. stony bottom and weedy banks	0.025	0.035	0.04
6. cobble bottom and clean sides	0.03	0.04	0.05
c. Dragline-excavated or dredged			
1. no vegetation	0.025	0.028	0.033
2. light brush on banks	0.035	0.05	0.06
3. Floodplains			
a. Pasture, no brush			
1. short grass	0.025	0.03	0.035
2. high grass	0.03	0.035	0.05
b. Cultivated areas			
1. no crop	0.02	0.03	0.04
2. mature row crops	0.025	0.035	0.045
3. mature field crops	0.03	0.04	0.05
c. Brush			
1. scattered brush, heavy weeds	0.035	0.05	0.07
2. light brush and trees, in winter	0.035	0.05	0.06
3. light brush and trees, in summer	0.04	0.06	0.08
4. medium to dense brush, in winter	0.045	0.07	0.11
5. medium to dense brush, in summer	0.07	0.1	0.16
d. Trees			
1. dense willows, summer, straight	0.11	0.15	0.2
2. cleared land with tree stumps, no sprouts	0.03	0.04	0.05
3. same as above, but with heavy growth of sprouts	0.05	0.06	0.08
4. heavy stand of timber, a few down trees, little undergrowth, flood stage below branches"	0.08	0.1	0.12
5. same as 4. with flood stage reaching branches	0.1	0.12	0.16

Figure 6.3: Photograph of river, as an example to estimate Manning's roughness, here n = 0.023 s/m$^{1/3}$ is indicated. From Soong et al. (2012).

6.5.3 The n-VR relationship

For a uniform canopy of grass-like vegetation, empirical n-VR relations have been established. Palmer (1945) proposed this relation between the velocity V and the hydraulic radius R to predict the Manning roughness coefficient n, given the knowledge of vegetation bending in function of the flow. Different regimes are recognised, which are depicted in Figure 6.4 and can be explained as follows (after Folkard (2011); Green (2005)):

1. vegetation is not deflected
2. orientation of stems and leaves downstream
3. vibration of vertical stems, sinuously moving of oblique and horizontal stems
4. stiff stems incline, further downstream orientation of submerged leaves, loss of dead parts
5. stems become densely compacted, surface leaves are submerged
6. damage and uprooting of (a part of) the plant

These n-VR relationships were established for flexible, grass-like vegetation. Due to the empirical nature of the n-VR relationship, Kouwen et al. (1981) claimed that the n-VR method is not valid if the vegetation is short and stiff.

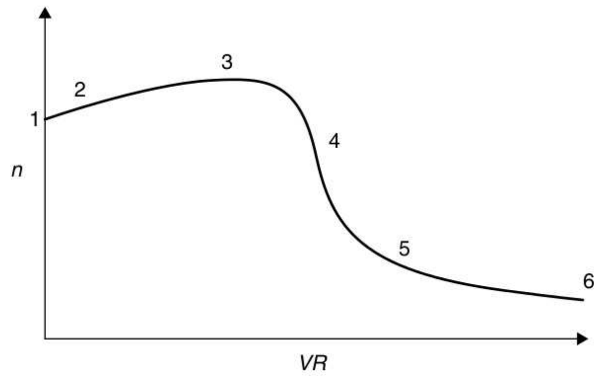

Figure 6.4: The relation of the Manning coefficient n with the product of V and R (after Folkard (2011); Green (2005)).

6.5.4 Relation between vegetation biomass and Manning coefficient

The vegetation biomass is defined here as the amount of mass of above-ground plant material per unit area and is expressed in kg/m^2. It is clear from previous section that a positive relation between the biomass and the Manning coefficient could be obtained, as more plant material will result in an increased blockage of the flow. Dawson (1978) found a relation between the biomass (for *Ranunculus penicillatus*) and the flow resistance as:

$$n = n_b \left(1 + 0.0143 \cdot 10^{-3} \cdot biomass\right) \tag{6.14}$$

However, it has been found, eg. De Doncker et al. (2009), that the Manning coefficient will not only vary with biomass, but also with the discharge Q. De Doncker et al. (2009) fitted a curve with variables Q and $biomass$ (eq. 6.15), based on field measurements.

$$n = 0.169 + \frac{0.1568}{Q} - 0.1593 \exp^{(-0.0047 \cdot biomass)} \tag{6.15}$$

This inverse relationship with the discharge Q is probably also due to the bending of the vegetation with increased velocities, and as such analogue with the $n - VR$ curves. However, these experimental data will be very dependent on the field study area and the present vegetation. Its generality is therefore questionable and such relations may not be applied straight on for other situations. The advantage however, is that in many biological studies the biomass is measured, as it is a basic parameter, and therefore this information is often available, even over a vegetation growth season.

6.5.5 Blockage factors

The macrophyte biomass, which changes over the vegetative season, can be linked to a hydraulic resistance by empirical formulae. In these approaches however, the vegetation is considered as uniform, which is mostly not the case in the field (Green (2006); Sukhodolov and Sukhodolova (2010),...). Green (2006) tried to set up a framework to incorporate the spatial variability on the global channel resistance, using the blockage factor B and a cross-sectional spatial variability parameter T as predictive variables. The blockage factor B for a cross-section with a wetted cross-section A $[\mathrm{m}^2]$ and a blocked wetted cross-section by vegetation A_v $[\mathrm{m}^2]$, can be defined as:

$$B = \frac{A_v}{A} \tag{6.16}$$

However, several types of blockage factors have been defined previously: the cross-sectional blockage factor, B defined as the proportion of one or several cross-sections blocked by macrophyte stands, the surface area blockage factor, B^{SA} defined as the proportion of the surface area of a study reach containing vegetation and volumetric blockage factor, B^{V} defined as the proportion of the volume of a study reach blocked. Green (2005) found relations very close to one between all these types of blockage factors. Green (2005) presents, for sites with *Ranunculus*, a regression equation between B and a resistance component n_4, defined in equation 6.12, as:

$$n_4 = 0.0043B_{WM} - 0.0497 \left(R^2 = 65.8\%\right) \tag{6.17}$$

where B_{WM} is the weighted median of the blockage factor in several cross-sections. This approach, however, only takes into account the exlusion of flow due to macrophyte stands. The spatial distribution, however, is not included. Green (2006) tried to incorporate this by adding an additional variable T, the vegetation cross-sectional spatial variability parameter T, defined as:

$$T = \frac{WP_e}{WP} \tag{6.18}$$

where WP is the length of the solid boundary [m] and WP_e the effective wetted perimeter [m]. The distinction between both is clearly shown in Figure 6.5, as WP is the sum of the solid boundaries of the channel bed itself whereas WP_e is the sum of the vegetation edges and solid boundaries, subjected to flowing water. Scattered vegetation will result in a value of T much higher than 1, for clumped vegetation WP_e will be close to or even smaller than WP, resulting in a value of T smaller than 1. As the generation of turbulence is occuring at boundaries, where shear stress is maximal, reaches with longer boundaries (T $>$ 1) are expected to show higher resistance factors.

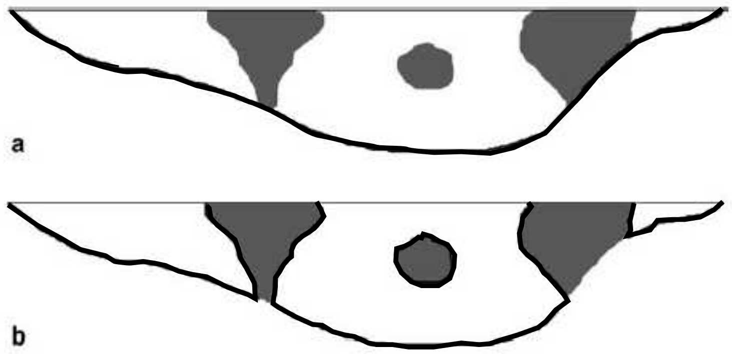

Figure 6.5: A schematised, representative cross-section occupied with vegetation patches. The shaded areas represent macrophytes. The thick line indicates the wetted perimeter as defined: (a) Conventionally (b) Effective wetted perimeter. From Green (2006).

Using both the definition of blockage (Equation 6.16) and T (Equation 6.18) an exponential fit was found for the Manning's vegetation component (Green, 2006):

$$n_4 = 0.0432e^{0.0281B_{69}} + 0.1361T_{16} - 0.205 \tag{6.19}$$

where B_{69} and T_{16} respectively the 69th percentile of the distribution of B for all cross-sections and the 16th percentile for the variable T. An overview of empirical relations between the blockage factor B and the Manning coefficient is given in Table 6.2. Except for a positive correlation between B and n (or n_4), no clear trends in these empirical fits could be distinguished. Both exponential and linear fits have been used, with in general strong correlations. Luhar et al. (2008) theoretically derived a non-linear relationship: namely $n \sim (1 - B)^{-1}$.

6.5.6 Velocity profiles

Many efforts have been done to reveal the flow structure in case of submerged vegetation (Kouwen and Unny, 1969; Stephan and Gutknecht, 2002) based on Prandtl's logarithmic velocity profile, for boundary layers, as in equation 6.20.

$$\frac{u}{u^*} = \frac{1}{\kappa} ln\left(\frac{z - d_p}{k_p}\right) + C \tag{6.20}$$

In this equation, u^* is the shear velocity [m/s], κ the von Kàrmàn constant [-], d_p a zero plane displacement, k_p [m] a roughness parameter for plants and C an integration constant. Many variations on this equation and expressions for k_p have been proposed, summarised by Stephan and Gutknecht (2002). Recent works have considered a separate vegetation and upper layer (or even more detailed divisions are made), describing an average velocity for each layer. If the depth-averaged

Table 6.2: Overview of empirical relations between the blockage factor B [-] and Manning coefficient n $[\mathrm{s/m^{1/3}}]$ or n_4 $[\mathrm{s/m^{1/3}}]$ for different studies. If provided, the vegetation type and the coefficient of determination R^2 are presented also.

Dominant vegetation type	Regression	R^2	Reference
Ranunculus sp.	$n_4 = 0.0043B_{WM} - 0.0497$	$R^2 = 0.66$	Green (2005)
Egeria densa; Potamogetum crispa sp.	$n = 0.0033 + 0.0048B$	$R^2 = 0.61$	Champion and Tanner (2000)
-	$n = 0.0337 + 0.0239(B^{SA}/VR)$	-	Wright et al. (1981.)
-	$n = 0.024 + 0.0012\ B$	$R^2 = 0.85$	Bakry (1996)
emergent vegetation	$n = 0.032 + 0.12\ B$	$R^2 = 0.345$	Bakry et al. (1992)
emergent vegetation	$n = 0.049 + .0072\ B$	$R^2 = 0.2$	Bakry et al. (1992)
emergent vegetation	$n = 0.036 + .067\ B$	$R^2 = 0.62$	Bakry et al. (1992)
Callitriche sp., Myriophyllum sp., Elodea Canadensis	$n = 0.025 \cdot \exp^{(3.0\frac{k}{H}B)}$	$R^2 = 0.89$	Nikora et al. (2008)
-	$n = \frac{0.0343}{(1-B)+0.0016}$	-	Pitlo (1989)

velocity is known in function of vegetative characteristics as stem density, vegetation height,..., a resistance coefficient based on these properties can be calculated using the Manning or Chézy equation (eq. 6.7 or 6.3)

6.5.6.1 Two-layer approach

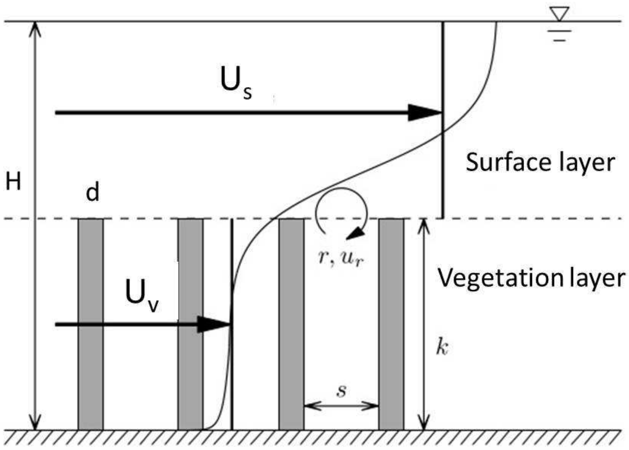

Figure 6.6: Schematised vertical profile for a submerged vegetation canopy, representing a 2-layer approach. Figure from Huthoff et al. (2007) and Baptist et al. (2007)

For emergent canopies, only a vegetation layer is observed, as the vegetation occupies the whole water depth. For submerged vegetation canopies however, the flow depth can be divided into a vegetated and non-vegetated layer, named surface layer, as indicated in Figure 6.6. Therefore, these methods are called two-layer methods here.

When vegetation is present, the drag exerted by the roughness elements is not limited to the solid boundary (the bed), but extends over the total height of the plant, with a maximum of the total flow depth in case of emergent vegetation. The force balance between gravitation and flow resistance, which leads to an equilibrium flow state, can be expressed as:

$$\tau_{total} = \tau_b + \tau_v \tag{6.21}$$

with τ_b the bottom shear stress $[\mathrm{N/m^2}]$ and τ_v the vegetation shear stress $[\mathrm{N/m^2}]$. Expressing both the bottom shear stress and total shear stress for fully-developed flow, results in equation 6.22,

$$\rho g H i = \rho f U^2 + \tau_v \tag{6.22}$$

with ρ the mass density $[\mathrm{kg/m^3}]$, g the gravitational constant $[\mathrm{m/s^2}]$, H the water depth [m], i the water slope [m/m] and f a friction factor [-]. The depth-averaged velocity U can be calculated as a weighted average of the velocity profiles over the entire flow depth.

$$U = \frac{k}{H}U_v + \frac{H-k}{H}U_s \tag{6.23}$$

For every layer, both the surface and vegetation layer, the respective velocity U_v and U_s can be calculated. If the vegetation extends above the water surface ($k > H$), the last term of equation 6.23 dissapears, as U_s is not defined. In this way, a unifying framework for emergent and submerged vegetation can be obtained. The theoretical approaches (and assumptions) to predict the velocity in the different layers are explained below.

6.5.6.2 Vegetation layer

Both in the work of Stone and Shen (2002), Baptist et al. (2007) and Huthoff et al. (2007) the vegetation is considered as a homogeneous field of identical cylinders, in a random or staggered array. The vegetation resistance force per unit of area τ_v $[\mathrm{N/m^2}]$ is expressed as a standard drag force term,

$$\tau_v = \frac{1}{2}\rho C_D m d k U_v^2 \tag{6.24}$$

with C_D the drag coefficient [-], m the number of stems per unit area $[1/\mathrm{m}^2]$, d the diameter of the individual stems [m], k the vegetation height [m] and U_v [m/s] the depth-averaged flow through the vegetation.

Some authors, e.g. Stone and Shen (2002), use a slightly different approach. In stead of using the average vegetation flow U_v, the maximum velocity U_{vm} in the vegetation layer is used. This maximum velocity U_{vm} takes into account the volume taken by the vegetation stems and can be related to U_v by simple mass continuity, as:

$$U_v = U_{vm}(1 - d\sqrt{m}) \tag{6.25}$$

For the emergent cases ($k > H$), the depth-averaged velocity U is independent of the flow depth. In many studies to estimate vegetation resistance, the drag of the bed is assumed negligible compared to the drag by the vegetation. Substituting equation 6.24 to estimate vegetation resistance in equation 6.22, and omitting the bed shear term, results in respectively equation 6.26 and 6.27. Both an expression of U_v or U_{vm} can be used, explaining the difference between equation 6.26 and 6.27.

$$U_v = \sqrt{\frac{2g}{C_D m d k}}\sqrt{Hi} \tag{6.26}$$

$$U_{vm} = \sqrt{\frac{2g(1-c)}{C_D m d k}}\sqrt{Hi} \tag{6.27}$$

By linking the expression of the velocity with one of the traditional roughness equations, an estimation of the channel conveyance can be found. The bed stress is not taken into account here, as in many (experimental) studies, because this bed friction is considered very small compared to the vegetation resistance (eg. in the experiments of Stone and Shen (2002) they were estimated < 3 %).

6.5.6.3 Surface layer

To estimate the surface layer velocity profile and its derived depth-averaged value, several approaches can be used. An overview of the different methods, together with their differences, is given below.

Stone and Shen (2002) hypothesize a relation between the maximum velocity in the vegetation layer U_{vm} and the depth-averaged velocity U as follows:

$$U_{vm} = \frac{F_v}{1 - d\frac{k}{H}\sqrt{m}}U \tag{6.28}$$

with F_v a function which is expected to be dependent on Re, k/H, m and λ, defined as the area concentration of stems.

$$\frac{U_v}{U} = F_v\left[\frac{1 - d\sqrt{m}}{1 - d\frac{k}{H}\sqrt{m}}\right] \tag{6.29}$$

F_v should satisfy the physical restriction that $U_v \to U$ when $k \to H$, and as such F_v should equal 1 in this limit. By fitting equation 6.29 with experiments, a relationship is found to estimate F_v (eq. 6.30).

$$F_v = \sqrt{\frac{k}{H}} \tag{6.30}$$

It should be noted that Stone and Shen (2002) use the volumetric concentration of vegetation c in their derivation.

A different procedure is used in Huthoff et al. (2007), however, still a relation between U_v and U is proposed. It is stated that the interface shear stress at the boundary of the vegetation layer, τ_k, scales with U_s and u_r (eq. 6.31), respectively the surface layer velocity [m/s] and the characteristic eddy velocity [m/s], following the approach of Gioia and Bombardelli (2002). Gioia and Bombardelli (2002) stated that stream wise velocity fluctuations scale with the average flow velocity, here U_s, and that vertical fluctuations are determined by eddies between the roughness elements with velocity u_r and associated with a characteristic spatial scale r.

$$\tau_k \sim \rho U_s u_r \tag{6.31}$$

with τ_k, derived from a momentum balance for fully-developed flow, written as:

$$\tau_k = \rho g i \,(H - k) \tag{6.32}$$

Kolmogorov suggests that energy is added to the large turbulent eddies by the mean flow velocity, U_s, and turbulent kinetic energy is dissipated at the smallest scales (here u_r). Considering this energy cascade framework, and assuming that the rate of energy production is balanced by the dissipation of energy, results in eq. 6.33:

$$\frac{U_s^3}{H-k} \sim \frac{u_r^3}{r} \tag{6.33}$$

Using the relations described in equation 6.33 and 6.31, an expression for U_s is found (eq. 6.34).

$$U_s \sim \left(\frac{H-k}{r}\right)^{(1/6)} \sqrt{g(H-k)i} \tag{6.34}$$

The velocity in the surface layer can be found by scaling U_s to the velocity in the resistance layer U_v. If one assumes that this dimensionless velocity shows similarity with the depth of the surface layer (H-k), the following power law can be hypothesized:

$$\frac{U_s}{U_v} = \left(\frac{H-k}{l}\right)^{\eta(\frac{H}{k})} \tag{6.35}$$

The scaling length l [m], was determined by experimental work and found to be equal to s [m], the distance between the roughness elements, in this case the cylinders representing the vegetation. In correspondence with the Manning's resistance law (Equation 6.7), the exponent η in equation 6.35 should approach a value of 2/3 for larger depths. On the other hand, when k approaches H or the vegetation grows closer to the water surface, U_s should approach U_v, and as such η should tend to 0. These conditions, in summary:

1. $\frac{H}{k} \gg 1$; $\eta \to$ 2/3

2. $\frac{H}{k} \rightarrow 1$; $\eta \rightarrow 0$

lead to the following expression for the exponent η, with the exponent α, defined as a positive value.

$$\eta = \frac{2}{3}\left(1 - \left(\frac{H}{k}\right)^{-\alpha}\right) \tag{6.36}$$

Combining equation 6.35 with the conditions summarised in equation 6.36 and, from comparison with experimental results, knowing that $l = s$ and $\alpha = 5$, leads to a final expression for the velocity in the surface layer U_s (equation 6.37).

$$U_s = U_v \left(\frac{H-k}{s}\right)^{\frac{2}{3}\left(1-\left(\frac{H}{k}\right)^{-5}\right)} \tag{6.37}$$

Another representation for the interface shear stress τ_k (eq. 6.32) is used by Luhar and Nepf (2013). A constant friction coefficient C_v was used to represent the friction at the interface between the surface and vegetation zone ($\tau_k = 0.5\rho C_v U_s^2$), valid for situations where $U_v < U_s$. This results in the following expression for U_s:

$$U_s = \frac{2gi\sqrt{H-k}}{C_v} \tag{6.38}$$

In Luhar and Nepf (2013) a value for C_v of 0.04 was given. Other studies, eg. Cheng (2011) tried to link C_v with vegetation characteristics.

Yet another approach is used in the work of Klopstra et al. (1997). For the surface layer, a logarithmic velocity profile is assumed (eq. 6.20), based on the Prandtl mixing hypothesis. Here, the zero-plane displacement d_p is replaced by the (k - h_s), with h_s the distance between the top of the vegetation and the virtual bed of the surface layer [m]. h_s and z_0 follow from the condition that the actual value and gradient of the flow velocity of both the vegetation and surface layer should be equal at the interface. These conditions lead to the following equations:

$$h_s = g\frac{1 + \sqrt{1 + \frac{4E^2\kappa^2(H-k)}{g}}}{2E^2\kappa^2} \tag{6.39}$$

$$z_0 = h_s e^{-F} \tag{6.40}$$

To obtain values for E and F, a momentum equation is used in the vegetation layer, assuming uniform and steady flow as in eq. 6.24, but in function of the depth z:

$$\frac{\partial \tau(z)}{\partial z} = mdC_D u(z)^2 - \rho gi \tag{6.41}$$

Using a Boussinesq equation for the turbulent shear stress τ [kg/ms^2], with ϵ_z the turbulent viscosity [kg/ms]. ϵ_z is characterised by a velocity scale and a length scale α [m], which is assumed to be independent of the depth z.

$$\tau(z) = \epsilon_z \frac{\partial u(z)}{\partial z} = \rho \alpha u(z) \frac{\partial u(z)}{\partial z} \tag{6.42}$$

Substituting in equations 6.41 yields:

$$\frac{\partial \left(\rho \alpha u(z) \frac{\partial u(z)}{\partial z} \right)}{\partial z} = mdC_D u(z)^2 - \rho g i \tag{6.43}$$

An analytical solution equation (6.43) can be found using eq. 6.32 and 6.26 as respectively upper and lower boundary condition, from which the parameters E and F (in eq. 6.39 and 6.40) can be derived. The derivation of E and F and the integration of the velocity profile over the depth to obtain U is given in Appendix A. The final expression to calculate the roughness for submerged vegetation using Klopstra et al. (1997) can be found in Table 6.3.

In Baptist et al. (2007) several approaches have been proposed and compared. A first method is based on the same assumptions as in Klopstra et al. (1997), namely the development of a logarithmic profile above the vegetation layer, however another (and easier) way to characterise d and z_0, respectively the zero-plane displacement and the roughness height, is obtained. The velocity profile of the two layers is connected using U_v as a slip velocity, added as extra term (Equation 6.44).

$$u_s(z) = \frac{u*}{\kappa} ln \left(\frac{z-k}{z_0} \right) + U_v \tag{6.44}$$

A height-averaged value can be found by integrating equation 6.44 over the surface layer depth $(H-k)$

$$\begin{aligned} U_s &= \frac{1}{H-k} \int_k^H \left[\frac{u*}{\kappa} ln \left(\frac{z-k}{z_0} \right) + U_v \right] dz \\ &= \frac{u*}{\kappa} ln \left(\frac{H-k}{z_0} - 1 \right) + U_v = \frac{u*}{\kappa} ln \left(\frac{H-k}{e z_0} \right) + U_v \end{aligned} \tag{6.45}$$

where e is the base of the natural logarithm. The shear velocity u^* is given by $\sqrt{g(H-k)i}$. An analytical expression for the unknown value of z_0, based on expressions for the turbulence intensity c_p, the stem spacing m and a length scale L, is given in Baptist et al. (2007) and can be found in Appendix A. Based on the same assumptions, Yang and Choi (2010) found an expression, very similar to eq. 6.45:

$$U_s = \frac{C_u u^*}{\kappa} \left[\frac{H}{H-k} \ln\left(\frac{H}{k}\right) - 1 \right] + U_v \tag{6.46}$$

with C_u a coefficient of 1 or 2, based on the frontal area per unit volume a [m^{-1}], respectively for $a < 5.0$ [m^{-1}] and $a > 5.0$ [m^{-1}]. Using genetic programming on a large data set, Baptist et al. (2007) found the following expression for U_s, which is dimensionally consistent, for the surface layer term.

$$U_s = \frac{\sqrt{g}}{\kappa} ln\left(\frac{H}{k}\right) \sqrt{Hi} \tag{6.47}$$

6.5.6.4 Three-layer model

Recently, the two layer-models described above, have been complemented with three layer models, eg. described in Hu et al. (2013). In such a 3 layer model, in addition to the two-layer model, the vegetation layer is divided into two layers, respectively a lower and upper vegetation zone, with respective velocities $U_{v,I}$ and $U_{v,II}$, as depicted in Figure 6.7.

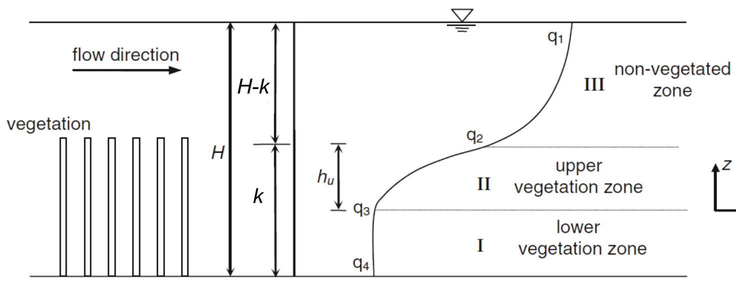

Figure 6.7: Vertical velocity profile, as schematised in a three-layer approach. The figure is taken from Hu et al. (2013).

For the lower-vegetation zone, the description is identical to the vegetation zone of the two-layer approach. Replacing k (the vegetation height) with k-h_u, equation 6.24 can be applied for this zone (eq. 6.48).

$$U_{v,I} = \sqrt{\frac{2gi}{C_D m d}} \tag{6.48}$$

At the top of the vegetation, because of the drag difference at the vegetation-water interface, vortices are created which penetrate into the vegetation. The upper-vegetation zone is defined between the height of this vortex penetration into the vegetation layer and the height of the vegetation itself, and is indicated by the symbol h_u [m]. For h_u, several values can be found in literature, however a zone with height h_u is not found for sparse cases. Hu et al. (2013) suggests a regression to find h_u (eq. 6.49) scaling with the total water depth H, with a fitting parameter β depending on the vegetation type (rigid cylinder, flexible cylinder, ...).

$$\frac{h_u}{H} = \frac{\beta}{C_D} \tag{6.49}$$

For the upper-vegetation zone, eq. 6.41 is used for fully-developed steady uniform flow. Based on the mixing length hypothesis, the shear stress can be written as:

$$-\frac{\partial \overline{u'w'}}{\partial z} = l_u^2 \left(\frac{\partial U_{v,II}}{\partial z}\right)^2 = \kappa^2 z^2 \left(\frac{\partial U_{v,II}}{\partial z}\right)^2 \tag{6.50}$$

Herein, $\overline{u'w'}$ is the Reynolds stress $[\mathrm{m}^2/\mathrm{s}^2]$, $U_{v,II}$ the velocity in the upper-vegetation zone $[[\mathrm{m/s}]]$, l_u the mixing length [m] and z the vertical coordinate from the interface between upper and lower vegetation zone to the water surface (see Figure 6.7). which gives, substituting in 6.41

$$2\kappa^2 z^2 \frac{\partial U}{\partial z} \cdot \frac{d^2 U}{dz^2} + 2\kappa^2 z^2 \left(\frac{\partial U}{\partial z}\right)^2 = 0.5 C_D m d U^2 - gi \tag{6.51}$$

Equation 6.51 can be solved using a power series, finally leading to expression 6.52, with a dimensional parameter ξ, estimated by equation 6.53 (the reader is referred to Hu et al. (2013) for more detailed information on this step).

$$U_{v,II} = U_{v,I}\left(1 + \frac{\xi}{2} + \frac{\xi^2}{40} + \frac{\xi^3}{4400} + \ldots\right) \tag{6.52}$$

$$\xi = \frac{F_v z}{\kappa_u^2 0.5 (\rho V) U^2} \tag{6.53}$$

with F_v the vegetation drag of the entire volume and (ρV) the mass of water. For the surface layer, a similar expression as eq. 6.41 can be used, but the vegetation drag term disappears. The Reynolds stress is estimated in a similar way as in eq. 6.51. The velocity in the surface layer U_s can be found by integrating over H - k.

$$U_s = 2\sqrt{\frac{gik}{\kappa^2}}\left\{ln\left[tan\left(0.5 arcsin\sqrt{\frac{z}{k}}\right)\right] + cos\left(arcsin\sqrt{\frac{z}{k}}\right)\right\} + U_{v,II}(k) \tag{6.54}$$

6.5.6.5 Comparison between different approaches

A wide range of prediction formulas exist to obtain a velocity profile $u(z)$ and a resulting depth-averaged velocity U in the case of emergent or submerged vegetation, as described in previous section. Most of the discussed formulas are developed and tested for dense canopies (Baptist et al., 2007; Huthoff et al., 2007).

These expressions range from relatively easy formulas with a limited number of parameters (vegetation height k, number of stems per area $m,\ldots$) to more complicated formulas with an increased number of parameters (vegetation penetration height $h_u, \ldots$), which are in general more difficult to determine.

It should be asked however, whether these different formulas result in different values for the depth-averaged velocities and in what extent. The vegetation characteristics (m, C_D, d, k) are strongly linked with the hydraulic parameters (i, U). For higher values of m and d, U will likely be smaller and i higher. As such, if parameter ranges are tested, the relative importance of differences between equations will vary and accordingly, no suited objective comparative method was found. As an alternative, for sparse canopies ($aH < 0.1$ (Nepf, 2012b)) and dense canopies ($aH > 0.1$) the result of the expressions of Baptist et al. (2007); Huthoff et al. (2007); Klopstra et al. (1997); Stone and Shen (2002) are shown for two water heights (1 and 2 m) and a constant energy slope i = 0.0005 [-]. In Figures 6.8 and 6.9, the calculated values of U are shown, for different submergence rates k/H.

It can be seen in Figures 6.8 and 6.9 that the difference between the methods increases with decreasing submergence rate. This can be explained easily, as the methods use different approaches to account for the velocity in the surface layer, however for the vegetation layer, all approaches are similar. The differences below $k/H \approx 0.2$ are so big for all cases, that it can be concluded that these methods are not suitable below this threshold. Further it is clear that the choice of the model, can have big influences on the results. For a submergence rate of 50 %, the difference between the highest and lowest prediction for the dense canopy is 0.178 m/s (0.227 $\pm$ 0.068 m/s) and 0.089 m/s (0.180 $\pm$ 0.038 m/s), for respectively a water height of 2 and 1 m. For the sparse canopy, values of respectively 0.177 m/s (0.600 $\pm$ 0.071 m/s) and 0.203 m/s (0.545 $\pm$ 0.087 m/s) are found. The values between brackets indicate the average and standard deviation at k/H = 0.5 for all predictions.

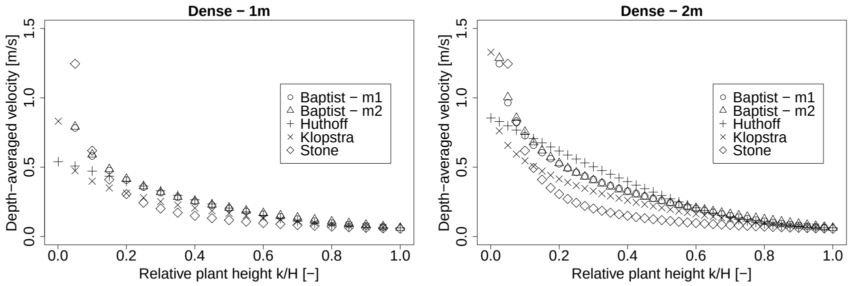

Figure 6.8: Depth-average velocity predicted by different equations for a dense canopy in function of the submergence rate k/H. Parameters for the calculation are: C_D = 1; m = 500; d = 0.005; i = 0.0005. Results are shown for 1 m water depth (left) and 2 m water depth (right).

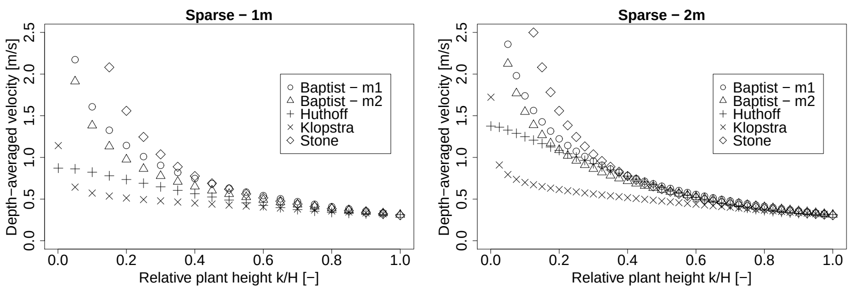

Figure 6.9: Depth-average velocity predicted by different equations for a sparse canopy in function of the submergence rate k/H. Parameters for the calculation are: C_D = 1; m = 20; d = 0.005; i = 0.0005. Results are shown for 1 m water depth (left) and 2 m water depth (right).

Once an analytical expression for the depth-averaged velocity is established, based on vegetation characteristics, a resistance factor can easily being calculated using the Chézy or Manning formula. An overview of the expressions in function of the Manning coefficient is given in Table 6.3.

6.5.7 The drag coefficient C_D

An important (calibration) parameter in the vegetative resistance models of previous sections is the drag coefficient C_D [-], defined in equation 6.55. For rigid objects, a value of 2 is taken for the coefficient β. For flexible objects, values lower than 2 are observed. The exponent β is sometimes written as $(2 + E)$, with E [-] the Vogel number, ranging between 0 and -2 (Vogel, 1994).

$$F \sim C_D U^{\beta} \tag{6.55}$$

Table 6.3: Table with an overview of the Manning roughness parameter n $[\mathrm{s/m^{1/3}}]$, based on the depth-averaged velocity description of different authors. For the Klopstra et al. (1997) case, the parameter values A, C_3 are defined in Appendix A. C_b is the Chézy coefficient of the bed $[\mathrm{m^{1/2}/s}]$. H is the water depth [m], g the gravitational constant $[\mathrm{m/s^2}]$, z_0 the roughness length [m]. k is the vegetation height [m], m the number of stems per area $[1/\mathrm{m}^2]$, d the stem diameter [m] and C_D the drag coefficient [-]. Other variables are explained in section 6.5.6.

Equation	Eq no.	Reference
$n = \frac{1}{H^{1/6}}\sqrt{\frac{1}{(C_D mdk/2g}}\sqrt{\frac{H}{k}}\cdot\left[\frac{1-d(k/H)\sqrt{m}}{1-d\sqrt{m}}\right]$	6.30	Stone and Shen (2002)
$n = \frac{1}{H^{1/6}}\sqrt{\frac{2g}{C_D mdH}}\left[\sqrt{\frac{k}{H}}\right]+\sqrt{\frac{2g}{C_D mdH}}\left[\frac{(H-k)}{H^{7/6}}\left(\frac{H-k}{s}\right)^{2/3\left(1-(H/k)^{-5}\right)}\right]$	6.37	Huthoff et al. (2007)
$n = \frac{1}{H^{10/6}}\left[\frac{2}{\sqrt{2A}}\left(\sqrt{C_3 e^{k\sqrt{2A}}+u_{v0}^2}-\sqrt{C_3+u_{v0}^2}\right)\right] + \frac{1}{H^{10/6}}\left[\frac{u_{v0}}{\sqrt{2A}}ln\left(\frac{(\sqrt{C_3 e^{k\sqrt{2A}}+u_{v0}^2}-u_{v0})\cdot(\sqrt{C_3+u_{v0}^2}+u_{v0})}{(\sqrt{C_3 e^{k\sqrt{2A}}+u_{v0}^2}+u_{v0})\cdot(\sqrt{C_3+u_{v0}^2}-u_{v0})}\right)\right] + \frac{1}{H^{10/6}}\left[\frac{\sqrt{g(H-(k-h_s))}}{\kappa}\left\{(H-(k-h_s))ln\left(\frac{H-(k-h_s)}{z_0}\right)-h_s ln\left(\frac{h_s}{z_0}\right)-(H-k)\right\}\right]$	see Appendix	Klopstra et al. (1997)
$n = \frac{1}{H^{1/6}}\sqrt{\frac{1}{C_D mdk/2g}}+\frac{(H-k)^{3/2}(\sqrt{g}/\kappa)}{H^{10/6}}ln(\frac{H-k}{ez_0})$	6.45	Baptist et al. (2007)
$n = \frac{1}{H^{1/6}}\sqrt{\frac{1}{C_D mdk/2g}}+\frac{1}{H^{1/6}}\frac{\sqrt{g}}{\kappa}ln\left(\frac{H}{k}\right)$	6.47	Baptist et al. (2007)
$n = \frac{1}{H^{1/6}}\sqrt{\frac{2g}{C_D a}}(H-k_s) + \frac{(k-k_s)}{H^{1/6}}\sqrt{\frac{2g}{C_D a}}\left(1+\xi/2+\xi^2/40+\xi^3/4400\right) + \frac{(H-k)}{H^{1/6}}\sqrt{\frac{gk}{\kappa^2}}h\left\{ln\left[tan\left(0.5arcsin\sqrt{\frac{z}{h_v}}\right)\right]+cos\left(arcsin\sqrt{\frac{z}{h_v}}\right)\right\}$	6.54	Hu et al. (2013)
$n_4 = \left[\sqrt{\frac{2gH}{mdC_D k}}+\frac{C_u\sqrt{(H-k)g}}{\kappa}\cdot ln\left(\frac{H}{k}\right)-\frac{(H-k)}{H}\frac{\sqrt{g(H-k)}}{\kappa}\right]^{-1}H^{2/3}$	6.46	Yang and Choi (2010)

However, this drag coefficient is not always easy to determine and dependent on several parameters as the Reynolds number Re. Several experimental studies have been performed to determine the drag coefficient, for single cylinders and arrays of cylinders.

For isolated cylinders, a relation (eq. 6.56) for the drag coefficient based on the experimental data of Wieselberger and Tritton was given by White (1991).

$$C_D = 1 + \frac{10}{Re^{2/3}} \tag{6.56}$$

This results in a drag coefficient of 1.0 to 1.2 for Reynolds numbers between 10^2 - 2.5 $\cdot$ 10^5 (Wu, 2007). For most studies described here, U is of the order $\mathcal{O}(10^{-1})$, the diameter d of the order $\mathcal{O}(10^{-3})$, resulting in Reynolds number of $\mathcal{O}(10^2\text{-}10^3)$.

Also for arrays of cylinders, estimates of the drag coefficient have been made. Stone and Shen (2002) state that a drag coefficient C_{Dm} based on the constricted cross-sectional velocity U_{vm} is more appropriate than C_D.

$$C_D = C_{Dm}\frac{U_{vm}^2}{U_v^2} \tag{6.57}$$

where U_v = U_{vm}(1-$d\sqrt{m}$), with m the number of stems per unit area. Tanino and Nepf (2008) estimated the drag coefficient in a random array of rigid, emergent cylinders. Equation 6.58 was used to determine a relationship for C_D.

$$C_D = 2\left(\frac{\alpha_{0,CD}}{Re_P} + \alpha_{1,CD}\right) \tag{6.58}$$

Herein, Re_P is the Reynolds number of an individual cylinder, $\alpha_{1,CD}$ = 0.46 + 3.8ϕ, where ϕ represents the solid volume fraction [-]. $\alpha_{0,CD}$ is also dependent on the solid volume fraction, but no linear regression was found. A value of 25 is taken for $\phi < 0.12$ and a value of 83.8 for $\phi > 0.12$.

Several experiments have been carried out to estimate the drag coefficient on real plants (Bal, 2009; Siniscalchi and Nikora, 2012; Wilson et al., 2008). Because of the flexibility of the plants, the frontal area of the plants will change with velocity. As mentioned by Luhar and Nepf (2013), there has been a debate about which area (eg. frontal area) best characterizes the drag as plants bend and which independent parameter (eg. Re) must be used to describe a relationship between the drag coefficient and velocity (see eg. Statzner et al. (2006)).

6.6 An overview of studies using the 2D-SWE for vegetated flows

Several models, using the 2D-SWE to study vegetated flow have been published before. A selection of studies is discussed below. These studies are regarded, focusing on small scale. As such, floodplain studies, etc. are not considered. An overview of these studies, together with their main characteristics, is given in Table 6.4.

Tsujimoto (1999) performed simulations of water flow and sediment transport, coupled with suspension and bedload transport, mainly focussing on morphological effects of vegetation presence. For intense bed-load transport with a vegetation patch on the side, erosion on the side of the vegetation and deposition in the upstream area of the vegetated zone is noted. When suspended sediment transport is added, the fine material covers the deposition areas. In the paper, attention is paid to the links between flow, sediment transport, geomorphology and vegetation development, where mainly human influences on the river landscape, e.g. dams, are assessed. Floods are seen as periods of morphological changes and vegetation adapts to the new morphology during dry seasons.

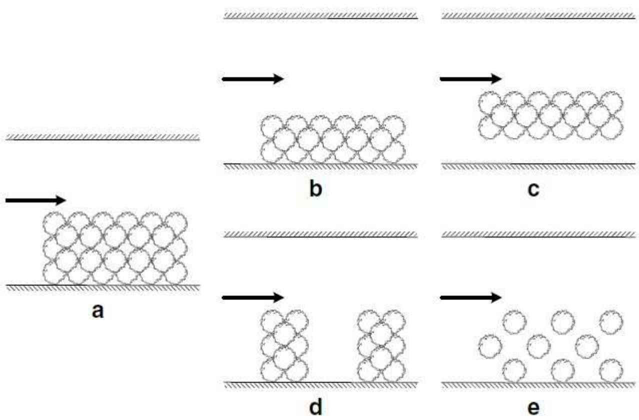

Figure 6.10: Overview of the different cutting management strategies investigated by Leu et al. (2008), taken from Leu et al. (2008). The five configurations are respectively (a) original, (b) cutting along the main channel, (c) cutting along the bank side, (d) alternative cutting and (e) reducing the vegetation density.

Leu et al. (2008) used the 2D-SWE (eqs. 4.49, 4.50, 4.51) and a finite volume discretisation using the SIMPLE method (Semi-Implicit Method for Pressure Linked

Equations, see for example Patankar (1980)) on a Cartesian grid to investigate the effect of cutting management of vegetation zones on the water depth and flow velocities. Five cutting scenarios were considered, namely: (a) original vegetation configuration (reference), (b) cutting along the main channel, (c) cutting along the bank side, (d) alternative cutting and (e) thinning out the vegetation (reducing their density), as is shown in Figure 6.10). These scenarios were considered for both a straight, rectangular flume and a compound channel (with the free-flowing section deeper than the vegetated section). For the straight channel, all cutting scenarios reduced the stream curvatures and velocities near the vegetation. The flow depths were reduced most for cutting scenarios b and c, scenarios for which the vegetation width is reduced. Another study has been performed by Ball et al. (1996) to model the effect of a pile group in a patch form, representing a vegetation patch. Here, equations 5.10 are implemented, using the TRIM method on a Cartesian, staggered grid (identical to the implementation sketched in section 5.4.4). In this study, the focus is set on the wake velocity pattern behind the pile patch, and more precisely the effect of the drag of the patch on the oscillatory behaviour of the far-wake velocities (Figure 6.11). In Figure 6.11 the velocity results for different patch densities are shown. A reduction of the steady wake length can be observed with increasing density of the patch. Ball et al. (1996) state that the Strouhal number of the oscillation is similar to the observed Strouhal number for cylinders of the same diameter. The model results were compared with their own velocity measurements, measured using PTV (Particle Tracking Velocimetry).

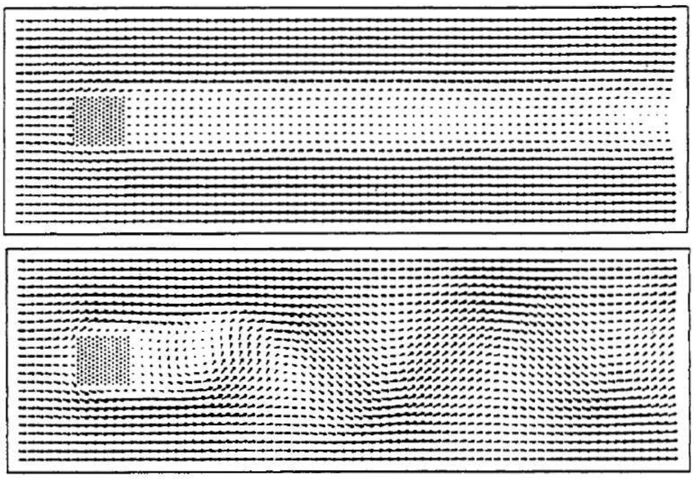

Figure 6.11: Model results presented by Ball et al. (1996) for a patch, modelled using a drag coefficient C_D of respectively 1.9 (above) and 19 (below) and a Manning coefficient of respectively 0.3 and 0.94 (from Ball et al. (1996)). Results are shown at a time of 240 s after the start of the simulations.

A series of publications of modeling vegetated flows in a 2D framework (and beyond) was submitted by Weimung Wu (Wu, 2007; Wu et al., 2004; Wu and Wang, 2004). As validation, the experiments of Bennett et al. (2002) were used, where vegetation zones with an equal spacing of 2.4 m were distributed alternately on one and the other flume wall, to achieve a meandering pattern. Good matches between the model and experimental runs were observed. Furthermore, the effect of vegetation in bends was considered as well, by adding extra dispersion terms in the momentum equations. Also, sediment transport was taken into account. The velocity distribution, thalweg meandering and changes in bed topography were predicted well for mobile-bed laboratory flume experiments with vegetated alternate bars. In a natural river meander bend where artificial large woody debris structures were constructed to protect the banks and provide aquatic habitats, mean flow velocities and bed changes were predicted reasonably well by the numerical model (Wu et al., 2004).

Zhang et al. (2013) also performed numerical simulations of vegetated flow using the 2D depth-averaged shallow water equations. A solution based on the SIMPLEC methodology (a variant of the SIMPLE method) was used, on a curvilinear grid. The velocities and pressures (water surfaces) in flumes with bends were considered. Both emergent and submerged vegetation were considered, using a Baptist-like incorporation of vegetation in the model (see Chapter 6), by adding the vegetative resistance to the bed friction term. Good agreement between measurements and the model simulations were observed.

6.7 Conclusion

Flow resistance is a parameter depending on many aspects and different roughness coefficients are used to express this. Depending on the research question and degree of information required and available, a point, local or reach value for such a roughness coefficient can be used. Furthermore, the framework (1D, 2D) will influence both the value of the resistance coefficient and the most appropriate way to determine it. Because of the enormous variety of vegetation appearance, the resistance caused by vegetation is very difficult to address. A wide variety of methods exist and are used, ranging from fully empirical to more theoretically based models. An overview of these approaches was given in this chapter. Furthermore, the use of these vegetation resistance models in numerical models using the 2D-SWE is reviewed. Formulations linking the Manning coefficient n and vegetation characteristics are used in Chapter 7 to simulate vegetated flows with the 2D extension of the STRIVE model.

Table 6.4: Overview of studies using the depth-averaged Shallow Water Equations to study vegetated flows.

Study	Leu et al. (2008)	Ball et al. (1996)	Wu (2007)	Zhang et al. (2013)
2D - SWE equation	eqs. 4.49,4.50,4.51	eqs. 5.10	eqs. 4.49,4.50,4.51	eqs. 4.37
Numerical method	SIMPLE	TRIM	SIMPLEC	SIMPLEC
Grid	cartesian	cartesian	curvilinear	curvilinear
Turbulence model	k-ϵ	algebraic formulation	k-ϵ	k-ϵ
Vegetation	Extra momentum term	Addition to Manning coefficient	Extra momentum term	Addition to Manning coefficient
Exp. for validations	Tsujimoto and Kitamura (1995), Pasche and Rouve (1985)	Ball et al. (1996)	Bennett et al. (2002), Tsujimoto (1999)	Tominaga et al. (1999)
Focus	cutting management, configurations	steady and unsteady wake velocities	velocity fields in compound channels, velocity and bed changes in bends	velocity in bends

7
Simulation Results

7.1 Introduction

The implemented Shallow Water Equations and the implemented methods to account for the vegetation resistance, using the methods of Baptist (6.45 and 6.47) and the method of Huthoff (6.37), are tested for different cases of vegetated flow, for which the degree of spatial heterogeneity was increased. In the first part of the chapter, the characterisation of vegetation resistance in the model is tested by comparing the model results with experimental results for uniform vegetation, extending over the whole width of the flume. In a second step, a simple form of heterogeneity is introduced, by considering mimics of vegetation placed on one side of the flume. In a third step, isolated patches are considered with free edges on each side. In a last step, patches, consisting of real vegetation and placed in a side-by-side configuration, are simulated.

7.2 Uniform vegetation

In this section, the model results are validated with experimental results from studies where vegetation is occupying the whole width of the flume. Both cases with emergent and submerged vegetation are tested. In the experimental studies, vegetation was represented by wooden dowels (Cheng, 2011; Dunn et al., 1996; Liu et al., 2008), plastic, flexible cylinders (Dunn et al., 1996; Kubrak et al., 2008; Li et al., 2013) or real vegetation (Jarvela, 2005), resulting in both rigid and flexible types of vegetation.

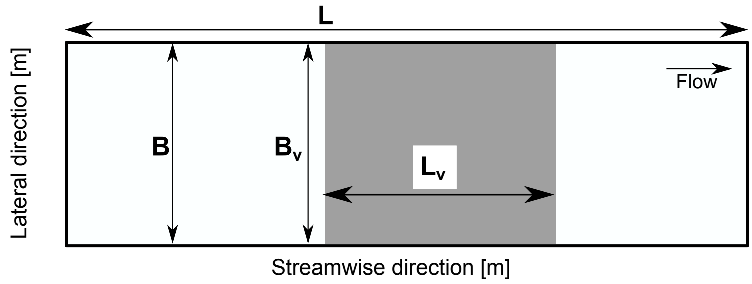

Figure 7.1: Indication of geometrical parameters on planview, the vegetation section is indicated by a gray zone. L is the length [m] and B the width [m] of the flume. L_v and B_v are respectively the length [m] and width [m] of the vegetation zone. In the case of uniform vegetation, $B = B_v$.

7.2.1 Selection of the experiments

Several studies have been performed to characterize the resistance caused by a uniform canopy of vegetation. However, all necessary data for modeling, are not always provided. To avoid as much as possible, the use of interpreted data and as such taking the risk of misinterpretation of the performance of the model, a limited number of studies (Cheng, 2011; Dunn et al., 1996; Jarvela, 2005; Kubrak et al., 2008; Li et al., 2013; Liu et al., 2008), with a total of 97 experimental runs, is selected for which all data (channel width, channel length, water height, bottom slope, flow velocity, bed roughness, (deflected) vegetation height, stem density, stem diameter, measured roughness coefficient) are provided and the calculation methods are clearly stated. The only parameter value which is mostly not available is the drag coefficient C_D. This parameter is set at a value of 1 for all experiments. A summary of the selected studies is given in Table 7.1, indicating the type of vegetation under investigation and the submergence rate of these vegetation canopies. The complete dataset is presented in Appendix B.1. For the experiments of Li et al. (2013), only the results for emergent vegetation are retained, as inconsistent values between graphs and tables were noticed for the submerged cases.

The selected experimental runs span a wide range of submergence values and depth-based Reynolds numbers $Re_H = UH/\nu$, with U the depth-averaged velocity [m/s], H the water depth [m] and ν the kinematic viscosity [m^2/s], as can be observed from Table 7.1 and Figure 7.2. The submergence rate k/H, with k the vegetation height [m], ranges from 30 % to emergent cases (100 %), the Reynolds number ranges from approx. 10000 to 200000. An overview of the range of parameters examined in the studies which were selected is given in Figure 7.2.

Table 7.1: Overview of the experiments with uniform vegetation used to validate the performance of the implemented vegetation resistance models and the range of parameter values used herein. No indicates the number of experimental runs [-], k the vegetation height [m], H the water depth [m] (k/H is the submergence rate of the plants) and Re_H the Reynolds number [-] based on the water depth. The complete dataset and overview of parameters is given in Appendix B.1.

Study	No #	k/H [%]	Re_H [-]	Vegetation type	
Dunn et al. (1996)	12	30-72	50500-199000	Submersed	rigid
Dunn et al. (1996)	6	41-58	85000-196000	Submersed	flexible
Jarvela (2005)	9	31-67	36000-130000	Submersed	flexible (real)
Liu et al. (2008)	18	64-100	14000-38000	Submersed & Emergent	rigid rigid
Li et al. (2013)	4	100	120000	Emergent	flexible
Kubrak et al. (2008)	25	61-83	47000-130000	Submersed	flexible
Cheng (2011)	23	50-77	10000-68000	Submersed	rigid

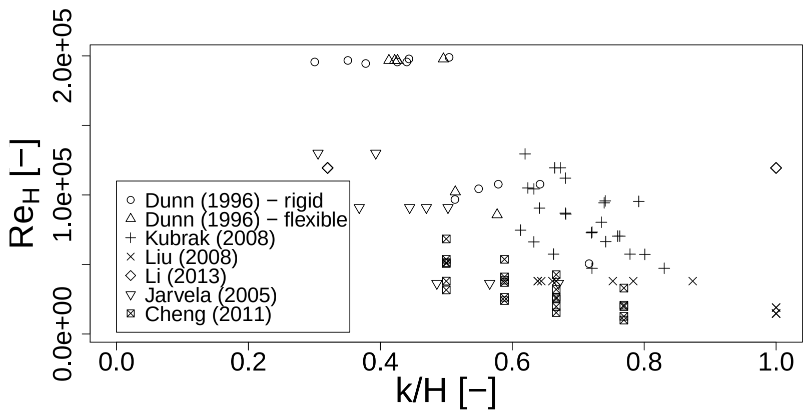

Figure 7.2: Overview of the experimental data used to validate the resistance models, presented by the range of submergence (k/H) and the Reynolds number (Re_H) based on the flow depth (H).

7.2.2 Methodology

For the model simulations, the computational domain was set identical to the physical domain of the experiments. As upstream boundary condition, the discharge was selected, as downstream boundary condition the indicated water height. The methods of Baptist (eqs. 6.45 and 6.47, indicated respectively as BaptistI and BaptistII) and the method of Huthoff (eq. 6.37), and summarised in Table 6.5.6, were used to estimate the vegetative roughness based on the vegetation characteristics, as indicated in the experiments (see Appendix B.1). The Bresse equation (7.1), with S_0 the bottom slope, S_f the energy slope and Fr the Froude number, was used to estimate the Manning coefficient from the model.

$$\frac{dH}{dx} = \frac{S_0 - S_f}{\sqrt{1 - S_0^2} - Fr^2} \tag{7.1}$$

The total length of the flume was used to estimate the friction coefficient, if no extra information was provided. It should be noted that a 1D formulation for the Manning coefficient is used. However the same approach is used in the experiments, with the assumption that the vegetation roughness is much higher compared to the friction values of the side walls or bottom roughness.

Resistance coefficients calculated based on the model simulations and measured resistance coefficients were compared. The goodness-of-fit values which are used to compare the model simulations and the experimental results are respectively the root mean square error (RMSE), the mean absolute error (MAE), the mean error (ME), the Nash-Sutcliffe efficiency (NS) and the relative Nash-Sutcliffe efficiency (rNS). The first three (RMSE, MAE, ME) indicate a difference between the measurements (M_i) and model simulations (S_i) and are respectively defined as:

$$RMSE = \sqrt{\frac{1}{N}\sum_{i=1}^{N}(S_i - M_i)^2} \tag{7.2}$$

$$MAE = \frac{1}{N}\sum_{i=1}^{N}|S_i - M_i| \tag{7.3}$$

$$ME = \frac{1}{N}\sum_{i=1}^{N}(S_i - M_i) \tag{7.4}$$

For all these measures, a value close to 0 indicates good agreement between the model and the observations. The Nash-Sutcliffe efficiency (NS) and relative Nash-Sutcliffe efficiency (rNS) are defined as:

$$NS = 1 - \frac{\sum_{i=1}^{N}(S_i - M_i)^2}{\sum_{i=1}^{N}\left(M_i - \bar{M}\right)^2} \tag{7.5}$$

$$rNS = 1 - \frac{\sum_{i=1}^{N}\frac{(S_i - M_i)^2}{\bar{M}}}{\sum_{i=1}^{N}\frac{\left(M_i - \bar{M}\right)^2}{\bar{M}}} \tag{7.6}$$

These measures give a relative magnitude of the residual variance (between observation and simulation) compared to the measured data variance. A value close to 1 indicates good agreement, a value below 0 indicates that model predictions are less accurate than the prediction by the mean.

7.2.3 Results

An overview of the results is given in Figure 7.3 and a summary of the goodness-of-fit values is given in Table 7.2. The model results for the experimental results of Kubrak et al. (2008) were not retained for the analysis. This was decided, due to unstable model simulations for the cases with the higher slope (S_0 = 0.0147), using the input data given in Kubrak et al. (2008) and the observation of inconsistent results for the lower slope cases (S_0 = 0.0087).

Table 7.2 gives an overview of the goodness-of-fit measures between measured and predicted Manning coefficient for the three models to account for vegetation roughness (BaptistI (eq. 6.45), BaptistII (eq. 6.47) and Huthoff (eq. 6.37)) and all considered experiments. It can be observed that the overall agreement between experimental and simulated data is good. The values of RMSE, MAE and ME are low, they amount on average approximately 10 % of the measured values. The Nash-Sutcliffe efficiency is in general high to very high, lower values could be found for the experiments of Jarvela (2005), with real vegetation and Liu et al. (2008), with a short measurement zone (3 m). Almost no difference could be found between the two methods given in Baptist et al. (2007), as expected. An exception on this, is the experimental data of Dunn et al. (1996), for rigid vegetation, for which no explanation could be found. The other exception is the case of Jarvela (2005). Due to the the large number of stems, the roughness length is larger (see Appendix A), and as such a larger difference between method I and method II can be explained. The only case where a big difference between the method of Huthoff et al. (2007) and Baptist et al. (2007) is found, is the case of Jarvela (2005), with real vegetation. It is mentioned by Galema (2009) that the method of Huthoff et al. (2007) performs less compared to method II of Baptist et al. (2007) for flexible vegetation.

The fit between the measured and predicted Manning coefficients can be found in Figure 7.3, where a linear fit between the predicted Manning coefficients (by the model) and the measured Manning coefficients from the experimental studies is shown. As the Manning values are close to the origin, the difference between linear fits with and without intercept (respectively Table 7.3 and 7.4) can be quite large. In most cases, the use of an intercept is insignificant (see Table 7.3). The R^2 values are always very high, and no trend or information can be extracted from this measure.

Table 7.2: Goodness of fit (GOF) values for the comparison between the measured Manning coefficients and the model results with the methods of Baptist et al. (2007) and Huthoff et al. (2007) as resistance formulas. The Root Mean Square Error ($RMSE$), Mean Absolute Error (MAE), Mean Error (ME), Nash-Sutcliffe parameter NS and relative Nash-Sutcliffe parameter (rNS) are used as goodness-of-fit values.

GOF	Baptist I	Baptist II	Huthoff
	Dunn et al. (1996), flexible vegetation		
RMSE	0.00366	0.00356	0.00089
MAE	0.00337	0.00324	0.00071
ME	0.000514	0.000656	0.000260
NS	0.914	0.918	0.995
rNS	0.922	0.930	0.994
	Dunn et al. (1996), rigid vegetation		
RMSE	0.00491	0.00567	0.00476
MAE	0.00372	0.00470	0.00314
ME	-0.00173	-0.00159	-0.00292
NS	0.611	0.482	0.633
rNS	0.683	0.562	0.658
	Cheng (2011), rigid vegetation		
RMSE	0.00667	0.00679	0.00762
MAE	0.00625	0.00635	0.00682
ME	0.00625	0.00635	0.00683
NS	0.932	0.929	0.911
rNS	0.930	0.927	0.902
	Jarvela (2005), flexible vegetation		
RMSE	0.00670	0.00867	0.014
MAE	0.00537	0.00788	0.0110
ME	-0.00119	0.00444	0.0110
NS	0.900	0.834	0.562
rNS	0.915	0.735	0.638
	Liu et al. (2008), rigid vegetation		
RMSE	0.00269	0.00268	0.00346
MAE	0.00241	0.00239	0.00296
ME	0.00241	0.00238	-0.000226
NS	0.738	0.739	0.5676012
rNS	0.774	0.777	0.6050253
	Li et al. (2013), flexible vegetation		
RMSE	0.00249	0.00249	0.00272
MAE	0.00237	0.00237	0.00231
ME	-0.000694	-0.000694	-0.00143
NS	0.915	0.915	0.898
rNS	0.920	0.920	0.915

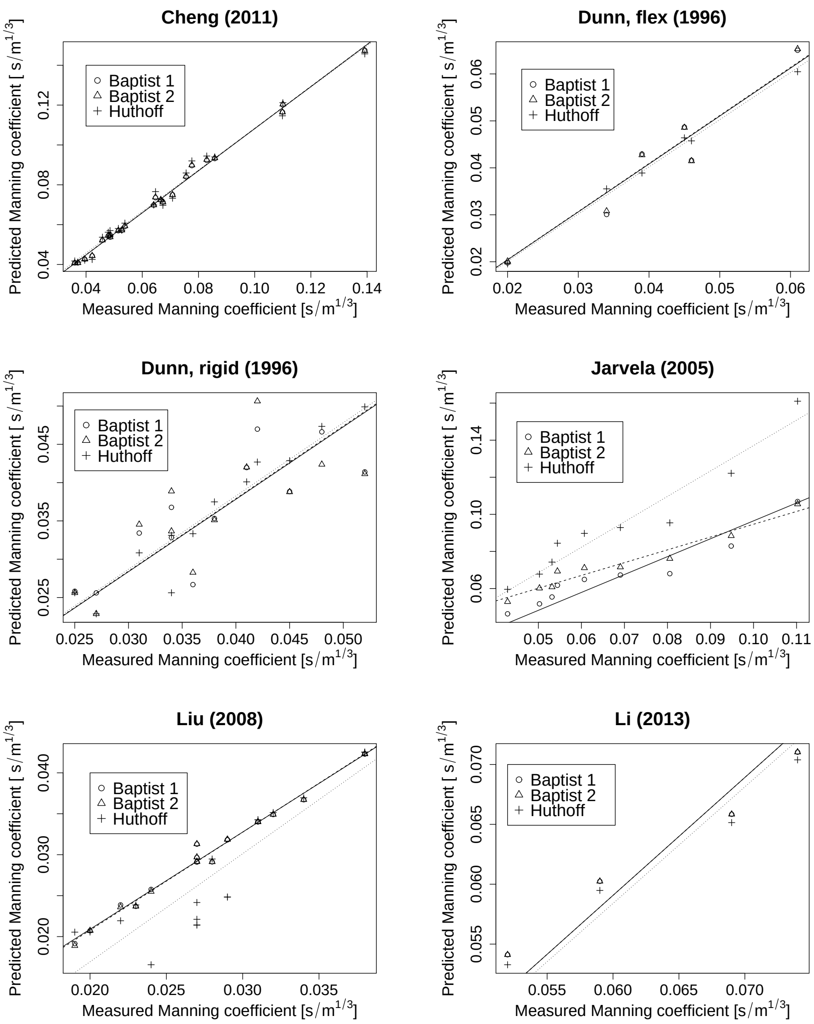

Figure 7.3: Overview of the relationship between observed and predicted Manning coefficients for the different cases. The linear fits shown are with intercept if the intercept is significant and without if the intercept is insignificant (see Table 7.3 and 7.4). The best fit for the Baptist I method is indicated by a solid line (−), for the Baptist II method with a dashed line (−−) and for the Huthoff method with a dotted line (...).

Table 7.3: Parameters of the linear fit $y = ax + b$ between measured and predicted Manning coefficients. a is the slope of linear fit, b the intercept, for which a mean value and standard deviation are given. R^2 the coefficient of determination. (*) indicates that the term is not significant (p $>$ 0.05).

	Baptist I	Baptist II	Huthoff
	Dunn et al. (1996), flexible vegetation		
a	1.106 $\pm$ 0.135	1.098 $\pm$ 0.132	0.993 $\pm$ 0.034
b	-0.0038 $\pm$ 0.0058 (*)	-0.0033 $\pm$ 0.0056 (*)	0.00057 $\pm$ 0.0015 (*)
R^2	0.944	0.946	0.995
	Dunn et al. (1996), rigid vegetation		
a	0.748 $\pm$ 0.167	0.719 $\pm$ 0.199	0.878 $\pm$ 0.146
b	0.0078 $\pm$ 0.0064 (*)	0.009 $\pm$ 0.007 (*)	0.0017 $\pm$ 0.0056 (*)
R^2	0.669	0.478	0.783
	Cheng (2011), rigid vegetation		
a	1.056 $\pm$ 0.016	1.056 $\pm$ 0.017	1.041 $\pm$ 0.027
b	0.0025 $\pm$ 0.0011	0.0026 $\pm$ 0.0012	0.0041 $\pm$ 0.0019
R^2	0.995	0.995	0.986
	Jarvela (2005), real vegetation		
a	0.780 $\pm$ 0.829	0.690 $\pm$ 0.062	1.193 $\pm$ 0.137
b	0.014 $\pm$ 0.0059 (*)	0.026 $\pm$ 0.0044	-0.0022 $\pm$ 0.0098 (*)
R^2	0.927	0.947	0.916
	Liu et al. (2008), rigid vegetation		
a	1.187 $\pm$ 0.032	1.197 $\pm$ 0.033	1.312 $\pm$ 0.144
b	-0.0028 $\pm$ 0.0009	-0.0031 $\pm$ 0.0009	-0.0090 $\pm$ 0.0041
R^2	0.988	0.988	0.838
	Li et al. (2013), flexible vegetation		
a	0.732 $\pm$ 0.057	0.732 $\pm$ 0.057	0.741 $\pm$ 0.057
b	0.016 $\pm$ 0.0036 (*)	0.016 $\pm$ 0.0036 (*)	0.015 $\pm$ 0.0037 (*)
R^2	0.988	0.988	0.988

Table 7.4: Parameters of the linear fit $y = ax$ between measured and predicted Manning coefficients. a is the slope of linear fit, for which a mean value and standard deviation are given. R^2 the coefficient of determination.

	Baptist I	Baptist II	Huthoff
	Dunn et al. (1996), flexible vegetation		
a	1.021 ± 0.037	1.023 ± 0.036	1.005 ± 0.009
R^2	0.993	0.994	0.999
	Dunn et al. (1996), rigid vegetation		
a	0.946 ± 0.035	0.948 ± 0.041	0.971 ± 0.048
R^2	0.985	0.971	0.989
	Cheng (2011), rigid vegetation		
a	1.090 ± 0.006	1.091 ± 0.006	1.095 ± 0.011
R^2	0.999	0.999	0.998
	Jarvela (2005), flexible vegetation		
a	0.965 ± 0.031	1.032 ± 0.041	1.164 ± 0.038
R^2	0.992	0.987	0.992
	Liu et al. (2008), rigid vegetation		
a	1.089 ± 0.007	1.089 ± 0.007	1.003 ± 0.029
R^2	0.999	0.999	0.986
	Li et al. (2013), flexible vegetation		
a	0.984 ± 0.021	0.984 ± 0.021	0.973 ± 0.019
R^2	.998	0.998	0.998

In Figure 7.4 and Table 7.5 the relationship between the measured and predicted Manning coefficients is given for all considered cases together. The null hypothesis for the linear fit model (the linear fit model of R was used, data are not shown), stating that the slope is not significant was rejected ($p < 0.01$), the null hypothesis stating that the intercept of the linear fit is not significant was confirmed ($p > 0.01$). A slope value, using the linear fit model without intercept, close to 1 is found for all resistance methods (see Table 7.5). It can be concluded that the use of the considered resistance formulations to incorporate vegetation roughness caused by emergent and submerged vegetation types in a 2D-depth averaged shallow water model results in reliable results when the vegetation stand occupies the full width of the channel. Especially in the case of submerged vegetation, where the estimation is more difficult, the depth-averaged assumption (small vertical variations) is not really valid and larger deviations between the resistance formulas are found (see Chapter 6), also satisfying results are found.

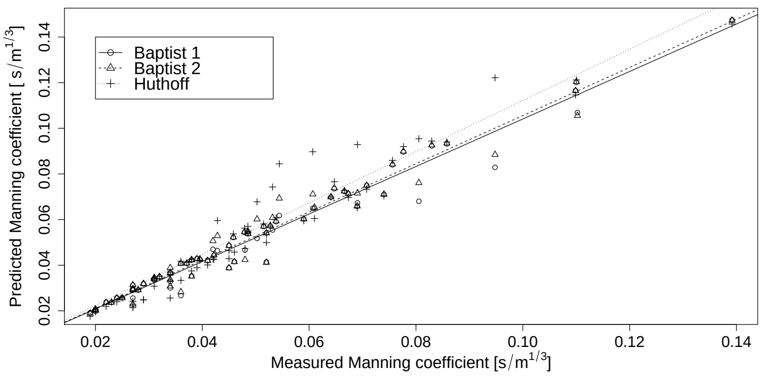

Figure 7.4: Overview of the relationship between observed and predicted Manning coefficients for all cases. The values of the linear fits can be found in Table 7.5. The best fit for the Baptist I method is indicated by a solid line (-), for the Baptist II method with a dashed line (–) and for the Huthoff method with a dotted line (...).

Table 7.5: Parameters of the linear fit $y = ax$ between measured and predicted Manning coefficients. a is the slope of linear fit, for which a mean value and standard deviation are given. R^2 the coefficient of determination.

Parameter	Baptist I	Baptist II	Huthoff
a	1.041 ± 0.010	1.056 ± 0.010	1.122 ± 0.018
R^2	0.993	0.993	0.981

7.3 Configurations with vegetation on 1 side

7.3.1 Overview of the experimental studies

The flow characteristics in a flume with emergent vegetation placed on a side of the flume and only partly obstructing the width of the channel, is e.g. described in the experiments of Tsujimoto and Kitamura (1995), White and Nepf (2007) and Zong and Nepf (2010, 2011). In Figure 7.5 such a configuration is sketched and the relevant geometrical parameters are indicated. An overview of the flow and vegetation parameters used in the experiments of Zong and Nepf (2011), which are used to validate the model, are given in Table 7.6.

Experiments have been carried out by Zong and Nepf (2011) in a horizontal, rectangular flume of 16 m long and 1.2 m width. The emergent vegetation zone has a width B_v of 40 cm (1/3 of the flume width) and a length L_v of 10 m. The vegetation characteristics are, except for the density, identical in all measurements, with a dowel diameter d = 0.006 m. Measurements are performed for sparse and dense cases and for several incoming discharges (low, medium and high flow) and accordingly slightly different water heights. The range of parameters is presented in Table 7.6.

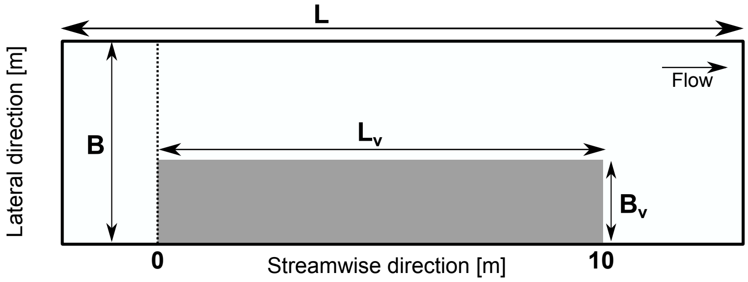

Figure 7.5: Overview of the definition of the parameters L_v and B_v for experiments with emergent vegetation on one side of the flume. The vegetation zone is indicated by the gray area. The flow direction is indicated with an arrow, from left to right. x = 0 m is defined at the upstream edge of the vegetation.

7.3.2 Model settings

The 2D-SWE are discretised as described in Chapter 5. We opted to use the method of Baptist et al. (2007) (equation 6.45) to implement the vegetation resistance. For the study under consideration, all parameters for this equation are provided (see Tables 7.6). The only exception is the drag coefficient C_D [-]. For this parameter, either a constant value can be selected or an equation to calculate C_D in function of the flow parameters can be used. Both are implemented, the equation proposed by Tanino and Nepf (2008) was used, described in Chapter 6 and repeated here.

$$C_D = 2\left(\frac{\alpha_{0,CD}}{Re_P} + \alpha_{1,CD}\right) \tag{7.7}$$

Herein, Re_P is the Reynolds number of an individual cylinder, $\alpha_{1,CD}$ = $0.46 + 3.8\phi$, with ϕ the solid volume fraction [-]. $\alpha_{0,CD}$ is also dependent on the solid volume fraction, but no linear regression is given. Based on Tanino and Nepf (2008) a value of 25 is taken for $\phi < 0.12$ and a value of 83.8 for $\phi > 0.12$. The value of C_D using eq. 7.7 is calculated based on the average flow characteristics in the vegetation zone, as such, a constant value for the vegetation canopy is obtained.

For the diffusion term, the turbulent eddy viscosity ν_t is calculated using an algebraic model (equation 4.44), which is repeated here:

$$\nu_t = \alpha_0 U^* H \tag{7.8}$$

Table 7.6: Overview of the flow and vegetation parameters of the experiments by Zong and Nepf (2011). L = length of the flume, B = width of the flume, S_0 the bottom slope. L Fl, M Fl and H Fl indicate respectively low, medium and high flow rate. For the vegetation is d the diameter of the dowels, a the frontal area per unit volume $[\mathrm{m}^{-1}]$ and m the number of dowels per unit area. For the hydraulic parameters C_f is the friction coefficient of the bed, n_b the Manning coefficient of the bed, U_∞ the upstream velocity and H the water depth. The velocity uncertainty was estimated at 0.005 m/s and the uncertainty for the water heights 0.005 m.

		Dense Vegetation			Sparse Vegetation		
		L Fl	M Fl	H Fl	L Fl	M Fl	H Fl
L	[m]				16		
B	[m]				1.2		
S_0	[m/m]				0.0		
d	[m]		0.006			0.006	
a	[1/m]		21			4	
m	[1/m^2]		3500			666	
C_f	[-]		0.006			0.006	
n_b	[s/m$^{1/3}$]		0.018			0.018	
U_∞	[m/s]	0.050	0.090	0.111	0.050	0.090	0.111
H	[m]	0.12	0.13	0.14	0.12	0.13	0.14

with H the water depth [m], U^* the friction velocity [m/s] and α_0 a proportional constant [-]. A value for ν_t is calculated in each grid cell, based on the local depth-averaged velocity and water depth.

A grid size of 5 cm in both streamwise and lateral direction is selected for the model simulations of Zong and Nepf (2011), resulting in a total of 7680 computational nodes in the domain of interest. Downstream, a zone of 10 m length was added to avoid downstream boundary effects, especially reflections. A small timestep of 0.1 s was selected. The model output was averaged over a sufficient number of time steps (minimal 6000), and only time-averaged values are shown hereafter. A flux boundary condition was selected upstream to set the discharge, a fixed water depth was imposed at the downstream end.

7.3.3 Results

The model simulations are validated with the experimental data of Zong and Nepf (2011). For the model simulations, both the drag coefficient C_D and the proportionality constant α_0 in the algebraic model to determine ν_t, were varied. For the drag coefficient values of 1.0, 2.0 and the equation proposed by Tanino and

Nepf (2008) were used. For the parameter α_0, the values ranged between 0.05 and 0.30 with intervals of 0.05, covering the range of values which are most frequently mentioned in literature (see Chapter 4).

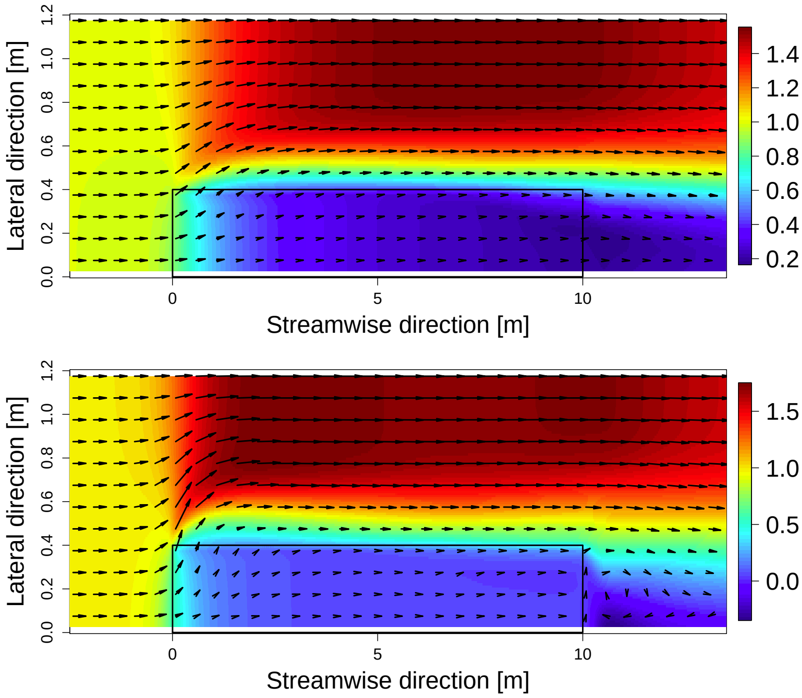

Figure 7.6: Planview of the averaged, streamwise velocities U normalised by the upstream velocity U_∞. The vegetation edge is indicated by the black contour line. The example shown is for the medium flow case with sparse (top) and dense (bottom) vegetation and a C_D coefficient calculated with the equation presented by Tanino and Nepf (2008).

The general flow patterns can be observed in Figure 7.6, for both the sparse (top) and dense (bottom) vegetation case. Because of the additional drag by vegetation, velocity at the vegetative side is retarded compared to the velocity in the free-flowing zone next to the vegetation. A small recirculation zone is observed just behind the vegetation patch in the case of dense vegetation. A representative longitudinal velocity profile through the center of the vegetation (at y = 0.2 m) is presented in Figure 7.7, for both the dense and sparse vegetation canopy, in case of low flow. In the first place, a good agreement between the data and the simulation results is noticed, as the general trends are well represented. Generally, better results are found for simulations with a C_D value of 2 and using equation 7.7. For the sparse case, the difference between the three different simulations, with different drag coefficients, is larger. Using the expression of Tanino and Nepf (2008), a value for C_D for the sparse and dense patches of respectively 1.61 and 4.60 is found for the low flow case. An overview of the drag coefficients calculated with eq. 7.7 and the averaged, obtained Manning coefficient in the vegetation zone, using the method of Baptist et al. (2007) is given in Table 7.7. A drag coefficient of 2 was used by Zong and Nepf (2011) and White and Nepf (2007) for the canopies under consideration.

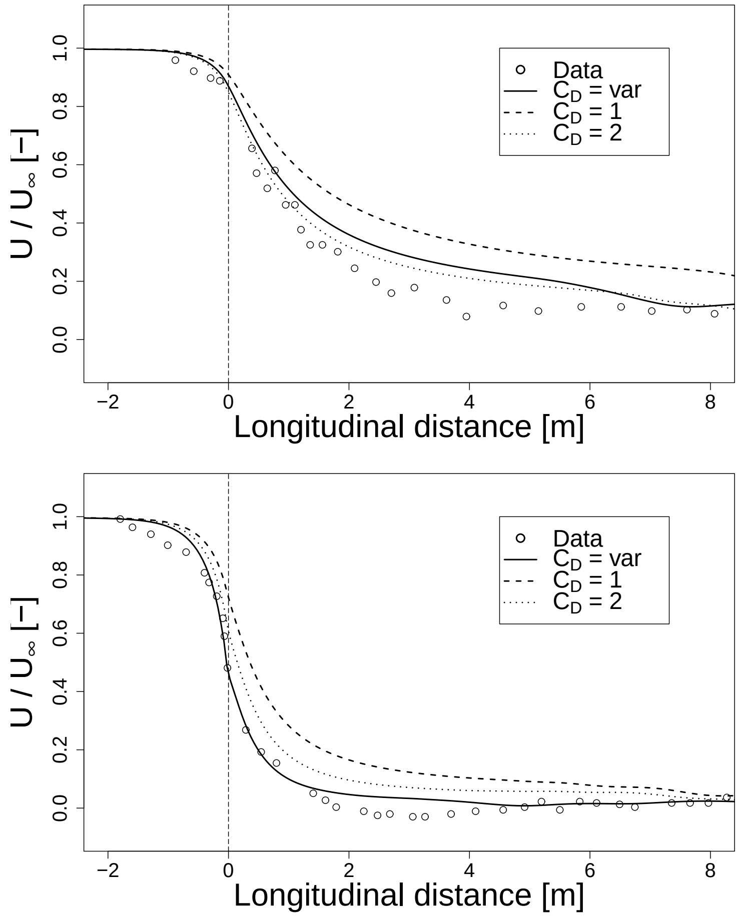

Figure 7.7: Model simulations of a longitudinal profile through the vegetation at y = 0.2 m for sparse (top) and dense (bottom) vegetation at low flow conditions. The vertical line at x = 0 m represents the upstream edge of the vegetation patch. Each plot contains three simulations, with C_D = 1, C_D = 2 and C_D according to equation 7.7. Measurement data are taken from Zong and Nepf (2011), Figure 6.

An overview of the data is presented in Table 7.8. U_1 is the streamwise velocity at y = 0.2 m, which is defined here as the average velocity in the vegetation patch from the diversion zone x_D (see below) till the end of the patch. U_2 is the streamwise velocity at y = 0.9 m, calculated over the same distance as U_1. For the sparse cases, U_1 doubled, using a value of C_D = 2 compared to a value of C_D = 1. For C_D = 2 and C_D = 4.6 the simulations match the data really well. For the dense case, the simulations results are within uncertainty independent of the drag coefficient and slightly higher than the measured data. From the experimental data, a difference between the values of U_2 and U_1 of 1.8 and 1.6 times U_∞ is found, respectively for the dense and sparse patches. Similar values are found for the simulations with higher drag coefficient.

The sensitivity for the parameter C_D in a range from 0.5 to 3.0, was tested for both the sparse and dense case. Values of U_1/U_∞ are shown in Figure 7.8, both at a position at the leading edge of the vegetation x = 0 m and x = 7m, in the developed flow region. It can be observed that the sensitivity for C_D is for both cases high at the leading edge of the patch. However, in the developed region, the effect of the drag is very limited in the case of dense vegetation, the density of the vegetation stems is clearly a dominant factor here. For the sparse case however, within the tested range, the results of U_1 in the developed region of the vegetation remain much more dependent on the drag coefficient.

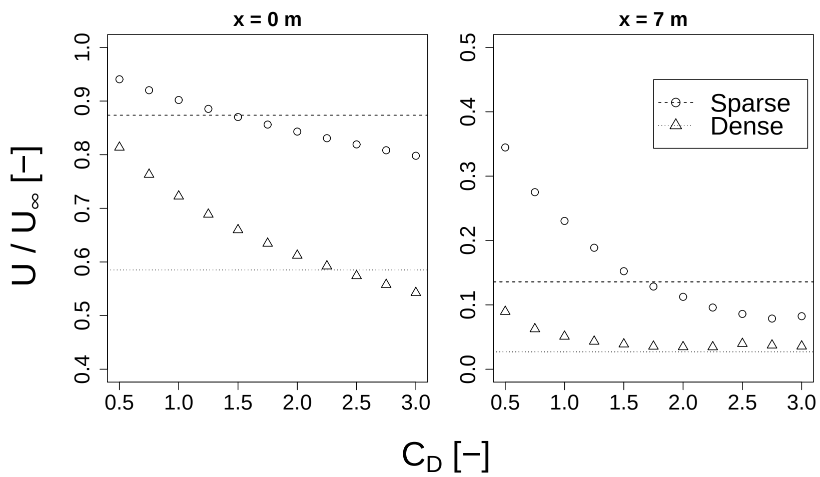

Figure 7.8: Normalised streamwise velocity at the leading edge (x = 0 m) and in the developed region (x = 7 m) of the vegetation patch in function of the drag coefficient C_D. Results are presented for both the sparse and dense vegetation cases. The measurement data for x = 7 m are added by a horizontal line.

Table 7.7: Overview of the Manning coefficients [$\mathrm{s/m^{1/3}}$] used in the simulations for different values of the drag coefficient C_D and low flow (Ul), medium flow (Um) and high flow (Uh) conditions. The Manning coefficient is calculated using the method of Baptist et al. (2007). For C_D = var, the C_D value is calculated using equation 7.7, the according C_D values are presented between brackets.

Run	n_{Veg} (C_D = 1)	n_{Veg} (C_D = 2)	n_{Veg} (C_D = var)
Sparse, Ul	0.115	0.161	0.145 (1.61)
Sparse, Um	0.121	0.171	0.141 (1.36)
Sparse, Uh	0.127	0.179	0.146 (1.32)
Dense, Ul	0.261	0.368	0.558 (4.60)
Dense, Um	0.275	0.389	0.474 (2.97)
Dense, Uh	0.290	0.409	0.480 (2.76)

Both for the sparse and dense vegetation, the cases with different incoming velocity (low, medium, high) are presented in Figure 7.9. As mentioned by Zong and Nepf (2011), the flow, scaled by the upstream velocity U_∞, is self-similar. This can be observed in Figure 7.9 (both top and bottom figure), as the normalised profiles collapse, which can be noted for both the simulations and the measurements. Therefore, the results for the different flow rates can be compared and averaged.

The upstream adjustment length L_0 is a zone before the leading edge of the vegetation patch, where the velocity starts to decrease. Zong and Nepf (2011) describe an upstream adjustment length L_0, for both dense and sparse cases, of respectively 1 m and 0.5 m from the leading edge of the vegetation (Table 7.9). The length of this upstream adjustment zone is estimated in the model simulations as well, where the starting edge of L_0 is defined at the position where $U/U_\infty < 0.95$ (Table 7.9). The adjustment length calculated from the simulations are found to be independent of the incoming flow condition and are slightly shorter than the measured values, namely 80 vs 100 cm for the dense cases and 35 vs. 50 cm for the sparse cases. Another flow characteristic is the diversion zone, which is the zone in the vegetation patch, where the velocity decelerates. Accordingly, the lateral velocity peaks in this zone. Beyond the diversion zone, the velocity in the patch is constant and the lateral velocity levels off. To delineate this diversion zone, a velocity threshold V/U_∞ = 0.01 was selected. The zone from the leading edge of the vegetation till the position where this velocity threshold is reached, is considered as the diversion zone x_D. However, also the lateral position has an influence on this value, e.g. Zong and Nepf (2011) define the values for the lateral velocities V at y = 0.20 m. In Table 7.9 the values x_D for y = 0.2 m and y = 0.4 m are given, which gives an idea of the uncertainty on the value of x_D. The measured data fall within the range of x_D given from the simulations. However, it should be mentioned that this range

Table 7.8: Overview of the flow characteristics. U_1 [m/s] is the velocity in the vegetation patch at y = 0.2 m, U_2 [m/s] is the velocity next to the vegetation patch at y = 0.9 m, and U_∞ the upstream velocity [m/s]. The characteristics for all flow cases are presented, for simulations with α_0 = 0.

			Dense Vegetation			
		C_D	Low flow	Medium flow	High flow	Mean
U_1/U_∞	[-]	Data:	0.02 ± 0.02	0.02 ± 0.01	0.03 ± 0.009	0.02 ± 0.01
		1	0.08 ± 0.03	0.07 ± 0.03	0.06 ± 0.03	0.06 ± 0.03
		2	0.05 ± 0.02	0.05 ± 0.02	0.05 ± 0.02	0.05 ± 0.03
		var	0.02 ± 0.02	0.02 ± 0.01	0.03 ± 0.01	0.02 ± 0.02
U_2/U_∞	[-]	Data:	1.80 ± 0.2	1.80 ± 0.2	1.80 ± 0.2	1.80 ± 0.2
		1	1.68 ± 0.01	1.70 ± 0.01	1.72 ± 0.01	1.70 ± 0.01
		2	1.72 ± 0.02	1.74 ± 0.02	1.75 ± 0.02	1.74 ± 0.02
		var	1.77 ± 0.03	1.76 ± 0.02	1.77 ± 0.02	1.77 ± 0.02
			Sparse Vegetation			
		C_D	Low flow	Medium flow	High flow	Mean
U_1/U_∞	[-]	Data:	0.12 ± 0.02	0.12 ± 0.01	0.13 ± 0.01	0.12 ± 0.01
		1	0.24 ± 0.03	0.23 ± 0.03	0.22 ± 0.04	0.23 ± 0.01
		2	0.14 ± 0.03	0.13 ± 0.04	0.12 ± 0.04	0.12 ± 0.01
		var	0.17 ± 0.05	0.16 ± 0.04	0.16 ± 0.04	0.16 ± 0.04
U_2/U_∞	[-]	Data:	1.70 ± 0.2	1.67 ± 0.1	1.78 ± 0.1	1.71 ± 0.1
		1	1.53 ± 0.01	1.55 ± 0.01	1.56 ± 0.01	1.55 ± 0.01
		2	1.61 ± 0.01	1.62 ± 0.01	1.64 ± 0.01	1.62 ± 0.01
		var	1.59 ± 0.01	1.58 ± 0.01	1.59 ± 0.01	1.59 ± 0.01

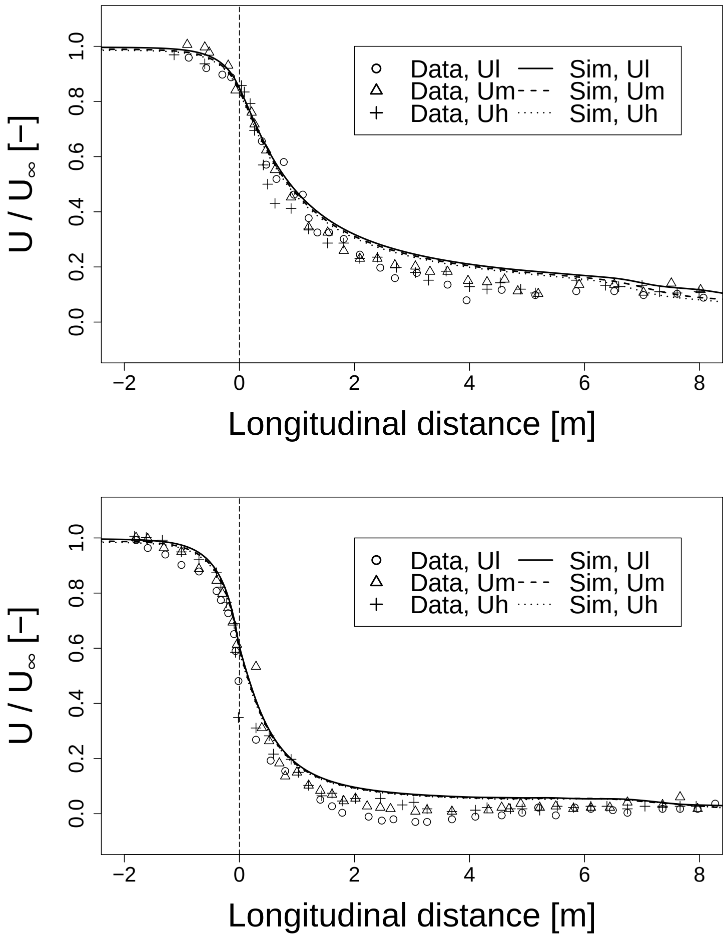

Figure 7.9: Model simulations of a longitudinal profile for the sparse (top) and dense (bottom) vegetation at different flow conditions, namely low flow (Ul), medium flow (Um) and high flow (Uh) for C_D = 2. The vertical line at x = 0 m represents the upstream edge of the vegetation patch. Measurement data are taken from Zong and Nepf (2011), Figure 6.

Table 7.9: Overview of the flow characteristics. L_0 indicates the upstream adjustment length [m], x_D the length of the diversion zone [m]. The range for x_D from the simulations is obtained by determining x_D at y = 0.2 m (minimum values) and at y = 0.4 m. Measurement data are found in Zong and Nepf (2011). The characteristics for the simulations with C_D = 2 are presented.

		Data	Dense Vegetation		
			Low flow	Medium flow	High flow
L_0	[m]	1.00	0.8 $\pm$ 0.1	0.8 $\pm$ 0.1	0.8 $\pm$ 0.1
x_D	[m]	2.00 $\pm$ 0.10	1.85 - 2.40	1.80 - 2.40	1.80 - 2.40
		Data	**Sparse Vegetation**		
			Low flow	Medium flow	High flow
L_0	[m]	0.5	0.35 $\pm$ 0.1	0.35 $\pm$ 0.1	0.45 $\pm$ 0.1
x_D	[m]	4.00 $\pm$ 0.1	3.0 - 4.3	2.95 - 4.3	2.95 - 4.25

is quite large.

Also some lateral transects of the streamwise velocity U are selected in selected cross-sections, consistent with the data presented in Zong and Nepf (2011). In these lateral profiles (Figure 7.10, at a distance x = 6.75 m (dense canopy) and x = 7.60 m (sparse canopy) from the upstream edge of the vegetation) a good prediction of the width of the shear layer (δ_0) can be observed. For the sparse case, a very good prediction of the shape layer is found for each simulations. Better agreement for the velocities U_1 and U_2 are found for C_D = 2 and a calculated C_D, as mentioned for the observations of the longitudinal profiles. A slight overestimation is observed for the flow through the patch, and due to mass conservation accordingly a small underestimation of the flow in the free flowing section. This phenomenon will be slightly enhanced due to the implementation of a free-slip boundary layer at the side wall (meaning that no gradient is assumed), compared to a more appropriate no-slip boundary. For the dense case, almost no difference between the different simulations can be observed. The width of the shear layer is adequately represented, but the simulations underestimate the measurements slightly, for which a steeper gradient is found close to the vegetation edge. This steep increase of the velocities in the shear layer is described in White and Nepf (2007). Comparing the dense and sparse lateral transects, one could conclude that the shear layer in the latter case is better represented.

As mentioned before, not only the drag coefficient C_D was varied, but also the proportional constant α_0 for the algebraic diffusion model. Till now, results are

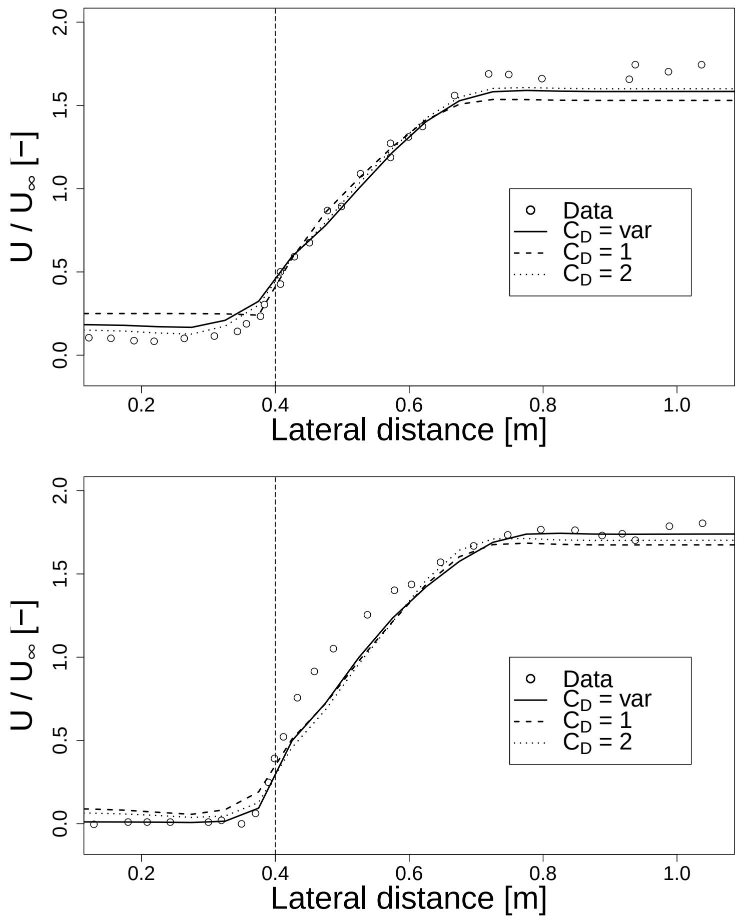

Figure 7.10: Model simulations of a lateral profile for the sparse (top) and dense (bottom) vegetation at low flow conditions. The position of this profile from the start of the vegetation is respectively x = 7.60 m and x = 6.75 m. The vertical line at y = 0.4 m represents the side edge of the vegetation patch. Each plot contains three simulations, with C_D = 1, C_D = 2 and C_D according to equation 7.7 and α_0 = 0.0. Measurement data are taken from Zong and Nepf (2011), Figure 7.

Table 7.10: Overview of the average eddy diffusivity $\bar{\nu}_t$ [m^2/s] in the simulations with different values for the proportional constant α_0. The average diffusivity was calculated in the region next to the vegetation ($\bar{\nu}_t, Side$) and in the vegetation zone itself ($\bar{\nu}_t, Veg$)

Run	α_0	$\bar{\nu}_t, Side$	$\bar{\nu}_t, Veg$
Sparse, Uh	0.05	7.684e-05	2.066e-05
	0.10	1.531e-04	4.195e-05
	0.15	2.293e-04	6.327e-05
	0.20	3.054e-04	8.574e-05
	0.25	3.812e-04	1.088e-04
	0.30	4.569e-04	1.324e-04
Dense, Uh	0.05	8.276e-05	7.788e-06
	0.10	1.653e-04	1.576e-05
	0.15	2.480e-04	2.256e-05
	0.20	3.298e-04	2.982e-05
	0.25	4.113e-04	3.694e-05
	0.30	4.925e-04	4.469e-05

shown with α_0 = 0. The effect of this parameter is shown in Figure 7.11 and in Table 7.10 with a drag coefficient C_D = 2 (for which the measurements and simulations agree best). Results for a lateral profile and the dense vegetation are shown, as in this case, gradients are the highest. For different α_0 values, no differences between the longitudinal profiles could be observed (data not shown). In the lateral direction, it can be observed that the gradients are smoothed when the value of α_0 is increased, which, of course, is what diffusion does! The effect of α_0 on the average eddy diffusivity is shown in Table 7.10. The average eddy diffusivity in the vegetation is lower compared to the eddy diffusivity in the zone next to the vegetation, because of higher velocities here. Based on the fact that the differences are small changing α_0, especially when $\alpha_0 > 0.10$ and based on previous studies by other authors (Ball et al., 1996; Vionnet et al., 2004), a value of α_0 = 0.1 is retained for further use.

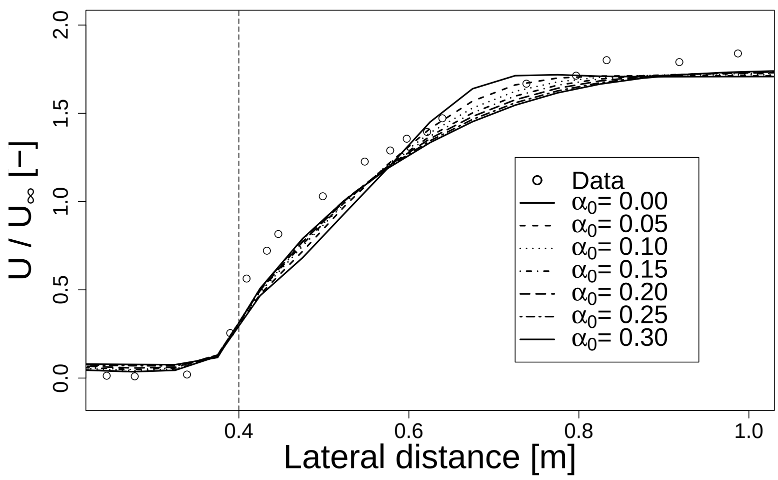

Figure 7.11: Model simulations of a lateral profile for the dense vegetation at high flow conditions. The position of this profile from the start of the vegetation is x = 6.75 m. The vertical line at y = 0.4 m represents the side edge of the vegetation patch. Simulations with α_0 = 0.00,0.05,0.10,0.15,0.20,0.25,0.30 are shown. Measurement data are taken from Zong and Nepf (2011), Figure 7.

7.4 Patches of vegetation

7.4.1 Overview of the experimental studies

Furthermore, the performance of the model is tested for patches of vegetation, which are considered as clumps of vegetation with free edges on each side (Figure 7.12). As validation data, the experiments of Zong and Nepf (2012) are used and the main flow characteristics are compared. In these experiments, circular patches with different densities are placed in a flume and their wake behaviour is analysed. A steady-wake zone, with length L_1 and constant low velocity U_1, is observed directly behind the patch after which a wake recovery is observed. This behaviour is explained in more detail in Chapter 3 and Zong and Nepf (2012). An overview of the used parameters is given in Table 7.11.

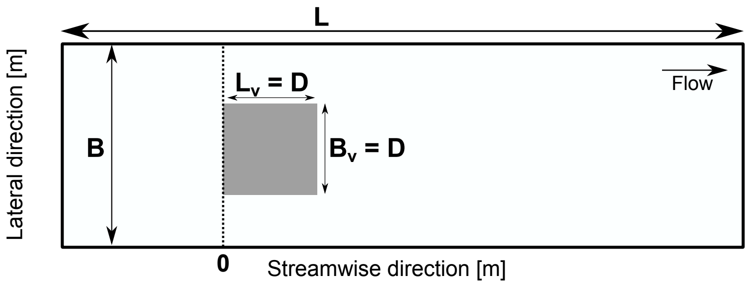

Figure 7.12: Overview of the configuration with an emergent vegetation patch of diameter D in the center of the flume. The vegetation zone is indicated by the gray area. The flow direction is indicated with an arrow, from left to right. x = 0 m is defined at the upstream edge of the vegetation.

The patches consist of wooden dowels with a diameter d of 0.006 m and contain respectively 1000, 1500, 3333, 4833 and 128333 dowels per square meter. The vegetation parameters are slightly adopted compared to the original experiments. The original patch diameter D of 22 cm, is changed to 22.5 cm and a rectangular shape is chosen, which is easier to represent with the rectangular grid. This is not supposed to change the main flow characteristics, as e.g. mentioned by Vandenbruwaene et al. (2011).

7.4.2 Model Settings

The model settings are mainly identical to the settings for the simulations with vegetation on 1 side (section 7.3). The grid size was set at 0.025 m, resulting in a total of 30720 grid cells in the domain of interest. Downstream, a zone of 10 m length was added to avoid downstream boundary effects. A small timestep of 0.1 s was selected. The model output was averaged over a sufficient number of time

Table 7.11: Overview of the flow parameters of the experiments by Zong and Nepf (2012). L = length of the flume, B = width of the flume, S_0 the bottom slope. For the vegetation is D the diameter of the patch, d the diameter of the dowels, a the frontal area per unit volume $[\mathrm{m}^{-1}]$ and m the number of dowels per unit area. For the hydraulic parameters C_f is a friction factor, n_b is the Manning coefficient of the bed, U_∞ the upstream velocity and H the water depth.

L	[m]			16		
B	[m]			1.2		
S_0	[m/m]			0.0		
D	[m]			0.22		
d	[m]			0.006		
a	[1/m]	77	29	20	9	6
m	[1/m^2]	12833	4833	3333	1500	1000
C_f	[-]			0.006		
n_b	[s/m$^{1/3}$]			0.018		
U_∞	[m/s]			0.098		
H	[m]			0.133		

steps (minimal 6000), both time-averaged and instantaneous values are shown below. As upstream boundary condition, a discharge flux boundary was selected. Downstream, a fixed water depth was imposed.

To account for the vegetation, the method of Baptist et al. (2007) is used. Additionaly, the vegetation drag was implemented by an additional drag term in the momentum equations, as described in equations 4.50 and 4.51. It should be mentioned that the method of Baptist et al. (2007), which is used for the implementation of vegetation in the model by translating vegetation characteristics to a Manning coefficient, is established for uniform flow. Also the expression used to determine the drag coefficient C_D, by Tanino and Nepf (2008), is experimentally established and developed for a long vegetation stand. In the case of vegetation patches, however, no uniform flow in the vegetation is reached. As such, both methods are used outside their tested domain.

For the diffusion term, the turbulent eddy viscosity ν_t is calculated using an algebraic model (equation 4.44), similar to the simulations with vegetation on one side of the flume. If no precision is made, this model is used, with α_0 = 0.1. Additionally, a depth-averaged mixing length model was tested also, which is described in Chapter 4, equation 4.47 and described in more detail in Cea et al. (2007).

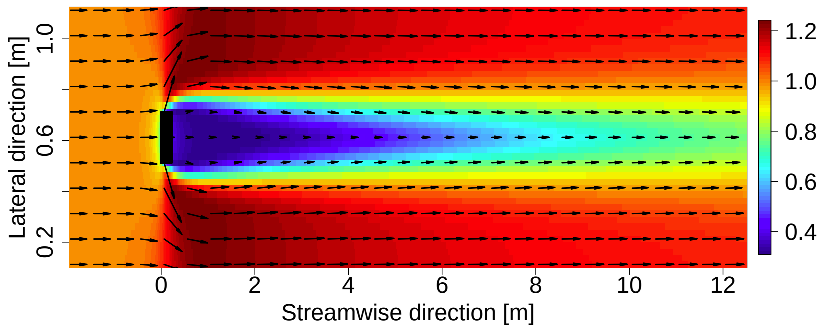

Figure 7.13: Planview of a simulation result of the normalised streamwise velocity for a patch with a density of 3333 dowels per unit area and a drag coefficient C_D of 2. The patch is indicated by a black rectangle. The velocity field is indicated by arrows. For clarity, to draw the arrows, the lateral velocities V are doubled compared to U.

7.4.3 Results

7.4.3.1 Mean values

An overview of the velocity field is shown in Figure 7.13. Uniform flow is disturbed because of the introduced vegetation drag, where accordingly a high flow diversion is observed. After the patch, low wake velocities are observed behind the vegetation, and consistently higher flow velocities are found next to the patch. Because of mixing and diffusion processes, the velocity gradient diminishes further away from the patch. An overview of the U_1 velocities is given in Table 7.12, for the simulations with five different densities, as described in Table 7.11, together with the experimental results of Zong and Nepf (2012). These values are given for several values of C_D and the implementation of both the method of Baptist et al. (2007) and a separate drag term. It is observed that the drag coefficient is an important calibration parameter to obtain a velocity behind the patch, consistent with the data, and this value is different for both implemented methods. It can be observed from Table 7.12 that the same C_D value for different implementations, lead to a slightly other prediction of the velocity behind the patch.

In Figure 7.14, the velocity in the steady wake zone found in Zong and Nepf (2012) are compared with the velocities in this zone, calculated from the model simulations. Simulations under consideration are performed using a drag coefficient C_D of 1, 2 and a calculated drag coefficient, using equation 7.7, as presented by Tanino and Nepf (2008). For simulations with an additional drag term, a drag coefficient C_D of 2 and a calculation of the drag coefficient was used. For low and high values of $C_D aD$ better agreements can be observed between model and simulations, for

Table 7.12: Overview of the velocity U_1 behind the patches, for patches with different densities (see Table 7.11). The experimental values from Zong and Nepf (2012), Table 1. Simulation results, using the Baptist et al. (2007) equation, are shown for C_D = 1, C_D = 2 and C_D = var, for which the drag coefficient is calculated using expression 7.7. Simulations results, using an extra drag term, are shown for C_D = 2 and C_D = var, calculated with eq. 7.7. The calculated drag coefficients are indicated between brackets. The velocities are expressed in m/s. For the simulations, a standard deviation on U_1 of approx. 0.003 was found for all values.

	Exp	Simulations				
		Baptist			Drag term	
		$(C_D = 1)$	$(C_D = 2)$	$(C_D = var)$	$(C_D = 2)$	$(C_D = var)$
Exp 1	0.058	0.078	0.063	0.073 (1.26)	0.046	0.057 (1.27)
Exp 2	0.038	0.070	0.052	0.062 (1.39)	0.036	0.044 (1.40)
Exp 3	0.003	0.050	0.033	0.034 (1.87)	0.021	0.021 (1.91)
Exp 4	0.003	0.040	0.025	0.020 (2.69)	0.015	0.012 (2.92)
Exp 5	0	0.020	0.013	0.007 (5.31)	0.010	0.004 (5.87)

appropriate combinations of C_D and implemented resistance term.

However, in the middle range, a big shift can be observed in the measurements going from sparse patches ($(C_D)aD < 4$), where U_1 is clearly larger than 0, to dense patches ($(C_D)aD > 4$), where the steady wake velocity is approximately 0. Such a shift cannot be observed in the model results, a more gentle decrease is observed. Clearly, the combination of C_D and resistance model is not able to simulate all the critical phenomenons to represent this faster shift to low exit and wake velocities, seen in the transition from high-flow to low-flow blockage. It is clear that in this range, the difference between U_1 calculated from the simulations, for the selected C_D values, and U_1 from the measurements is largest. In Figure 7.15, the calculated Manning values for the patches, using the method of Baptist et al. (2007), are shown. The trend of the slowly decreasing exit velocities behind the patch with increasing $C_D aD$, is confirmed here by slowly increasing Manning coefficients for the patch with increasing $C_D aD$.

In Figure 7.16, the velocities through the patch center are depicted for two dense patch cases, with a solid volume fraction of respectively ϕ = 0.36 and 0.10. C_D values of 5.87 (ϕ = 0.36) and 1.91 (ϕ = 0.10) where found using equation 7.7. For the patch with a solid volume fraction ϕ of 0.36, simulations with two C_D values are shown. Both curves are very similar. The case with C_D = 5.87 has a more pronounced recirculation zone and starts to accelerate faster behind the patch compared to the case with C_D = 2. However, the rate of acceleration is equal for both cases. Beyond this acceleration, a clear dip is observed before the velocity

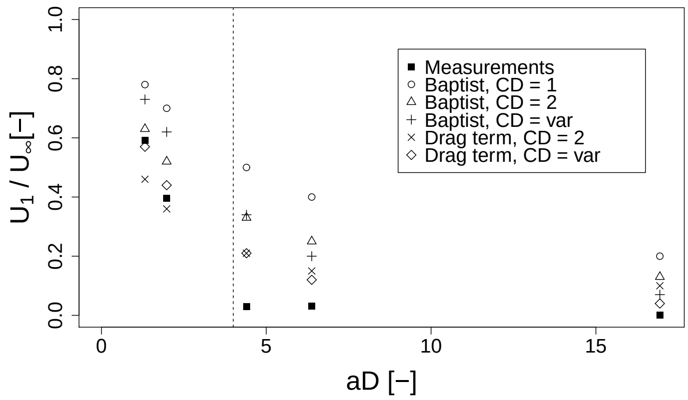

Figure 7.14: Measurement (Zong and Nepf, 2012) and simulation results, using a value of 1, 2 and equation7.7 for C_D for the velocity in the steady wake zone behind the patch. The vertical line represents the transition between high and low-flow blockage, as suggested by Chen et al. (2012), assuming C_D for the measurements.

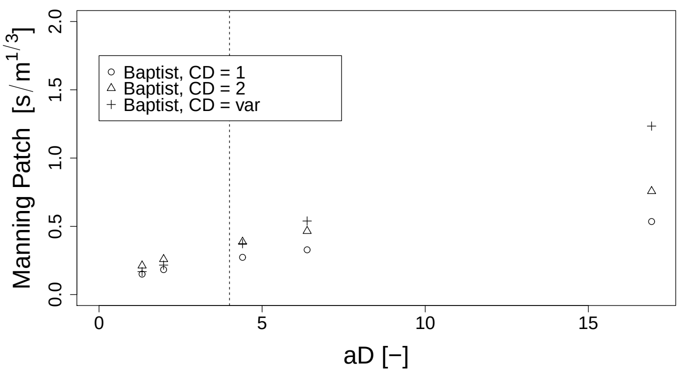

Figure 7.15: Mean Manning coefficient $[\mathrm{s/m^{1/3}}]$ in the patch for simulations with C_D = 1, C_D = 2 and C_D calculated using the method of Tanino and Nepf (2008).

starts to level off, this dip is neither observed in the experimental values, neither expected from the simulations. Still, no clear reason for this observation can be found. Using either a sponge layer (zone with increased viscosity) or an analytical solution didn't change the results in the domain of interest. Also implementing an additional zone of higher viscosity upstream didn't result in profiles without this "‘observed"’ dip in the profile. This profile is consistent for all simulations where strong oscillations appear (see further). In the case ϕ = 0.1 and C_D = 1.91 such a steep increase was not observed, and as such the simulations differ consistently from the measurements. For the upstream adjustment zone L_0, the distance before the patch where $U/U_\infty < 0.95$, a range of 1.35 - 1.75 D is found for the velocity profiles shown, slightly smaller than the value predicted by Rominger and Nepf (2011) (2.0 $\pm$ 0.35 D), but the same order of magnitude. This good agreement can be observed in Figure 7.16 as well, for ϕ = 0.1.

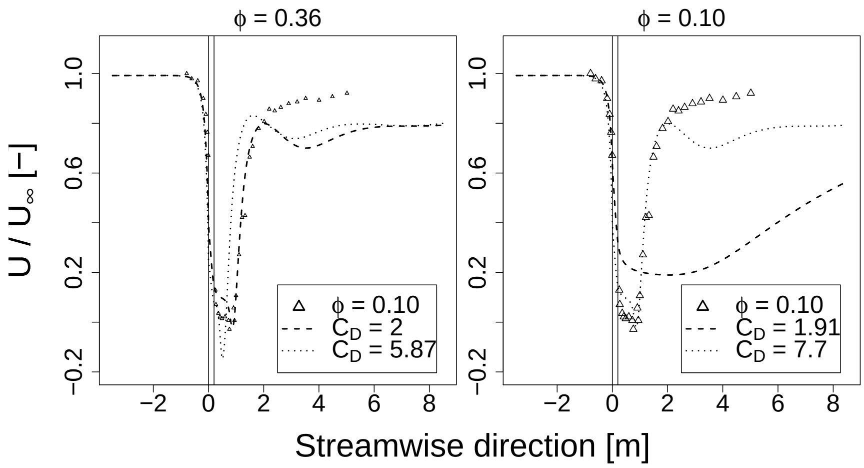

Figure 7.16: Overview of the centerline velocity profiles of the normalised stream wise velocity. Simulations are shown for patches consisting of 12833 dowels per m^2 (ϕ = 0.36) in the left plot and 3333 dowels per m^2 (ϕ = 0.10) in the plot on the right. To represent vegetation in these simulations, a separated drag term was used. The patch is indicated by vertical lines. C_D values of 5.87 (ϕ = 0.36) and 1.91 (ϕ = 0.10) where found using equation 7.7. Measurements are shown for a single patch density (ϕ = 0.10), as no velocity profile was shown for denser patches (ϕ = 0.36) in Zong and Nepf (2012).

The steep recovery of the velocity is due to oscillations which are appearing in the simulations, and shown in Figure 7.17 (top right). In cases where a slower recovery of the velocity is observed (ϕ = 0.10 and C_D = 1.9), no oscillations are observed (Figure 7.17, top left). The averaged values for the velocities, in plan-view, are also shown in Figure 7.17. A stability parameter $S = C_f \cdot D/H$ is used to describe the stability of the shallow wake, with C_f a friction coefficient [-], D the diameter of the object [m] and H the water depth [m]. If this stability parameter is above a certain threshold, the vortex shedding and consequent vortex street is suppressed by the bed friction, indicated by C_f (Stansby, 2006; Zong and Nepf, 2012), below that threshold, vortex shedding is occurring. A threshold for S of 0.2 is mentioned by Chen and Jirka (1995) for solid cylinders (Zong and Nepf, 2012), for conical islands Stansby (2006) mentions a critical value of 0.4. It is stated by Chen et al. (2012) that in the case of very high porosity, also no vortex streets are formed. In the simulations these oscillations appear also (see further description below). However as diffusivity is added by bed friction and a diffusion term, but also because of numerical diffusion, they will not appear for the same conditions as in the lab flume.

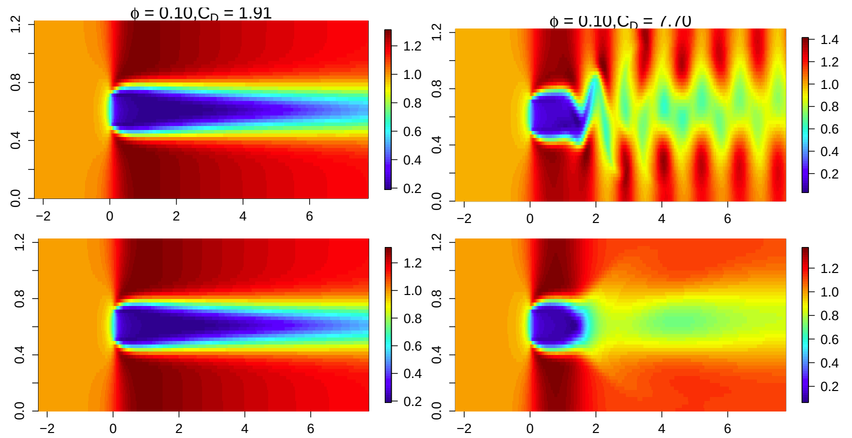

Figure 7.17: Planview of the simulation output after 5000 s (top) and time-averaged simulations (bottom). Simulations are shown for patches with ϕ = 0.10 and C_D = 1.91 (left) and C_D = 7.7 (right).

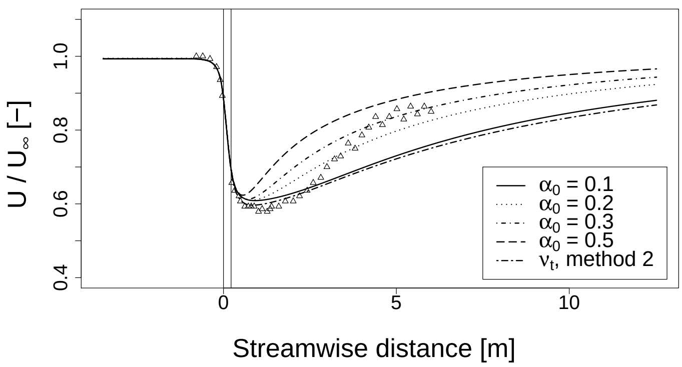

Figure 7.18: The normalised stream wise velocity in the centerline of the patch. Simulations are shown for different values of α_0. An additional simulation was performed with another expression (eq. 4.47) for ν_t. The patch has a density of 1000 dowels per unit area and a drag coefficient C_D of 2 was selected, with Baptist's method. The patch is indicated by vertical lines.

Profiles for sparse patches are depicted in Figure 7.18. It can be seen here that the simulations, using α_0 = 0.1, agree well till the moment that the velocity starts to re-accelerate. At this moment, the mixing in the model is slower compared to the experiment. As such, the value of α_0 was increased to enhance mixing. However, in these cases the mixing exceeds the observed process. Another expression for the calculations of ν_t was implemented, based on a mixing length model. However, no significant improvement was observed. In the simulations, no oscillations are observed. In the measurements however, a von Kàrmàn vortex street was observed starting/developping at the point, where the increasing values for the stream wise velocity are observed (beyond L_1). This mixing process was not accounted for in the simulations, resulting in lower acceleration rates. It should be noted, both in Figure 7.18 and 7.16 that in the case the velocities behind the patch are agreeing with the measurements, a reasonable prediction of the length L_1 is found. In this zone, however, velocities keep slowly descending in the simulation, compared to constant velocity values in the experiments.

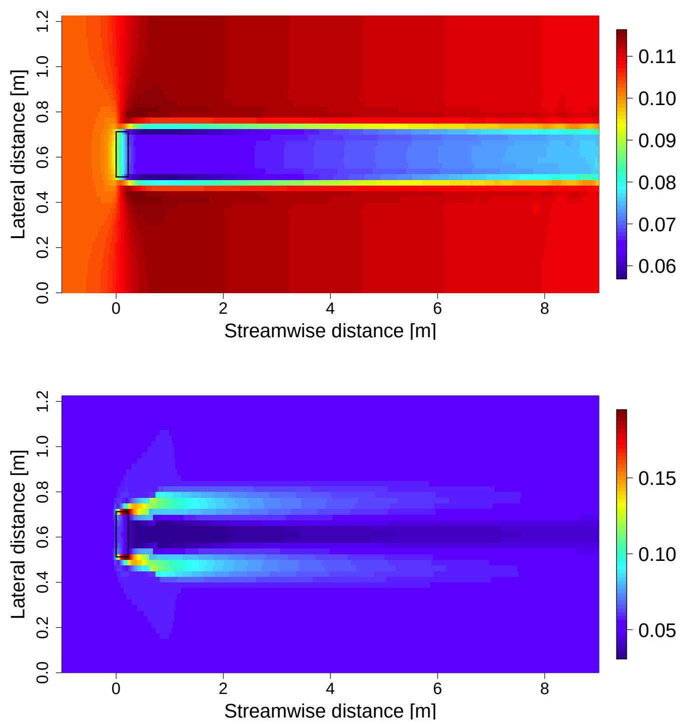

Figure 7.19: Planview of the viscosity coefficient ν_t $[\mathrm{m}^2/\mathrm{s}]$ using a depth-averaged parabolic eddy viscosity model, equation 4.44 (top) and a depth-averaged mixing length model, equation 4.47 (bottom). The values indicated in the legend are multiplied by 10^3. The patch is indicated by a black contour line.

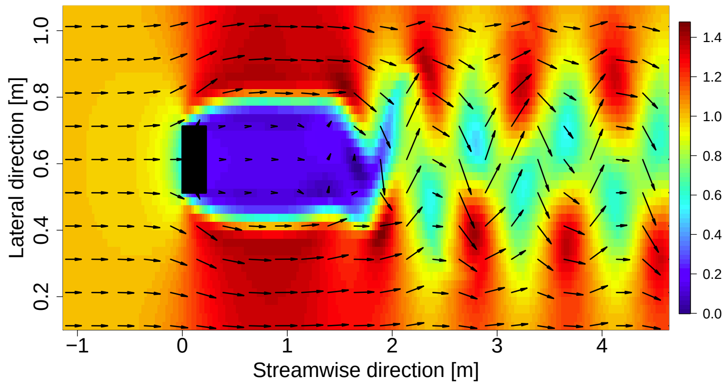

Figure 7.20: Planview of a simulation result after 20 000 s of simulation. The normalised stream wise velocity for a patch with a density of 12833 dowels per unit area and a drag coefficient C_D of 2 is depicted. The patch is indicated by a black polygon.

7.4.3.2 Oscillations

In cases where the C_D parameter is increased, to obtain smaller velocities in the wake, or in case of high patch densities, oscillations behind the patch starts to appear. As can be seen in Figure 7.20, beyond the vegetation patch, close to the patch a zone without oscillations is observed. Here, at a distance of approximately 1.5 m ($\approx 7D$) from the trailing edge of the patch, oscillations starts to appear. This reflects to the behaviour of a steady wake zone followed by a von Kàrmàn vortex street, as described by e.g. Zong and Nepf (2012).

To view the flow behaviour of these oscillations in the course of time, some selected points in the wake behind the patch are described. The position of the three selected points plotted, are depicted in Figure 7.21 and chosen to be in the zone behind the patch without oscillations, at the zone where these oscillations starts to appear and within this zone of oscillations. They are positioned at respectively 0.15 m, 1.65 m and 2.525 m behind the patch. After a periodic steady state is reached, the simulation results are written as output every 0.1 s and plotted in Figure 7.22. Both the lateral and stream wise velocities show no variations in time for a point closely behind the patch (Fig. 7.22). For the lateral velocities V further behind the patch, a regular pattern can be observed, with an estimated frequency of approximately 0.09 1/s (approximately 4 periods are experienced per 45 s). This agrees with a Strouhal number St of 0.2, which is similar to observations for cylinders with the same diameter (see e.g.Zong and Nepf (2012)). A small time lag between is observed for V at point 2 and V at point 3. For the stream wise velocity, at point 2 1.65 m from the patch, a superposition of oscillations can be observed. A longer

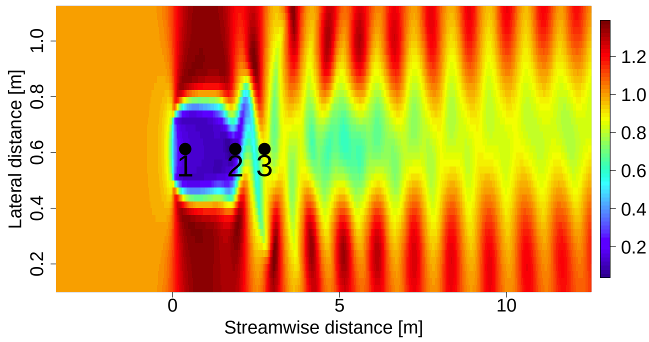

Figure 7.21: Planview of a simulation result after 10 200 s of simulation. The normalised stream wise velocity for a patch with a density of 12833 dowels per unit area and a drag coefficient C_D of 2 is depicted. The points which are selected for time output are indicated and depicted by black dots, positioned respectively 0.15 m, 1.65 m and 2.525 m from the trailing edge of the vegetation.

wave, with period T of approximately 100 s, corresponds with a wavelength of approx. 10 m ($U_\infty \cdot T$ = 0.1 m/s · 100 s $\approx$ 10 m). This wavelength corresponds with twice the distance to the upstream boundary, and as such a standing wave between this boundary and point 2 is supposed. No clear explanation for the variation in point 3 could be found. To account for this, additional viscosity was added in the first section of the flume ($\nu_t = 0.005\mathrm{m}^2/\mathrm{s}$). The results of this are shown in Figure 7.23. Here indeed a much more regular pattern of the oscillations is observed.

7.5 Patches of vegetation in a side-by-side configuration

7.5.1 Overview of the experimental study

The measurements described in Vandenbruwaene et al. (2011) are used as a validation data set for the configuration of patches, where two patches of vegetation are placed side-by-side, perpendicular on the flow direction. This case was preferred over the data set described in Chapter 3, as the flume was wider, and as such less influences of the side can be expected. Furthermore, the dimensions of the experiment are closer to the field scale. However, the empirical expressions found in Chapter 3 are also tested with the model results.

Vandenbruwaene et al. (2011) performed measurements in the wave basin of Deltares (Delft, the Netherlands), a flume 26 m long and 16 m width. In this flume, two square patches of equal size are placed in a side-by-side configuration with a

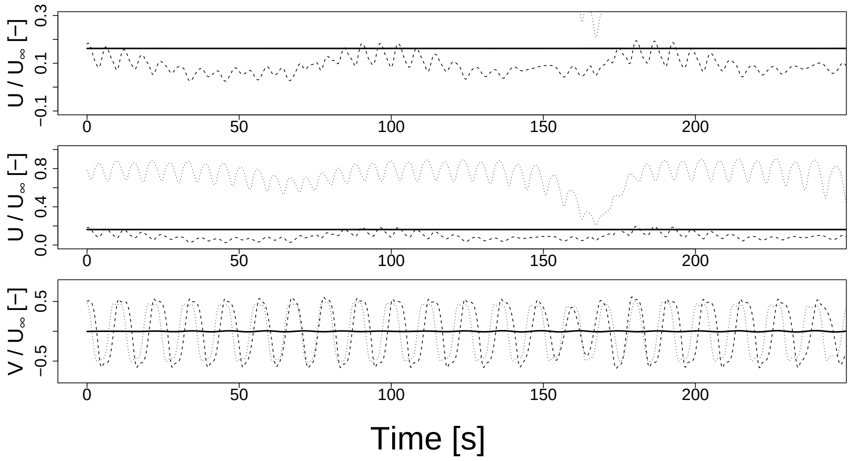

Figure 7.22: Time-evolution of the normalised streamwise U and lateral V velocity at three points on the centerline of the patch, indicated in Figure 7.21. The simulations shown are for a patch with a density of 12833 dowels per unit area and a drag coefficient C_D of 2. Simulations at point 1 are indicated by a full line, at point 2 by a an interrupted line and at points 3 by a dashed line.

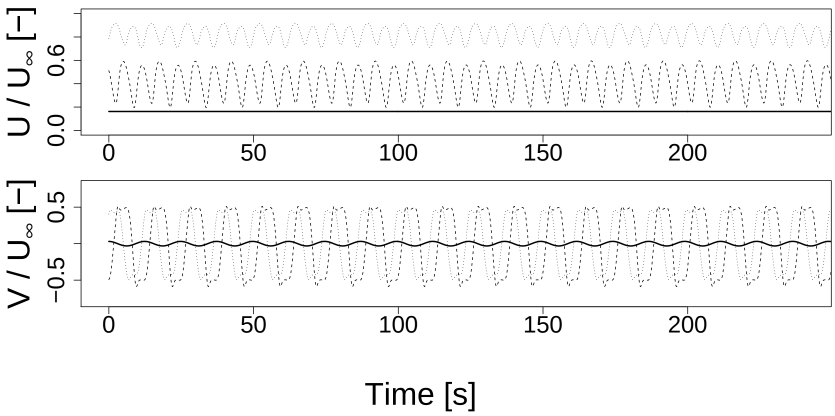

Figure 7.23: Time-evolution of the normalised streamwise U and lateral V velocity at three points on the centerline of the patch, indicated in Figure 7.21. The simulations shown are for a patch with a density of 12833 dowels per unit area and a drag coefficient C_D of 2. Simulations at point 1 are indicated by a full line, at point 2 by a an interrupted line and at points 3 by a dashed line. An additional zone of viscosity was added upstream.

Table 7.13: Overview of the flow and vegetation parameters of the experiments by Vandenbruwaene et al. (2011). L = length of the flume, B = width of the flume, S_0 the bottom slope. For the vegetation is D the diameter of the patch, Δ the distance between the patches, d the diameter of the dowels and m the number of dowels per unit area and ΔS the average distance between the dowels. For the hydraulic parameters n_b is the Manning coefficient of the bed, U_∞ the upstream velocity and H the water depth. (*) are estimated based on the description in Vandenbruwaene et al. (2011)

L	[m]	26
B	[m]	16
S_0	[m/m]	0.0
D	[m]	1 / 2 / 3
Δ	[m]	0 / 0.3 / 1.3 / 2.3 / 3
d	[m]	0.043 $\pm$ 0.012 and 0.03 $\pm$ 0.011
m	[1/m^2]	658 $\pm$ 8
$n_b^{(*)}$	[s/m$^{1/3}$]	0.02
U_∞	[m/s]	0.1 / 0.2 / 0.3
H	[m]	0.30

variable gap spacing between the patches and variable patch sizes. Patch sizes varied from 1 to 3 m and gap spacings between 0 and 3 m. As such, the relative gap distance Δ/D is varied between 0 and 1.5. Flow measurements were performed with electromagnetic flow measurement devices (EMF) and Acoustic Doppler Velocimeters (ADV). The aim of the experiments was to quantify the effect of increasing patch size and decreasing patch inter-distance on the amount of flow acceleration next to and in between the patches. In contrast with previous sections, measurements were performed with real vegetation, an emergent plant species *Spartina anglica*. Based on the data, a shoot density of 658 stems/m^2 was used with an average shoot diameter of 0.0365 m. An overview of the parameters used for the measurements is given in Table 7.13 and a detailed overview of the tested and simulated configurations is given in Figure 7.24.

7.5.2 Model Settings

For this test cases, the 2D-SWE model is used, with the Baptist et al. (2007) equation to represent the vegetation resistance. In this equation, a drag coefficient C_D of 2 is selected, based on several test runs. For the diffusion term, a value of 0.1 is used for the α_0 parameter. Simulations were run for 20 000 s, with a time step of 0.1 s. For these parameters, steady state was assured. The values of the simulations shown are averaged values, over at least 6000 runs. The spatial grid discretisation

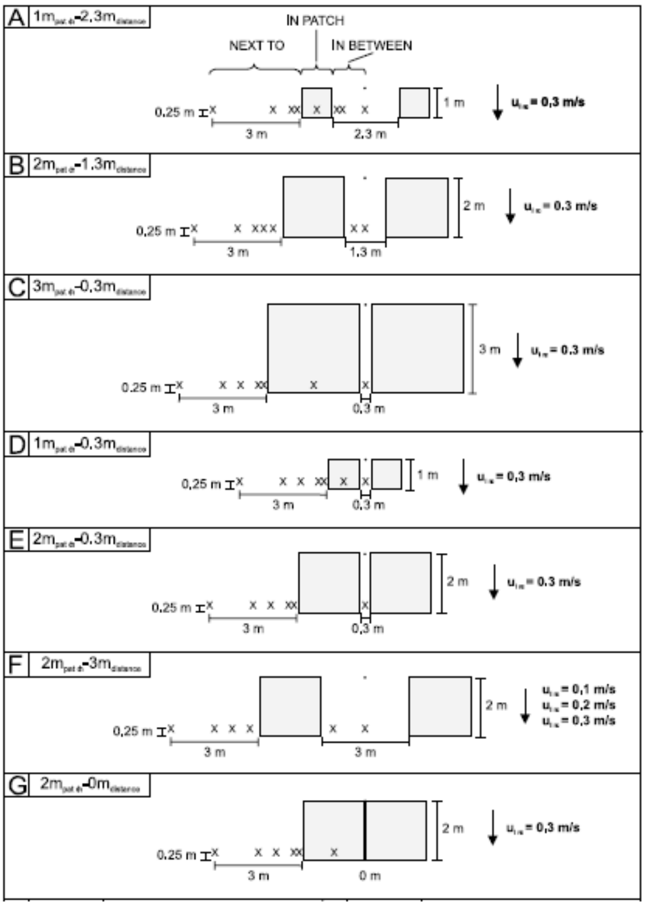

Figure 7.24: Overview of all the configurations (combination of patch sizes and gap distances) used in the experiments of Vandenbruwaene et al. (2011) and simulated with the 2D-model. The incoming velocities are only varied for configuration F. Figure integrally taken from Vandenbruwaene et al. (2011).

is 10 cm, equal in x and y direction, resulting in 160 · 260 = 41600 grid cells in the domain of interest. At the downstream boundary, an additional 10 m were used to avoid undesirable effects from the downstream boundary condition which was set. Upstream a flux boundary was set, setting the discharge through the flume, downstream a water depth was imposed.

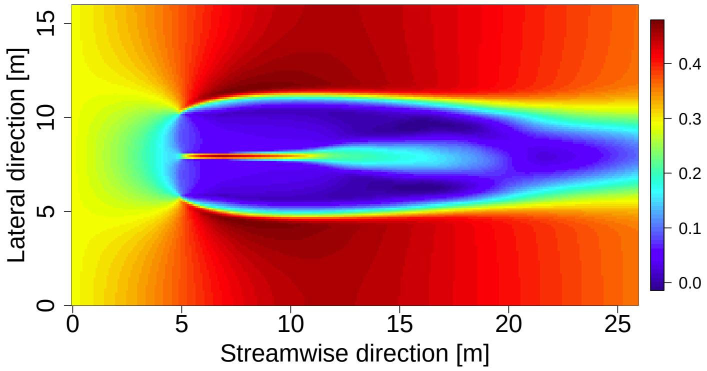

Figure 7.25: Planview of the streamwise velocity U for patch sizes D of 2 m and a gap distance of Δ = 0.3 m. The patches are indicated by black rectangles.

7.5.3 Results

Both the experimental and simulation results for the different configurations can be found in Figures 7.26, 7.27, 7.29 and 7.31. These plots present lateral transects at a distance of 0.25 m before the trailing edge of the vegetation patches. To be able to plot the simulations of the different configurations in one plot, and consistent with Vandenbruwaene et al. (2011), the transects next to the vegetation (both at the outside edge and in between the patches) is shown and the patch size itself is not depicted. The transects at the outside edge have negative values of y (positioned left of the patches in the plots), the transects in between the patches have positive values of y (positioned right of the patches in the plots). For some selected cases, where measurement data were available, transects behind the patches are depicted as well (Figures in 7.30).

In Figure 7.26, configurations with increasing patch sizes D and decreasing inter-patch distances Δ are shown (configuration A, B and C in Figure 7.24). In general, a good agreement between the measurements and the simulated data can be observed, with slightly better results for the smaller patches compared to the patch of 3 m diameter. The differences are the biggest in the steep shear layers just next to the patch. Due to the steep gradients in these zones, a small difference in measurement position can have a significant impact on the velocity magnitude measured. Furthermore, because of the flexibility of the plant, the surface area of the rooting zone of the plants can differ from the surface area covered by the canopy of the plants, and as such the position of the vegetation can vary a little bit. The maximum velocities next to the patch and in between the patch are almost identical for the configurations with the smaller patch sizes. For D = 1 and 2 m, U_{max} is 0.374 and 0.466 m/s outside of the patches and 0.379 and 0.482 m/s inside of the patches (see also Table 7.14), which is within 5 % equal. For the largest patch, D = 3 m, in the measurements, a difference of approx. 25 % is found between the maximum values next and in between the patches, which is approx. 10% for the simulations. As mentioned, this deviation is however larger than for the smaller patches.

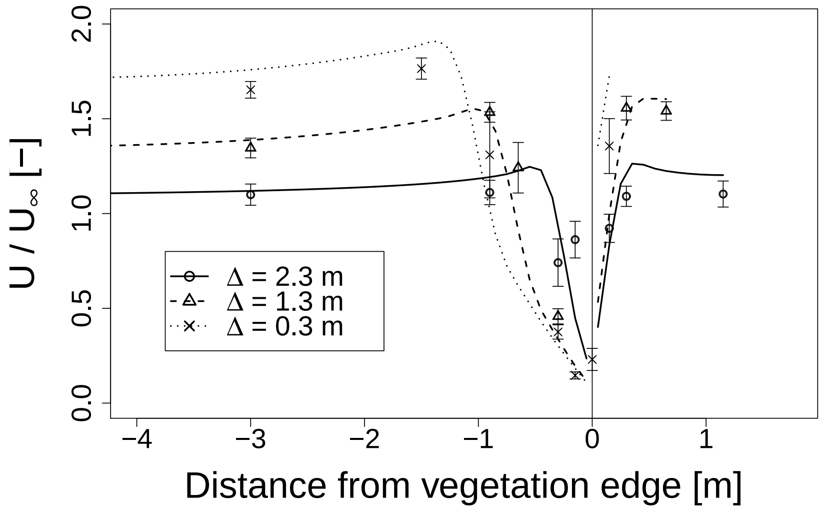

Figure 7.26: Lateral, normalised velocity profiles of the stream wise velocity U over one half of the flume. Both measurements and simulations for 3 different gap spacings and 3 different patch sizes are shown. The combinations are (D = 3 m, Δ = 0.3 m), (D = 2 m, Δ = 1.3 m) and (D = 1 m, Δ = 2.3 m). The error bars on the measurements points are the calculated rms values on the measurements. The patch is located at y = 0m, as such its actual width is not shown.

Table 7.14: Maximum velocities in the transect 0.25 m from the trailing edge of the vegetation patch. Both simulations (Sim) and experimental (Exp) values are given.

		Outside		In between	
D	Δ	Exp	Sim	Exp	Sim
1	2.3	0.333 ± 0.019	0.374	0.327 ± 0.016	0.379
2	1.3	0.460 ± 0.016	0.466	0.466 ± 0.019	0.482
3	0.3	0.529 ± 0.017	0.573	0.407 ± 0.043	0.518

The effect of the patch size D and a constant gap distance Δ, on the velocity pattern in a lateral transect is depicted in Figure 7.27. Combinations of D and Δ give a range of Δ/D from 0.3 till 0.1. From both the simulations and the measurements it can be concluded that only for a value Δ/D = 0.1 (here, a patch size of 3 m), a reduction of the maximum flow compared to the other side of the patch is observed. However, a reduction compared to the incoming velocity is never observed, which is also consistent with the observations in Chapter 3. On the outside edge of the patch, the simulations agree well with the observations, with increasing fitting when the patch sizes become smaller. At y = -3 m from the vegetation edge, the model simulations differ respectively 2 % (0.332 m/s vs 0.337 $\pm$ 0.026 m/s), 5 % (0.407 m/s vs 0.389 $\pm$ 0.015 m/s) and 4 % (0.516 m/s vs 0.496 $\pm$ 0.013 m/s) from the measurements, for patch sizes of 1 m, 2 m and 3 m.

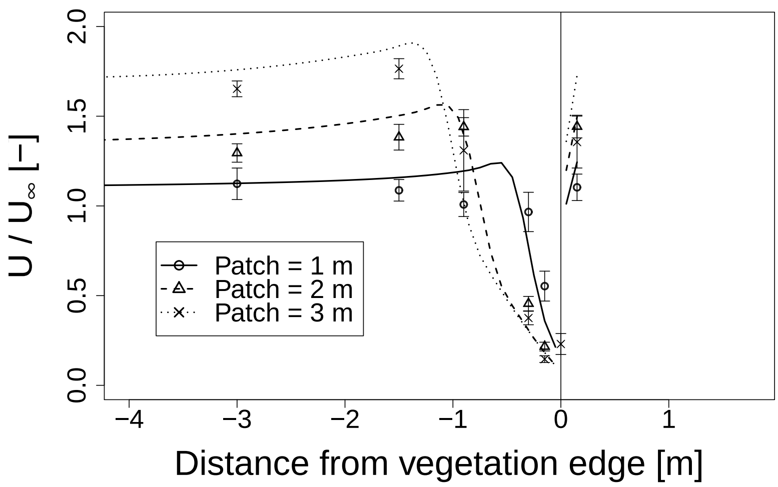

Figure 7.27: Lateral, normalised velocity profiles of the stream wise velocity U over one half of the flume. Both measurements and simulations for 3 different patch sizes are shown, with a size of respectively D = 3 m, D = 2 m and D = 1 m. The gap distance Δ is constant and amounts 0.3 m. The error bars on the measurements points are the calculated rms values on the measurements. The patch is located at y = 0 m, as such its actual width is not shown.

In Figures 7.26 and 7.27 next to the steep shear layer, a clear peak is observed in the lateral velocity profiles, which levels off further from the patches. This peak is also observed in the measurements, albeit somewhat less pronounced, which could be due to the coarser grid of measurements, and as such the maximum level of the peak is not observed or a slightly higher bed friction in the lab flume compared to the simulations. The peak is observed further from the patch, with increasing patch diameter D, respective values of 1.35 m, 1.05 m and 0.55 m for D = 3 m, 2 m and 1 m are found for the configurations shown in Figure 7.27. Identical values are found for the configurations plotted in Figure 7.27. However, scaling the lateral distance to the patch with the patch diameter D, as is shown in Figure 7.28, it can be observed that these peaks almost fall together at y/D = 0.55 $\pm$ 0.1 m.

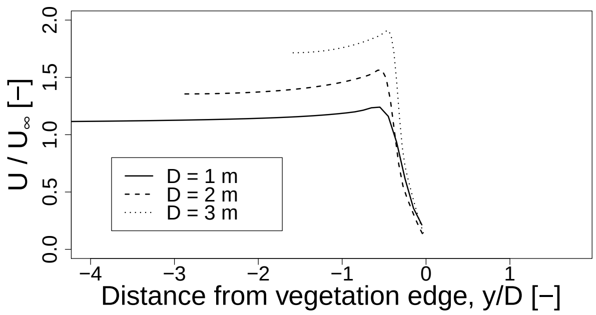

Figure 7.28: Lateral, normalised velocity profiles of the streamwise velocity U, one half of the flume is shown. Simulations for 3 different patch sizes, with a size of respectively D = 3 m, D = 2 m and D = 1 m. The gap distance Δ is constant and 0.3 m. The patch is located at y = 0 m.

Next, in Figure 7.29, configurations with a constant patch diameter D and variable interpatch distances Δ are shown (corresponding with configurations G, E, B and F in Figure 7.24). In general, model and experimental results agree well. As observed in the data (Vandenbruwaene et al., 2011), the maximum velocities change almost not at all with different gap spacings. Furthermore, no important differences can be observed between the different configurations. The steepness of the flow recovery next to the patches decreases slightly, with increasing gap distances.

For two configurations, namely with a patch size D of 2 m and a gap distance Δ of 0 m (Figure 7.30 (bottom)) and 3 m (Figure 7.30 (top)), transects further down from the patch are measured as well. Additional to the transects at x = 1.75 m (0.25 m from the trailing edge of the patch) which are shown before, transects are measured at x = 5 m and x = 7 m from the patch front. Both the velocities behind the patches as the profiles next to the patches are modelled adequately.

In a last step, the effect of different incoming velocities are tested. Both the absolute and relative values are shown in Figure 7.31. For the absolute values of U (Figure 7.31, left plot), a good agreement between the observations and simulations can be observed. These absolute values are important in the field, as they determine the initiation of erosion or sedimentation at certain thresholds (Vandenbruwaene et al., 2011). Looking at the normalised simulations (Figure 7.31, right plot), all simulations fall together. As such, it can be concluded that the observed velocity patterns in the considered transect, at a distance of 0.25 m before the trailing edge of the patches, scale perfectly with the imposed upstream velocity U_∞. A maximum deviation of 1.557 $\pm$ 0.006 and 1.586 $\pm$ 0.006 times the upstream

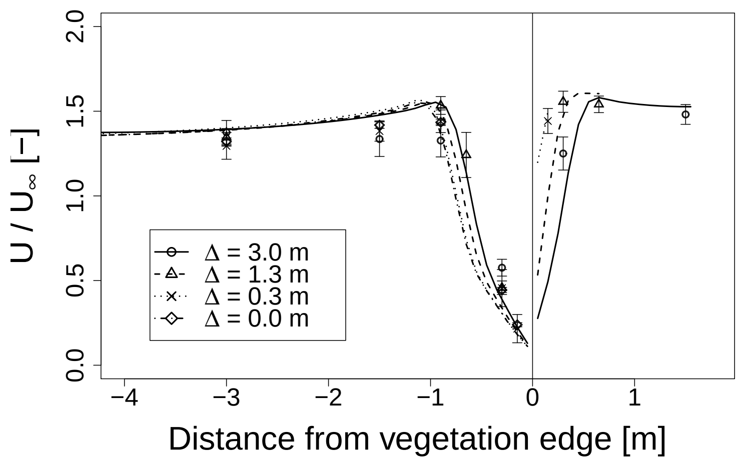

Figure 7.29: Lateral velocity profiles of the streamwise velocity U over one half of the flume. Both measurements and simulations for 4 different gap spacings, Δ = 3 m, Δ = 1.3 m, Δ = 0.3 m and Δ = 0 m are shown. The patch size is constant and equal to 2 m. The error bars on the measurements points are the calculated rms values on the measurements. The patch is located at y = 0 m, as such its actual width is not shown.

velocity was found, respectively at the outside of the patch and in between the patches. These peaks are located at respectively 95 $\pm$ 10 cm and 75 $\pm$ 10 cm from the patch edges. At a lateral distance of 3 m outside of the patches, the position of the furthest measurement point from the patch, a value for the simulations is found of 1.398 $\pm$ 0.005 times U_∞, whereas for the measurements a mean value of 1.385 $\pm$ 0.12 is calculated. These values agree within uncertainty.

7.5.3.1 Flow characteristics behind the patches

In Zong and Nepf (2012) and Chen et al. (2012) formulas for the prediction of the length of the steady wake zone (L_1) behind the patch and the magnitude of the velocity in these steady wake zones U_1 are formulated. Based on experimental results, described in Chapter 3, it was shown that these predictive formulas remain valid, in the case of 2 patches placed in a side-by-side configuration. Both in the experiments of Chen et al. (2012); Zong and Nepf (2012) and the simulations of the measurements in Vandenbruwaene et al. (2011), a value of the stability parameter S below the threshold of 0.2 is found (see Chapter 3).

The characteristics of the velocities behind the patch are shown in Table 7.15. Chen et al. (2012) predicts a value for U_1, in case of high flow blockage ($C_D a D >$

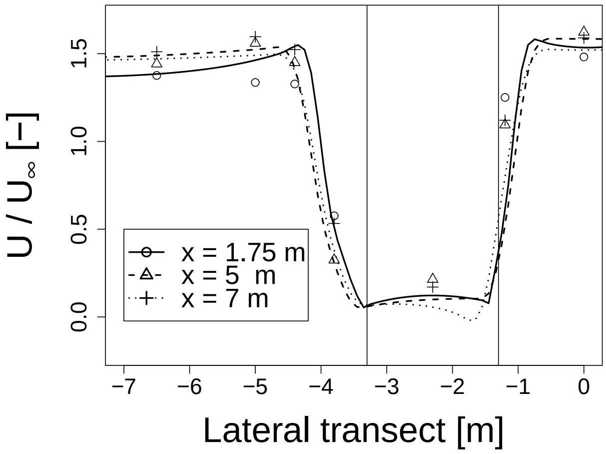

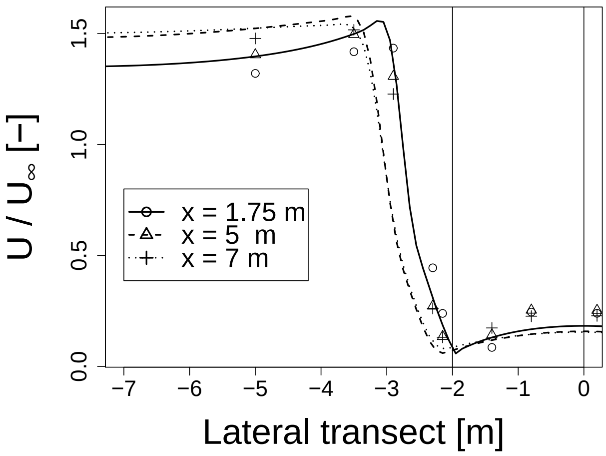

Figure 7.30: Three lateral, normalised velocity profiles of the streamwise velocity U over one half of the flume are depicted at x = 1.75 m, x = 5 m and x = 7 m. These transects are plotted for vegetation patches of diameter D = 2 m and Δ = 3m (top) and Δ = 0 m (bottom). The vertical lines indicate the edges of the patches.

4), which is the case here ($C_D a D > 40$), a negligibly small value ($U_1/U_\infty \approx 0.03$) is reported. Values found here are for all cases, clearly higher, $U_1/U_\infty \approx 0.10$. However, they are agreeing well with the measurements (see Figure 7.30). Furthermore, these values are not exactly equal for the different cases, but differences are within 7 % (maximal vs. minimal value), which can be considered small. Chen et al. (2012) predicted a length of the steady wake zone, for high-flow blockage,

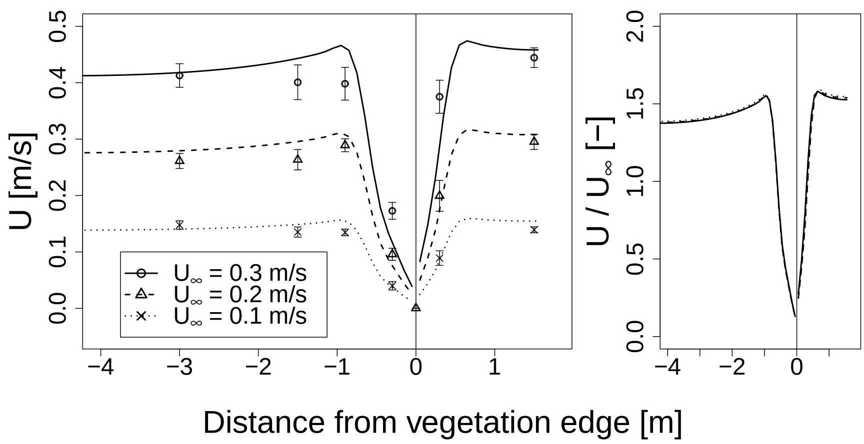

Figure 7.31: Lateral velocity profiles of the streamwise velocity U over one half of the flume for different incoming velocities U_∞ of 0.1 m/s, 0.2 m/s and 0.3 m/s respectively. Absolute (left plot) and normalised (right plot) streamwise velocities are shown. A lateral transect at 0.25 m before the trailing edge of the patch was selected. The patch is located at y = 0 m, as such its actual width is not shown.

of $L_1/D \approx 2.5$. The values found for this experiments are larger (Table 7.15), a range of 2.5 till 5.7 is found for values of L_1/D.

For the velocities on the centerline, the maximum velocities (U_{max}) and the distance behind the patches over which the velocity is higher than 0.95 times U_{max} (L_{max}) is given in Table 7.16. A linear fit between Δ and L_{max} is found, with an R^2 of 0.986:

$$L_{max} = 1.731 \pm 0.078\Delta \tag{7.9}$$

This value is clearly lower than the value found for dense patches in the experiments (2.8 $\pm$ 0.2, Chapter 3), but similar, a linear trend is found. An estimation of the minimum velocity on the centerline is more difficult, as in many configurations these values lie at the very downstream end of the computational mesh (indicated by an (*) in Table 7.16).

7.6 Discussion and Conclusion

The presented hydraulic model is implemented within the STRIVE (STReam RIVer Ecosystem) model package to simulate aquatic ecosystems as a whole. Therefore, an assessment has to be made between model complexity (and therefore the accuracy of the simulation of the flow field) and the computational effort. After all, the hydraulic model represents only part of the ecosystem processes. A 1D-

Table 7.15: Flow characteristics on the vegetation centerline. D is the diameter of the patch, Δ the gap distance between the patches, U_∞ the upstream velocity, U_1 the wake velocity and L_1 the length of the steady wake zone. (*) indicates values close to the downstream end of the computational domain.

Conf.	D [m]	Δ [m]	U_∞ [m/s]	Δ/D [-]	U_1/U_∞ [-]	L_1 [m]	L_1/D [-]
D	1	0.3	0.3	1.5	0.068 ± 0.075	5.5 ± 0.1	5.5
A	1	2.3	0.3	0.65	0.101 ± 0.020	4 ± 0.1	4
F	2	3.0	0.3	1.5	0.090 ± 0.019	8 ± 0.1	4
B	2	1.3	0.3	0.65	0.085 ± 0.038	5.5 ± 0.1	2.75
E	2	0.3	0.3	0.15	0.104 ± 0.032	6.5 ± 0.1	3.25
G	2	0.0	0.3	0.0	0.137 ± 0.003	15.5 ± 0.1	7.75
							3.875 (*)
C	3	0.3	0.3	0.1	0.101 ± 0.039	8 ± 0.1	2.67
F	2	3.0	0.2	1.5	0.087 ± 0.014	$8.5 \pm$	4.25
F	2	3.0	0.1	1.5	0.089 ± 0.011	8 ± 0.1	4.0

Table 7.16: Flow characteristics on the centerline of the flume, in the center of the gap between the patches. D is the diameter of the patch, Δ the gap distance between the patches, U_∞ the upstream velocity, U_{max} the maximum velocity between the patches and L_{max} the length over which this maximum velocity is sustained. (*) indicates values close to the downstream end of the computational domain.

Conf.	D [m]	Δ [m]	U_∞ [m/s]	Δ/D [-]	U_{max}/U_∞ [-]	L_{max} [m]	U_{min}/U_∞ [-]	L_{min} [m]
D	1	0.3	0.3	1.5	1.230 (1.274 $\pm$ 0.024)	0.7 $\pm$ 0.1	0.164	14.2
A	1	1.3	0.3	0.65	1.323 (1.230 $\pm$ 0.022)	3.5 $\pm$ 0.1	0.738	25.6
F	2	3.0	0.3	1.5	1.589 (1.560 $\pm$ 0.024)	5.4 $\pm$ 0.1	0.851 (*)	26.5 (*)
B	2	1.3	0.3	0.65	1.632 (1.607 $\pm$ 0.023)	3 $\pm$ 0.1	0.333	18.6
E	2	0.3	0.3	0.15	1.515 (1.486 $\pm$ 0.024)	0.6 $\pm$ 0.1	0.099	21.6
G	2	0.0	0.3	0	-	-	-	-
C	3	0.3	0.3	0.1	1.735 (1.571 $\pm$ 0.024)	0.6 $\pm$ 0.1	0.156 (*)	27.6 (*)
F	2	3.0	0.2	1.5	1.601 (1.700 $\pm$ 0.029)	5.5 $\pm$ 0.1	0.927 (*)	27.2 (*)
F	2	3.0	0.1	1.5	1.609 (1.580 $\pm$ 0.024)	5.5 $\pm$ 0.1	0.944 (*)	27.2 (*)

hydraulic model has already been implemented within the STRIVE model during previous research (De Doncker, 2008; De Doncker et al., 2011), performing well to predict water heights and corresponding average cross-sectional velocities. However, a 2D model was desired to obtain more information on the velocity fields in case of heterogeneous vegetation distributions.

Although depth-averaged modeling based on the Shallow Water Equations is widespread, the number of studies assessing the performance of these models to vegetated flows on smaller scales (river reaches with patches of vegetation rather than vegetation on large floodplains) is relatively limited. Examples found are Leu et al. (2008) focusing on the effect of the cutting management of riparian vegetation. Several studies have been published by the group of Weimung Wu (Wu, 2007; Wu et al., 2004; Wu and Wang, 2004), focusing on the predictions of the flow fields and change of bed topography because of vegetation presence. A similar goal was found in the study of Tsujimoto (1999), where morphological changes because of vegetation presence were studied. Ball et al. (1996) focused on the wake behaviour found behind a group of piles, representing vegetation stems, in function of the density. An overview of these studies and the basic model choices made, is given in section 6.6 and Table 6.4 herein.

The implemented, 2D-hydraulic model was tested for different cases, and overall a good performance was noticed. For uniform canopies, with vegetation covering the whole flume width, it could be concluded that the methods to account for resistance, presented by Baptist et al. (2007) and Huthoff et al. (2007) worked out very well. The resistance coefficient calculated using the model, by implementing the vegetation characteristics, was compared with measured resistance coefficients in experimental studies. A general linear fit (for all investigated experimental runs) between Manning coefficients obtained through the simulations and measured values, showed a variation of less than 10 % from the 1:1 bisector.

Simulations for a canopy on one side of the flume, revealed the capacity of the implemented resistance and depth-averaged model to predict the velocity profiles, both longitudinal through the vegetation patch and lateral profiles from the vegetation zone to the free-flowing side of the flume. Especially for sparse canopies, an adequate determination of the drag coefficient C_D is important to obtain reliable results. The method of Tanino and Nepf (2008) has shown to perform well here, but it should be mentioned that it was used in a quasi similar situation for which the relation was set up (wooden dowels in a staggered array). Both in the studies of Leu et al. (2008), Wu and Wang (2004) similar agreements for cross-section velocity distributions were found between model predictions and validation values, from experiments performed by Tsujimoto and Kitamura (1995) and Pasche and

Rouve (1985).

The simulations for short patches were more cumbersome. To predict the velocity behind the patch, an appropriate combination of drag coefficient and resistance model is necessary. For the dense patches, oscillations starts to appear, which account for mixing agreeing well with the simulations. Similar results have been found by Ball et al. (1996) for pile groups. Oscillations starts to appear when the patch Manning's coefficient is greater than approx. 0.5, whereas for Ball et al. (1996) oscillations starts to appear for $n \approx 0.2$, with patch diameters of respectively 0.225 m and 0.410 m. The appearance of these oscillations however, ask for a more careful treatment of the boundary conditions. For the sparse cases, a reasonable prediction of the steady wake length was found, after an appropriate estimation of U_1 was obtained. However, the re-accelerating of the flow behind L_1, the position of the minimum velocity, was not modeled accurately. Stansby (2006) describes also such a dual interpretation of the prediction performance for wake behaviour, using the 2D-SWE, depending on the flow characteristics. They found, for simulations of flow around conical islands, that model predictions were less accurate in case of unstable wakes (where $S < 0.4$ and oscillations appear) compared to stable wakes (where $S > 0.4$ and oscillations do not appear). Such isolated patches, or vegetation islands, were also simulated by Wu and Wang (2004), however, it's difficult to assess the performance of the model based on the reported information.

To account for this, probably additional and more complex turbulence models could be considered. However, the main goal of the project should be kept in mind, as there was aimed for a hydraulic routine as a basic tool for ecological modeling. Additional and more complicated turbulence models (e.g. k-ϵ,...) result in additional equations which should be solved, and accordingly longer simulation times can be expected and probably additional parameters (to calibrate). Furthermore, idealised flows and vegetation characteristics are considered here. In the field, vegetation will bend, move with the flow,... All these effects will change the flow-mixing characteristics. It should be questioned therefore if all processes should be implemented, and to which degree of accuracy, and if it is decided to do so, in which order. The addition of more complex turbulence predictions can result in better predictions of the hydraulic variables for idealised cases, but inserting some aspects of the vegetation movement (e.g. bending in function of flow velocities or waving of the vegetation stems) may result in better predictions of vegetated flows in the field.

In a last step a set-up with real vegetation was modelled, patches in a side-by-side configuration. Good predictions of the flow distributions between and next to the patches could be observed. Only a few measurement data were available further downstream of the patches. However, model simulations for those available revealed good agreement, within uncertainty.

It should be mentioned that the analysis of the uncertainties in the model results is not discussed in depth in this manuscript. Besides the model choices (and its parameter values), uncertainties are also present in the input data. For the vegetated flows under study, these uncertainties originate on one hand from uncertainties on the hydraulic input data (measurement error on the (upstream) velocities, the (downstream) water depth measurements, the friction value of the bottom,...). It has been shown that taking into account the uncertainty on the upstream boundary condition (a known velocity) alone, will not alter the results of the normalized velocity fields significantly, due to the similarity of the flow. To examine the effect of uncertainties of the boundary conditions on the results, these should be altered both on the up- and downstream edge simultaneously, which was out of scope of this thesis. On the other hand, uncertainties originate from uncertainties on the vegetation input data (vegetation density, height, drag coefficient, etc.). Especially for real vegetation, the uncertainties on the vegetation input data will be larger, as these variables are more difficult to determine.

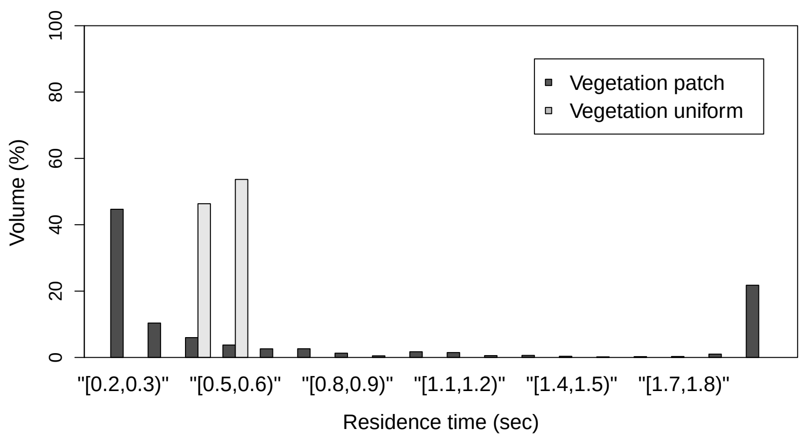

Figure 7.32: Distribution of the calculated residence times using a 1D-approach (uniform vegetation) and 2D-approach (vegetation on 1 side). The number of dowels was equal for both calculations. Residence time is calculated per computational cell for a vegetation stand of 3500 dowels per m^2 on 1 side.

As the results of the simulations in general are satisfying, this hydraulic model can be used and coupled with other modules in the STRIVE ecosystem model. In this way, important ecological parameters as e.g. water residence time, can be simulated much more adequately for heterogeneous systems in 2D-modelling compared to 1D-modeling. Such exercise is made for a situation with vegetation on 1 side of the flume, as described in a previous section. A situation where the spatial configuration is incorporated and one where the same vegetation biomass was considered, but distributed over the whole cross-section as is done in 1D-hydraulic modeling. This latter situation results in a single peak of the residence time per cell (Figure 7.32), whereas the former situation results in a more distributed estimation of the residence time, with two peaks for the higher flow velocities next to the vegetation and lower flow velocities in the vegetation. The full impact of the incorporation of spatial information on ecosystem functioning has to be assessed in more detail by simulations of the coupled STRIVE model.

8 Conclusions and Recommendations for future Research

The general objective of this PhD-research was to contribute to a deeper insight into the effect of vegetation patches on flow and sedimentation. This has been carried out by field and laboratory experiments and numerical simulations. This PhD-work resulted on the one hand in extra knowledge on the effect of spatially distributed patches of vegetation on flow and sedimentation based on the acquired data through field measurements and a study in a laboratory flume. Besides the analysis that were performed on these data, they can be used as validation data for numerical models as well. On the other hand, a tool has been developed in the form of a numerical model, that can be used to tackle further research questions. Some recommendations for future research are put forward.

8.1 Answers on specific Research Questions.

Three main research questions have been stated in the Introduction. These questions are repeated here, together with the specific conclusions on each of these questions based on the research presented in this manuscript.

1. How is a patch of *Callitriche Platycarpa sp.* avoiding hydrodynamic stress?

   In situ flume measurements have been used to study the flow and sedimentation around a patch of *Callitriche Platycarpa sp.*. The zones with enhanced flow and increased turbulence intensities have been observed. In the free flowing section next to the patch, an increase of the velocities of approx. 10 to 30 % was observed. The depth-averaged velocities behind the patch were reduced by 50 to 70 %. For the Reynolds stresses, maximal values were found on the top of the canopy and adjacent to the canopy, with maximum values going up to 8 $\mathrm{cm}^2\,\mathrm{s}^{-2}$ for $\overline{u'w'}$. During the course of the experiments, the bathymetry evolution was measured. The highest sedimentation have been observed behind the patch. A zone of marginal change was observed on the free flowing side next to the patch, consistent with observations of the bed shear stress. However no erosion zones have been observed, as the velocities in the *in-situ* flume could not be increased enough, as was aimed for. Probably, real high-flow events should be studied to observe these erosion events. However the zones where erosion would occur, will probably coincide with the zones of limited sedimentation in our test cases. Additionally, different patch characteristics of a *Callitriche* patch were measured in function of a range of incoming velocities. Because of its flexibility, it was observed that with increasing discharge, the patch reduces its frontal area by taking a deeper position in the water column and becomes more streamlined by adapting its length to width ratio. This means that both canopy depth and patch length/width ratio have a tempering effect on flow acceleration adjacent to the patch.

2. How are patches in a side-by-side configuration influencing the flow field and sedimentation patterns compared to single, isolated patches?

   Several characteristics of flow and deposition in the case of two circular patches, placed in a side-by-side configuration perpendicular to the flow direction, have been investigated. Both the velocity profiles behind the vegetation patches and in the centerline of the flume, in the center of the gap between the patches, have been investigated. For the profiles on the patch centerline, no distinction was found from velocity profiles for isolated vegetation patches. For the centerline velocity profile, several features have been examined. Firstly, as in the study of Vandenbruwaene et al. (2011), with real vegetation, no reduction of the maximum velocity between the patches has been observed when the gap spacing was decreased. The magnitude of this maximum velocity was found to be predictable by a simple mass conservation over the whole channel width. Secondly, the length over which this maximum velocity was sustained, is found to be linear with the gap spacing. Third, behind this zone of enhanced maximum velocity, a zone with minimum velocity was found. The magnitude of this minimum velocity was predicted by a mass conservation between the centers of the two adjacent patches. The deposition patterns agreed well with the flow field. Especially the zone of minimal velocity was found to be particularly interesting, as enhanced deposition was observed here also. Former hypothesis explained the merging of two patches through lateral growth of each patch, growing towards each other. This has been found, however, to be difficult because of the consistent, high maximum values in between the patches. Therefore, a new hypothesis was stated. Herein, the merging of patches is predicted to be induced from vegetation growth on the ceneterline between the patches, behind the original patches, with upstream effects on the velocity in the gap between the patches.

3. Can we use the depth-averaged shallow water equations and an appropriate resistance model to simulate flow fields influenced by vegetation?

   A 2D depth-averaged hydraulic routine has been developed to simulate flow velocities in vegetated streams, specifically focusing on spatially distributed configurations of vegetation. This hydraulic routine has been written as part of the STRIVE model package, to study the functioning of aquatic ecosystems, especially vegetated river reaches. The hydraulic routine is based on the depth-averaged Shallow Water Equations, which have been implemented based on a semi-implicit, semi-Lagrangian numerical method. A vegetation resistance model was added based on the method of Baptist et al. (2007), developed for developed flow through vegetation and by a separate drag term. The model has been validated for different forms of heterogeneity, ranging from uniform vegetation covering the whole width of the flume, over vegetation on 1 side of the flume to patches of vegetation, in either an isolated case or in a side-by-side configuration. Using several methods to implement vegetation roughness, based on vegetation characteristics, an overall agreement within approximately 10% was found between predicted Manning coefficient from model simulations and calculated Manning coefficients from different experimental studies. For long canopies on one side of the flume, the velocity profiles, both longitudinal through the vegetation and lateral cross-sections were represented well. Especially for sparser canopies, the drag coefficient is a sensitive parameter which can be used as calibration parameter. Predictive formulas, using flow characteristics and the vegetation density as parameters, have been shown to result in good estimates of the drag coefficient. Also for isolated patches, an appropriate fitting of the drag coefficient was necessary to obtain wake velocities behind the patch in agreement with the experimental results, used as validation. For dense patches, oscillations were observed in the wake zone, accounting for mixing and resulting flow recovery behind the patch, in good agreement with the experiments. For sparser patches, the position of the steady wake length was reasonably well simulated, however the recovery of the velocities behind this point have not been accounted for very well. Simulations for patches of vegetation placed in a side-by-side configuration, where vegetation consisted of real plants, resulted in good predictions of the flow distribution next to and in between the patches. Based on these simulation results for flows of different complexity, it can be concluded that a useful tool for the study of vegetated flow is developed. The results of this hydraulic routine can be used in an ecosystem model, to take into account the flow fields associated with spatially distributed vegetation patches.

8.2 Recommendations for future Research

Based on the findings and experience acquired during the research period, several ideas and recommendations for future research are stated below.

In the field flume studies, although enhanced velocities were found in the zone next to the vegetation, no erosion was observed. By enhancing the flume entrance, the discharge and velocities in the field flume were enhanced, but clearly not enough to invoke erosion processes. However, the tempering effect by the plants' bending probably also played a role by the tempered velocity increase next to the patch. Erosion is a process associated with high flood events. It would be very interesting to observe the topography before and after such a high flood event, to study if erosion is found and if so, where these erosion zones are situated. Such experiments are difficult to execute as they are very difficult to plan, as high flood events are not manageable and surveys should be carried out closely before and after the event.
Another important issue, especially relevant in the field studies, is the impact of uncertainty on the measurements. Especially the manner in which a quantity is measured has a big influence on the measurement uncertainty, besides the measurement error of the instrument itself. Although vegetation can occur in a wide variety and are e.g. continuously moving, no guidelines exist how and where to measure the (average) plant height, the (depth)-averaged stem diameter,... Such a guideline can consist of a minimum time to determine the canopy height, as it is waving (or a minimum number of wave cycles), etc. These guidelines could help to better estimate the uncertainty on the measurements and compare the values from different researchers.

Based on the laboratory experiments for patches in a side-by-side configuration, some interesting results have been found, however, new questions have arisen. Only a limited number of parameters have been varied in the experiments, namely the density and the gap distance. However, it would be interesting to see the effect of parameters as length/width ratio of the patch, shape of the patches, sediment size (and associated including bed transport) and the submergence rate of the patches, on the obtained results. The maximum velocity in/just behind the gap spacing has been found to be independent of the gap spacing. Changing the length/width ratio of the patches could change these findings, as, in cases where the patch is longer, the shear layers originating at the edges of the patches can grow to the center of the gap. Furthermore, it would be very worthwhile to repeat the experiments for submerged patches. It's very likely that the submergence rate of the vegetation will strongly influence the observed flow patterns and associated sedimentation patterns. Based on the experimental results, a new hypothesis for the merging of patches is stated. However, this hypothesis is not (yet) verified with field data. It would be extremely interesting if this theoretical basis for merging could be confirmed with practical evidence. This could be done in the first place in a lab flume, by adding extra patches on the centerline and verify if the hypothesis of reduced flow in the gap between the patches is attained. In the field, the analysis of photographs over a time period could be an opportunity to test the hypothesis.

The developed numerical routine can be used to tackle many more research questions, especially to study the behaviour of the aquatic ecosystem as a whole. Several additions to the model are worthwhile to be considered, both on a short term as on a longer term. In the short term, simulations can be run for field situations, as till now, only idealized flume cases have been simulated. It should be noted however that both input and validation data for these field studies are scarce, especially spatially distributed data. To account for this, additional research projects have been started up (FWO-Digicam), to obtain spatially distributed data using digital photography. They can be used, when (natural) tracers are available, to capture the heterogeneous, surface flow on the one hand and to capture the position and characteristics (size, shape and eventually average depth) of the vegetation coverage on the other hand. Furthermore, the flexibility of the vegetation should be taken into account. The submergence rate of the vegetation plays an important role in the resistance caused by vegetation and incorporating bending of the vegetation in function of the incoming velocity in the model, will result in more realistic model predictions. Some small numerical additions which can be added are the addition of a more flexible downstream boundary condition, more precisely a Q-H boundary relation and the addition of an appropriate side wall roughness formulation, especially for field studies where grasses, etc. form a side wall boundary with high roughness.

On a longer term, the hydraulic routine should be completed by additional routines like a sediment transport routine, a vegetation growth routine,... to really address all the main components of the aquatic ecosystem in a spatially distributed framework. Furthermore, as 2D-modelling takes much more computational time compared to 1D modelling, an efficient linking between 1D- and 2D-modelling could be considered, combining both the simulation speed of 1D modelling for longer time evolutions (e.g. simulating over a vegetative season) and taking into account the effect of important spatial characteristics of the systems. To avoid the drawback of data availability, also scenario analysis studies can be performed. Here, the input can be created using feasible values for plant morphology and configuration (position, size, type of vegetation) . Both the analysis of the input as the output can be based on general spatial statistics and physical laws. In this way a relative difference between the different scenarios under study can be made and major explanatory variables to detect eg. the effect of vegetation on resistance can be derived. To study the hydrodynamics around patches in more detail, more detailed turbulence models should be implemented (k-ϵ models, etc.). If more detailed calculations or additional variables are required, to address answers on specific research questions from an ecosystem point of view, additional processes should be implemented in the model. Therefore, the order and relevance of the suggested improvements to the model will be determined by demands from an ecological context.

References

Afshar, M. A., 2010. Numerical Wave Generation in OpenFOAM. Master's thesis, Chalmers University of Technology.

Akima, H., 1978. A method of bivariate interpolation and smooth surface fitting for irregularly distributed data points. ACM Transactions on Mathematical Software 4 (2), 148–164.

Angers, D., Caron, J., 1998. Plant-induced changes in soil structure: Processes and feedbacks. Biogeochemistry 42 (1-2), 55–72, Symposium on Plant-Induced Soil Changes - Processes and Feedbacks at the American Society of Agronomy Soil Science Society of America Annual Meeting, Indianapolis, Indiana, Nov. 04-08, 1996.

Bakry, M. F., 1996. Impact of Mechanical Cutting on the Channel Roughness. Water Resources Management 10 (6), 479–486.

Bakry, M. F. M., Gates, T., Khattab, A., 1992. Field-measured hydraulic resistance characteristics in vegetation-infested canals. Journal of Irrigation and Drainage Engineering-ASCE 118 (2), 256–274.

Bal, K., 2009. Interactions between macrophyte ecology and hydraulic functioning of lowland rivers. Ph.D. thesis, Antwerp University.

Bal, K. D., Bouma, T. J., Buis, K., Struyf, E., Jonas, S., Backx, H., Meire, P., 2011. Trade-off between drag reduction and light interception of macrophytes: comparing five aquatic plants with contrasting morphology. Functional Ecology 25 (6), 1197–1205.

Bal, K. D., Meire, P., 2009. The Influence of Macrophyte Cutting on the Hydraulic Resistance of Lowland Rivers. Journal of Aquatic Plant Management 47, 65–68.

Ball, D., Stansby, P. K., Alliston, N., 1996. Modelling shallow water flow around pile-groups. In: Marit. & Energy. pp. 226–236.

Baptist, M. J., Babovic, V., Uthurburu, J. R., Keijzer, M., Uittenbogaard, R. E., Mynett, A., Verwey, A., 2007. On inducing equations for vegetation resistance. Journal of Hydraulic Research 45 (4), 435–450.

Belcher, S., Jerram, N., Hunt, J., 2003. Adjustment of a turbulent boundary layer to a canopy of roughness elements. Journal of Fluid Mechanics 488, 369–398.

Bennett, S., Pirim, T., Barkdoll, B., 2002. Using simulated emergent vegetation to alter stream flow direction within a straight experimental channel. Geomorphology 44 (1-2), 115–126.

Biggs, B., 1996. Hydraulic habitat of plants in streams. Regulated Rivers-Research & Management 12 (2-3), 131–144, 1st International Symposium on Habitat Hydraulics, Trondheim, Norway, Aug. 18-20, 1994.

Biron, P., Robson, C., Lapointe, M., Gaskin, S., 2004. Comparing different methods of bed shear stress estimates in simple and complex flow fields. Earth Surface Processes and Landforms 29 (11), 1403–1415.

Bloemendaal, F., Roelofs, J., 1988. Waterplanten en waterkwaliteit. Stichting Uitgeverij Koninklijke Nederlandse Natuurhistorische Vereniging, Den Haag, (in Dutch).

Boerema, A., Schoelynck, J., Bal, K., Vrebos, D., Jacobs, S., Staes, J., Meire, P., 2014. Economic valuation of ecosystem services, a case study for aquatic vegetation removal in the Nete catchment (Belgium). Ecosystem Services.

Bouma, T., De Vries, M., Low, E., Peralta, G., Tanczos, C., Van de Koppel, J., Herman, P., 2005. Trade-offs related to ecosystem engineering: A case study on stiffness of emerging macrophytes. Ecology 86 (8), 2187–2199.

Bouma, T. J., Friedrichs, M., van Wesenbeeck, B. K., Temmerman, S., Graf, G., Herman, P. M. J., 2009. Density-dependent linkage of scale-dependent feedbacks: a flume study on the intertidal macrophyte Spartina anglica. Oikos 118 (2), 260–268.

Bousmar, 2002. Flow modelling in compound channels. momentum transfer between main channel and prismatic or non-prsimatic floodpflood. Ph.D. thesis, Univerisité Catholique de Louvain.

Brock, T., Boon, J., Paffen, B., 1985. The effects of the season and of water chemistry on the decomposition of Nymphaea-alba L - weight-loss and pyrolysis mass-spectrometry of the particulate matter. Aquatic Botany 22 (3-4), 197–229.

Buis, K., Anibas, C., Bal, K., Banasiak, R., de Doncker, L., Desmet, N., Gerard, M., van Belleghem, S., Batelaan, O., 2007. Fundamental study of the exchange processes in river ecosystems: an integrated model development. Water 32, 51:54.

Castellanos, E., Figueroa, M., Davy, A., 1994. Nucleation and facilitation in saltmarsh succession - interactions between Spartina-Maritima and Arthrocnemum Perenne. Journal of Ecology 82 (2), 239–248.

Casulli, V., 1990. Semi-Implicit Finite-Difference methods fot the 2-Dimensional Shallow-Water Equations. Journal of Computational Physics 86 (1), 56–74.

Casulli, V., 2012. Advanced numerical methods for free-surface hydrodynamics. Course Notes.

Casulli, V., Cheng, R., 1992. Semi-implicit finite-difference methods for 3-dimensional shallow-water flow. International Journal for Numerical Methods in Fluids 15 (6), 629–648.

Casulli, V., Dumbser, M., Toro, E. F., 2012. Semi-implicit numerical modeling of axially symmetric flows in compliant arterial systems. International Journal for Numerical Methods in Biomedical Engineering 28 (2), 257–272.

Casulli, V., Stelling, G. S., 2011. Semi-implicit subgrid modelling of three-dimensional free-surface flows. International Journal for Numerical Methods in Fluids 67 (4), 441–449.

Casulli, V., Walters, R., 2000. An unstructured grid, three-dimensional model based on the shallow water equations. International Journal for Numerical Methods in Fluids 32 (3), 331–348.

Casulli, V., Zanolli, P., 2002. Semi-implicit numerical modeling of nonhydrostatic free-surface flows for environmental problems. Mathematical and Computer Modelling 36 (9-10), 1131–1149.

Cea, L., Puertas, J., Vazquez-Cendon, M.-E., 2007. Depth averaged modelling of turbulent shallow water flow with wet-dry fronts. Archives of Computational Methods in Engineering 14 (3), 303–341.

Chambers, P., Prepas, E., 1994. Nutrient dynamics in riverbeds - The impact of sewage effluent and aquatic macrophytes. Water Research 28 (2), 453–464.

Champagne, F., Pao, Y., Wygnanski, I., 1976. 2-Dimensional mixing region. Journal of Fluid Mechanics 74, 209–250.

Champion, P., Tanner, C., 2000. Seasonality of macrophytes and interaction with flow in a New Zealand lowland stream. Hydrobiologia 441 (1-3), 1–12.

Chaudry, M., 1993. Open-Channel Flow. Prentice-Hall Inc.

Chen, D., Jirka, G., 1995. Experimental-study of plane turbulent wakes in a shallow-water layer. Fluid Dynamics Research 16 (1), 11–41.

Chen, S., Kuang, C., Liu, S., Gu, J., 2009. A Semi-Implicit Eulerian-Lagrangian Finite-Volume Model for Coastal Circulation. In: Tan, SK and Huang, Z (Ed.), Proceedings of the 5th international Conference on Asian and Pacific Coasts, Vol. 1. World Scientific Publ Co Pte Ltd, PO BOX 128 Farrer Rd, Singapore 9128, Singapore, pp. 244–250, 5th International Conference on Asian and Pacific Coasts, Singapore, Oct 13-18, 2009.

Chen, Z., Ortiz, A., Zong, L., Nepf, H., 2012. The wake structure behind a porous obstruction and its implications for deposition near a finite patch of emergent vegetation. Water Resources Research 48.

Cheng, N.-S., 2011. Representative roughness height of submerged vegetation. Water Resources Research 47.

Cheng, N.-S., R., Casulli, V., Gartner, J., 1993. Tidal, Residual, Intertidal Mudflat (TRIM) Model and its Applications to San-Fransisco Bay, California. Estuarine Coastal and Shelf Science 36 (3), 235–280.

Chézy, A., 1768. The Chézy formula.

Chow, V., 1959. Open Channel Hydraulics. McGraw-Hill.

Corenblit, D., Tabacchi, E., Steiger, J., Gurnell, A. M., 2007. Reciprocal interactions and adjustments between fluvial landforms and vegetation dynamics in river corridors: A review of complementary approaches. Earth-Science Reviews 84 (1-2), 56–86.

Cornelisen, C., Thomas, F., 2004. Ammonium and nitrate uptake by leaves of the seagrass Thalassia testudinum: impact of hydrodynamic regime and epiphyte cover on uptake rates. Journal of Marine Systems 49 (1-4), 177–194, Joint Meeting of the American-Society for Limnology and Oceanography/American Geophysical Union, Honolulu, HI, Feb, 2002.

Costanza, R., dArge, R., deGroot, R., Farber, S., Grasso, M., Hannon, B., Limburg, K., Naeem, S., ONeill, R., Paruelo, J., Raskin, R., Sutton, P., vandenBelt, M., 1997. The value of the world's ecosystem services and natural capital. Nature 387 (6630), 253–260.

Cotton, J. A., Wharton, G., Bass, J. A. B., Heppell, C. M., Wotton, R. S., 2006. The effects of seasonal changes to in-stream vegetation cover on patterns of flow and accumulation of sediment. Geomorphology 77 (3-4), 320–334, 100th Annual Meeting of the Association-of-American-Geographers, Philadelphia, PA, MAR 14-19, 2004.

Cowan, W., 1956. Estimating hydraulic roughness coefficients. Agricultural Engineering, 37, 473–475.

Dawson, F., 1978. The seasonal effects of aquatic plant growth on the flow of water in a stream. In: Proceedings, 5th International Symposium on Aquatic Weeds. European Weed Research Society:.

De Doncker, L., 2008. A fundamental study on exchange processes in river ecosystems. Ph.D. thesis, Ghent University.

De Doncker, L., Troch, P., Verhoeven, R., Bal, K., Desmet, N., Meire, P., 2009. Relation between resistance characteristics due to aquatic weed growth and the hydraulic capacity of the river Aa. River Research and Applications 25 (10), 1287–1303.

De Doncker, L., Troch, P., Verhoeven, R., Buis, K., Meire, P., 2011. Validation of the strive model for coupling ecological processes and surface water flow. Journal of Hydroinformatics 13, 741–759.

Denny, M., 1994. Extreme drag forces and the survival of wind-swept and water-swept organisms. Journal of Experimental Biology 194, 97–115.

Denny, M., Gaylord, B., 2002. The mechanics of wave-swept algae. Journal of Experimental Biology 205 (10), 1355–1362.

Dollar, E., 2004. Fluvial geomorphology. Progress in Physical Geography 28 (3), 405–450.

Dunn, C., Lopez, F., Garcia, M., 1996. Mean flow and turbulence in a laboratory channel with simulated vegetation. Tech. rep., Hydrosystems Laboratory, Department of Civil Engineering, University of Illinois at Urbana-Champaign Urbana, Illinois.

EU, 2000. Directive 2000/60/ec ofthe european parliament and ofthe council. Tech. rep., European Union.

Ferziger, J., Peric, M., 2002. Computational Methods for Fluid Dynamics, 3rd Edition. Springer.

Folkard, A., 2011. Vegetated flows in their environmental context: a review. Proceeding of the ICE - Engineering and Computational Mechanics 164, 3–24.

Franklin, P., Dunbar, M., Whitehead, P., 2008. Flow controls on lowland river macrophytes: A review. Science of the Total Environment 400 (1-3), 369–378.

Galema, 2009. Vegetation resistance. evaluation of vegetation resistance descriptors for flood management. Master's thesis, Univeristy of Twente.

Gaskin, S., McKernan, M., Xue, F., 2004. The effect of background turbulence on jet entrainment: an experimental study of a plane jet in a shallow coflow. Journal of Hydraulic Research 42 (5), 531–540.

Gibbins, C., Vericat, D., Batalla, R. J., 2007. When is stream invertebrate drift catastrophic? The role of hydraulics and sediment transport in initiating drift during flood events. Freshwater Biology 52 (12), 2369–2384.

Giger, M., Dracos, T., Jirka, G., 1991. Entrainment and mixing in plane turbulent jets in shallow-water. Journal of Hydraulic Research 29 (5), 615–642.

Gioia, G., Bombardelli, F., 2002. Scaling and similarity in rough channel flows. Physical Review Letters 88 (1).

Green, J., 2005. Comparison of blockage factors in modelling the resistance of channels containing submerged macrophytes. River Research and Applications 21 (6), 671–686.

Green, J., 2006. Effect of macrophyte spatial variability on channel resistance. Advances in Water Resources 29 (3), 426–438.

Grenouillet, G., Pont, D., Seip, K., 2002. Abundance and species richness as a function of food resources and vegetation structure: juvenile fish assemblages in rivers. Ecography 25 (6), 641–650.

Gurnell, A., Petts, G., Hannah, D., Smith, B., Edwards, P., Kollmann, J., Ward, J., Tockner, K., 2001. Riparian vegetation and island formation along the gravel-bed Fiume Tagliamento, Italy. Earth Surface Processes and Landforms 26 (1), 31–62.

Gurnell, A., Tockner, K., Edwards, P., Petts, G., 2005. Effects of deposited wood on biocomplexity of river corridors. Frontiers in Ecology and the Environment 3 (7), 377–382.

Gurnell, A. M., O'Hare, J. M., O'Hare, M. T., Dunbar, M. J., Scarlett, P. M., 2010. An exploration of associations between assemblages of aquatic plant morphotypes and channel geomorphological properties within British rivers. Geomorphology 116 (1-2), 135–144.

Harrison, S., Pretty, J., Shepherd, D., Hildrew, A., Smith, C., Hey, R., 2004. The effect of instream rehabilitation structures on macroinvertebrates in lowland rivers. Journal of Applied Ecology 41 (6), 1140–1154.

Henderson, F., 1966. Open Channel Flow. Macmillan.

Horppila, J., Nurminen, L., 2003. Effects of submerged macrophytes on sediment resuspension and internal phosphorus loading in Lake Hiidenvesi (southern Finland). Water Research 37 (18), 4468–4474.

Hu, Y., Huai, W., Han, J., 2013. Analytical solution for vertical profile of streamwise velocity in open-channel flow with submerged vegetation. Environmental Fluid Mechanics 13 (4), 389–402.

Huthoff, F., Augustijn, D. C. M., Hulscher, S. J. M. H., 2007. Analytical solution of the depth-averaged flow velocity in case of submerged rigid cylindrical vegetation. Water Resources Research 43 (6).

Jarvela, J., 2005. Effect of submerged flexible vegetation on flow structure and resistance. Journal of Hydrology 307 (1-4), 233–241.

Jones, C., Lawton, J., Shachak, M., 1994. Organisms as ecosystem engineers. Oikos 69 (3), 373–386.

Jones, J. I., Collins, A. L., Naden, P. S., Sear, D. A., 2012. The relationship between fine sediment and macrophytes in rivers. River Research and Applications 28 (7), 1006–1018.

Keirsebelik, E., 2009. Studie van de numerieke modellering van oppervlaktewater ten behoeve van de gentegreerde modellering van een rivierecosysteem. Master's thesis, Ghent University.

Kemp, J., Harper, D., Crosa, G., 2000. The habitat-scale ecohydraulics of rivers. Ecological Engineering 16 (1), 17–29, International-Hydrological-Programme Symposium on Ecohydrology, Univ Lodz, Lodz, Poland, May, 1998.

Klopstra, D., Barneveld, H., van Noortwijk, J., van Velzen, E., 1997. Analytical model for hydraulic roughness of submerged vegetation. In: Proceedings of Theme A, Managing Water: Coping with scarcity and Abundance. American Society of Civil Engineers (ASCE), pp. 775–780.

Knight, D. W., Mc Gahey, C., Lamb, R., P.G., S., 2010. Practical Channel Roughness: roughness, conveyance, and afflux. CRC Press.

Kouwen, N., Unny, T., 1975. Flexible roughness in open channels. Journal of the Hydraulics Division-ASCE 101 (1), 194–196.

Kouwen, N., Unny, T. E., 1969. Flow retardance in vegetated channels. J. Irrig. and Drain. Div., ASCE, 95(2), 329–342.

Kubrak, E., Kubrak, J., Rowinski, P. M., 2008. Vertical velocity distributions through and above submerged, flexible vegetation. Hydrological Sciences Journal - Journal des Sciences Hydrologiques 53 (4), 905–920.

Kundu, P., Cohen, I., Dowling, D., 2012. Fluid Mechanics, 5th Edition. Elsevier.

Lancaster, J., Hildrew, A., 1993. Characterizing in-stream flow refugia. Canadian Journal of fisheries and aquaatic sciences 50 (8), 1663–1675.

Laval, B., Imberger, J., Hodges, B., Stocker, R., 2003. Modeling circulation in lakes: Spatial and temporal variations. Limnology and Oceanography 48 (3), 983–994.

Lee, J. H., Chu, V., 2003. Turbulent jets and plumes: a Lagrangian Approach. Kluwer Academic Publishers.

Lejeune, O., Tlidi, M., Lefever, R., 2004. Vegetation spots and stripes: Dissipative structures in arid landscapes. International Journal of Quantum Chemistry 98 (2), 261–271, Workshop on Complexity: Microscopic and Macroscopic Aspects, Tourtour, France, Jul 08-14, 2002.

Leu, J. M., Chan, H. C., Jia, Y., He, Z., Wang, S. S. Y., 2008. Cutting management of riparian vegetation by using hydrodynamic model simulations. Advances in Water Resources 31 (10), 1299–1308.

Li, Y., Anim, D. O., Wang, Y., Tang, C., Du, W., Yu, Z., Acharya, K., 2013. An open-channel flume study of flow characteristics through a combined layer of submerged and emerged flexible vegetation. Ecohydrology.

Liu, D., Diplas, P., Fairbanks, J. D., Hodges, C. C., 2008. An experimental study of flow through rigid vegetation. Journal of Geophysical Research-Earth Surface 113 (F4).

Lloyd, P., Stansby, P., 1997a. Shallow-water flow around model conical islands of small side slope .1. Surface piercing. Journal of Hydraulic Engineering-ASCE 123 (12), 1057–1067.

Lloyd, P., Stansby, P., 1997b. Shallow-water flow around model conical islands of small side slope .2. Submerged. Journal of Hydraulic Engineering-ASCE 123 (12), 1068–1077.

Lopez, F., Garcia, M., 2001. Mean flow and turbulence structure of open-channel flow through non-emergent vegetation. Journal of Hydraulic Engineering-ASCE 127 (5), 392–402.

Luhar, M., Nepf, H. M., 2013. From the blade scale to the reach scale: A characterization of aquatic vegetative drag. Advances in Water Resources 51, 305–316.

Luhar, M., Rominger, J., Nepf, H., 2008. Interaction between flow, transport and vegetation spatial structure. Environmental Fluid Mechanics 8 (5-6, SI), 423–439, 5th International Symposium on Environmental Hydraulics, Arizona State Univ, Tempe, AZ, DEC 02-07, 2007.

Madsen, J., Chambers, P., James, W., Koch, E., Westlake, D., 2001. The interaction between water movement, sediment dynamics and submersed macrophytes. Hydrobiologia 444 (1-3), 71–84.

Madsen, T., Enevoldsen, H., Jorgensen, T., 1993. Effect of water velocity on photosynthesis and dark respiration in submerged stream macrophytes. Plant cell and environment 16 (3), 317–322.

Manning, R., 1891. On the flow of water in open channels and pipes. Transactions Inst. Civil Engineers of Ireland 20, 161–207.

Manson, J., Wallis, S., Hope, D., 2001. A conservative semi-Lagrangian transport model for rivers with transient storage zones. Water Resources Research 37 (12), 3321–3329.

Manz, D., Westhoff, D., 1988. Numerical-analysis of the effects of aquatic weeds on the performance of irrigation conveyance systems. Canadian Journal of Civil Engineering 15 (1), 1–13.

Martin, N., 2004. MOD FreeSurf2D Manual.

McLelland, S., Nicholas, A., 2000. A new method for evaluating errors in high-frequency ADV measurements. Hydrological Processes 14 (2), 351–366.

Meire, D., De Doncker, L., Declercq, F., Buis, K., Troch, P., Verhoeven, R., 2010. Modelling river-floodplain interaction during flood propagation. Natural Hazards 55 (1), 111–121.

Mignone, A., 2012. Pluto v4.0, user's guide. Tech. rep.

Mitsch, W., Gosselink, J., 1993. Wetlands, 2nd Edition. Wiley, New York.

Monin, A., Yaglom, A., 1971. Statistical Fluid Mechanics. Mechanics of turbulence. Vol.1. Vol. 1. MIT Press.

Morris, E. P., Peralta, G., Brun, F. G., van Duren, L., Bouma, T. J., Perez-Llorens, J. L., 2008. Interaction between hydrodynamics and seagrass canopy structure: Spatially explicit effects on ammonium uptake rates. Limnology and Oceanography 53 (4), 1531–1539.

Morvan, H., Knight, D., Wright, N., Tang, X., Crossley, A., 2008. The concept of roughness in fluvial hydraulics and its formulation in 1D, 2D and 3D numerical simulation models. Journal of Hydraulic Research 46 (2), 191–208.

Naden, P., Rameshwaran, P., Mountford, O., Robertson, C., 2006. The influence of macrophyte growth, typical of eutrophic conditions, on river flow velocities and turbulence production. Hydrological Processes 20 (18), 3915–3938.

Nepf, H., 1999. Drag, turbulence, and diffusion in flow through emergent vegetation. Water Resources Research 35 (2), 479–489.

Nepf, H. M., 2012a. Flow and Transport in Regions with Aquatic Vegetation. In: Davis, SH and Moin, P (Ed.), Annual Review of Fluid Mechanics, Vol 44. Vol. 44 of Annual Review of Fluid Mechanics. Annual Reviews, 4139 El Camino Way, PO BOX 10139, Palo Alto, CA 94303-0897 USA, pp. 123–142.

Nepf, H. M., 2012b. Hydrodynamics of vegetated channels. Journal of Hydraulic Research 50 (3), 262–279.

Nikora, V., Lamed, S., Nikora, N., Debnath, K., Cooper, G., Reid, M., 2008. Hydraulic resistance due to aquatic vegetation in small streams: Field study. Journal of Hydraulic Engineering-ASCE 134 (9), 1326–1332.

Ortiz, A.and Ashton, A., Nepf, H., 2014. Mean and turbulent velocity field near rigid and flexible plants, and the implications for deposition. Journal of Geophysical Research 118 (4), 2585–2599.

Palmer, V., 1945. A method for designing vegetated waterways. Agricultural Engineering 26(12), 516–520.

Pasche, E., Rouve, G., 1985. Overbank flow with vegetatively roughened floodplains. Journal of Hydraulic Engineering-ASCE 111 (9), 1262–1278.

Patankar, S., 1980. Numerical Heat Transfer and Fluid Flow. Taylor & Francis.

Petryk, S., Bosmajian, G., 1975. Analaysis of flow through vegetation. Journal of the Hydraulics Division-ASCE 101 (7), 871–884.

Pitlo, R. H., 1989. Towards a larger capacity of vegetated channels. In: Proceedings EWRSI/AAB Seventh Symp. on Aquatic Weeds.

Pollock, D., 1994. A particle tracking post-processing package for modflow, the u.s. geological survey finite-difference ground-water flow model. Tech. rep., U.S. Geological survey.

Rajaratnam, N., 1976. Turbulent jets. Elsevier Scientific Publishing Company.

Rietkerk, M., Van de Koppel, J., 2008. Regular pattern formation in real ecosystems. Trends in Ecology & Evolution 23 (3), 169–175.

Riis, T., Biggs, B., 2003. Hydrologic and hydraulic control of macrophyte establishment and performance in streams. Limnology and Oceanography 48 (4), 1488–1497.

Riis, T., Sand-Jensen, K., Vestergaard, O., 2000. Plant communities in lowland Danish streams: species composition and environmental factors. Aquatic Botany 66 (4), 255–272.

Rodi, W., 1993. Turbulence Models and Their Application in Hydraulics. A.A. Balkema.

Rominger, J. T., Nepf, H. M., 2011. Flow adjustment and interior flow associated with a rectangular porous obstruction. Journal of Fluid Mechanics 680, 636–659.

Rouse, H., 1965. Critical analysis of open-channel resistance. J. Hydraul. Div. 91, 1–25.

Saad, Y., 1994. Sparsekit: a basic tool kit for sparse matrix computations. Tech. rep.

Sand-Jensen, K., 1998. Influence of submerged macrophytes on sediment composition and near-bed flow in lowland streams. Freshwater Biology 39 (4), 663–679.

Sand-Jensen, K., 2003. Drag and reconfiguration of freshwater macrophytes. Freshwater Biology 48 (2), 271–283.

Sand-Jensen, K., Madsen, T., 1992. Patch Dynamics of the stream macrophyte, Callitriche-Cophocarpa. Freshwater Biology 27 (2), 277–282.

Sand-Jensen, K., Mebus, J., 1996. Fine-scale patterns of water velocity within macrophyte patches in streams. Oikos 76, 169–180.

Sand-Jensen, K., Pedersen, M. L., 2008. Streamlining of plant patches in streams. Freshwater Biology 53 (4), 714–726.

Sand-Jensen, K., Pedersen, O., 1999. Velocity gradients and turbulence around macrophyte stands in streams. Freshwater Biology 42 (2), 315–328.

Schaminée, J., Weeda, E., Westhoff, V., 1995. De Vegetatie van Nederland. Vol. Deel 2: Plantengemeenschappen van wateren, moerassen en natte heiden. Opulus Press, Uppsala, Leiden, (in Dutch).

Schanz, A., Polte, P., Asmus, H., 2002. Cascading effects of hydrodynamics on an epiphyte-grazer system in intertidal seagrass beds of the Wadden Sea. Marine Biology 141 (2), 287–297.

Schoelynck, J., 2011. Macrophyte patches as biogeochemical hotspots: what is the impact on river water quality? Ph.D. thesis, Antwerp University.

Schoelynck, J., Bal, K., Backx, H., Okruszko, T., Meire, P., Struyf, E., 2010. Silica uptake in aquatic and wetland macrophytes: a strategic choice between silica, lignin and cellulose? New Phytologist 186 (2), 385–391.

Schoelynck, J., Bal, K., Puijalon, S., Meire, P., Struyf, E., 2012a. Hydrodynamically mediated macrophyte silica dynamics. Plant Biology 14 (6), 997–1005.

Schoelynck, J., De Groote, T., Bal, K., Vandenbruwaene, W., Meire, P., Temmerman, S., 2012b. Self-organised patchiness and scale-dependent bio-geomorphic feedbacks in aquatic river vegetation. Ecography 35 (8), 760–768.

Schulz, M., Kozerski, H., Pluntke, T., Rinke, K., 2003. The influence of macrophytes on sedimentation and nutrient retention in the lower River Spree (Germany). Water Research 37 (3), 569–578.

Schutten, J., Dainty, J., Davy, A., 2005. Root anchorage and its significance for submerged plants in shallow lakes. Journal of Ecology 93 (3), 556–571.

Siniscalchi, F., Nikora, V. I., 2012. Flow-plant interactions in open-channel flows: A comparative analysis of five freshwater plant species. Water Resources Research 48.

Soetaert, K., deClippele, V., Herman, P., 2002. FEMME, a flexible environment for mathematically modelling the environment. Ecological Modelling 151 (2-3), 177–193.

Soong, D., Prater, C., Halfar, T., Wobig, L., 2012. Manning's roughness coefficients for illinois streams. Tech. rep., USGS.

Spencer, W., Bowes, G., 1990. Aquatic Weeds: The Ecology and Management of Nuisance Aquatic Vegetation. Oxford University Press, Oxford, UK, Ch. Ecophysiology of the worlds most troublesome aquatic weeds, pp. 39–73.

Spink, A., Rogers, S., 1996. The effects of a record flood on the aquatic vegetation of the Upper Mississippi River System: Some preliminary findings. Hydrobiologia 340 (1-3), 51–57, 9th International Symposium on Aquatic Weeds, Dublin, Ireland, 1994.

Stansby, P., 2006. Limitations of depth-averaged modeling for shallow wakes. Journal of Hydraulic Engineering-ASCE 132 (7), 737–740.

Stansby, P., Lloyd, P., 1995. A SemiImplicit Lagrangian Scheme for 3D Shallow-Water flow with a 2-layer turbulence model. International Journal for Numerical Methods in Fluids 20 (2), 115–133.

Statzner, B., Lamouroux, N., Nikora, V., Sagnes, P., 2006. The debate about drag and reconfiguration of freshwater macrophytes: comparing results obtained by three recently discussed approaches. Freshwater Biology 51 (11), 2173–2183.

Stephan, U., Gutknecht, D., 2002. Hydraulic resistance of submerged flexible vegetation. Journal of Hydrology 269 (1-2), 27–43, 26th General Assembly of the European Geophysical Society, Nice, France, Mar 26-30, 2001.

Stewart, H., 2004. Hydrodynamic consequences of maintaining an upright posture by different magnitudes of stiffness and buoyancy in the tropical alga Turbinaria ornata. Journal of Marine Systems 49 (1-4), 157–167, Joint Meeting of the American Society for Limnology and Oceanography/American Geophysical Union, Honolulu, HI, Feb, 2002.

Stone, B., Shen, H., 2002. Hydraulic resistance of flow in channels with cylindrical roughness. Journal of Hydraulic Engineering-ASCE 128 (5), 500–506.

Sukhodolov, A. N., Sukhodolova, T. A., 2010. Case Study: Effect of Submerged Aquatic Plants on Turbulence Structure in a Lowland River. Journal of Hydraulic Engineering-ASCE 136 (7), 434–446.

Sumner, D., 2010. Two circular cylinders in cross-flow: A review. Journal of Fluids and Structures 26 (6), 849–899.

Sumner, D., Wong, S., Price, S., Paidoussis, M., 1999. Fluid behaviour of side-by-side circular cylinders in steady cross-flow. Journal of Fluids and Structures 13 (3), 309–338.

Tal, M., Paola, C., 2007. Dynamic single-thread channels maintained by the interaction of flow and vegetation. Geology 35 (4), 347–350.

Tanaka, N., Yagisawa, J., 2010. Flow structures and sedimentation characteristics around clump-type vegetation. Journal of Hydro-Environment Research 4 (1), 15–25.

Tanino, Y., Nepf, H. M., 2008. Laboratory investigation of mean drag in a random array of rigid, emergent cylinders. Journal of Hydraulic Engineering-ASCE 134 (1), 34–41.

Temmerman, S., Bouma, T. J., Van de Koppel, J., Van der Wal, D., De Vries, M. B., Herman, P. M. J., 2007. Vegetation causes channel erosion in a tidal landscape. Geology 35 (7), 631–634.

Thorne, C., 1990. Vegetation and erosion. Wiley, Chichester, Ch. Effect of vegetation on riverbank erosion and stability, pp. 125–143.

Tominaga, A., Nagao, M., Nezu, I., 1999. Flow structures and momentum transport processes in curved open channels with vegetation. In: 28th IAHR Congress. Graz, Austria.

Tsujimoto, T., 1999. Fluvial processes in streams with vegetation. Journal of Hydraulic Research 37 (6), 789–803.

Tsujimoto, T., Kitamura, T., 1995. Lateral bed-load transport and sand ridge formation near vegetation zone in an open channel. Journal of Hydroscience and Hydraulic Engineering 13, 35–45.

Udden, J., 1914. Mechanical composition of clastic sediments. Bulletin of the Geological Society of America 25, 655–744.

van de Koppel, J., Rietkerk, M., Dankers, N., Herman, P., 2005. Scale-dependent feedback and regular spatial patterns in young mussel beds. American Naturalist 165 (3), E66–E77.

Van Rijn, L., 1993. Principles of sediment transport in rivers, estuaries and coastal seas.Principles of sediment transport in rivers, estuaries and coastal seas. Aqua Publications,, Amsterdam, The Netherlands.

van Wesenbeeck, B. K., van de Koppel, J., Herman, P. M. J., Bouma, T. J., 2008. Does scale-dependent feedback explain spatial complexity in salt-marsh ecosystems? Oikos 117 (1), 152–159.

Vandenbruwaene, W., Temmerman, S., Bouma, T. J., Klaassen, P. C., de Vries, M. B., Callaghan, D. P., van Steeg, P., Dekker, F., van Duren, L. A., Martini, E., Balke, T., Biermans, G., Schoelynck, J., Meire, P., 2011. Flow interaction with dynamic vegetation patches: Implications for biogeomorphic evolution of a tidal landscape. Journal of Geophysical Research-Earth Surface 116.

Versteeg, H., Malalasekera, W., 1995. An introduction to Computational Fluid Dynamics. The finite volume method. Longman Group Ltd.

Vionnet, C., Tassi, P., Vide, J., 2004. Estimates of flow resistance and eddy viscosity coefficients for 2D modelling on vegetated floodplains. Hydrological Processes 18 (15), 2907–2926.

Vogel, S., 1994. Life in Moving Fluids: The Physical Biology of Flow. Princeton University Press.

Voulgaris, G., Trowbridge, J., 1998. Evaluation of the acoustic Doppler velocimeter (ADV) for turbulence measurements. Journal of Atmospheric and Oceanic Technology 15 (1, 2), 272–289.

Vreugdenhill, C., 1994. Numerical Methods for Shallow-Water Flow. Kluwer Academic Publishers.

Webster, J., Benfield, E., 1986. Vascular plant breakdown in fresh-water ecosystems. Annual review of ecology and systematics 17, 567–594.

Weerman, E. J., van de Koppel, J., Eppinga, M. B., Montserrat, F., Liu, Q.-X., Herman, P. M. J., 2010. Spatial Self-Organization on Intertidal Mudflats through Biophysical Stress Divergence. American Naturalist 176 (1), E15–E32.

Wentworth, C., 1922. A scale of grade and class terms for clastic sediments. Journal of Geology 30, 377–392.

White, B. L., Nepf, H. M., 2007. Shear instability and coherent structures in shallow flow adjacent to a porous layer. Journal of Fluid Mechanics 593, 1–32.

White, F., 1991. Viscous Fluid Flow. McGraw-Hill.

Wilson, C. A. M. E., Hoyt, J., Schnauder, I., 2008. Impact of foliage on the drag force of vegetation in aquatic flows. Journal of Hydraulic Research 134 (7), 885–891.

Wright, J., Hiley, P., Ham, S., Berrie, A., 1981. Comparison of three mapping procedures developed for river macrophytes. Freshwater Biology 11(4), 369379.

Wu, W., 2007. Computational River Dynamics. Taylor & Francis.

Wu, W., Wang, P., Chiba, N., 2004. Comparison of five depth-averaged 2-D turbulence models for river flows. Archives of Hydro-Engineering and Environmental Mechanics 51 (2), 183–200.

Wu, W., Wang, S., 2004. Riparian Vegetation and Fluvial Geomorphology. American Geophysical Union, Ch. A Depth-Averaged Two-Dimensional Numerical Model of Flow and Sediment Transport in Open Channels with Vegetation, pp. 253–265.

Yang, W., Choi, S.-U., 2010. A two-layer approach for depth-limited open-channel flows with submerged vegetation. Journal of Hydraulic Research 48 (4), 466–475.

Yen, B., 1991. Hydraulic resistance in open channels. Water Resource Publications, Highlands Ranch, CO.

Yen, B., 2002. Open channel flow resistance. Journal of Hydraulic Engineering-ASCE 128 (1), 20–39.

Zhang, M., Li, C. W., Shen, Y., 2013. Depth-averaged modeling of free surface flows in open channels with emerged and submerged vegetation. Applied Mathematical Modelling 37 (1-2), 540–553.

Zhang, Y., Baptista, A. M., 2008. SELFE: A semi-implicit Eulerian-Lagrangian finite-element model for cross-scale ocean circulation. Ocean Modelling 21 (3-4), 71–96.

Zienkiewicz, O., Taylor, R., 2000. Finite Element Method, 5th Edition. Vol. 3 - Fluid Dynamics. Elsevier.

Zong, L., Nepf, H., 2010. Flow and deposition in and around a finite patch of vegetation. Geomorphology 116 (3-4, SI), 363–372, 40th Binghamton Geomorphology Symposium, Virginia Tech Blacksburg, Blacksburg, VA, Oct 02-04, 2009.

Zong, L., Nepf, H., 2011. Spatial distribution of deposition within a patch of vegetation. Water Resources Research 47.

Zong, L., Nepf, H., 2012. Vortex development behind a finite porous obstruction in a channel. Journal of Fluid Mechanics 691, 368–391.

A

Vegetation Characteristics

A.1 Definition of geometric variables

water height	H	[m]
vegetation height	k	[m]
stem diameter	d	[m]
stem separation (center to center)	ΔS	[m]
stem separation (edge to edge)	ΔS_e	[m]
stem number	m	[1/m^2]
unit surface area	A	[m^2]
vegetation surface area	A_v	[m^2]

A.2 Relation between geometric variables

stem number and stem spacing

$$m = \frac{1}{l_s l_n} \tag{A.1}$$

with l_s and l_n respectively the average longitudinal and transversal spacing.

stem number and stem separation

$$\Delta S = \frac{1}{\sqrt{m}} \tag{A.2}$$

$$\Delta S_e = \frac{1}{\sqrt{m} - d} \tag{A.3}$$

solid volume fraction, c or ϕ

$$\begin{cases} submerged: & \mathrm{c} = \phi = \frac{A_v k}{AH} = \frac{m\pi D^2/4k}{H} \\ emergent: & \mathrm{c} = \phi = \frac{A_v k}{AH} = \frac{m\pi D^2}{4} \end{cases} \tag{A.4}$$

frontal area per stem: a_s $[\mathrm{m}^2]$

$$\begin{cases} submerged: & a_s = \alpha_v dk \\ emergent: & a_s = \alpha_v dH \end{cases} \tag{A.5}$$

with α_v a shape factor for the vegetation, which can be set on 1 for a rigid cylinder.

frontal area per canopy volume: a $[\mathrm{m}^{-1}]$

$$a = md = \frac{dh}{\Delta S^2 H} = \frac{d}{\Delta S^2} \tag{A.6}$$

roughness density = projected frontal area: λ_v [-]

$$_v = ma_s = m\alpha_v dk = mdk \tag{A.7}$$

$$= \frac{4\alpha_v k c_v}{\pi d} \tag{A.8}$$

$$= ah \tag{A.9}$$

A.3 Coefficients to calculate velocity profiles.

In this section of the Appendix, expressions for coefficients or parameters which are not mentioned, but used in the resistance equations described in Chapter 6 are written completely.

A.3.1 Parameters of Baptist et al. (2007)

In this subsection, the coefficients and parameters to obtain a velocity profile in case of submerged vegetation using the method of Baptist et al. (2007) are summarised. The parameters are written down in the order as they are calculated in the hydraulic routine. In the equations below is c_p the turbulent intensity [-], l a mixing length [m], L the length scale for eddies between the vegetation [m] and z_0 the roughness height in the logarithmic velocity profile [m].

$$
\begin{aligned}
l &= \sqrt{\tfrac{1-A_v}{m}} \\
c_p &= \tfrac{0.015\sqrt{Hk}}{l} \\
L &= \sqrt{\tfrac{c_p l}{C_D m d}} \\
z_0 &= (k-d)\exp -\kappa\sqrt{\tfrac{2L}{c_p l}\left(1+\tfrac{L}{H-k}\right)}
\end{aligned}
$$

A.3.2 Parameters of Klopstra et al. (1997)

In this subsection, the coefficients and parameters to obtain a velocity profile in case of submerged vegetation using the method of Klopstra et al. (1997) are summarised. z_0 is the length scale for bed roughness of the surface layer [m], u_{s0} is the characteristic constant flow velocity in non-submerged vegetation [m/s], h_s the distance between the top of the vegetation and the virtual bed of surface layer [m] and α a characteristic length scale [m]. C_1, C_2, C_3, A, E and F are coefficients

$$
\begin{aligned}
\alpha &= 0.0793\ k\ ln\tfrac{H}{k}\text{ - 0.00090 and } \alpha >= 0.001\\
A &= \tfrac{mdC_D}{2\alpha}\\
C_1 &= \tfrac{-2g(H-k)i}{\alpha\sqrt{2A}\left(\exp^{-k\sqrt{2A}}+\exp^{-k\sqrt{2A}}\right)}\\
C_2 &= \text{-}C_1\\
C_3 &= C_2/i\\
E &= \tfrac{\sqrt{2A}C_3\exp^{k\sqrt{2A}}}{2\sqrt{C_3\exp^{k\sqrt{2A}}+u_{v0}^2}}\\
F &= \tfrac{\kappa\sqrt{C_3\exp^{k\sqrt{2A}+u_{v0}^2}}}{\sqrt{g(H-(k-hs))}}\\
h_s &= g\tfrac{1+\sqrt{1+\frac{4E^2\kappa^2(H-k)}{g}}}{2E^2\kappa^2}\\
u_{s0} &= \sqrt{\tfrac{2gi}{C_D mD}}\\
u_{v0} &= u_{s0}/\sqrt{i}
\end{aligned}
$$

$$
\begin{aligned}
U = \frac{\sqrt{i}}{H^{1/2}}&\left[\frac{2}{\sqrt{2A}}\left(\sqrt{C_3e^{k\sqrt{2A}}+u_{v0}^2}-\sqrt{C_3+u_{v0}^2}\right)\right]\\
+\frac{\sqrt{i}}{H^{1/2}}&\left[\frac{u_{v0}}{\sqrt{2A}}\ln\left(\frac{(\sqrt{C_3e^{k\sqrt{2A}}+u_{v0}^2}-u_{v0})\cdot(\sqrt{C_3+u_{v0}^2}+u_{v0})}{(\sqrt{C_3e^{k\sqrt{2A}}+u_{v0}^2}+u_{v0})\cdot(\sqrt{C_3+u_{v0}^2}-u_{v0})}\right)\right]\\
+\frac{\sqrt{i}}{H^{1/2}}&\left[\frac{\sqrt{g(H-(k-h_s))}}{\kappa}\left\{(H-(k-h_s))\ln\left(\frac{H-(k-h_s)}{z_0}\right)-h_s\ln\left(\frac{h_s}{z_0}\right)-(H-k)\right\}\right]
\end{aligned}
\tag{A.10}
$$

B
Studies selected for Configurations of uniform Vegetation

Table B.1: Overview of the experimental data of uniform vegetation used to validate the model with vegetation resistance formulae. L represents the flume length, B the flume width, S the channel slope, n_m the total Manning coefficient, H the water depth, k the vegetation height, m the number of stems per unit area, ΔS the distance between the stems, d the diameter of the stems and C_d the used drag coefficient.

No.	L [m]	B [m]	S [m/m]	Q [$\mathrm{m^3/s}$]	n_m [$\mathrm{s/m^{1/3}}$]	H [m]	k [m]	k/H [%]	m [$\mathrm{1/m^2}$]	ΔS [m]	d [m]	Cd [-]
Dunn et al. (1996)												
Rigid dowels, vegetation over full flume length												
1	19.5	0.91	0.0036	0.179	0.034	0.335	0.1175	0.35	172	0.0762	0.0064	1
2	19.5	0.91	0.0036	0.088	0.041	0.229	0.1175	0.51	172	0.0762	0.0064	1
3	19.5	0.91	0.0036	0.046	0.048	0.164	0.1175	0.72	172	0.0762	0.0064	1
4	19.5	0.91	0.0076	0.178	0.038	0.276	0.1175	0.43	172	0.0762	0.0064	1
5	19.5	0.91	0.0076	0.098	0.045	0.203	0.1175	0.58	172	0.0762	0.0064	1
6	19.5	0.91	0.0036	0.178	0.025	0.267	0.1175	0.44	43	0.1524	0.0064	1
7	19.5	0.91	0.0036	0.098	0.027	0.183	0.1175	0.64	43	0.1524	0.0064	1
8	19.5	0.91	0.0036	0.178	0.042	0.391	0.1175	0.30	388	0.0508	0.0064	1
9	19.5	0.91	0.0036	0.095	0.034	0.214	0.1175	0.55	388	0.0508	0.0064	1
10	19.5	0.91	0.0161	0.180	0.052	0.265	0.1175	0.44	388	0.0508	0.0064	1
11	19.5	0.91	0.0036	0.177	0.031	0.311	0.1175	0.38	97	0.1016	0.0064	1
12	19.5	0.91	0.0110	0.181	0.036	0.233	0.1175	0.50	97	0.1016	0.0064	1
Dunn et al. (1996)												
Flexible dowels, vegetation over full flume length												
1	19.5	0.91	0.0036	0.179	0.039	0.368	0.152	0.41	172	0.0762	0.0064	1
2	19.5	0.91	0.0101	0.180	0.034	0.232	0.115	0.50	172	0.0762	0.0064	1
3	19.5	0.91	0.0036	0.093	0.045	0.257	0.132	0.51	172	0.0762	0.0064	1
4	19.5	0.91	0.0076	0.179	0.020	0.230	0.097	0.42	43	0.1524	0.0064	1
5	19.5	0.91	0.0076	0.078	0.061	0.279	0.161	0.58	388	0.0508	0.0064	1
6	19.5	0.91	0.0101	0.179	0.046	0.284	0.121	0.43	388	0.0508	0.0064	1

Table B.2: Table Cont'd

No.	L [m]	B [m]	S [m/m]	Q [m^3/s]	n_m [$s/m^{1/3}$]	H [m]	k [m]	k/H [%]	m [$1/m^2$]	ΔS [m]	d [m]	Cd [-]
Liu et al. (2008)												
Acrylic dowels (rigid). Length of vegetation zone is 3 m.												
1	4.3	0.3	0.003	0.0057	0.023	0.060	0.0076	> 1	199	0.071	0.00635	1
2	4.3	0.3	0.003	0.0057	0.028	0.071	0.0076	> 1	370	0.051	0.00635	1
3	4.3	0.3	0.003	0.0057	0.020	0.055	0.0076	> 1	96	0.102	0.00635	1
4	4.3	0.3	0.003	0.0114	0.022	0.097	0.0076	0.78	199	0.071	0.00635	1
5	4.3	0.3	0.003	0.0114	0.024	0.101	0.0076	0.75	370	0.051	0.00635	1
6	4.3	0.3	0.003	0.0114	0.019	0.087	0.0076	0.87	96	0.102	0.00635	1
7	4.3	0.3	0.003	0.0044	0.031	0.065	0.0076	> 1	494	0.045	0.00635	1
8	4.3	0.3	0.003	0.0044	0.032	0.066	0.0076	> 1	494	0.045	0.00635	1
9	4.3	0.3	0.003	0.0044	0.034	0.068	0.0076	> 1	494	0.045	0.00635	1
10	4.3	0.3	0.003	0.0044	0.038	0.074	0.0076	> 1	494	0.045	0.00635	1
11	4.3	0.3	0.003	0.0044	0.031	0.065	0.0076	> 1	494	0.045	0.00635	1
12	4.3	0.3	0.003	0.0044	0.038	0.074	0.0076	> 1	494	0.045	0.00635	1
13	4.3	0.3	0.003	0.0114	0.027	0.114	0.0076	0.67	494	0.045	0.00635	1
14	4.3	0.3	0.003	0.0114	0.027	0.115	0.0076	0.66	494	0.045	0.00635	1
15	4.3	0.3	0.003	0.0114	0.027	0.118	0.0076	0.64	494	0.045	0.00635	1
16	4.3	0.3	0.003	0.0114	0.029	0.119	0.0076	0.64	494	0.045	0.00635	1
17	4.3	0.3	0.003	0.0114	0.027	0.114	0.0076	0.67	494	0.045	0.00635	1
18	4.3	0.3	0.003	0.0114	0.029	0.119	0.0076	0.64	494	0.045	0.00635	1

Table B.3: Table Cont'd

No.	L	B	S	Q	n_m	H	k	k/H	m	ΔS	d	Cd
	[m]	[m]	[m/m]	$[\mathrm{m^3/s}]$	$[\mathrm{s/m^{1/3}}]$	[m]	[m]	[%]	$[1/\mathrm{m^2}]$	[m]	[m]	[-]
Cheng (2011)												
Rigid, cylindrical dowels in staggered pattern. Length of vegetation zone is 9.6 m												
1	12	0.3	0.004	0.0076	0.067	0.15	0.1	0.67	2221	0.0212	0.0032	1
2	12	0.3	0.004	0.0111	0.054	0.17	0.1	0.59	2221	0.0212	0.0032	1
3	12	0.3	0.004	0.0152	0.049	0.20	0.1	0.50	2221	0.0212	0.0032	1
4	12	0.3	0.004	0.0099	0.042	0.13	0.1	0.77	556	0.0424	0.0032	1
5	12	0.3	0.004	0.0128	0.040	0.15	0.1	0.67	556	0.0424	0.0032	1
6	12	0.3	0.004	0.0161	0.037	0.17	0.1	0.59	556	0.0424	0.0032	1
7	12	0.3	0.004	0.0205	0.036	0.20	0.1	0.50	556	0.0424	0.0032	1
8	12	0.3	0.004	0.0038	0.109	0.13	0.1	0.77	2221	0.0212	0.0066	1
9	12	0.3	0.004	0.0059	0.086	0.15	0.1	0.67	2221	0.0212	0.0066	1
10	12	0.3	0.004	0.0079	0.076	0.17	0.1	0.59	2221	0.0212	0.0066	1
11	12	0.3	0.004	0.0095	0.078	0.20	0.1	0.50	2221	0.0212	0.0066	1
12	12	0.3	0.004	0.0062	0.067	0.13	0.1	0.77	556	0.0424	0.0066	1
13	12	0.3	0.004	0.0096	0.053	0.15	0.1	0.67	556	0.0424	0.0066	1
14	12	0.3	0.004	0.0123	0.049	0.17	0.1	0.59	556	0.0424	0.0066	1
15	12	0.3	0.004	0.0161	0.046	0.20	0.1	0.50	556	0.0424	0.0066	1
16	12	0.3	0.004	0.0030	0.139	0.13	0.1	0.77	556	0.0424	0.0083	1
17	12	0.3	0.004	0.0046	0.110	0.15	0.1	0.67	2221	0.0212	0.0083	1
18	12	0.3	0.004	0.0072	0.083	0.17	0.1	0.59	2221	0.0212	0.0083	1
19	12	0.3	0.004	0.0114	0.065	0.20	0.1	0.50	2221	0.0212	0.0083	1
20	12	0.3	0.004	0.0059	0.071	0.13	0.1	0.77	2221	0.0212	0.0083	1
21	12	0.3	0.004	0.0079	0.064	0.15	0.1	0.67	556	0.0424	0.0083	1
22	12	0.3	0.004	0.0116	0.051	0.17	0.1	0.59	556	0.0424	0.0083	1
23	12	0.3	0.004	0.0154	0.048	0.20	0.1	0.50	556	0.0424	0.0083	1

Table B.4: Table Cont'd

No.	L	B	S	Q	n_m	H	k	k/H	m	ΔS	d	Cd
	[m]	[m]	[m/m]	[m^3/s]	[$s/m^{1/3}$]	[m]	[m]	[%]	[$1/m^2$]	[m]	[m]	[-]
Jarvela (2005)												
Natural, flexible wheat plants. Length of vegetation zone is 6 m. Non-uniform conditions.												
1	36	1.1	0.0	40	0.110	0.3060	0.205	0.67	12000	0.00912	0.0028	1
2	36	1.1	0.0	100	0.069	0.3084	0.155	0.50	12000	0.00912	0.0028	1
3	36	1.1	0.0	40	0.095	0.4065	0.230	0.57	12000	0.00912	0.0028	1
4	36	1.1	0.0	100	0.061	0.4044	0.190	0.47	12000	0.00912	0.0028	1
5	36	1.1	0.0	143	0.053	0.4070	0.160	0.39	12000	0.00912	0.0028	1
6	36	1.1	0.0	40	0.081	0.5044	0.245	0.49	12000	0.00912	0.0028	1
7	36	1.1	0.0	100	0.054	0.4950	0.220	0.44	12000	0.00912	0.0028	1
8	36	1.1	0.0	100	0.050	0.7065	0.260	0.37	12000	0.00912	0.0028	1
9	36	1.1	0.0	143	0.042	0.7037	0.215	0.31	12000	0.00912	0.0028	1
Li et al. (2013)												
flexible												
1	30	0.5	0.0	0.0597	0.052	0.5	0.65	> 1	40	0.0212	0.01808	1
2	30	0.5	0.0	0.0597	0.059	0.5	0.65	> 1	50	0.0212	0.01808	1
3	30	0.5	0.0	0.0597	0.069	0.5	0.65	> 1	60	0.0212	0.01808	1
4	30	0.5	0.0	0.0597	0.074	0.5	0.65	> 1	70	0.0212	0.01808	1

Table B.5: Table Cont'd

No.	L [m]	B [m]	S [m/m]	Q [m^3/s]	n_m [$\mathrm{s}/\mathrm{m}^{1/3}$]	H [m]	k [m]	k/H [%]	m [$1/\mathrm{m}^2$]	ΔS [m]	d [m]	Cd [-]
Kubrak et al. (2008)												
Uniform flow conditions, flexible vegetation consists of cylindrical stems of elliptical cross-section												
1	16	0.58	0.0087	0.0433	0.089	0.2661	0.163	0.61	10000	0.01	0.000825	1
2	16	0.58	0.0087	0.0384	0.096	0.2576	0.163	0.63	10000	0.01	0.000825	1
3	16	0.58	0.0087	0.0333	0.105	0.2475	0.164	0.66	10000	0.01	0.000825	1
4	16	0.58	0.0087	0.0274	0.113	0.2275	0.164	0.72	10000	0.01	0.000825	1
5	16	0.58	0.0174	0.0422	0.102	0.2236	0.161	0.72	10000	0.01	0.000825	1
6	16	0.58	0.0174	0.0385	0.108	0.2184	0.162	0.74	10000	0.01	0.000825	1
7	16	0.58	0.0174	0.0333	0.116	0.2068	0.161	0.79	10000	0.01	0.000825	1
8	16	0.58	0.0174	0.0274	0.130	0.1951	0.162	0.83	10000	0.01	0.000825	1
9	16	0.58	0.0087	0.0525	0.063	0.2386	0.153	0.64	2500	0.02	0.000825	1
10	16	0.58	0.0087	0.0425	0.067	0.2136	0.154	0.72	2500	0.02	0.000825	1
11	16	0.58	0.0087	0.0332	0.075	0.1935	0.155	0.80	2500	0.02	0.000825	1
12	16	0.58	0.0174	0.0751	0.053	0.2131	0.132	0.62	2500	0.02	0.000825	1
13	16	0.58	0.0174	0.0650	0.053	0.1925	0.131	0.68	2500	0.02	0.000825	1
14	16	0.58	0.0174	0.0547	0.058	0.1799	0.133	0.74	2500	0.02	0.000825	1
15	16	0.58	0.0087	0.0605	0.055	0.2386	0.151	0.63	2500	0.02	0.000825	1
16	16	0.58	0.0087	0.0504	0.060	0.2234	0.152	0.68	2500	0.02	0.000825	1
17	16	0.58	0.0087	0.0408	0.064	0.2005	0.153	0.76	2500	0.02	0.000825	1
18	16	0.58	0.0174	0.0693	0.052	0.1962	0.132	0.67	2500	0.02	0.000825	1
19	16	0.58	0.0174	0.0555	0.061	0.1876	0.139	0.74	2500	0.02	0.000825	1
20	16	0.58	0.0087	0.0609	0.056	0.2421	0.151	0.62	2500	0.02	0.000825	1
21	16	0.58	0.0087	0.0500	0.061	0.2246	0.153	0.68	2500	0.02	0.000825	1
22	16	0.58	0.0087	0.0408	0.066	0.2053	0.156	0.75	2500	0.02	0.000825	1
23	16	0.58	0.0174	0.0693	0.056	0.2077	0.138	0.66	2500	0.02	0.000825	1
24	16	0.58	0.0174	0.0466	0.075	0.1932	0.142	0.73	2500	0.02	0.000825	1
25	16	0.58	0.0174	0.0553	0.058	0.1806	0.143	0.79	2500	0.02	0.000825	1

C
Model Description - Numerical Implementation

C.1 Numerical approximation: full-matrix

Equation 5.18 can be further rearranged, with unknown values of η at a time (N+1) collected on the left side and known values of η at time N.

$$\begin{aligned}
&\left[1+\frac{g\theta^2\Delta t^2}{\Delta x^2}\frac{H^N_{i+1/2,j}}{A^N_{i+1/2,j}}+\frac{g\theta^2\Delta t^2}{\Delta x^2}\frac{H^N_{i-1/2,j}}{A^N_{i-1/2,j}}+\frac{g\theta^2\Delta t^2}{\Delta y^2}\frac{H^N_{i,j+1/2}}{A^N_{i,j+1/2}}+\frac{g\theta^2\Delta t^2}{\Delta y^2}\frac{H^N_{i,j-1/2}}{A^N_{i,j-1/2}}\right]\eta^{N+1}_{i,j}-\\
&\left[\frac{g\theta^2\Delta t^2}{\Delta x^2}\frac{H^N_{i+1/2,j}}{A^N_{i+1/2,j}}\right]\eta^{N+1}_{i+1,j}-\left[\frac{g\theta^2\Delta t^2}{\Delta x^2}\frac{H^N_{i-1/2,j}}{A^N_{i-1/2,j}}\right]\eta^{N+1}_{i-1,j}-\\
&\left[\frac{g\theta^2\Delta t^2}{\Delta y^2}\frac{H^N_{i,j+1/2}}{A^N_{i,j+1/2}}\right]\eta^{N+1}_{i,j+1}-\left[\frac{g\theta^2\Delta t^2}{\Delta y^2}\frac{H^N_{i,j-1/2}}{A^N_{i,j-1/2}}\right]\eta^{N+1}_{i,j-1}=\eta^N_{i,j}\\
&-\theta\frac{\Delta t}{\Delta x}\left(\frac{H^N_{i+1/2,j}G^N_{i+1/2,j}}{A^N_{i+1/2,j}}-\frac{H^N_{i-1/2,j}G^N_{i-1/2,j}}{A^N_{i-1/2,j}}\right)+\\
&\theta\frac{\Delta t}{\Delta y}\left(\frac{H^N_{i,j+1/2}G^N_{i,j+1/2}}{A^N_{i,j+1/2}}-\frac{H^N_{i,j-1/2}G^N_{i,j-1/2}}{A^N_{i,j-1/2}}\right)\\
&-(1-\theta)\frac{\Delta t}{\Delta x}\left(H^N_{i+1/2,j}U^N_{i+1/2,j}+H^N_{i-1/2,j}U^N_{i-1/2,j}\right)\\
&-(1-\theta)\frac{\Delta t}{\Delta y}\left(H^N_{i,j+1/2}U^N_{i,j+1/2}+H^N_{i,j-1/2}U^N_{i,j-1/2}\right)
\end{aligned} \tag{C.1}$$

On the left hand side, the different coefficients for the unknown variables are the elements of the main diagonal d (for $\eta_{i,j}$ and side-diagonals of the left-hand side matrix d_1, d_2, d_3 and d_4 for respectively $\eta_{i+1,j}$, $\eta_{i,j+1}$, $\eta_{i-1,j}$ and $\eta_{i,j-1}$. The implementation of the matrices is worked out in section C.2.2.

C.2 Implementation in the STRIVE2D package

C.2.1 System module

The grid and index definitions are all defined in the system module. In Figure C.1, the positions of the three state variables of the 2D-SWE are depicted. The U-velocity calculation points are situated on the north and south faces of a cell, illustrated with an "X". The V-velocity points are denoted with a square and situated on the east and west side of each grid cell. The free surface η is defined in the center of the computational cell. For the indices, the system described in Martin (2004) is used.

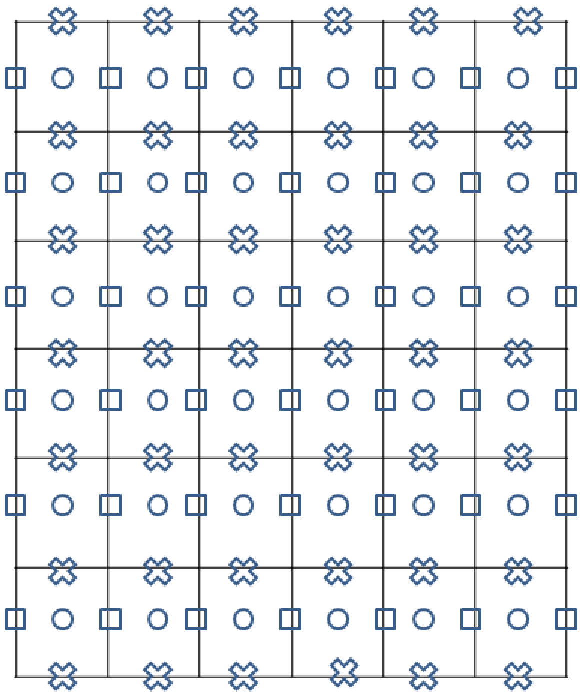

Figure C.1: Grid layout for the 2D-SWE using a cartesian, staggered grid.

As such, the number of calculation points for each variable can be easily calculated:

$$U : \text{Numincx} = (\text{ Numrows} + 1\ ) * \text{Numcols}$$
$$V : \text{Numincy} = \text{Numrows} * (\text{ Numcols} + 1\ )$$
$$\eta : \text{Numnodes} = \text{Numrows} * \text{Numcols}$$

Most grid indices are calculated in the FORTRAN subroutine ”System-initialise”, and are explained and summarized below.

C.2.1.1 Node points

For η, a numbering along the rows is selected, as deptictedd in Figure C.2.

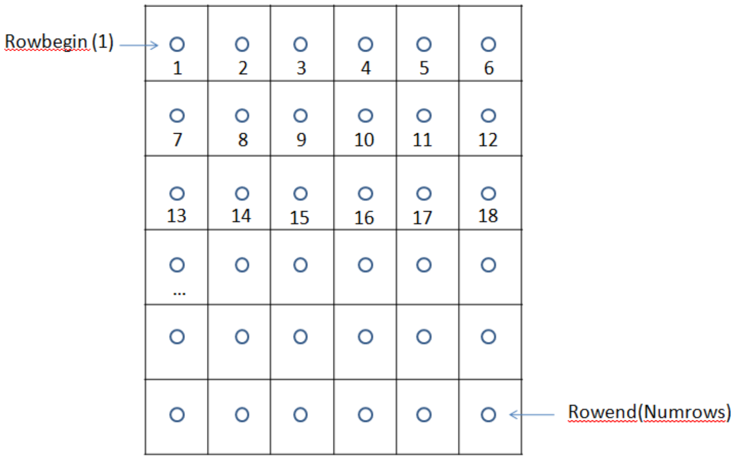

Figure C.2: Position of the computational nodes for the water surface elevation.

The variables Rowbegin and Rowend (each with length $Numrows$) respectively indicate the starting and ending node number of each row. The variables which are indicating neighbouring node cells are respectively YP1, YM1, XP1 and XM1. The position of these variables in the grid are indicated in Figure C.3. It should be noted that at the edges, the value of the neighbours will coincide with cell (i,j).

XM1 : Row 1, Row , Row 2, , Row $(Numrows - 1)$
YM1 : Col 1, Col 1, Col 2, , Col $(Numcols - 1)$
XP1 : Row 2, Row3 , , Row $(Numrows - 1)$, Row $(Numrows)$, Row $(Numrows)$
YP1 : Col 2, Col 3, Col 4, , Col $(Numcols)$, Col$(Numcols)$

The surrounding face values for cell (i,j) are implemented in a similar way.

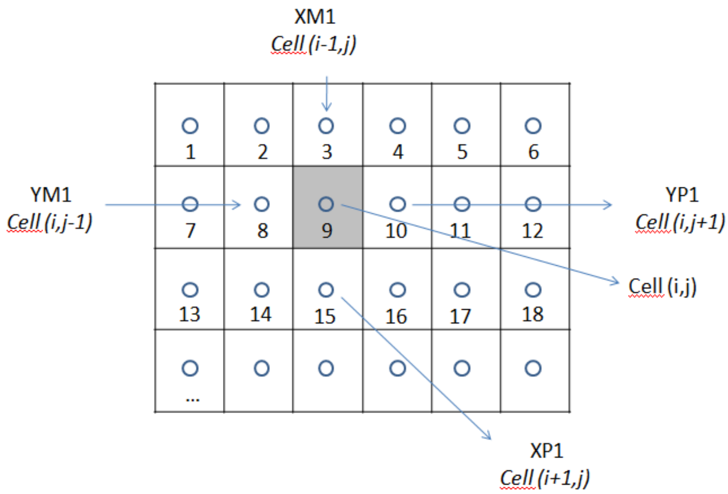

Figure C.3: Definition of the neighbouring cells of cell (i,j).

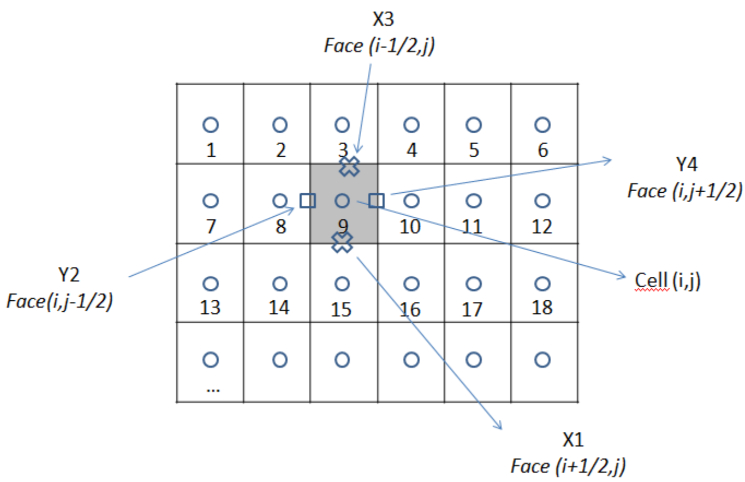

Figure C.4: Definition of the neighbouring faces of cell (i,j).

X1 : Numnodes + Numcols

Y2 : (Row1$(Numcols + 1)$): 1, 2, . . . , Numcols-1

X3 : Numnodes

Y4 : (Row1$(Numcols + 1)$): 2, 3, . . . , Numcols, Numcols+1

C.2.1.2 X face points

For the numbering of the faces, a system like in the picture below is followed:

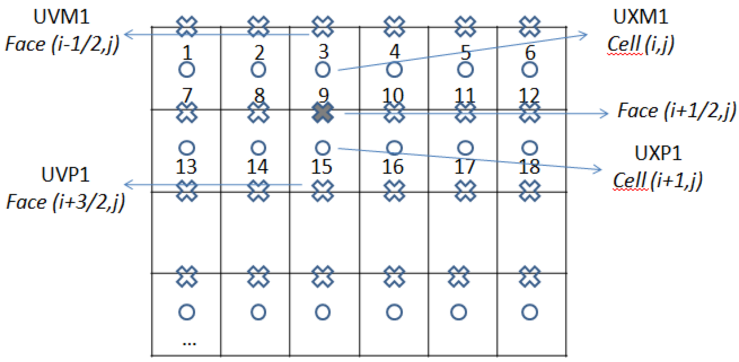

Figure C.5: Non regular grid with several options. Every white box represents a section with another option and has its own length.

C.2.1.3 Y face points

For the numbering of the faces, a system like in the picture below is followed:

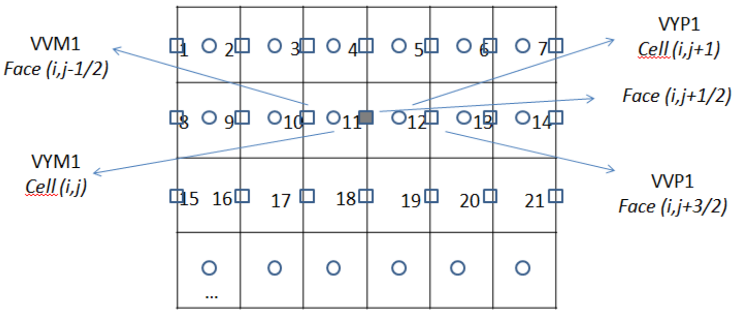

Figure C.6: Non regular grid with several options. Every white box represents a section with another option and has its own length.

All the indices have a length Numincy. For the values of VYM1 and VYP1, respectively the first and last column value are taken twice. For VVM1 and VVP1 the same is done, but face values are taken. This means $Numcols + 1$ values are available, and respectively the last and first value for the row is omitted.

C.2.2 Transwater module

C.2.2.1 Flow chart of the Transwater module.

A general flow chart of the numerical implementation of the 2D numerical code is given in section 5.9. Below, the detailed flow chart, in pseudo-code, of the "'DynamicsTranswater2"' module is given. This is the FORTRAN subroutine where the new velocities and water depths are calculated, and form as such the core of the TRANSWATER module of STRIVE-2D.

```
DynamicsTranswater2
 |__! Resistance coefficient
 |   |__SetResistPar
 |      Update variables are MnX, Mny, CzX, CzY .
 |__! A* faces
 |   Update variables are AvX, AvY .
 |__! Semi-Lagrangian method
 |   Update variables are FuX, FvY .
 |__! G* faces
 |   Update variables are GuX, GvY .
 |__! New Free Surface (EtaNew)
 |   Update variables is EtaNew .
 |   |__Delta
 |   |  Update variable Delta (eq 38) .
 |   |__qRHS
 |   |  Update variable qRHS (eq 39) .
 |   |__LHS
 |       |__Diagonals
 |       |  Update diagonals d, d1, d2, d3, d4 (eq 40) .
 |       |__Boundary condtions
 |       |  Update diagonals d, d1, d2, d3, d4, qRHS (eq 40) .
 |       |__Solve Matrix
 |__! New values ! Depth
 |   Update variable Eta .
 |   |__Adjacent faces
 |   |  Update variable EtaXP1, EtaXM1, EtaYP1, EtaYM1 based on new Eta.
 |   |__Boundary conditions
 |      Update variable EtaXP1, EtaXM1, EtaYP1, EtaYM1 based on BC.
 |__! New values ! Velocity
     |__Velocity calculation
     |  Update variables UVel and VVel (eq 34 and 35) .
     |__Boundary conditions
        Update variable UVel and VVel based on BC .
```

```
├─ Set Total Depth
│   Update depth variables Hux, Hvy, BHux, BHvy .
├─ Average Depth
│   Update average depth variables HTD, BHTD, h1, h2, h3, h4 .
└─ Average Velocity
    Update average velocity variables AveU, AveV, DirectU, DirectV .
```

C.2.2.2 Matrix implementation.

The set of algebraic equation, resulting from the discretisation of equations 5.10, results in the following matrix multiplication.

$$[\,LHS\,] * [\,x\,] = [\,RHS\,] \tag{C.2}$$

C.2.2.3 Implementation of vector of unknowns (X).

The vector of the unknowns X is numbered using the convention depicted in C.2. As such, the vector of unknowns X is built by adding row by row. The vector has $Numnodes$ elements, as is the number of unknowns.

$$RHS = \begin{bmatrix} \eta(1)^{N+1} \\ \eta(2)^{N+1} \\ \eta(3)^{N+1} \\ \eta(4)^{N+1} \\ \eta(5)^{N+1} \\ \dots \\ \eta(20)^{N+1} \\ \eta(21)^{N+1} \\ \dots \\ \eta(end)^{N+1} \end{bmatrix} = \begin{bmatrix} \eta(1,1)^{N+1} \\ \eta(1,2)^{N+1} \\ \eta(1,3)^{N+1} \\ \eta(1,4)^{N+1} \\ \eta(1,5)^{N+1} \\ \dots \\ \eta(1,end)^{N+1} \\ \eta(2,1)^{N+1} \\ \dots \\ \eta(end,end)^{N+1} \end{bmatrix} \tag{C.3}$$

C.2.2.4 Implementation of the Right-Hand Side (RHS).

RHS is the vector of the terms which are a function of known variables, at a time N. The numbering convention is equal as for vector X, with a total size of the matrix of $Numnodes$ elementes.

$$RHS = \begin{bmatrix} f(\eta(1)^N) \\ f(\eta(2)^N) \\ f(\eta(3)^N) \\ f(\eta(4)^N) \\ f(\eta(5)^N) \\ \cdots \\ f(\eta(20)^N) \\ f(\eta(21)^N) \\ \cdots \\ f(\eta(end)^N) \end{bmatrix} = \begin{bmatrix} f(\eta(1,1)^N) \\ f(\eta(1,2)^N) \\ f(\eta(1,3)^N) \\ f(\eta(1,4)^N) \\ f(\eta(1,5)^N) \\ \cdots \\ f(\eta(1,end)^N) \\ f(\eta(2,1)^N) \\ \cdots \\ f(\eta(end,end)^N) \end{bmatrix} \tag{C.4}$$

For a position (i,j) in the grid, an element of this right-hand side vector is defined as follows:

$$\begin{aligned} fr_x &= \frac{\Delta t}{\Delta x} \\ fr_y &= \frac{\Delta t}{\Delta y} \end{aligned} \tag{C.5}$$

$$\begin{aligned} RHS(i,j) = \eta_{i,j}^N &- (1-\theta) fr_x \left[(HU)_{i+1/2,j}^N - (HU)_{i-1/2,j}^N \right] \\ &- (1-\theta) fr_y \left[(HU)_{i,j+1/2}^N - (HU)_{i,j-1/2}^N \right] \\ &- \theta fr_x \left[\left(\frac{HG}{A} \right)_{i+1/2,j}^N - \left(\frac{HG}{A} \right)_{i-1/2,j}^N \right] \\ &- \theta fr_y \left[\left(\frac{HG}{A} \right)_{i,j+1/2}^N - \left(\frac{HG}{A} \right)_{i,j-1/2}^N \right] \end{aligned} \tag{C.6}$$

C.2.2.5 Implementation of the Left-Hand Side (LHS).

The sparse matrix is square and has a size of Numnodes * Numnodes. The matrix LHS is a pentadiagonal matrix. The matrix is positive definite and symmetric.

$$LHS = \begin{bmatrix} d(1) & -d4(1) & \cdots & \cdots & -d1(1) & \cdots & \cdots & \cdots & \cdots \\ -d2(2) & d(2) & -d4(2) & \cdots & \cdots & -d1(2) & \cdots & \cdots & \cdots \\ \cdots & -d2(3) & d(3) & -d4(3) & \cdots & \cdots & -d1(3) & \cdots & \cdots \\ \cdots & \cdots & \cdots & \cdots & \cdots & \cdots & \cdots & \cdots & \cdots \\ -d3(21) & \cdots & \cdots & -d2(21) & d(21) & -d4(21) & \cdots & \cdots & -d1(21) \end{bmatrix} \tag{C.7}$$

For a position (i,j) in the grid, an element of this left-hand side matrix is defined as follows:

$$
\begin{aligned}
f_x &= g\frac{\theta^2 \Delta t^2}{\Delta x^2} \\
f_y &= g\frac{\theta^2 \Delta t^2}{\Delta y^2}
\end{aligned}
\tag{C.8}
$$

Following, different diagonals of the matrix are defined

$$
\begin{aligned}
d1(i+1/2,j) =&\ f_x \frac{H^{N^2}_{i+1/2,j}}{A^N_{i+1/2,j}} \\
d2(i,j-1/2) =& f_y \frac{H^{N^2}_{i,j-1/2,j}}{A^N_{i,j-1/2}} \\
d3(i-1/2,j) =&\ f_x \frac{H^{N^2}_{i-1/2,j}}{A^N_{i-1/2,j}} \\
d4(i,j+1/2) =& f_y \frac{H^{N^2}_{i,j+1/2,j}}{A^N_{i,j+1/2}}
\end{aligned}
\tag{C.9}
$$

The definitions before are used for the determination of the left hand side matrix, together with the matrix of the unknowns X.

$$
\begin{aligned}
LHS(i,j) =& [1 + d1 + d3 + d2 + d4]\, \eta^{N+1}_{i,j} \\
- & \qquad [d1]\, \eta^{N+1}_{i+1,j} - [d3]\, \eta^{N+1}_{i-1,j} \\
- & \qquad [d2]\, \eta^{N+1}_{i,j-1} - [d4]\, \eta^{N+1}_{i,j+1}
\end{aligned}
\tag{C.10}
$$

D List of publications

D.1 International journal publications - a1

- Verschoren, V., Meire, D., Schoelynck, J., Buis, K., Troch, P., Meire, P., Temmerman, S. (submitted) Resistance and reconfiguration of natural flexible submerged vegetation in hydrodynamic river modeling.

- Roldan, R., Creëlle, S., Van Oyen, T., Meire, D., Herremans, A., Buis, K., Meire, P. and Troch, P. (submitted) Validation of LSPIV to acquire 2D free-surface flow fields for vegetated rivers. Flow measurements and instrumentation.

- Meire, D., Kondziolka, J., Nepf, H.M. (accepted) Interaction between neighbouring vegetation patches: impact on flow and deposition. Water Resources Research. 50, doi:10.1002/2013WR015070.

- Schoelynck J.*, Meire D.*, Bal K., Buis K., Troch P., Bouma T., Meire P, Temmerman S. (2013) Submerged macrophytes avoiding a negative feedback in reaction to hydrodynamic stress. Limnologica 43, 371-380.
  (*) both authors contributed equally.

- Meire, D., De Doncker L., Declercq F., Buis K., Troch P., Verhoeven R. (2010) Modelling river-floodplain interaction during flood propagation. Natural Hazards 55(1), 111-121. doi: 10.1007/s11069-010-9554-1

D.2 International conference publications - p1

- Meire, D., Kondziolka, J., Nepf, H.M. (accepted) Patches in a side-by-side configuration: a description of the flow and deposition fields. River Flow 2014.

- Meire D., Schoelynck J., Troch P., Bal K., Temmerman S., Meire P. (2012) Flow measurements around a submerged macrophyte patch in an in-situ flume setup. 9th International symposium on Ecohydraulics.

- Herremans A., Meire D., Troch P., Verhoeven R., Buis K., Meire P., Temmerman S., Verhoeven G. (2011) Development of a new optical imaging technique for studying the spatial heterogeneity in vegetated streams and rivers conference. Extended Abstracts of Ecohydraulics: linkages between hydraulics, morphodynamics & ecological processes in rivers.

- Meire D., De Doncker L., Troch P., Verhoeven R. (2009) Simulation of the filling and emptying processes between a river and its storage areas. International workshop on Environmental Hydraulics, 1st, Proceedings

D.3 International conference proceedings - c1

- Verschoren, V., Schoelynck, J., Buis, K., Meire, D., Bal, K., Meire, P., Temmerman, S. (2014) Implementation and implications of macrophyte reconfiguration in hydraulic river modeling, EGU- General Assembly conference, Vienna, 27/04/2014 - 02/05/2014.

- Buis K., Meire D., Schoelynck J., Verschoren V., Troch P., Meire P. (2013) The effect of spatial distributions of vegetation in lowland streams on hydraulic resistance. 4rd international multidisciplinary conference on hydrology and ecology (Hydro-Eco), Rennes, 13-16/05/2013.

- Verschoren V., Buis K., Schoelynck J., Meire D., Troch P., Meire P., Temmerman S. (2013) Modelling macrophyte growth to define 2D hydraulic resistance parameters in lowland rivers. 4rd international multidisciplinary conference on hydrology and ecology (Hydro-Eco), Rennes, 13-16/05/2013.

- Meire D., Troch P. (2012) An overview of the implementation of macrophytes as ecosystem engineers in hydrological modelling. 10791, EGU General Assemby, Vienna, 22-27/04/2012.

- Putteman J., Meire D., Troch P., Verhoeven R. (2011) Integrated water resources management in the Orange-Senqu-Fish catchment. International Conference on the Status and Future of the World's Large Rivers, Vienna, 11-14/04/2011.

- Meire D., Troch P. (2011) Flow-vegetation interaction in an integrated river ecosystem model. EGU General Assemby, Vienna, 03-08/04/2011.

- Meire D., Troch P., Buis K., Meire P. (2011) Incorporating spatial heterogeneity of flow-vegetation interaction in an integrated river ecosystem model. 3rd international multidisciplinary conference on hydrology and ecology (HydroEco), Vienna, 2-5/05/2011.

- De Doncker L., Verhoeven R. Troch P., Meire D., Buis K. (2011) Modelling of river flow and interaction with the ecosystem using the STRIVE model. International Conference on the Status and Future of the World's Large Rivers, Vienna, 11-14/04/2011.

- De Doncker L., Van Damme B., Meire D., Troch P., Verhoeven R., Buis K. (2011) Ecohydraulic modelling over different seasons with varying vegetation, 3rd international multidisciplinary conference on hydrology and ecology (HydroEco), Vienna, 2-5/05/2011.

- Buis K., Meire P., De Doncker L., Meire D., Anibas C., Batelaan O., Desmet N. (2011) An integrated model study on the role of lateral connections and process interactions in retention of matter in streams, 3rd international multidisciplinary conference on hydrology and ecology (HydroEco), Vienna, 2-5/05/2011.

D.4 National conference proceedings - c1

- Meire D., Troch P. (2010) The role of spatial heterogeneity in exchange processes of river ecosystems. 11th FirW PhD-symposium, Ghent University, 1/12/2010.